TILL GEOTECHNICS

AND

ICE SHEET DYNAMICS

KAREN ELIZABETH DOBBIE

A thesis submitted for the degree of Doctor of Philosophy

University of Edinburgh

1992

This thesis is entirely my own work except where otherwise stated.

Karen E. Dobbie

ABSTRACT

This thesis studies geotechnical properties of former subglacial sediments to establish the conditions found at the base of an ice sheet. Whilst many advances have been made in the theoretical analysis of ice sheet dynamics, little quantitative information exists about the physical processes that occur beneath an ice sheet. These processes depend on the type of surface over which the ice flows and on whether the base of the ice is melting. Until recently, most models of ice sheet flow have assumed that ice moves over a rigid surface as a result of deformation within the ice, or by sliding at its base. It has subsequently become clear that where ice overlies unlithified sediments they can deform, thus contributing to the forward motion of the ice. The basal boundary is difficult to observe directly. However information can be obtained indirectly by studying the sediments left behind when the ice has retreated.

An advancing ice sheet loads the sediments over which it flows. Sediments consolidate in response to this additional load, providing that water can drain from the sediment pores. Sediments underlying a basally melting ice sheet must still allow melt water to drain through them and thus will not consolidate to the same extent as a non-glacial sediment under the same load. The sediments expand on retreat of the ice. However they retain a record of the maximum pressure to which they were subjected, known as the preconsolidation pressure. The preconsolidation pressure is assumed to have occurred at the glacial maximum when the ice sheet was in a steady state, however the existence of a meltwater flux means that the preconsolidation pressure preserved is not a simple consequence of the overburden of ice and sediments.

A one dimensional drainage model is adopted to investigate subglacial groundwater flow. Melt water is assumed to drain vertically through an upper layer of low permeability sediments into an aquifer. The theoretical distribution of pressure in the one dimensional model is derived and a relationship between the effective pressure gradient, potential pressure gradient and gravitational gradient established.

This theory is tested for a site in the northern Netherlands. Preconsolidation pressures are measured in samples taken from different depths in a sediment core and the resulting vertical profile equated to the effective pressure gradient at the glacial maximum. The palaeopotential pressure gradient is inferred, from which a minimum basal melt rate is obtained. The effective pressure and potential pressure

components at the base of the ice are determined allowing the ice thickness to be calculated. Melt rate and ice thickness can be predicted by numerical ice sheet models. Results of this study can therefore be used to test these predictions and thus act as a constraint on the models. The Saalian ice sheet profile over the northern Netherlands is reconstructed and the basal shear stress inferred. The basal shear stress implied is lower than the yield strength of ice and thus ice sheet motion could not be due to internal deformation of the ice alone.

The shear strength of a sediment depends on the effective pressure acting on it. In subglacial sediments high water pressures can reduce effective pressure and hence the shear strength of the sediment. If the shear strength of the sediment is reduced below the yield strength of ice, the sediment will deform thus contributing to the forward motion of the ice.

The mechanical properties of subglacial sediments are an essential component of a deforming bed model, however they are only poorly constrained. A non-linear flow law is determined from ring shear tests for a typical till from the northern Netherlands. Results suggest that the subglacial system was sensitive to variations in basal effective pressure and shear stress. Modelling till deformation using this flow law indicates that, for a constant basal shear stress, stable sediment deformation can only occur within a narrow range of effective pressures. If ice sheet motion in the northern Netherlands was governed by a deforming sediment bed, then there must have been a mechanism which constrained the effective pressure within the narrow band defined by the flow law.

An inverse model is developed in which ice flux is inferred by superimposing a mass balance distribution on to the ice sheet profile obtained from the consolidation tests. The ice flux is assumed to be a result of a deforming till layer and thus the till flux is inferred. The effective pressure at the base of the ice and the thickness of the deforming layer are calculated to be relatively constant along the flow line. This also suggests that there must be a mechanism whereby the effective pressure at the base of the ice is constrained within a narrow range of values.

Channel formation at the ice/bed interface is considered as one possible mechanism through which effective pressures are sensitively adjusted so that they fall within the narrow range of values that permit till deformation to balance ice flux and thus stabilise the system.

ACKNOWLEDGEMENTS

I would like to thank Professor Geoffrey Boulton for setting up this project, for being a source of ideas and encouragement, and for reading through the first draft of the thesis. Dr. Mike Paul was very helpful throughout the project and is thanked for his interest and advice. He also read through the later edition of the thesis from a geotechnical point of view and is thanked for his comments. Dr. John Little is acknowledged for his help in the initial stages of the project.

Richard Hindmarsh is thanked for his help with the initial groundwater modelling. He was always incredibly patient, taking a lot of time to explain his "sumz" to me. He also read through the rheology chapter at very short notice. Paul Caban did not appear in Edinburgh until my final year and unwittingly offered to check through some equations one day. Since then his mathematical expertise and logistical support have been very valuable, especially in the final stages of the thesis and for these I am very grateful. Paul also read an earlier edition of the thesis and is thanked for his useful comments. Tony Payne also deserves thanks for taking an interest in my work and helping with the ice sheet modelling.

The Department of Civil and Offshore Engineering at Heriot Watt University and The Department of Civil Engineering and Building Science at Edinburgh University are acknowledged for the use of their soil mechanics laboratories. The Rijks Geologische Dienst in Haarlem are thanked for providing the sediment core and for the use of their laboratory. Mike Paul, Hugh Barras, David Ponniah, Jim Huchison and Floris Schokking are thanked for advice and discussion about the geotechnical experiments. Hugh Barras deserves special mention. Hughie was incredibly helpful at various stages of the project and always showed an interest in its progress.

Numerous people in the Department of Geology and Geophysics at Edinburgh University have helped with different aspects of the project: Geoff Angell, Ann Mennim, Diana Baty and Yvonne Cooper all deserve thanks. Shane is thanked for making the Departmental computer system "user friendly" and for his good humour. The geosecs are also acknowledged for their patience and good nature.

Pete Kinny, Tony Payne, Jon Turner and Gordon Watt are thanked for proof reading chapters of the thesis. Gordon is also thanked for helping me overcome my computer phobia.

Life in the Grant Institute would not have been the same without the fellow inmates of Research Room 4, who over the years have shared in the trials and tribulations of life as a Ph.D. student. Kevin Fielding and Gillie Hatton are thanked for the occasional long (?) lunch breaks, especially during the final stages of writing up.

Outwith the Grant Institute, various people have helped maintain my sanity over the past few months. Susan Hopkin, Jane Foster, Jean Curran, Jerry Parker, David Walker, Pete Kinny, and my flatmates are all thanked for trying to remind me that there is more to life than a thesis.

The project was supported financially by the Natural Environmental Research Council.

Finally, I would like to thank my parents for their constant support and encouragement over the years and it is to them that this thesis is dedicated.

CHAPTER 1

INTRODUCTION

CHAPTER 2

THE PROPERTIES OF SEDIMENTS AND THEIR RESPONSE TO APPLIED STRESS

CHAPTER 5

DEFORMATION OF SUBGLACIAL SEDIMENTS: DETERMINATION OF A FLOW LAW FOR THE DRENTHE TILL

CHAPTER 6

RECONSTRUCTION OF SUBGLACIAL CONDITIONS FROM ICE DYNAMICS

SYMBOLS USED IN TEXT

Symbols for equations defined in each chapter are listed in the order in which they appear in the text. Symbols are not repeated in each chapter where they remain the same as the initial derivation.

CHAPTER 1

τ_b	basal shear stress	ρ	density of ice
g	acceleration due to gravity	h	ice thickness
α	ice surface slope	τ_o	plastic yield strength of ice
L	distance from ice divide to the terminus		
x	point along ice sheet flow line, measured from the ice divide		
$\dot{\varepsilon}$	strain rate	τ	shear stress
A,n	ice flow law parameters	H	ice thickness at the ice divide
u	component of ice velocity in the x direction		

CHAPTER 2

σ	stress	σ_n	normal stress
τ	shear stress	$\sigma_1, \sigma_2, \sigma_3$	principal stresses
x,y,z	coordinates of the stress system (z is depth)		
ρ_b	bulk density	ρ_w	density of water
n	porosity	ρ_s	density of solid particles
V_v	volume of voids	V_s	volume of solids
p_w	pore water pressure	H	pressure head of water
σ'	effective stress	p	pressure
p'	effective pressure	P	potential
Z	potential head	V	velocity head
Q	volumetric flow rate	k	permeability
A	cross sectional area of water flow	L	length of flow path

q	rate of flow per unit area	s	direction of flow
ψ	potential pressure	t	time
c_v	coefficient of consolidation	e	void ratio
p_{wi}	initial excess pore water pressure		
m	a constant	M	defined by m
T_v	time factor	p'_c	preconsolidation pressure
τ_f	Coulomb shear strength	C	cohesion
ϕ	internal friction angle	τ'_f	peak shear strength at failure

C'_e effective cohesion as a function of void ratio

ϕ'_e effective angle of internal friction as a function of void ratio

σ'_f normal effective pressure on the failure plain at the moment of failure

CHAPTER 4

k_c	vertical clay permeability	m	melt rate of ice
z	thickness of clay layer		

ψ_x potential pressure at base of ice at a point x

ψ_a potential pressure at the top of the aquifer

Q water discharge per unit width

b point along flow line where melting initiates

q	water discharge per unit area	T	aquifer thickness
k_a	horizontal permeability in the till		

ψ_b potential at top of the aquifer at the point x=b

p_i	pressure due to ice overburden	h	thickness of ice at a point x
H	thickness of ice at the ice divide		

x a point along the flow line measured from the ice divide

L distance from the ice divide to the terminus

ρ_i density of ice

CHAPTER 5

k	constant	n,m	till flow law parameters
c	constant	ε	strain

δx horizontal displacement along the shear surface

a sample height

v integrated strain rate velocity in till

CHAPTER 6

u_z horizontal ice velocity at a depth z in the ice sheet

u_s horizontal ice velocity at the ice sheet surface

A,n	ice flow law parameters	$\bar{u}$	average ice velocity
h	ice thickness	q	surface accumulation

Q normalised mass balance

H_e normalised equilibrium line altitude

H_s normalised snow line altitude

g_a ablation gradient

g_s linear portion of normalised mass balance profile

Q_s	value of Q at H = Hs	a_1,a_2,a_3	constant

b net upstream accumulation

L distance from the terminus to the ice divide

h_e	equilibrium line altitude	h_s	snow line altitude

v till velocity

p'_b effective pressure at the base of the deforming layer

p'_t effective pressure at the top of the deforming layer

p_w water pressure

k	roughness coefficient	n,A	flow law parameters for ice
Q	water discharge	B	constant

c_m energy of fusion of water

CHAPTER 1

INTRODUCTION

1.1 Introduction

The dynamics of ice sheets are governed by the fundamental flow properties of ice and the interactions of the ice body with the atmosphere, oceans and solid earth. Whilst the surface boundary can be easily observed, observations of the basal boundary are rare. Inferences about the conditions at the bed are therefore a combination of limited observations, laboratory experiments and theory. The study of ancient ice sheets is valuable because former subglacial beds are easily accessed, and the features on them and their sediments contain information about subglacial processes.

Most models of ice sheet flow developed over the last thirty five years have been based on observations of valley glaciers and polar ice sheets in mountainous terrains, where the bed appears primarily to be of rock. The models have therefore assumed that all ice sheets move over a rigid surface. Nye (1959) stated that two processes constitute ice sheet motion: (i) internal deformation of ice as a result of stresses produced by its own weight (e.g. Nye, 1952a) and, (ii) sliding of the ice mass over the underlying bedrock (e.g. Weertman, 1957; Lliboutry, 1958). The mechanics of glacier flow as an isolated system are well documented and many of the problems associated with the physics of ice sliding over rigid beds have been solved.

However, it has subsequently become clear that where ice overlies soft sediments, a third process may be of great importance. Under certain circumstances, unlithified sediments may deform and contribute to the forward motion of the ice sheet (e.g. Boulton and Jones, 1979; Alley *et al.*, 1986). This is particularly important for the mid-latitude Pleistocene ice sheets which were underlain by large areas of soft sediment (Boulton, 1986).

Reconstruction of the mid-latitude Pleistocene ice sheets therefore depends on a realistic deforming bed model. Many of the parameters essential to the deforming bed model are impossible to measure directly as no modern analogues of these ice sheets exist. Indirect methods of obtaining these parameters are therefore required.

One such method involves the experimental determination of the past maximum pressure to which a sediment has been subjected. Point estimates of ice load derived in this way have been used in the past to determine ice sheet thickness (e.g. Harrison, 1958; MacDonald and Sauer, 1970; Khera and Schulz, 1984). However these estimates did not consider a meltwater flux draining through the sediment. This thesis considers the vertical distribution of effective pressure in former subglacial sediments, from which the palaeopotential gradient is calculated. A theory is outlined which relates the potential pressure gradient in the sediment to other important ice sheet parameters such as the basal melt rate of ice and the ice sheet thickness. Specific estimates of these parameters are obtained. These values can be used as a constraint on existing ice sheet models, allowing bed deformation to be more realistically modelled and the behaviour of ice sheets resting on deformable sediments to be predicted.

The purpose of this thesis is therefore:

(i) to determine the conditions found at the ice/bed interface where ice is basally melting and the bed consists of soft sediments;

(ii) to establish how subglacial sediments behave under such conditions and how this affects ice sheet dynamics.

This discussion sets the context within which the aims and structure of the thesis are defined.

1.2 The Basal Boundary Condition

Conditions at the ice/bed interface depend upon the stresses acting at the boundary, the temperature of the ice, the properties of the substrate and any subglacial water flow. Ice sheets show a mosaic of basal temperature conditions ranging from areas with temperate beds, in which the ice is at its melting point, to cold beds, where the ice is below the melting point. The mechanism by which the ice sheet moves depends on the thermal conditions at the base. Three types of boundary condition exist:

(i) the cold bed condition,
(ii) the temperate hard bed condition,
(iii) the temperate soft bed condition.

1.2.1 The Cold Bed Condition

When the glacier sole is below its freezing point, ice adheres to the underlying surface which may be rock or frozen sediment. This is the case in many polar glaciers. Since the ice/rock bond is stronger than any bonds within the ice (Jellinek, 1959), an applied shear stress will cause deformation within the ice itself rather than at the ice/bed interface. This has been confirmed from observations made in tunnels in Greenland (Goldthwait, 1960) and Antarctica (Holdsworth and Bull, 1970). The forward motion of the ice is therefore due only to internal deformation of the ice body in response to gravitational stresses. Thus, in order to understand ice sheet motion, it is important to ascertain how ice will deform under an applied stress.

Ice is is thought to deform in one of three ways:

(i) as a linearly viscous material
(ii) as a perfectly plastic material
(iii) as a non-linearly viscous material.

The variation of strain rate with applied shear stress for each of the three models is shown schematically in figure 1.1.

1.2.1.i Ice as a Linearly Viscous Material

Early observers of Alpine glacier flow concluded that ice deformed as a viscous material (e.g. Rendu, 1841; Forbes, 1842). This led various researchers to attempt to describe glacier flow using the equations of fluid dynamics. For instance, Weinberg (1907) treated ice as a linear viscous fluid in which the strain rate is directly proportional to the applied stress with the constant of proportionality given by the viscosity (figure 1.1). However the velocity of a glacier appeared to be more sensitive to small perturbations than this law predicted and ice was shown to behave in a non-linear fashion (e.g. Glen, 1952, 1955).

1.2.1.ii Ice as a Plastic Material

Orowan (1949) explained that ice deformed plastically like other crystalline solids and that perfectly plastic deformation could account for the principal features of ice sheet flow. Plasticity theory assumes that ice does not deform until the stress increases to the value of its yield strength after which it deforms indefinitely (figure 1.1).

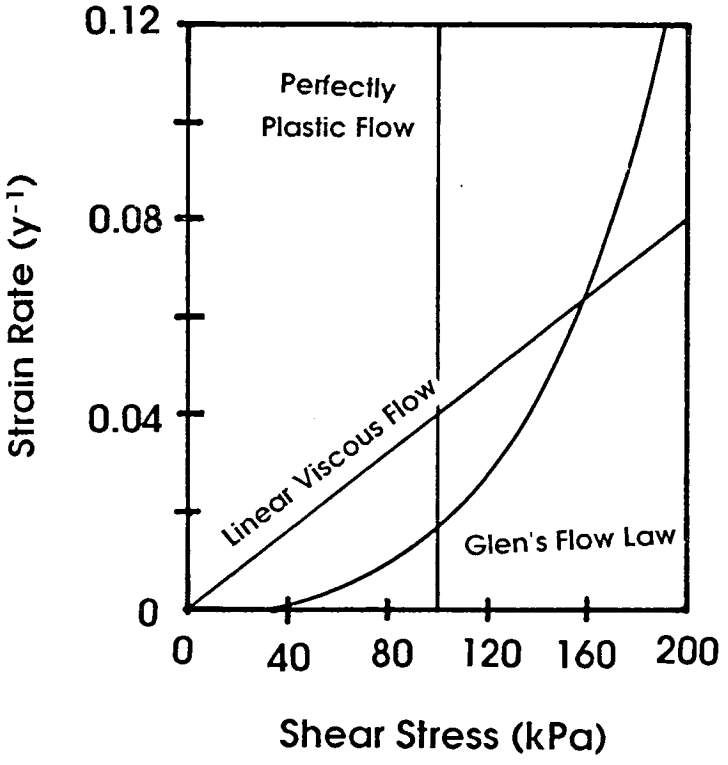

Figure 1.1: Relationship between strain rate and shear stress for the linearly viscous, perfectly plastic and non linearly viscous flow laws discussed in the text.

Nye (1951, 1952a & b) used this approach to develop a mathematical theory which accounted for the major features of ice sheet geometry and flow. He considered a parallel slab of ice of uniform thickness, resting on an inclined plane. The length and width of the slab are large with respect to the height. Since the ice is frozen to its bed, the forward movement of the ice will be due entirely to internal plastic flow. Resolution of the forces in the downslope direction gives:

$$\tau_b = \rho g h \sin\alpha \qquad 1.1$$

where τ_b is the basal shear stress,

ρ is the ice density,

g the acceleration due to gravity,

h the ice thickness,

α is the surface slope.

The shear stress at the base of an ice sheet can thus be calculated from measurements of ice thickness and surface slope (Nye 1952b). The basal shear stress has been determined for many Alpine valley glaciers resulting in values ranging between 50 and 150kPa (Nye, 1952b). A reasonable approximation is therefore to regard cold ice as a perfectly plastic material with a yield strength of 100kPa (Paterson, 1981).

The steady state solution for an ice sheet of constant temperature resting on a horizontal bed of uniform roughness can be shown to be (Nye, 1959):

$$h^2 = \left(\frac{2\tau_o}{\rho g}\right)(L - x) \qquad 1.2$$

where τ_o is the plastic yield strength of ice

L is the distance from the divide to the terminus

h is the ice thickness at a point x from the divide

The coordinate system for such an ice sheet is shown in figure 1.2.

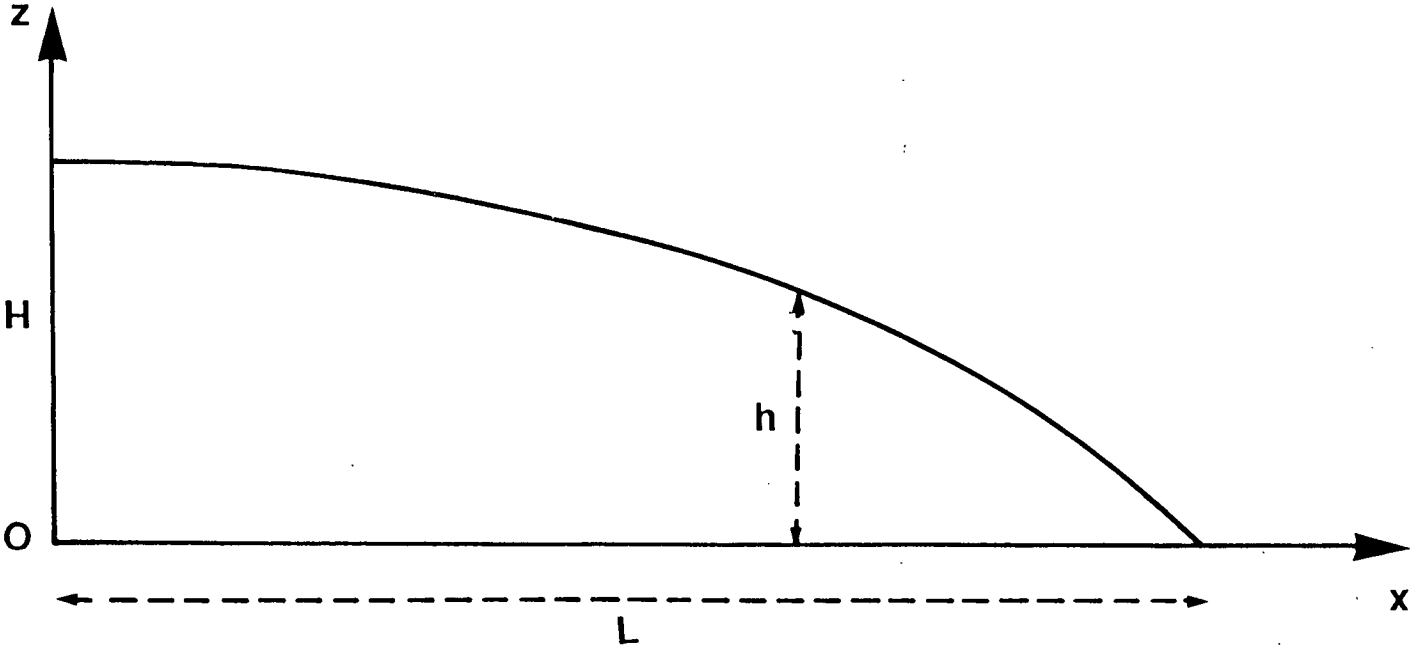

Figure 1.2: Coordinate system for the steady state ice sheet discussed in the text.

The profile of a perfectly plastic ice sheet can also be shown to be a parabola (Nye, 1959):

$$\left(\frac{h}{H}\right)^2 + \left(\frac{x}{L}\right) = 1 \qquad 1.3$$

where H is the thickness of ice at the ice divide,

For a cold based ice sheet the surface profile is given by equation 1.3. The ice sheet is reconstructed without reference to mass balance, and the profile is therefore independent of mass balance. If a mass balance is imposed on the surface, the average horizontal velocity of the ice sheet at any point can be obtained by dividing the ice flux by the ice sheet thickness at that point.

1.2.1.iii Ice as a Non-linearly Viscous Material

As a consequence of Orowan's (1949) suggestion, Glen (1952, 1955) carried out laboratory studies of the deformation of polycrystalline ice and showed that ice was neither a linearly viscous nor a perfectly plastic material. He found that strain rates in ice varied as the third or fourth power of the applied stress as well as being dependent on temperature (figure 1.1).

Nye (1957) adapted Glen's results to obtain a generalised flow law which is often referred to as Glen's Law. It gives the relationship between the shear strain rate and the shear stress and has the form (Paterson, 1981):

$$\dot{\varepsilon} = A\tau^n \qquad 1.4$$

where $\dot{\varepsilon}$ is the strain rate,

τ is the shear stress,

A and n are flow law parameters

The value of n is a constant for a given ice material in the range 3 - 4, demonstrating that the strain rate is highly sensitive to the shear stress. The value of A is dependent on many factors including temperature. The flow law results in a curve with the general shape shown in figure 1.1.

Nye (1952a) based his theory of glacier motion on the generalised power law showing that, for laminar flow, for a slab of ice deforming in simple shear (z component of velocity is zero and $2\dot{\varepsilon} = du/dz$) the flow law reduces to

$$\frac{du}{dz} = -2A(\rho g z \sin\alpha)^n \qquad 1.5$$

where u is the component of velocity in the x direction.

Integrating equation 1.5 with respect to depth in the ice results in a vertical velocity profile in the ice such as illustrated in figure 1.3. This shows that the velocity is a maximum at the surface but decreases with depth, and is zero at the bed.

1.2.2 Adoption of the Ice Sheet Model used in this Thesis

Before the basal boundary condition can be considered, a model must be adopted for the shape of the ice sheet. For ease of analysis, the shape must be sufficiently smoothed to be represented by an analytical or simple geometrical surface. The model should also be able to simulate approximately modern ice sheets. As a first approximation, a perfectly plastic ice sheet is considered in this study. Perfect plasticity allows calculations to be carried out concerning the ice sheet profile and is also representative of modern ice sheets. The ice sheet is treated as being infinitely wide, having no vertical variation in geometry or physical properties, and as being in plastic equilibrium.

1.2.3 The Temperate Hard Bed Condition

The base of a temperate hard base glacier is at its melting point and thus is not frozen to the bed. Ice will therefore slide over bedrock as well as deforming internally. Basal sliding is a difficult process to study directly although some observations have been made in subglacial tunnels in which the ice/bedrock interface is exposed (e.g. Kamb and LaChapelle, 1964). Despite the paucity of direct observations, theories have been developed to explain ice sheet sliding. Empirical laws relating driving forces and sliding rates have been developed but predictive theory has not been very successful (Weertman, 1979).

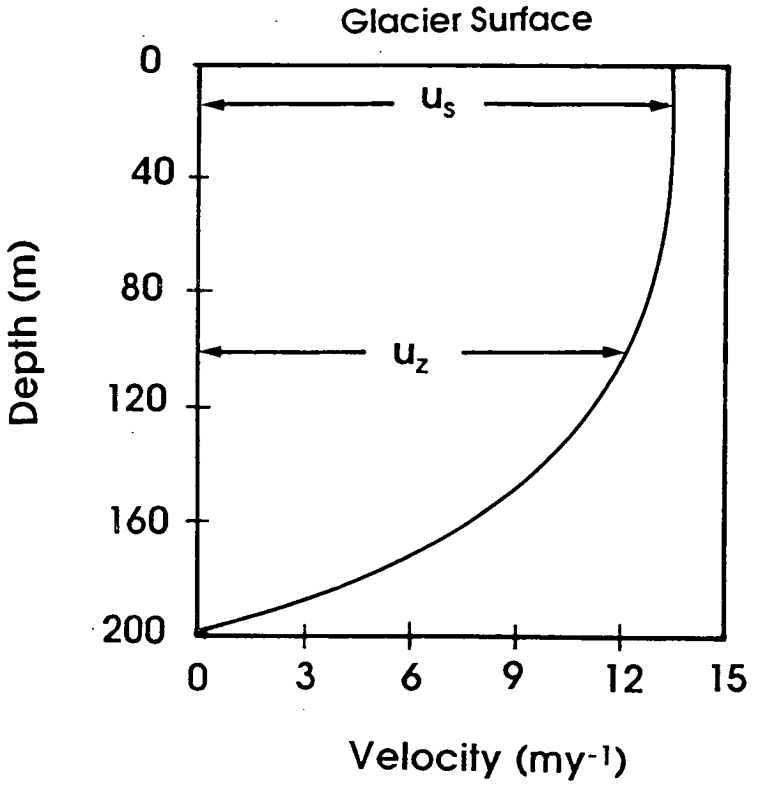

Figure 1.3: Distribution of horizontal velocity with depth in a perfectly plastic ice sheet; u_s is the horizontal surface velocity whilst u_z is the horizontal velocity at a depth z.

1.2.3.i Early Work

Agassiz (1840, 1867) attributed sliding theory to Gruner and de Saussure who were among the first to recognise glacier flow. Forbes (1845) claimed that sliding could not occur due to the friction between ice and its bed and if sliding did start it would accelerate and be unstable. Hopkins (1845, 1849) carried out the first experiments to determine if and how ice slides over a rigid substrate. He proposed a sliding law demonstrating that ice could slide over rock at a steady, unaccelerating rate.

Deeley and Parr (1913) proposed a simple friction law identical to that of Hopkins stating that the slip was directly proportional to the force producing it and inversely proportional to the frictional resistance, while the resistance was directly proportional to the ice overburden pressure. They went on to identify the mechanisms of regelation and creep around obstacles and introduced a roughness function based on pyramidal asperities, and analysed its contribution to sliding resistance (Deeley and Parr, 1914).

Most current hypotheses of basal sliding are derived from Weertman (1957).

1.2.3.ii Weertman's Theory

The bed of an ice sheet is almost certainly an irregular surface. Weertman (1957) considered a perfectly smooth glacier bed with cubic asperites. He postulated that regelation and ice flow around obstacles were the key processes that allowed sliding to occur.

He used Glen's power law to describe ice rheology, rather than using a linearly viscous law. Unlike previous work, Weertman's proportionality constant is explicitly related to the physical properties of ice and rock and not empirically determined. Hence Weertman's (1957) law was the first complete theory of ice sheet sliding.

Weertman later modified and improved his theory by considering how a water layer might influence sliding (Weertman, 1962) and by introducing a more complex obstacle geometry and the possibility of cavitation in the lee of obstacles (Weertman, 1964).

Kamb and LaChapelle (1964) confirmed, from observations made in a tunnel driven to bedrock, that both regelation and plastic deformation were taking place at the base of Blue Glacier, in Washington State, U.S.A.

1.2.3.iii Sliding with Cavitation

Liboutry (1958, 1959) showed that introducing two new factors into Weertman's theory led to a different sliding law. He introduced a more realistic sinusoidal bed and identified a third sliding process; sliding by subglacial cavitation. Cavities reduce the area of contact between the ice and the bed and thus reduce basal friction. The cavities may also fill with water, in which case the water pressure will support part of the ice overburden pressure, which will further reduce the frictional contact between the ice and the bed, allowing the ice sheet to slide more easily. The sliding velocity must therefore depend on the effective normal pressure, the basal shear stress and the roughness of the bed. Liboutry has continued to refine this theory (Liboutry, 1968, 1979).

1.2.3.iv Sliding without Cavitation

Weertman's sliding theory is very much dependent on an adequate description of bed roughness. Nye (1969, 1970) and Kamb (1970) have since independently developed theories considering a more complex bed morphology, described either by Fourier series or by integrals. Ice is assumed to be a linearly viscous fluid and the ice sheet bed a plane surface with small random topographic fluctuations superimposed upon it. Ice is assumed to be in close contact with the bed so that the effects of cavitation can be ignored. Using this theory, Nye and Kamb have determined the relative contributions of regelation and creep to basal sliding, showing how bed roughness contributes to sliding resistance. The theory, however, breaks down when cavitation is introduced.

Fowler (1986) extended the Nye/Kamb theory to obtain an exact solution for flow with cavitation but had to assume a simple periodically repeating bed geometry and that the regelation process did not occur.

These sliding theories are based on highly simplified assumptions: that ice is free of impurities; that the bed is rigid and impermeable; that cavities may or may not be present and may or may not contain water; and that the ice/bed contact is a sharp plane without debris fragments. However, the interactions between ice sheets and their beds are complex, even when they are simple rock beds, and the problems of features such as variable temperature, a realistic ice flow law, the presence of water and characteristic bed roughness are continuing major problems (Drewry, 1986).

1.2.4 The Temperate Soft Bed Condition

In the previous sections, and in most theories of ice sheet movement prior to 1979, it was assumed that ice flows over a rigid surface and that glacier dynamics were a product of ice rheology (e.g. Nye, 1957) and basal sliding (e.g. Weertman, 1967; Lliboutry, 1968). This may stem from the fact that original theories of ice flow were based on observations made on Alpine glaciers. Ice sheets were explored later and the existing ideas of glacier motion applied to them. However, although modern ice sheets rest mainly on rigid substrata, this is patently not true for the mid-latitude ice sheets of the Pleistocene, which were underlain, for as much as eighty percent of their area, by soft sediments (Boulton, 1986). It has also been shown to be untrue for at least certain Antarctic ice streams (Alley *et al.*,1986). This is reflected in the geomorphology of the mid-latitude areas affected by the Pleistocene glaciation, which have features such as till sheets, push moraines and drumlins as opposed to typical Alpine features such as *roches moutonées*, corries and striae (e.g. Sugden and John, 1976). However early mathematical modellers did not take these features into account and although the features are well known, the processes which produced them are not.

1.2.4.i The Deforming Bed Model

It is now recognised that soft sediments beneath ice sheets can deform and make a significant contribution to ice sheet dynamics (Boulton *et al.*, 1974; Engelhardt *et al.*, 1978; Boulton, 1979; Boulton and Jones, 1979; Alley *et al.*, 1986, 1987a & b, 1989, Alley, 1989a & b, 1991; Kamb, 1991) and various deforming bed models have been developed (e.g. Alley *et al.*, 1986; 1987a & b; 1989; Boulton and Hindmarsh, 1987; Clarke, 1987; Alley, 1989a & b).

Evidence of subglacial sediment deformation is revealed in tills by tectonic structures such as folds. Such sediments have been identified by Aber (1979); Rappol and Stoltenberg (1985); Åmark (1986); and Hart (1987). Boulton (1987) also suggests that many laminated tills are a product of this process, and indeed that extreme deformation can lead to a homogeneous till. Direct observations of the processes that produce these features are rare however.

1.2.4.ii Observations of Deforming Beds

A study of glacier sliding by Engelhardt *et al.* (1978) using borehole photography revealed a 10cm layer of actively deforming subsole drift between the bedrock and the base of the ice. The sliding velocity at the glacier sole was less than half the velocity of the surface ice and deformation of the subsole drift was therefore thought to make a significant contribution to basal sliding.

Observations made by Boulton and Jones (1979) show that a large proportion (90%) of the forward motion of a temperate glacier lying on a deformable bed can be contributed by the deformation of the bed (figure 1.4). They suggest that, under certain circumstances, basal melting of ice may cause high water pressures to develop in subglacial sediments. The resulting effective pressure acting on the sediments may be low enough to reduce the sediment shear strength below that of ice, causing the sediment to deform and the ice sheet to reach equilibrium at a relatively low basal shear stress with a low surface profile. The resulting form of the glacier is thus largely controlled by the mechanical properties of the substratum.

Seismic experiments carried out on Ice Stream B in Antarctica (Blankenship *et al.*, 1986; Rooney *et al.*, 1987) show that the ice stream is underlain by a water saturated, unconsolidated material of 40% porosity and that the effective pressure at the base of the ice is 50kPa ± 40kPa. Alley *et al.* (1986) argue that such a thin, unconsolidated layer beneath an active, wet based ice sheet must be till, and that deformation within this till could account for most of the ice stream velocity. Alley *et al.* (1987a&b) present further evidence for subglacial deformation: the porosity of the sediment is too high for lodged till but consistent with till undergoing deformation; basal shear stress exceeds the estimated strength of the subglacial sediment; and there is insufficient water available. It is therefore not possible to explain the high ice stream velocity by any previously published, physically based, sliding mechanism, without bed deformation (Alley, 1989a).

1.2.4.iii Implications of a Deforming Bed

A deforming bed will almost certainly play an important part in determining ice sheet dynamics because it can contribute to the forward motion of the ice. This is thought to be the case for the West Antarctic ice sheet where a large proportion of the overall ice discharge is thought to occur through fast flowing ice streams, which account for only a small percentage of the area of the ice sheet as a whole (e.g. Alley *et al.*, 1989; Engelhardt *et al.*, 1990). These ice streams are thought to be

underlain by a deforming till layer (Alley *et al.*, 1986) whereas the surrounding, generally slow moving, ice is thought to rest on a rigid bed. The mid-latitude Pleistocene ice sheets, resting entirely on deformable beds, would therefore have behaved very differently to modern polar ice sheets.

The mechanical properties of subglacial sediment are an essential component of a deforming bed model. The geometry and pressure of the basal water system are also important because they control the properties of the sediment.

1.2.4.iv Physical Properties of Subglacial Sediment

The physical processes that control subglacial conditions and hence till mechanics are not fully understood and the parameters required to model these processes are difficult to obtain. Clarke (1987) develops a framework around which he organises the properties of subglacial till by considering the continuum theory of mixtures and highlights areas in which more information is required. He shows that till is highly responsive to changes in the subglacial environment. Investigation of till in geotechnical engineering studies has provided much of the current knowledge of till properties. However while these studies are useful, they do not provide enough detail to allow a quantitative description of till rheology. Studies specific to these problems are therefore required.

One such study was carried out by Boulton and Hindmarsh (1987). They establish a weakly non-linear flow law for till, based on the results of experiments carried out near the terminus of Breidamerkurjökull in Iceland. As a consequence, most subsequent deforming bed models have adopted a linear or weakly non-linear rheology (e.g. Alley *et al.*, 1987b, 1989; Alley, 1989b; MacAyeal, 1989). Kamb (1991), however, considered the properties of clay rich soils at large strains and suggested that a highly nonlinear relationship was more likely. Further study is therefore required to determine more accurately how till will deform under subglacial conditions before comments can be made about the nature of subglacial sediment deformation and how it can be used to constrain the deforming bed model.

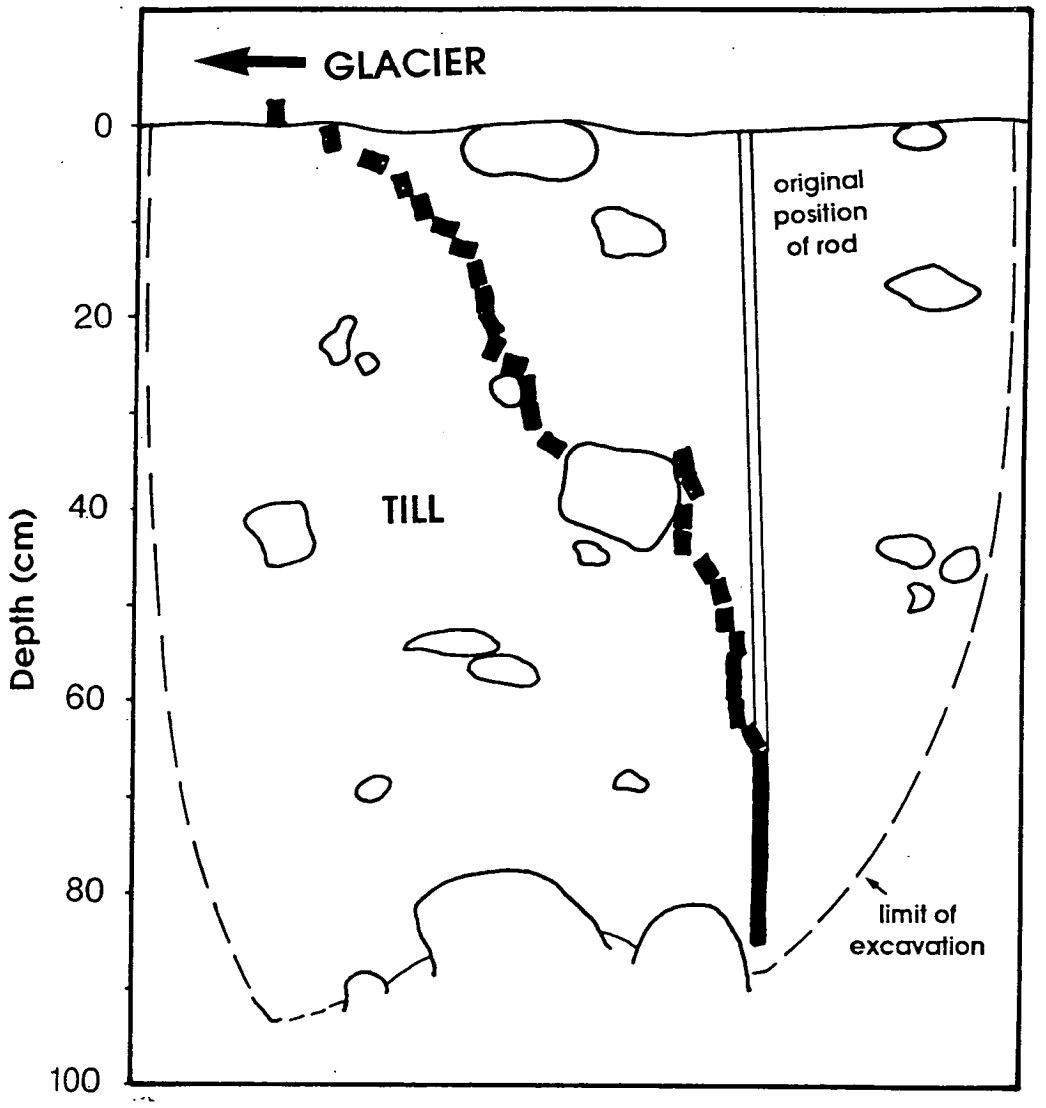

Figure 1.4: Distribution of a series of markers in till beneath Breidamerkurjökull in Iceland, *ca.* ten days after insertion (modified from Boulton, 1979).

1.3 Thesis Outline

This thesis determines specific ice sheet parameters indirectly from the geotechnical properties of former subglacial sediments. Subglacial groundwater flow patterns are inferred and the ice sheet profile reconstructed. Till rheology is established and a theory developed in which this rheology is used to analyse the role of the deforming bed in ice sheet dynamics. The thesis is organised into seven chapters which are outlined below.

Chapter 2 discusses the factors influencing the properties of subglacial sediments. Groundwater flow is discussed and its influence in the subglacial pressure regime considered. A one dimensional drainage model is proposed and the theoretical distribution of pressure in subglacial sediments determined.

In chapter 3, the geology of the northern Netherlands is outlined and it is suggested that this is a suitable area in which to test the one dimensional model. The geotechnical and sedimentological tests carried out to establish the suitability of the sediments in this area for further study are discussed.

Chapter 4 describes the consolidation testing of former subglacial sediments. Groundwater flow beneath the Saalian ice sheet and the resulting ice sheet profile in the northern Netherlands are reconstructed.

In chapter 5, the rheology of a typical Saalian till is established and compared to the existing flow laws for till. The flow law obtained from the experiments is used to model Saalian ice sheet flow.

An ice flux is inferred from mass balance considerations in chapter 6. This is coupled to the till rheology determined in chapter 5 and the ice/till interaction modelled. Subglacial tunnels are proposed as a mechanism for controlling effective pressure and their effects discussed.

The conclusions of the thesis are presented and discussed in chapter 7 and suggestions made on the direction of future research.

CHAPTER 2

THE PROPERTIES OF SEDIMENTS AND THEIR RESPONSE TO APPLIED STRESS

2.1 Introduction

An ice sheet applies a force to the underlying sediments which can be resolved into normal stress and shear stress components. This chapter describes the stress system acting on a sediment, both in a glacial and non-glacial environment, and discusses the response of a sediment to changes in that stress system.

The response of a sediment to an increase in normal stress is considered in terms of groundwater flow and consolidation. The shear strength of a sediment and its response to an imposed shear stress are then discussed. The dependence of shear strength on effective pressure is outlined and the relationship between shear strength, effective pressure and ice sheet dynamics discussed.

It is concluded that subglacial water pressures play a fundamental role in ice sheet dynamics as they determine the properties of the sediment. Subglacial groundwater flow is therefore discussed and two subglacial drainage models proposed.

2.2 Elementary Definitions

If a force is applied to a cubic element of sediment, the magnitude of the force acting on each face of the cube depends on the relative size of the face. To allow comparisons to be made, it is convenient to have a measure of force independent of size. This can be achieved by considering the force per unit area, otherwise known as the stress.

The stress acting on each face (σ) can be resolved into three orthogonal components, one perpendicular to the surface, known as the normal stress (σ), and two shearing stresses (τ) which are parallel to the surface (illustrated in figure 2.1a). The stress components acting on the cube can be represented in matrix notation:

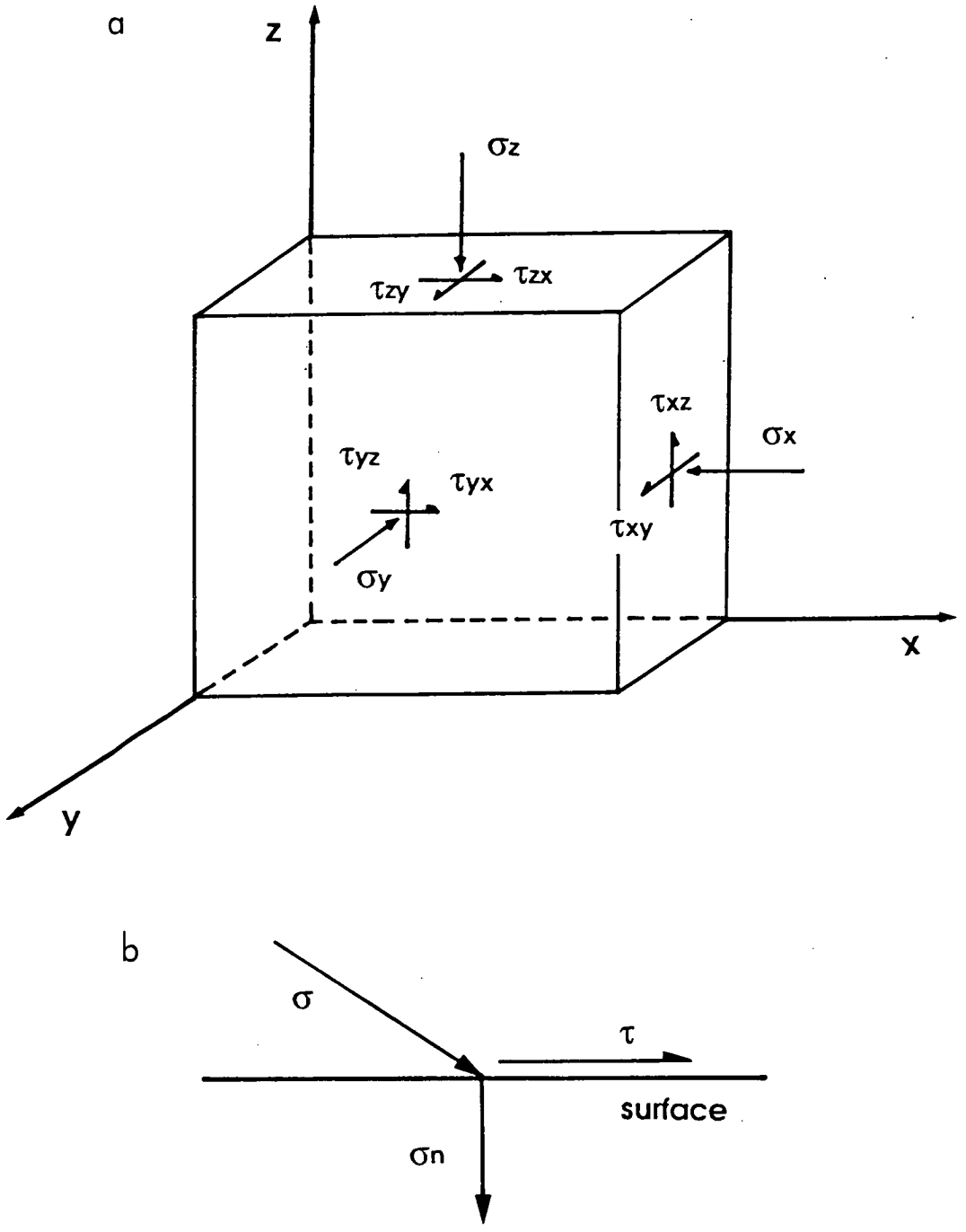

Figure 2.1: **(a)** The stress components acting on the faces of a cube. **(b)** The resolution of an applied stress (σ) acting on a surface into normal (σ_n) and shear (τ) stress components.

$$\sigma = \begin{pmatrix} \sigma_x & \tau_{xy} & \tau_{xz} \\ \tau_{yz} & \sigma_y & \tau_{yz} \\ \tau_{zx} & \tau_{zy} & \sigma_z \end{pmatrix} \qquad 2.1$$

where σ_x is the normal stress component acting in the x direction, that is perpendicular to the yz face, and τ_{xy} and τ_{xz} are the shear stresses acting on the yz face. For the state of stress at any point, three mutually perpendicular planes can be defined on which the shear stresses are zero. These are known as the planes of principal stress. The normal stresses to these planes are known as the principal stresses, denoted by σ_1, σ_2 and σ_3 with the convention $\sigma_1 > \sigma_2 > \sigma_3$. The array representing the principal planes is therefore:

$$\begin{pmatrix} \sigma_1 & 0 & 0 \\ 0 & \sigma_2 & 0 \\ 0 & 0 & \sigma_3 \end{pmatrix} \qquad 2.2$$

When considering the consolidation of sediments it is valid to assume that at depth, when all shear stresses have decayed, the vertical stress acting on a horizontal plane at depth is a principal stress.

2.3 Stress in Sediments

In the field, a sediment body will be subjected to a system of stresses which are divisible into an internal pore water pressure and a shear stress between the sediment particles. For simplicity, vertical stresses only are considered in the following discussion, but the argument can be expanded to three dimensions.

2.3.1 Total Stress

The vertical or normal stress measured on a horizontal surface at a depth z is determined by the intensity of loading due to the weight of the overlying material, i.e. the overburden. It is given by:

$$\sigma_n = \int_0^z \rho_b \, g \, dz \qquad 2.3$$

where σ_n is the normal vertical stress

ρ_b is the bulk density

g is the acceleration due to gravity.

The bulk density is the weight of both solid grains and pore fluid within a unit volume of sediment and is given by

$$\rho_b = \rho_w n + \rho_s (1-n) \qquad 2.4$$

where ρ_w and ρ_s are the density of water and solid particles respectively
n the porosity.

Porosity is defined as the ratio of the volume of voids to the total volume of the sediment;

$$n = \frac{V_v}{V_v + V_s} \qquad 2.5$$

V_v and V_s being the volume of voids and solid particles respectively.

If density is assumed to be constant with depth, then

$$\sigma_n = \rho_b g z \qquad 2.6$$

In the geological situation, the pressure generated at depth in the ground due to the weight of the overlying sediment is known as the lithostatic pressure (p). If it is assumed that all shear stresses have relaxed then the lithostatic pressure acting on the sediment, at a depth z below the ground surface, is a principal stress. Thus

$$\sigma_1 = p = \rho_b g z \qquad 2.7$$

2.3.2 Pore Water Pressure

Water in sediment obeys the laws of hydraulics (Todd, 1959). At a given point and at rest, it exerts a pressure consistent with the height to which water would rise above that point if an open ended stand pipe were inserted into the sediment column. This is illustrated in figure 2.2.

The pore water pressure (p_w) is

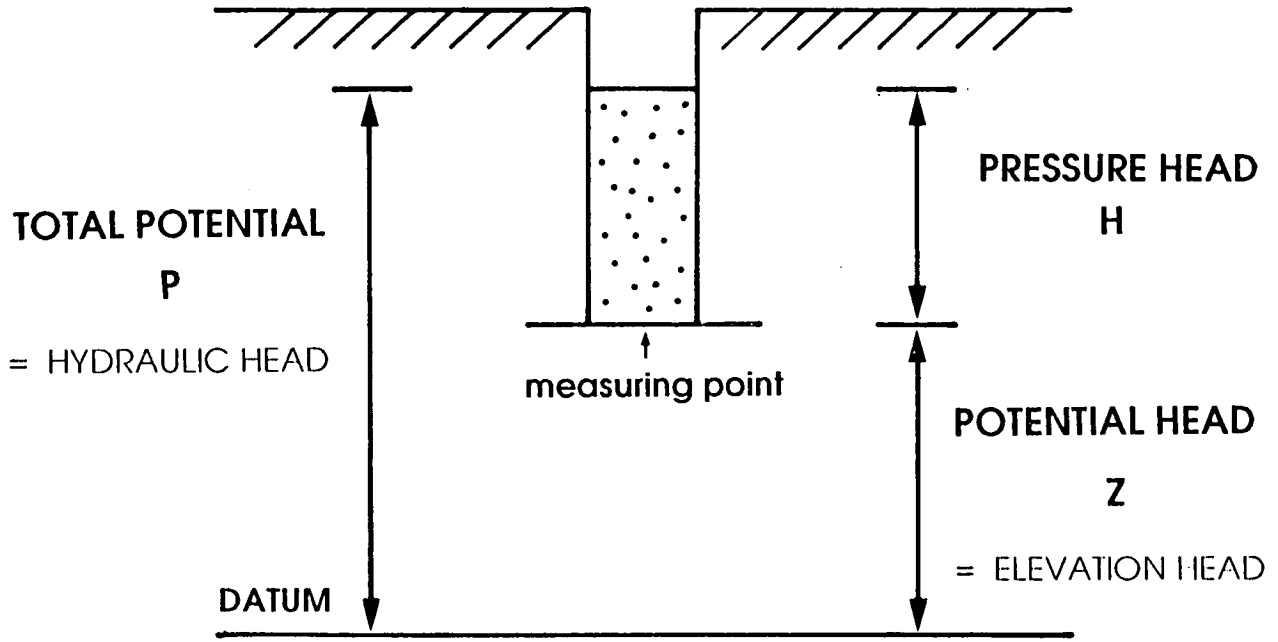

Figure 2.2: The relationship between total potential, pressure head and potential head for a point in a sediment column (modified from Ward, 1975).

$$p_w = \rho_w g H \quad 2.8$$

where H, known as the pressure head of water, is the height to which water would rise in the stand pipe.

2.3.3 Effective Stress

The porewater pressure opposes the normal stress, so the stress apparently acting on the sediment, known as the effective stress (σ'), is the difference between the applied stress (the normal stress) and the pore water pressure. This is a fundamental relationship in soil mechanics and was first stated by Terzaghi (1936). It is expressed mathematically:

$$\sigma' = \sigma_n - p_w \quad 2.9$$

Terzaghi went on to clarify the importance of effective stress by stating that "all measurable effects of a change of stress, for example compression or distortion, are due to changes in the effective stress". This implies that, if a sediment is subjected to a given normal stress, its behavior is also dependent on the magnitude of the pore water pressure as this controls the effective stress.

2.3.4 Effective Pressure

In the following discussion, the normal vertical stress is assumed to be a principal stress ($\sigma_n = \sigma_1$). If gravity is the only force acting on a sediment then the vertical effective pressure is a principal stress and equal to the lithostatic pressure as described above.

The effective pressure (p') acting on the sediment is therefore the difference between the total vertical pressure (the lithostatic pressure, p) and the pore water pressure:

$$p' = p - p_w \quad 2.10$$

This relationship is illustrated in figure 2.3.

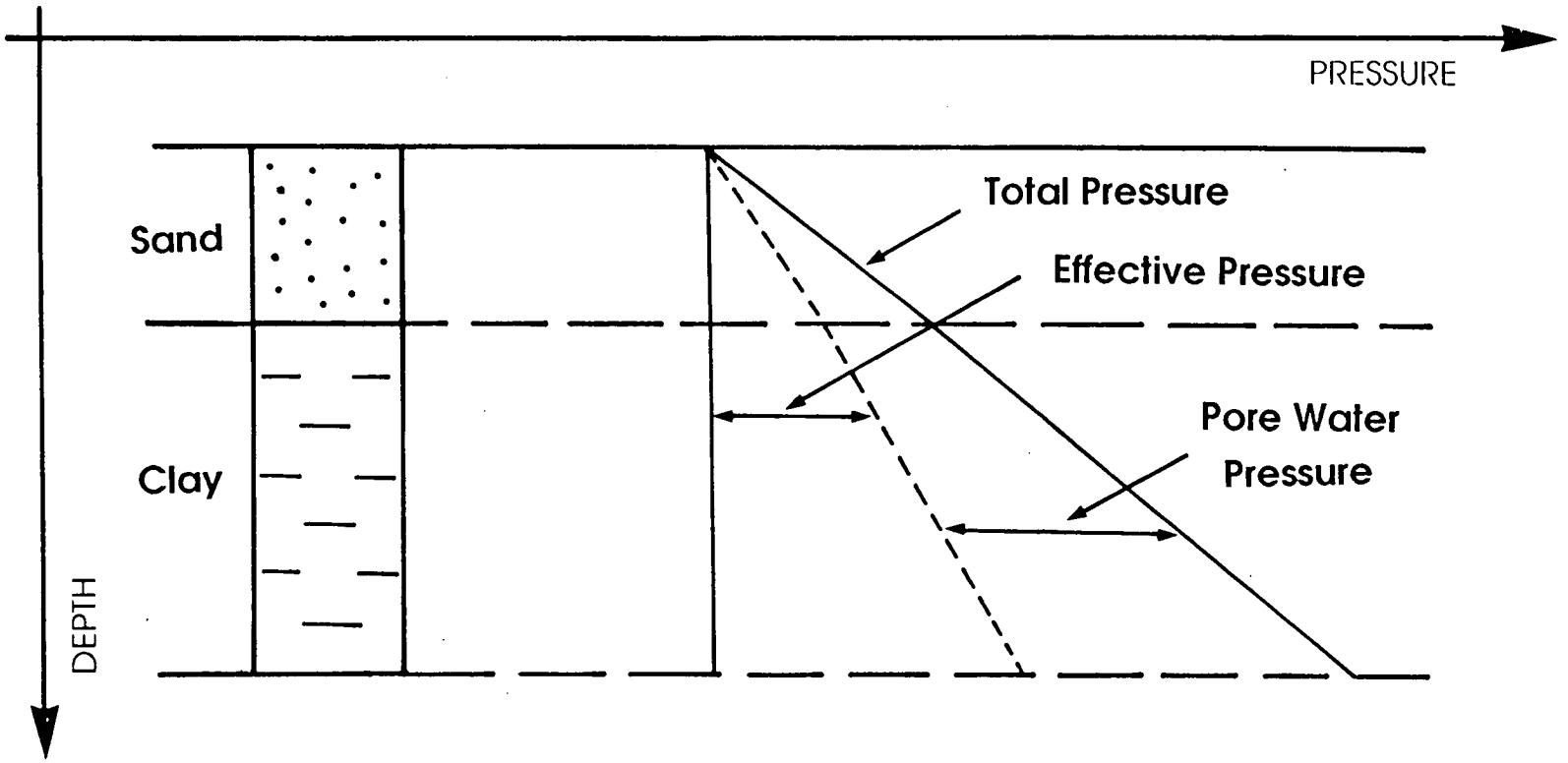

Figure 2.3: The relationship between total pressure, pore water pressure and effective pressure.

2.4 Groundwater Flow

2.4.1 Pore Pressure and Potential

Groundwater flow occurs in response to a potential gradient. In a porous sediment, water flows from an area of high potential to one of lower potential, providing the pores are interconnected.

The potential (P) is often referred to as the hydraulic head and is measured relative to an arbitrary datum. It consists of the pressure head (H), the potential head (Z), and the velocity head (V) and may be expressed by the Bernoulli equation (Ward, 1975):

$$P = H - Z + V \qquad 2.11$$

where Z is the elevation of the stand pipe base above the datum and is assumed to be positive downwards. The velocity head for flow through sediments is usually small and thus may be neglected without appreciable error (Todd, 1959). Equation 2.11 therefore reduces to

$$P = H - Z \qquad 2.12$$

This relationship is illustrated in figure 2.2. Since it is the potential gradient that controls flow, the position of the datum is not important.

2.4.2 Potential Gradient

Consider two points A and B connected by a pipe shown in figure 2.4. The potential P_A at A is greater than the potential P_B at B so water flows from A to B through the pipe over a distance ds. The potential gradient is therefore dP/ds, where dP is the difference between P_A and P_B. The rate of water flow through a permeable sediment is given by Darcy's Law.

2.4.3 Darcy's Law

Water flowing through a sediment is driven by the potential gradient. It is resisted by the drag of the sediment grains (i.e. the sediment permeability) as water flows through the pores. The amount of water flowing through the sediment depends on

this resistance and on the rate of drop in water energy with distance. Darcy (1856) expressed this mathematically:

$$Q = k A \left(\frac{P_A - P_B}{L} \right) \qquad 2.13$$

where Q is the volumetric flow rate

k is the hydraulic conductivity (permeability in velocity units)

A is the cross sectional area of the flow

L is the distance over which the potential drop $P_A - P_B$ takes place.

This assumes that Q, k and A are constant over the whole length of the drainage path and that P varies linearly with distance. These assumptions are unlikely to hold over large distances, so a more general form of the equation is required. This is a differential equation:

$$q = -k \left(\frac{dP}{ds} \right) \qquad 2.14$$

where q (= Q/A) is the rate of flow per unit area of the column and s is the direction of flow. A negative sign indicates that the potential gradient is negative in the direction of flow. The flow rate of water through the sediment is therefore proportional to the sediment permeability and the potential drop over the length of the flow path. Typical values of permeability for various sediments are contained in table 2.1.

In the simplest case, if the permeability of a sediment is constant, then the water flow is controlled only by the potential gradient.

2.5 Spatial Distribution of Pressures within Sediments

If a vertical flow path through a sediment layer is considered, ie p = p(z), the vertical effective pressure gradient at any point on the flow path is obtained by differentiating equation 2.10 with respect to depth to obtain

$$\frac{dp'}{dz} = \frac{dp}{dz} - \frac{dp_w}{dz} \qquad 2.15$$

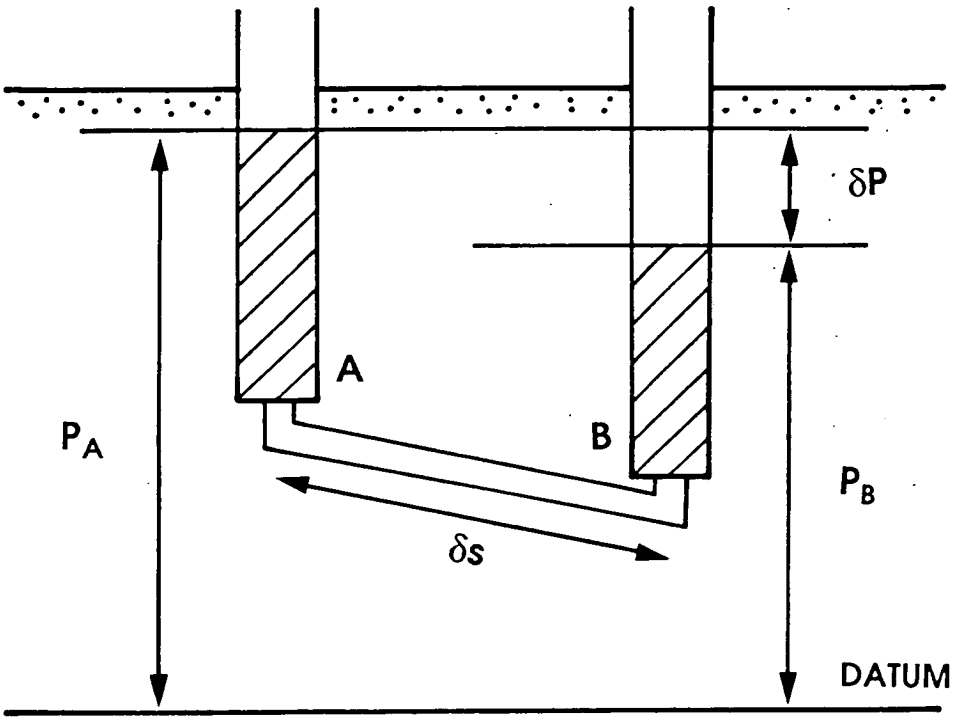

Figure 2.4: The potential at the point A is greater than the potential at point B, so water in a pipe connecting the two points flows from A to B. The potential gradient driving water flow in the pipe is therefore dP/ds where dP is the potential difference between the points and ds is the length of the flow path (modiried from Atkinson and Bransby, 1978).

Table 2.1: Typical values of the coefficient of permeability (Freeze and Cherry, 1979).

Sediment Type	Coefficient of Permeability (ms^{-1})
Gravel	$> 10^{-2}$
Sand	$10^{-2} - 10^{-5}$
Silt	$10^{-5} - 10^{-8}$
Clay	$< 10^{-8}$

The total pressure equivalent to the potential at any point is defined by a potential pressure (ψ), where

$$\psi = \rho_w g P \qquad 2.16$$

and thus the vertical potential pressure gradient is

$$\frac{d\psi}{dz} = \rho_w g \left(\frac{dP}{dz}\right) \qquad 2.17$$

Differentiating 2.12 to obtain dP/dz, then rearranging and differentiating 2.8 to obtain dH/dz, and substituting into 2.17 gives

$$\frac{d\psi}{dz} = \rho_w g \left(\frac{1}{\rho_w g} \frac{dp_w}{dz} - \frac{dz}{dz}\right) \qquad 2.18$$

which can be simplified to

$$\frac{d\psi}{dz} = \frac{dp_w}{dz} - \rho_w g \qquad 2.19$$

If the whole system is now considered (that is both sediments and water), substituting dp_w/dz from 2.15 into 2.19 gives an expression describing the relationship between the various pressure components and how this varies with depth;

$$\frac{d\psi}{dz} = \frac{dp}{dz} - \frac{dp'}{dz} - \rho_w g \qquad 2.20$$

2.6 Groundwater Flow and its Relationship with Effective Pressure

Water flow within a sediment can be induced in several ways. If the sediment is compressible, water flow may be induced by the application of a load (for example caused by the weight of a building or an ice sheet). This increases the pore water pressure above its static value causing a potential imbalance and thus water flow. It may also be induced by an influx of water to the sediment (for example meltwater from an ice sheet) which again increases the initial pore water pressure resulting in a potential pressure gradient.

If a sediment is not loaded or recharged, and the water in the pores is static, there is no potential pressure gradient (i.e. $d\psi/dz = 0$). The effective pressure gradient in the sediment is therefore given by rearranging equation 2.20:

$$\frac{dp'}{dz} = \frac{dp}{dz} - \rho_w g \qquad 2.21$$

Differentiating equation 2.6, and using the term effective pressure rather than stress, gives

$$\frac{dp}{dz} = \rho_b g \qquad 2.22$$

and substituting ρ_b from 2.4 into 2.22 gives

$$\frac{dp}{dz} = \left((1-n)\rho_s + n\rho_w\right) g \qquad 2.23$$

Substituting this into 2.15 gives the effective pressure gradient in terms of the whole sediment;

$$\frac{dp'}{dz} = (\rho_s - \rho_w)(1-n)g = \left(\frac{dp'}{dz}\right)_g \qquad 2.24$$

$(dp'/dz)_g$ is defined here as the vertical "gravitational" gradient since it describes how the weight of sediment and water vary with depth in the absence of any forces apart from gravity.

2.7 Consolidation of Sediments

2.7.1 The Process of Consolidation

In the following discussion, sediment is assumed to be a two phase material consisting of an elastic matrix of solid particles separated by voids fully saturated with water. Applying a load to a sediment results in a change of volume which may occur in three ways:

(i) by compression of the pore fluid
(ii) by compression of the mineral grains
(iii) by expulsion of the pore fluid.

The mineral particles and pore water are assumed to be incompressible in comparison to the sediment skeleton, and thus in a fully saturated sediment application of a load will result in a rearrangement of the solid skeleton, providing the pore water is allowed to drain.

A load applied to a sediment is initially borne entirely by the pore water, inducing an excess pore water pressure equal to the pressure applied by the load. If drainage is allowed, this potential pressure gradient causes intergranular flow of water along the path of least resistance to an area of lower potential pressure, i.e. the drainage surface. Pore water pressure decreases gradually as water drains from the sediment. This corresponds to an increase in effective pressure, and a reduction in volume as the load is transferred from the pore water to the granular matrix forcing the particles to become more closely packed. After an infinite time, all the excess pore water pressure dissipates and the resulting effective pressure acting on the sediment is equal to the applied pressure due to the overlying sediment and additional load. This process is known as consolidation and is best explained by Terzaghi's (1943) spring and piston analogy. The consolidation process is illustrated in figure 2.5. Figure 2.5a shows the physical response of a sediment to an applied load, i.e. the rearrangement of the solid matrix, whilst figure 2.5b shows how water pressure and effective pressure vary through time.

2.7.2 The Rate of Consolidation

The rate at which excess pore water pressure dissipates and transfers to the sediment structure, that is the rate of consolidation, depends on the rate at which groundwater drains from the sediment. The time taken for this to occur is obtained from the one dimensional consolidation theory first proposed by Terzaghi (1925). The basic differential equation for this theory is

$$\frac{\partial p_w}{\partial t} = c_v \left(\frac{\partial^2 p_w}{\partial z^2} \right) \qquad 2.25$$

where c_v is the coefficient of consolidation.

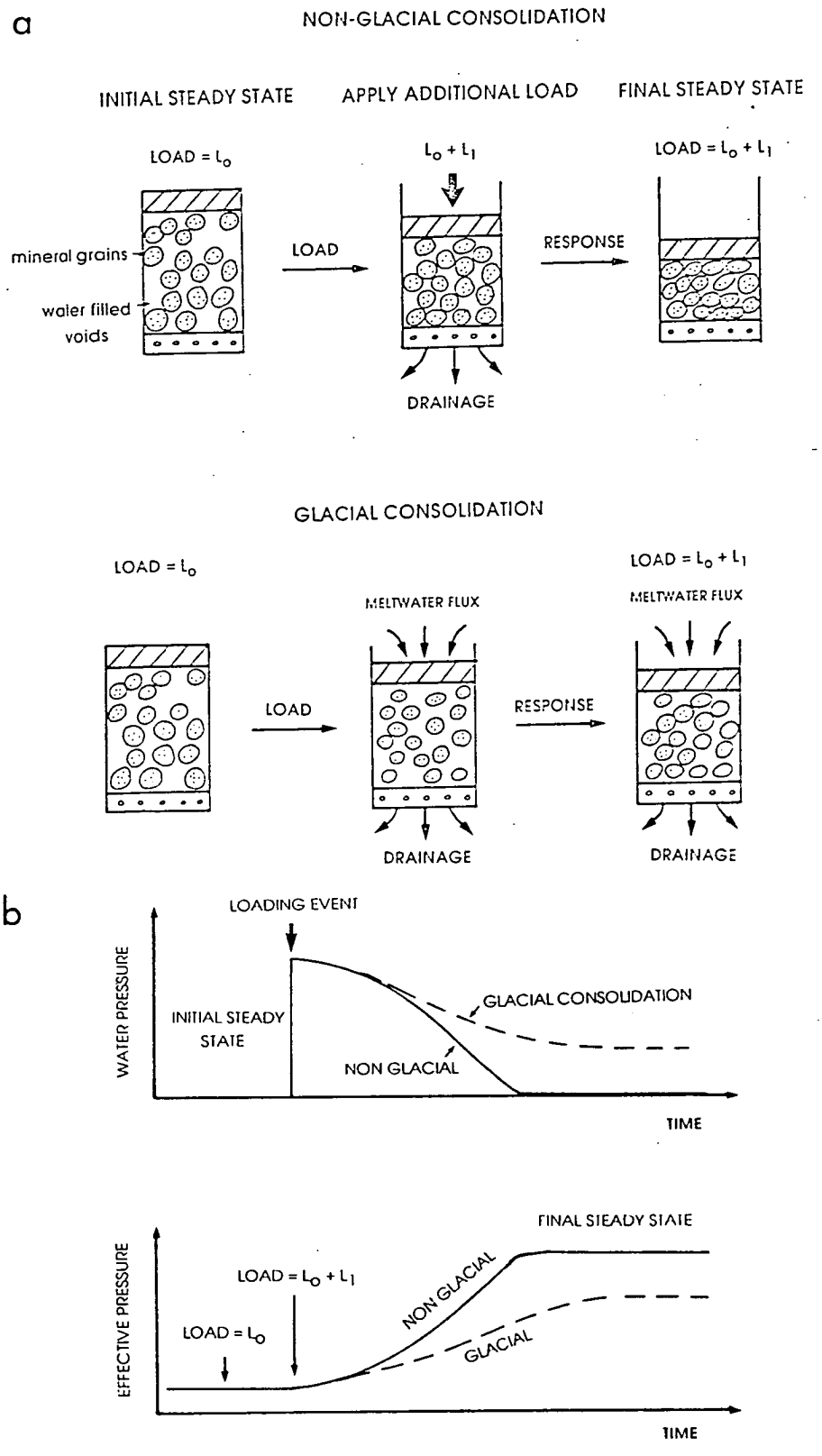

Figure 2.5: **(a)** The consolidation process. An applied load increment results in the decrease in volume of a saturated porous sediment as pore water drains from the sediment until a final steady state is reached in which the effective pressure acting on the sediment is equal to the pressure applied by the overlying sediment and the additional load. A sediment underlying a basally melting ice sheet does not consolidate to the same extent as a non - glacial sediment under the same load. **(b)** The response of pore water pressure and effective pressure to the application of an additional load under both non-glacial and glacial conditions.

The coefficient of consolidation is related to the elastic and fluid properties of the matrix. It can also be calculated from a consolidation test:

$$c_v = \frac{k\,\Delta p\,(1+e)}{\rho_w\, g\,\Delta e} \qquad 2.26$$

where k is the sediment permeability

e is the void ratio.

Equation 2.25 can be solved analytically for simple boundary conditions.

If complete drainage is allowed at both the upper and lower boundary surfaces of a sediment body, illustrated in figure 2.6, and the length of the drainage path is H, then at $z = 0$, $p_w = 0$, and at $z = 2H$, $p_w = 0$, for all times. If the initial excess pore water pressure is taken as p_{wi}, then at $t = 0$, $p_w = p_{wi}$ (shown in figure 2.7a&c).

A solution for equation 2.25 satisfying these conditions is obtained (Terzaghi, 1943), giving the value of the excess pore water pressure at a depth z (p_{wz}), at time t as;

$$p_{w_z} = \sum_{m=0}^{m=\infty} \frac{2\,p_{w_i}}{M}\left(\sin\frac{M\,z}{H}\right) e^{-M^2 T_v} \qquad 2.27$$

where p_{wi} is the initial excess pore water pressure, constant with depth,

$$M = 0.5\,\pi\,(2m+1) \qquad 2.28$$

m being a positive integer varying from zero to infinity,

T_v is the time factor, equal to

$$T_v = \frac{c_v\, t}{H^2} \qquad 2.29$$

The value of p_{wi} will fall to zero at the top and bottom surfaces of the sediment layer where drainage occurs (assuming there is no water input to the sediment). The above solution (equation 2.27) allows the pore water pressure to be determined for a point within the layer at any time t. Plotting values of pore water pressure against depth at a particular time produces an isochron which shows the maximum excess pore water pressure occurs at the centre of the layer (figure 2.7b).

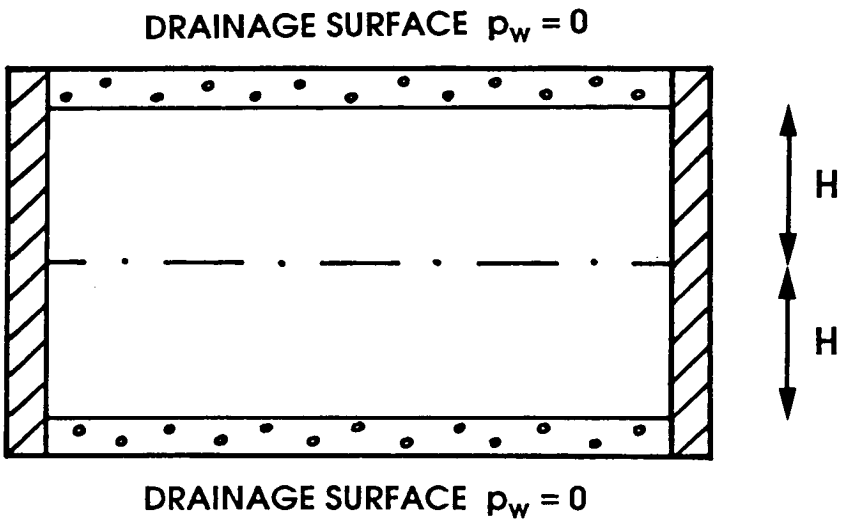

Figure 2.6: The sediment sample considered in one dimensional consolidation theory in which drainage occurs at both the top and bottom boundaries. H is the length of the drainage path.

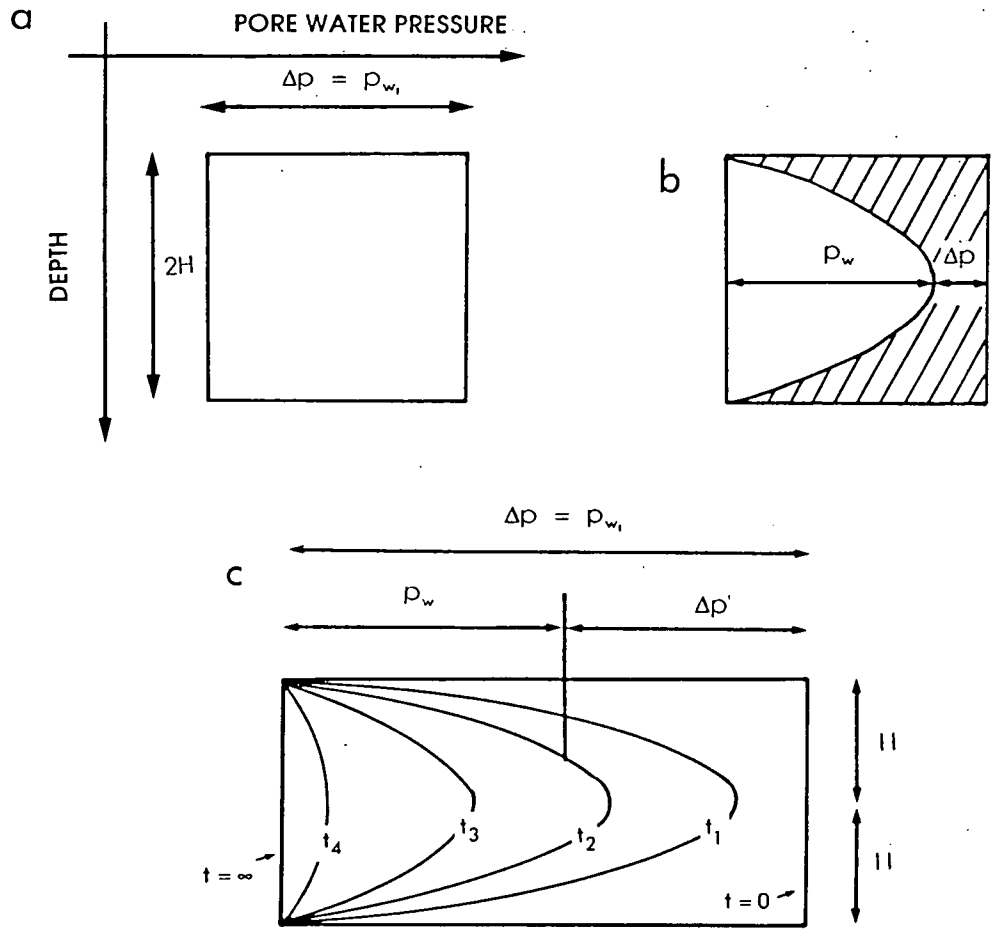

Figure 2.7: (modified from Smith, 1982); **(a)** The application of a load increment (Δp) to a sediment induces an excess pore water pressure (p_w), equal to the magnitude of the pressure applied by the additional load. **(b)** The excess water pressure immediately falls to zero at the top and bottom surfaces of the sediment where drainage occurs. At any point in time the effective pressure increment acting on the sediment is equal to the applied pressure increment minus the remaining excess pore water pressure. **(c)** The middle of the sediment layer equilibrates more slowly as water continues to drain from the sediment. At any time t, the water pressure is greatest in the middle of the layer. This figure shows the variation of water pressure through time as the sediment consolidates.

Consolidation continues until all the excess pore water pressure dissipates and the potential pressure gradient in the sediment becomes zero. The resulting effective pressure acting on the sediment will be due entirely to the applied load as discussed in section 2.7.1. The final effective pressure gradient is therefore purely gravitational as in equation 2.24, that is due only to the weight of the sediment. Isochrons can be plotted for different time intervals, as in figure 2.7c, to illustrate how water pressure dissipates through time as consolidation occurs.

If the sediment is of low permeability there will be a time lag before water will be able to drain from the centre of the layer. Consolidation will therefore be inhibited as an excess pore water pressure is retained. The time taken for the sediment to drain and thus to consolidate is a function of the sediment permeability, the length of the drainage path and the compressibility of the skeleton.

2.7.3 States of Consolidation

If the sediment is allowed to consolidate to such a point where it is at equilibrium, and then subsequently unloaded, it expands and takes in water. However, it does not rebound to its original structure but preserves within it a record of the former load (eg Casagrande, 1936). Such a sediment is said to be overconsolidated. Two conditions of a sediment can therefore be defined:

(i) normally consolidated; in which the present effective pressure is the maximum to which the sediment has been subjected, and

(ii) overconsolidated; in which the present effective pressure is less than a previous maximum (resulting from, for example, the reduction of an applied load or an increase in pore water pressure). The maximum effective pressure to which the sediment has been subjected is in this case known as the preconsolidation pressure (p'_c).

Preconsolidation pressures can be determined experimentally and so it is possible to obtain the past maximum pressure to which a sediment was subjected.

2.7.4 Consolidation of Subglacial Sediments

In non-glacial systems, loading a sediment causes it to consolidate. The time taken for consolidation to occur depends on the permeability of the sediment and the length of the drainage path. Once drained, the resulting effective pressure acting

on the sediment is due only to the overburden of sediment and any additional load, as shown in figure 2.5. Thus the effective pressure gradient is purely gravitational.

It is believed that most present and former ice sheets melt at their base (Huybrechts, 1992). Hence, when a sediment is loaded by an ice sheet, the final consolidated state must allow a meltwater flux to discharge through the system and permit a potential gradient to exist. The resulting effective pressure gradient is therefore obtained by rearranging equation 2.20 and incorporating equations 2.23 and 2.24:

$$\frac{dp'}{dz} = \left(\frac{dp'}{dz}\right)_g - \frac{d\psi}{dz} \qquad 2.30$$

The effective pressure acting at the ice/bed interface includes a potential pressure component and is therefore less than it would be for the same load applied under non-glacial conditions. If the subglacial sediments are of low permeability then the potential pressure gradient required to drive the meltwater flux will be relatively large (from Darcys Law, equation 2.14) and so the potential pressure component will have a significant effect on the effective pressure at the base of the ice. Hence a sediment will not consolidate to the same extent under a basally melting ice sheet as it would when subjected to a similar load in a non glacial environment. The differences between consolidation under glacial and non-glacial conditions are outlined in figure 2.5.

On retreat of an ice sheet, the effective pressure acting on the sediments is reduced and the former subglacial sediments become overconsolidated. The preconsolidation pressure retained in the sediment is assumed to result from the loading of ice and sediment at the glacial maximum. At the maximum extent of the ice sheet,however, the meltwater flux will ensure that the effective pressure acting on the sediment is not a simple consequence of the overburden of sediments and ice. Hence the preconsolidation pressure preserved in the sediment will not necessarily be a reflection of ice thickness as has been suggested by previous workers (eg Harrison, 1958; Kazi and Knill, 1969).

The effective pressure acting on low permeability sediments at the base of an ice sheet will consequently remain low over glaciologically significant time periods. This has important implications for the strength of the sediment (discussed in section 2.8).

2.8 Shear Strength of Sediments

2.8.1 Definition of Shear Strength

The shear strength of a sediment (τ_f) is its maximum resistance to shearing stresses. Shear strength consists of internal friction, due to the interlocking of particles, and cohesion, as a result of forces tending to hold the particles together in a solid mass. If a shear stress acting on a sediment rises to the magnitude of its shear strength then continuous sediment deformation and failure will occur.

2.8.2 Mohr-Coulomb Failure Theory

2.8.2.i Coulomb's Failure Theory

Coulomb (1776) originally suggested that the shear strength (τ_f) of a sediment could be expressed as a linear function of the normal stress (σ);

$$\tau_f = C + \sigma \tan\phi \qquad 2.31$$

where τ_f is the shear strength of a sediment

C is cohesion

σ is the normal stress

ϕ is the internal friction angle.

This assumes that sediment strength is governed by the total normal stress. However in a saturated sediment as discussed above, the stress borne by the matrix is an effective stress. Terzaghi (1943) therefore expressed the shear strength of a sediment as a linear function of the effective stress in a revised form of the Coulomb equation;

$$\tau_f = C' + \sigma' \tan\phi' \qquad 2.32$$

where σ' is the effective stress

C' is the effective cohesion

ϕ' is the effective angle of shearing resistance.

2.8.2.ii Mohr's Failure Theory

Mohr (1914) presented a theory predicting that failure would occur when the major and minor principal stresses are related by some function of the form

$$\sigma_1 - \sigma_3 = f(\sigma_1 + \sigma_3) \qquad 2.33$$

where σ_1 and σ_3 are the major and minor principal stresses respectively.

This is most conveniently depicted by a Mohr stress circle (eg Hobbs *et al.*, 1976). The failure condition may be defined in terms of a Mohr envelope which is tangential to all such failure circles.

2.8.2.iii Mohr-Coulomb Failure Theory

The Mohr envelope, to a close approximation, can be taken to be identical to Coulomb's equation and the resulting combination of these two failure conditions is known as the Mohr-Coulomb failure theory. The Mohr-Coulomb theory takes the general form:

$$\sigma_1 - \sigma_3 = 2\,C\cos\phi + (\sigma_1 + \sigma_3)\sin\phi \qquad 2.34$$

In practice, this theory is the one most commonly used when discussing sediment failure. It does, however, have its limitations which are discussed below.

2.8.2.iv Limitations of the Mohr-Coulomb Failure Theory

The Mohr-Coulomb theory implies that the magnitude of the intermediate principal stress does not affect the shear strength of the sediment. It also does not take into consideration the volume changes associated with changes in stress. Shear strains developing in the sediment cause a change in volume as the particles are rearranged. After large deformations, the original sediment structure is destroyed and the void ratio increases, tending to a critical value e_c. This critical void ratio is independent of the original sediment structure but dependent on the effective stress. One theory which attempts to take into account the void ratio at failure is that of Hvorslev (1937).

2.8.3 Hvorslev's Failure Theory

Hvorslev (1937) shows that the peak shear strength at failure of a sediment is a function of the total normal stress, and of the voids ratio in the plane of failure at the moment of failure and that this function is independent of the stress history. Hvorslev's equation for the peak shear strength at failure is

$$\tau'_f = C'_e + \sigma'_f \tan\phi'_e \qquad 2.35$$

where τ'_f is the peak shear strength at failure

C'_e the effective cohesion, dependent on the void ratio

σ'_f the normal effective pressure on the failure plane at the moment of failure

ϕ'_e the effective angle of internal friction.

Roscoe *et al.* (1958) developed Hvorslev's theory further in their critical state theory.

2.8.4 Critical State Theory

Dividing the above discussion of consolidation and shear strength into two separate parts is somewhat artificial since they are both very much related. Roscoe *et al.* (1958) combined both these aspects in their critical state model. This applies plasticity theory to soils and states that a soil will deform until it flows as a fluid with friction, at which point it will be in a critical state. This state is mathematically defined by a yield surface, as a function of shear stress, void ratio and effective stress (e.g. Atkinson and Bransby, 1978).

However such theories are not necessary for the scope of this research, the Mohr-Coulomb theory being adequate. In the following discussion effective pressures rather than effective stresses are considered.

2.8.5 The Dependence of Shear Strength on Effective Pressure

The shear strength of sediment depends on the effective pressure acting on the sediment, which itself is controlled by the pore water pressure in the sediment. Pore water pressure has long been recognised as an important factor in shear movements within the unlithified sediments involved in landslides (Mathews and MacKay, 1960; Skempton, 1964). Rubey and Hubbert (1959) indicate that pore fluid pressure within a sedimentary sequence facilitates tectonic overthrusting and Mathews and MacKay (1960) suggest that such pore fluid pressure may be equally important in subglacial thrusting.

Loading a sediment induces an excess pore water pressure which dissipates through time, providing water can drain from the pores, allowing the sediment to consolidate. If the sediment is highly permeable, drainage occurs relatively quickly and the excess pore water pressure dissipates. This increases the effective pressure acting on the sediment, the sediment becomes stronger, and thus a higher shear

stress is required for failure to occur. However if the sediment is of low permeability, drainage occurs relatively slowly and thus an excess pore water pressure may be retained. The resulting effective pressure acting on the sediment is less than would be expected from the overburden and consequently the sediment is weaker. Sediment deformation and failure can therefore occur at lower shear stresses.

The properties of sediments are therefore very much dependent on the effective pressure acting on them, which is determined by a number of factors, the most important being the ease and rate of groundwater flow. This in turn is dependent on many variables including sediment permeability and additional loading.

2.8.6 Shearing of Subglacial Sediments

A shear stress is imposed by ice moving over its bed. If the shear stress (τ) at the base of the ice sheet rises to the magnitude of the shear strength (τ_f) of sediment at some point beneath the glacier sole, sediment failure and deformation will occur (Boulton *et al.*, 1974). As stated in section 2.8.2 the shear strength of a sediment can be expressed as a linear function of the effective pressure in a revised form of the Coulomb equation (Terzaghi, 1943),

$$\tau_f = C' + \sigma' \tan\phi' \qquad 2.32$$

The shear stress imposed at the glacier sole is normally assumed to have a constant value of 100kPa (Paterson, 1981) and is independent of effective pressure. However the shear strength of a sediment increases with increasing effective pressure (equation 2.32) and thus sediment deformation only occurs where the applied pressure is relatively low, such as at the margins of an ice sheet, or where pore water pressures are very high.

Observations suggest that significant water pressures exist beneath ice sheets (e.g. Mathews, 1964; Boulton *et al.*, 1974; Hodge, 1979) which in some cases can almost equal the overburden pressure (Alley *et al.*, 1986) and thus support the weight of the ice. This results in very low effective pressures and therefore has important implications for sediment strength and ice sheet dynamics.

2.9 The Relationship between Ice Sheet Dynamics, Shear Stress and Effective Pressure.

The effective pressure acting on a sediment determines the shear strength of the sediment. In the subglacial environment relatively high pore water pressures may exist as a result of glacial loading and the additional meltwater flux through the sediment. High water pressures reduce the effective pressure acting on the sediment and as a result reduce the shear strength of the sediment. Sediment deformation can therefore occur at lower basal shear stresses. If the shear strength of sediment at the base of the ice is reduced to such an extent that it is lower than the plastic yield strength of ice then the sediment will deform rather than the ice and the forward motion of the ice sheet will be a result of the deforming bed. Thus the effective pressure and shear stress imposed by an ice sheet on the underlying sediments have an important influence on the dynamics of the ice sheet.

Mathews (1974) uses geomorphological evidence to reconstruct the profile of the south western part of the Laurentide ice sheet at its maximum extent, concluding that the mean surface slope may have been as little as one sixth as steep as typical modern profiles from Antarctica. He estimates that the basal shear stress required to form this lower profile was only a fraction (7 to 21%) of the 100kPa considered normal for active ice tongues (Nye, 1952b), a value much less than the plastic yield strength of ice. He suggests that the deformation involved in ice sheet advance therefore takes place below the base of the ice, where the shearing resistance of the underlying sediments was significantly reduced by excess pore water pressure.

Boulton and Jones (1979) report an experiment carried out in the till bed underlying Breidamerkurjökull in Iceland. The results indicate that 90% of the basal movement of the glacier is a result of deformation of its bed (figure 1.4). They suggest that subglacial sediment deformation occurs as a result of high pore water pressures developing in the sediment. The ice sheet therefore reaches equilibrium at a low basal shear stress with a low surface profile. The form of the glacier is consequently controlled by the pore water pressure in the underlying sediments.

The nature of the basal motion of ice sheets is an important determinant of their dynamic behaviour (Alley, 1989a). The mechanical properties of subglacial sediment may play a critical role in controlling ice flow and thus it is important to establish how sediments respond to the applied stresses found in the subglacial environment.

2.10 Subglacial Groundwater Flow

Ice sheet motion by sediment deformation is possible only if water pressure is relatively close to the overburden pressure (Boulton and Hindmarsh, 1987; Clarke, 1987; Alley, 1989a). Water pressure depends on water supply and drainage path. Water is generated at the base of a glacier by melting as a result of frictional heat and the geothermal heat flux. It is then discharged either by intergranular flow downward through the sediment; in channels between the ice and bed (Röthlisberger, 1972; Nye, 1973); or by flow in a sheet along the ice/bed interface (Weertman, 1972). In the following discussion only the case where groundwater flows through sediment is considered.

Two mechanisms exist whereby an ice sheet can generate a potential gradient and thus groundwater flow. An ice sheet advancing over unlithified sediment increases the load applied to the sediment. This induces an excess pore water pressure which dissipates as water drains from the pores and the sediment consolidates. Meltwater from the base of the ice sheet may also drain through the sediment and thus contribute to the increase in pore water pressure.

The rate of intergranular flow is determined by Darcy's Law (equation 2.14) and the ability of the sediment system to transport water is limited by the sediment permeability and the potential gradient. The transmissibility of a sediment is defined as the permeability multiplied by the length of the flow path. If the transmissibility of a subglacial sediment is high compared to the rate of water supply, water will drain easily through the sediment. Water pressure will therefore be low, the shear strength of the sediment high, and deformation unlikely to occur. If, however, the sediment has a low transmissibility in comparison to the water supply, the basal water pressure will be high and the shear strength of the sediment relatively low, allowing sediment deformation to occur.

2.11 Subglacial Drainage Models

The character and geometry of subglacial sediments therefore determines the nature and rate of groundwater drainage, and the rate and degree of consolidation and shear deformation. Ice sheets over lowland terrain are commonly underlain by till, a relatively fine grained sediment of low permeability (table 2.1). The hydrological conditions beneath basally melting ice sheets moving over unlithified sediments are likely to lie between two extremes. It is possible to

construct models of the subglacial permeability distribution which produce these two extreme drainage patterns. These are termed the one dimensional model, where till (or any low permeability sediment) is underlain by a highly permeable aquifer, and the two dimensional model, where till is underlain by an aquiclude.

2.11.1 The One Dimensional Drainage Model

In this case, illustrated in figure 2.8, the subglacial sediment consists of a low permeability material (e.g. till) overlying a material of much higher permeability (an aquifer). The aquifer therefore acts as a drain for the till allowing meltwater to flow down from the glacier sole through the till and out into the aquifer in response to a vertical potential gradient. Ideally the drainage path through the low permeability material can be assumed to be vertical and equal to the till thickness. Water flow in the aquifer is assumed to be in response to a horizontal potential pressure gradient, towards an area of lower potential pressure at the terminus. The drainage path through the aquifer can therefore be assumed to be horizontal.

In the simple case shown in figure 2.8 the water pressure at the base of the ice is a result of the potential pressure at the top of the aquifer plus the potential pressure difference across the till, shown in figure 2.9. The resulting effective pressure at the base of the ice is therefore the difference between the pressure due to the overburden of ice and the water pressure, illustrated schematically in figure 2.10. The vertical effective pressure gradient in the sediment is dependent on the potential presssure gradient which in turn is dependent on the permeability of the sediment (from Darcy's Law, equation 2.14).

Two end members of the one dimensional model can be identified. One in which a relatively low permeability till overlies the aquifer and one in which a till of high permeability overlies an aquifer. In the former case, a significant potential pressure gradient is required to drive the meltwater through the low permeability material (Darcy's Law, equation 2.14) and thus the effective pressure gradient will be greater than the gravitational gradient in the till. In the latter case, however, the potential pressure gradient required to drive the water flow will be much less and thus the effective pressure gradient in the till will be almost gravitational. These two end members are illustrated in figure 2.11.

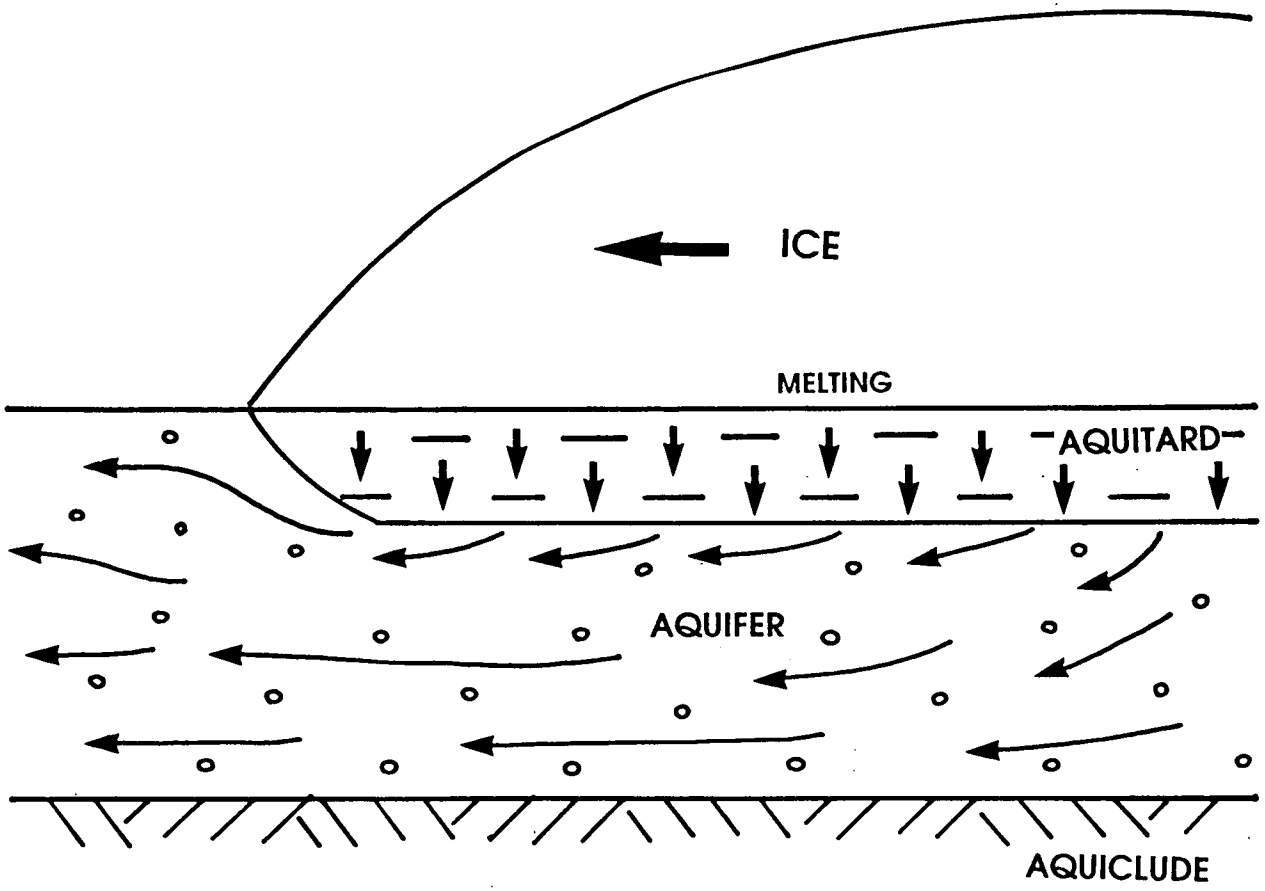

Figure 2.8: The one dimensional drainage model.

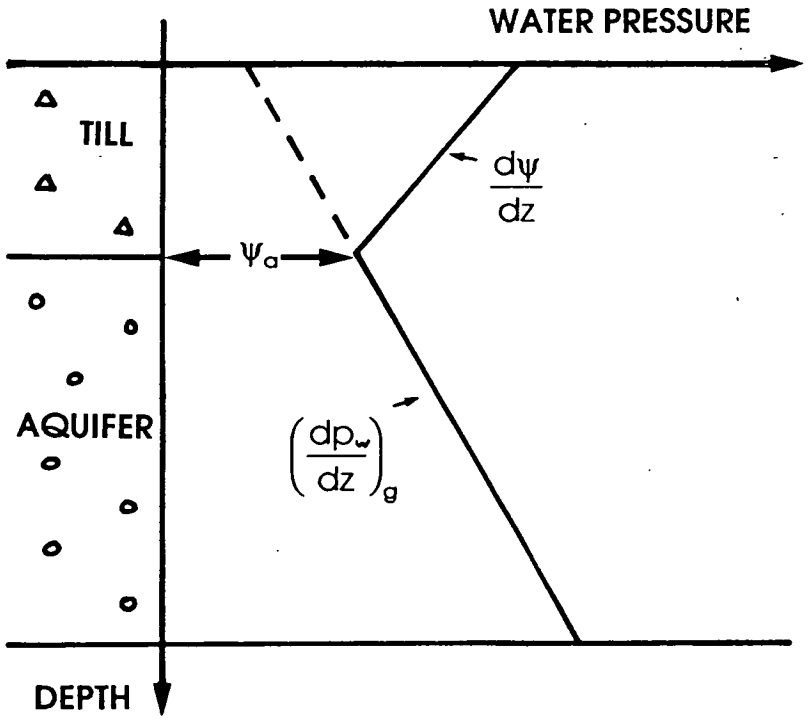

Figure 2.9: Vertical water pressure gradients in the one dimensional model, showing that the water pressure at the base of the ice is a result of the water pressure at the top of the aquifer and the potential difference across the low permeability stratum.

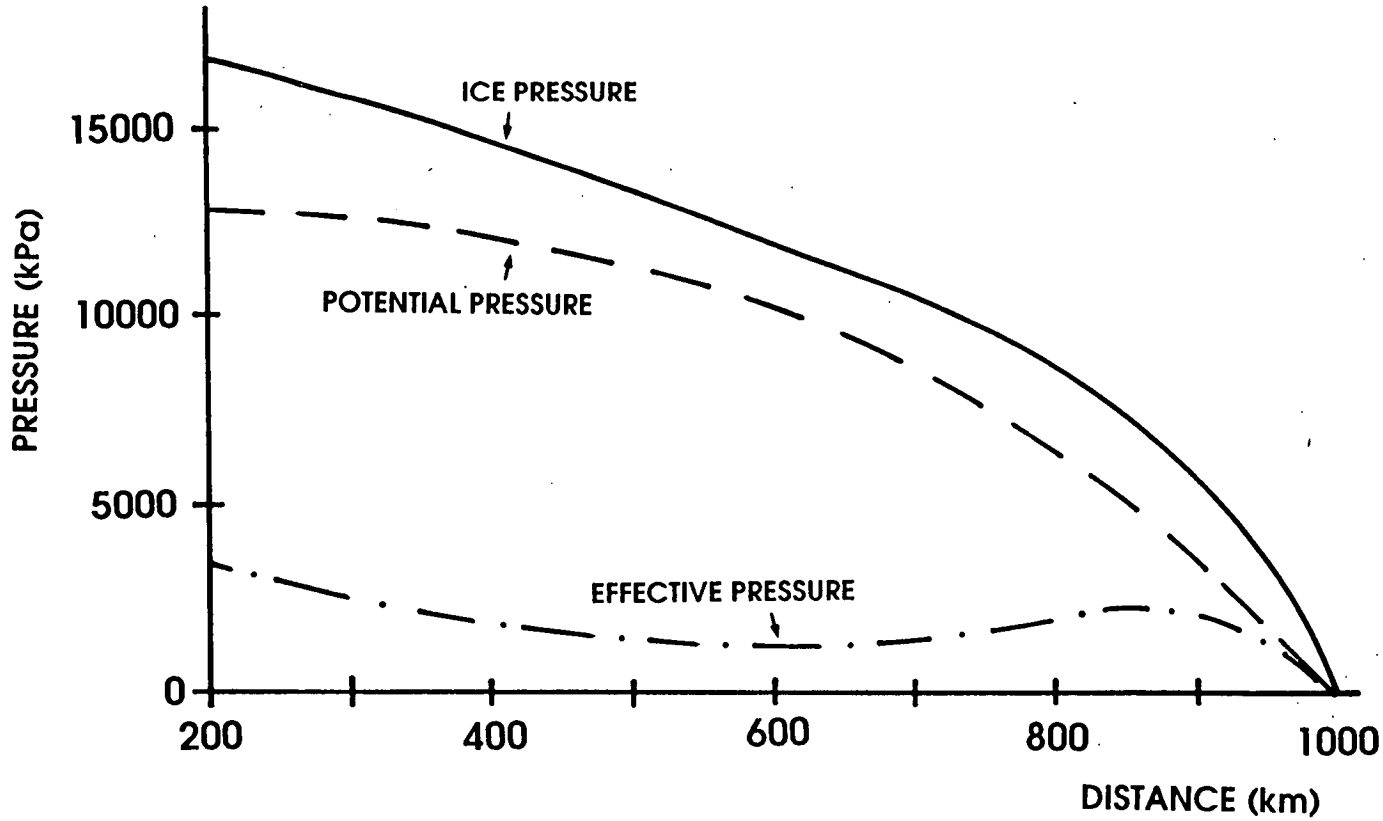

Figure 2.10: The relationship between the pressure applied by the ice sheet, the potential pressure and the effective pressure at the base of the ice for the one dimensional model. The effective pressure is the difference between the applied pressure and the potential pressure.

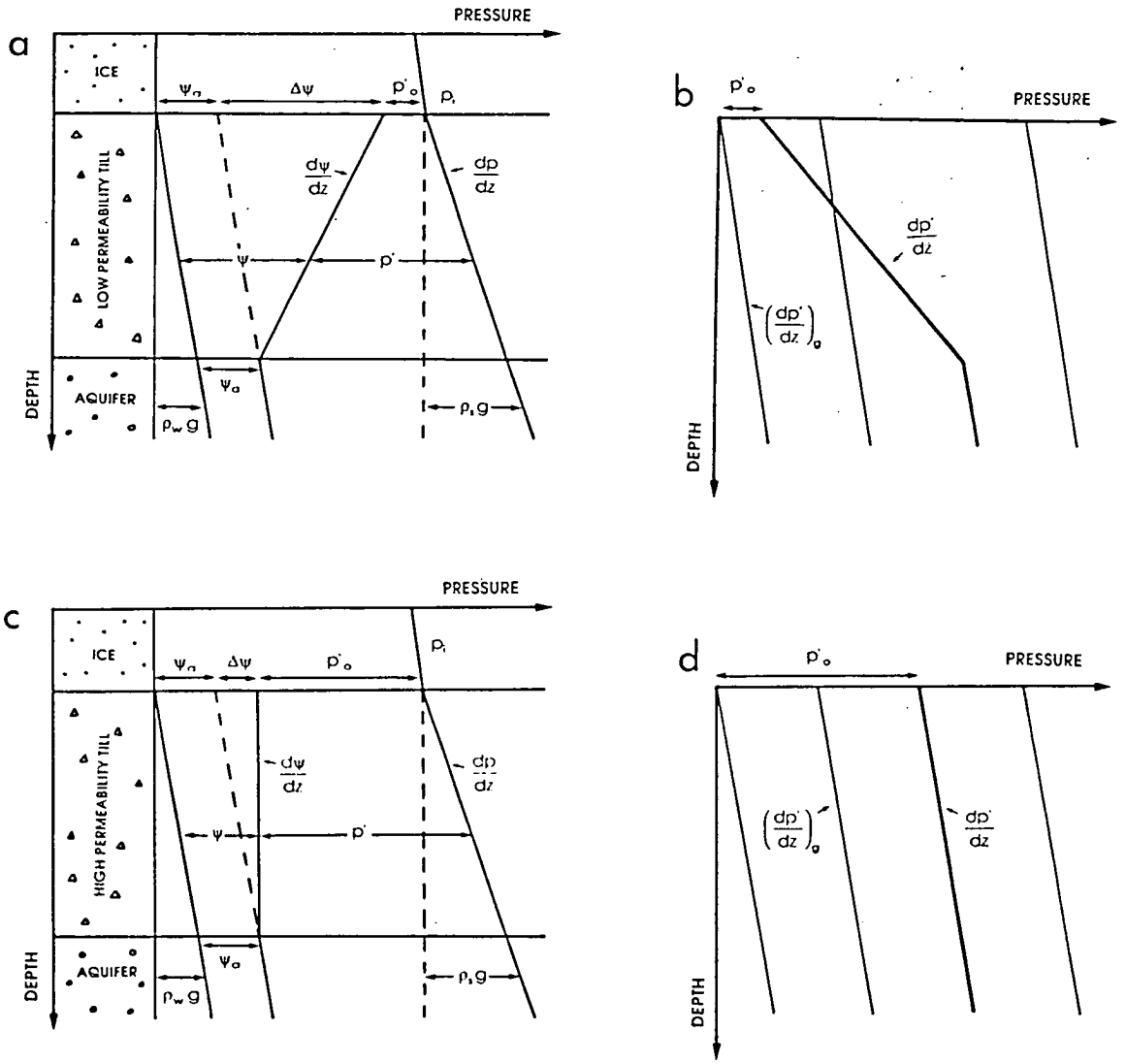

Figure 2.11: The two extreme permeability distributions in the one dimensional model: **(a)** shows the theoretical distribution of pressure in a low permeability till overlying an aquifer; **(b)** shows the comparison between the vertical effective pressure gradient and the vertical gravitational gradient in the low permeability till; **(c)** shows the theoretical distribution of pressure in a till of high permeability; **(d)** shows the comparison between the vertical effective pressure gradient and the vertical gravitational gradient in the high permeability till.

2.11.2 The Two Dimensional Drainage Model

In this case, shown in figure 2.12, the subglacial till directly overlies an aquiclude (eg impermeable bedrock) and meltwater is forced to flow horizontally through the till. The discharge of water increases in the down glacier direction. If the permeability and thickness of the sediment remain constant, the potential gradient required to drive the flow increases until the water pressure at the glacier sole exceeds the ice overburden pressure and the ice sheet becomes unstable (Boulton and Jones, 1979).

This model is included for completeness but is not considered further in this study.

2.12 Conclusions

An advancing ice sheet imposes a force on the underlying sediments which can be resolved into a normal vertical effective pressure and a shear stress. The magnitude of the vertical effective pressure determines the shear strength of the sediment. If high water pressures are sustained in glacial sediments by basal melting, the resulting effective pressure may be sufficiently low to make the sediments much softer than ice and allow them to deform at low basal shear stresses. Under these circumstances, there may be a strong interaction between the ice sheet and its bed of sediment, which will determine the response of the ice sheet to atmospheric conditions, and the form, structure and dispersal of its sediments.

Subglacial water pressures therefore play a fundamental role in glacier dynamics. Subglacial groundwater flow is determined by the hydraulic geometry of the underlying sediments. Two models of subglacial permeability distribution are identified, one of which is studied in more detail in the following chapters. The aim is to establish the effect of the properties of subglacial sediments on ice sheet dynamics.

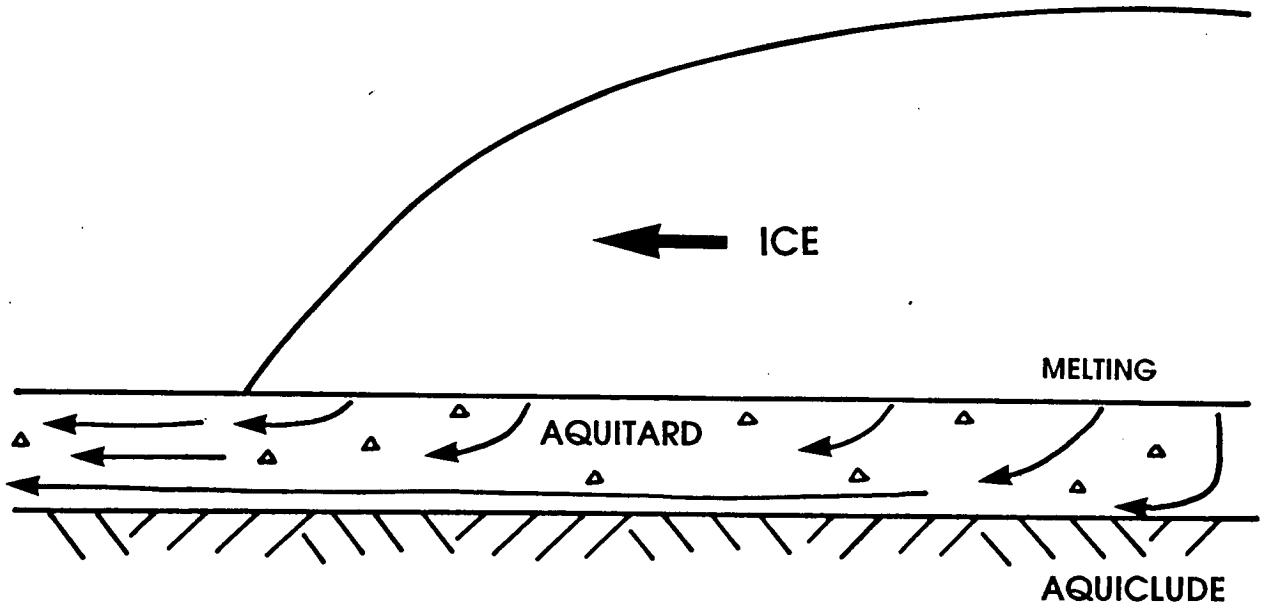

Figure 2.12: The two dimensional model.

CHAPTER 3

THE NORTHERN NETHERLANDS: AN EXAMPLE OF THE ONE DIMENSIONAL DRAINAGE MODEL

3.1 Introduction

Drainage and state of consolidation are integral parts of a subglacial sediment deformation theory. Data on the state of consolidation of an appropriate glacially overridden sequence could provide both a test of the theory and be a valuable constraint in its application as it yields information on the pressure regime found at the base of an ice sheet at its maximum extent.

The geological setting of the northern Netherlands provides an example of the one dimensional model. In this area, a homogeneous Elsterian clay overlies a thick lower Pleistocene aquifer which in turn overlies relatively impermeable Upper Tertiary strata. This sequence, schematically illustrated in figure 3.1, was subsequently overridden by the Saalian ice sheet which deposited a thin layer of till on top. The Elsterian clay, being fine grained and homogeneous, should be an ideal medium to preserve a record of preconsolidation and was therefore chosen to test the theory.

This chapter outlines the Quaternary geology of the Netherlands in general terms before going on to discuss the glacial history in more detail. The geotechnical and sedimentological tests carried out to confirm that the clay was suitable for consolidation testing are then outlined and their results discussed.

3.2 The Quaternary Geology of the Netherlands

The Netherlands lie at the eastern margin of the North Sea Basin. During the Tertiary (Pannekoek, 1956) and Quaternary (Zagwijn and Doppert, 1978) periods, this basin subsided and was filled with marine, fluvial, and glacial deposits (de Jong and Maarleveld, 1983). The Tertiary deposits are mainly of marine origin and consist predominantly of clays and clayey glauconitic sands. In most areas these are conformably overlain by Quaternary deposits of marine and continental origin. Fluvial sedimentation progressively replaced marine sedimentation until the sea withdrew completely during the latter part of the Quaternary and mainly fluvial

sediments were deposited on the present mainland (van Staalduinen *et al.*, 1979). The modern surface geology of the Netherlands is shown in figure 3.2 and a more detailed lithological map of the Pleistocene deposits in the north and central Netherlands is presented in figure 3.3.

3.2.1 Stratigraphy and Geological History

The Quaternary sediments are grouped into the formations shown in figure 3.4. These formations are defined on the basis of their origin, lithology and in some cases sedimentary petrology (van Staalduinen *et al.*, 1979).

The principal feature of the Quaternary period was its fluctuating climate. This provides a natural basis for its subdivision. Climate change depends on a number of factors, the most important being temperature. Figure 3.5 shows the subdivision of the Quaternary in the Netherlands based on temperature change. In northern Europe and North America, colder periods gave rise to permanent glaciers. hence the name glacial periods. These glaciers dispersed under warmer conditions, in phases known as interglacials. This changing climate had a direct effect on the vegetation of the area. In the Netherlands the boundaries between glacial and interglacial periods are identified biostratigraphically, where pollen indicates the change from a dominantly non-arboreal (open tundra) environment to one with boreal (temperate) woodland and vice versa (Zagwijn, 1975).

The lowermost Pleistocene sediments are of both marine and continental origin, the boundary between them representing the coastline at the time of deposition. The Maasluis Formation is the only marine formation identified in the Lower Pleistocene. It was deposited in a shallow sea and lies conformably on Upper Tertiary strata. Fluvial sedimentation occurred inland, with material being brought in by the Rhine-Meuse river system from the south east (forming the Tegelen and Kedichem Formations) and from the north east by rivers with a north German provenance (forming the Harderwijk Formation). A rapid regression then occurred resulting in a large alluvial fan forming at the junction of both river systems.

The oldest Middle Pleistocene sediments consist of fluvial deposits from the river systems mentioned above. The Rhine and Meuse rivers in the south depositing the Sterksel Formation, whilst the eastern rivers gave rise to the Enschede Formation. These deposits have been correlated palaeobotanically with the Menapian and the lower "Cromerian Complex" (van Staalduinen *et al.*, 1979).

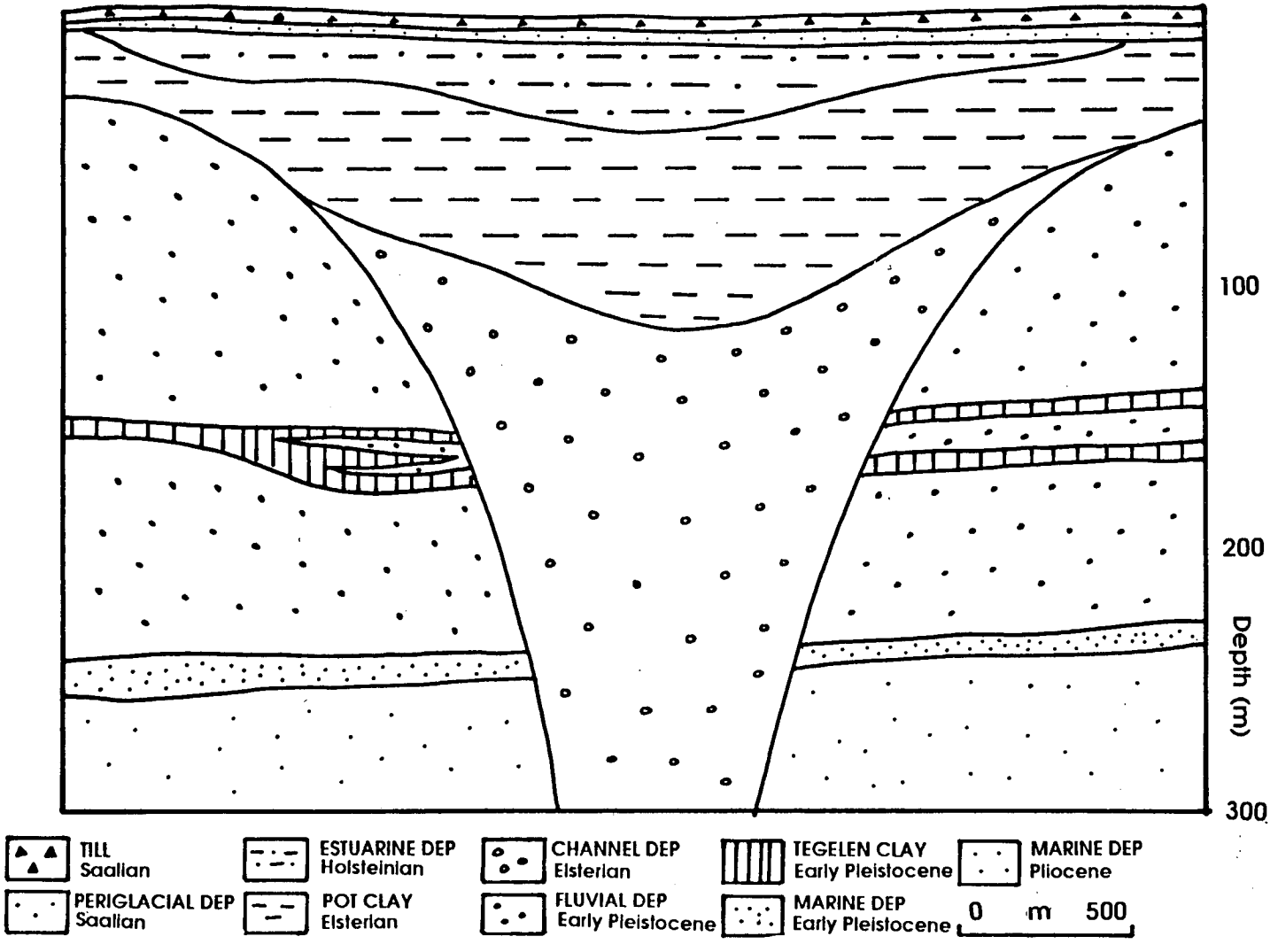

Figure 3.1: Cross section through an Elsterian channel (ter Wee, 1983a).

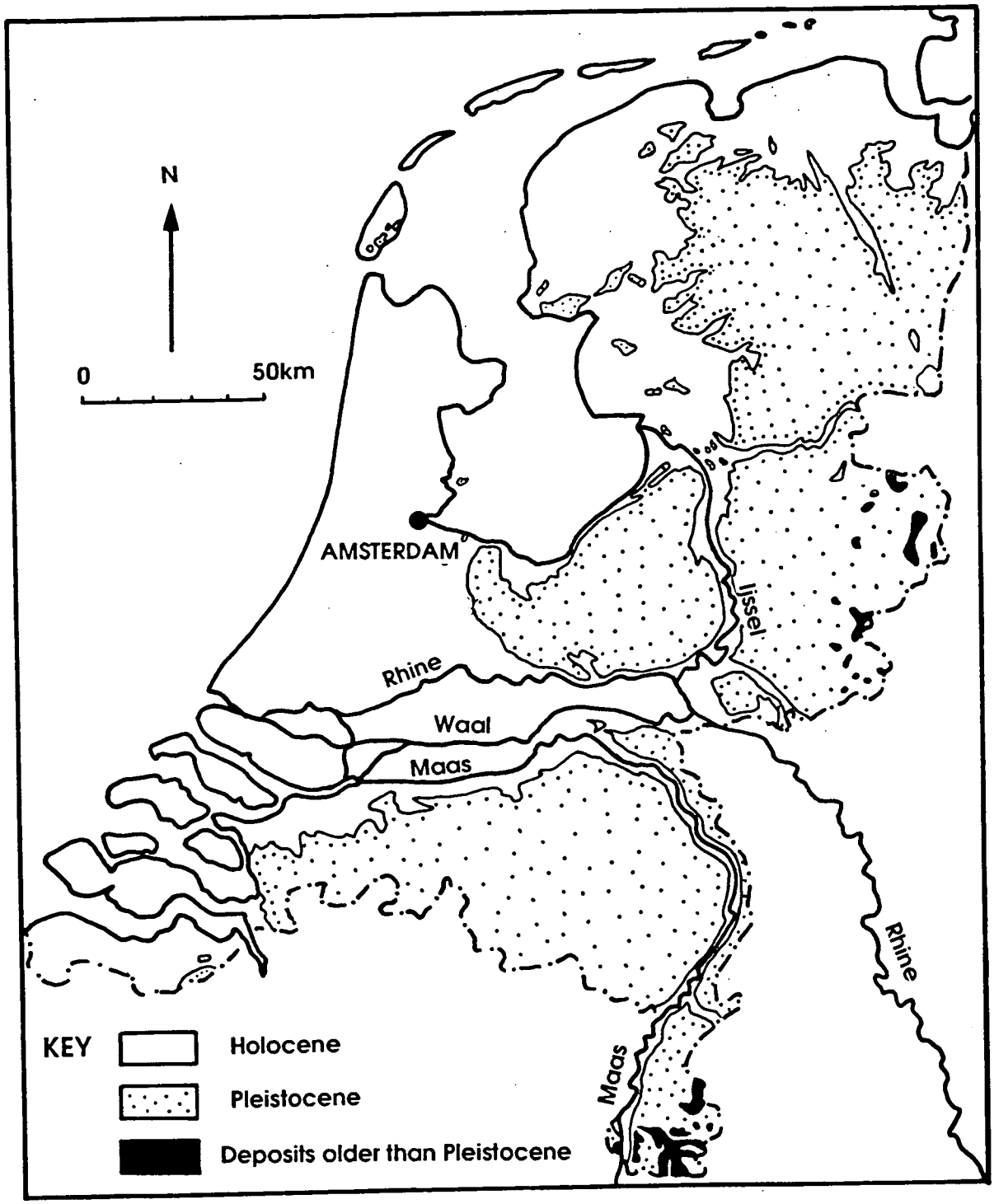

Figure 3.2: Simplified geological map of the Netherlands (Pannekoek, 1956).

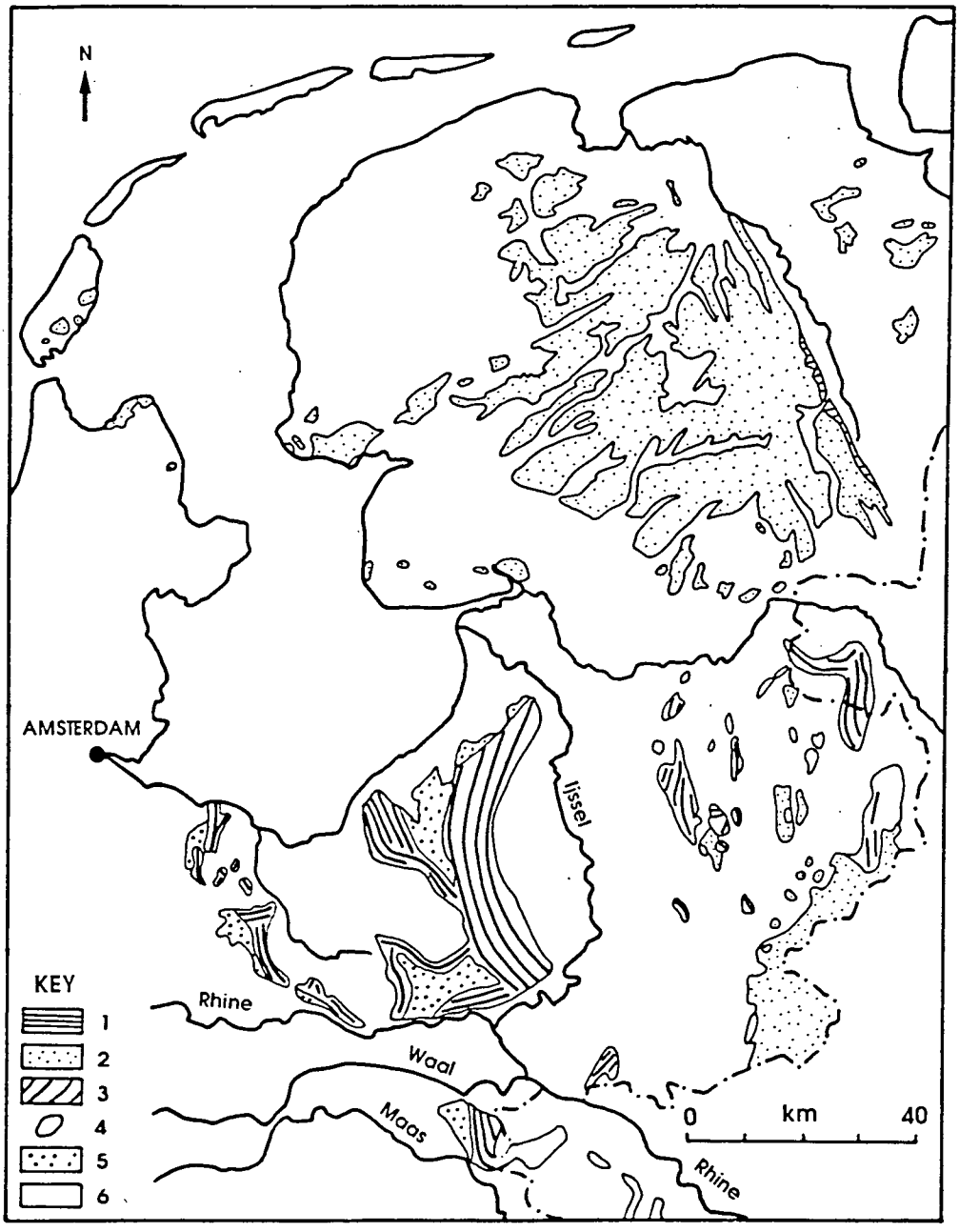

KEY

1	Fluvio - glacial deposits older than Saalian Till
2	Saalian Till
3	Saalian push moraine (showing strike)
4	Saalian push moraine (strike not indicated)
5	Fluvio - glacial deposits
6	Deposits younger than Saalian

Figure 3.3: Pleistocene deposits in the northern and central Netherlands (Pannekoek, 1956).

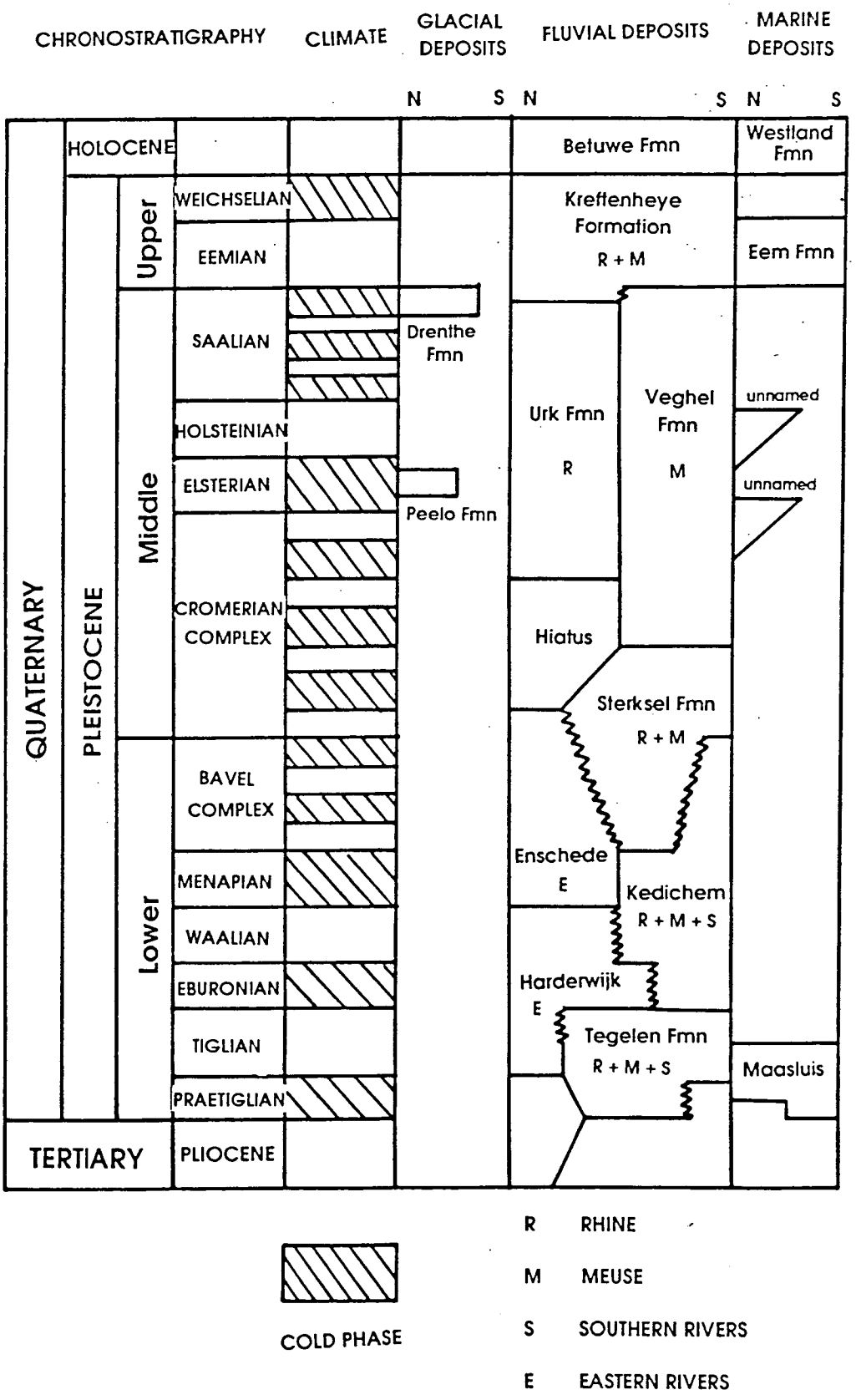

Figure 3.4: Quaternary Stratigraphy of the northern Netherlands (modified from Zagwijn, 1974, 1985).

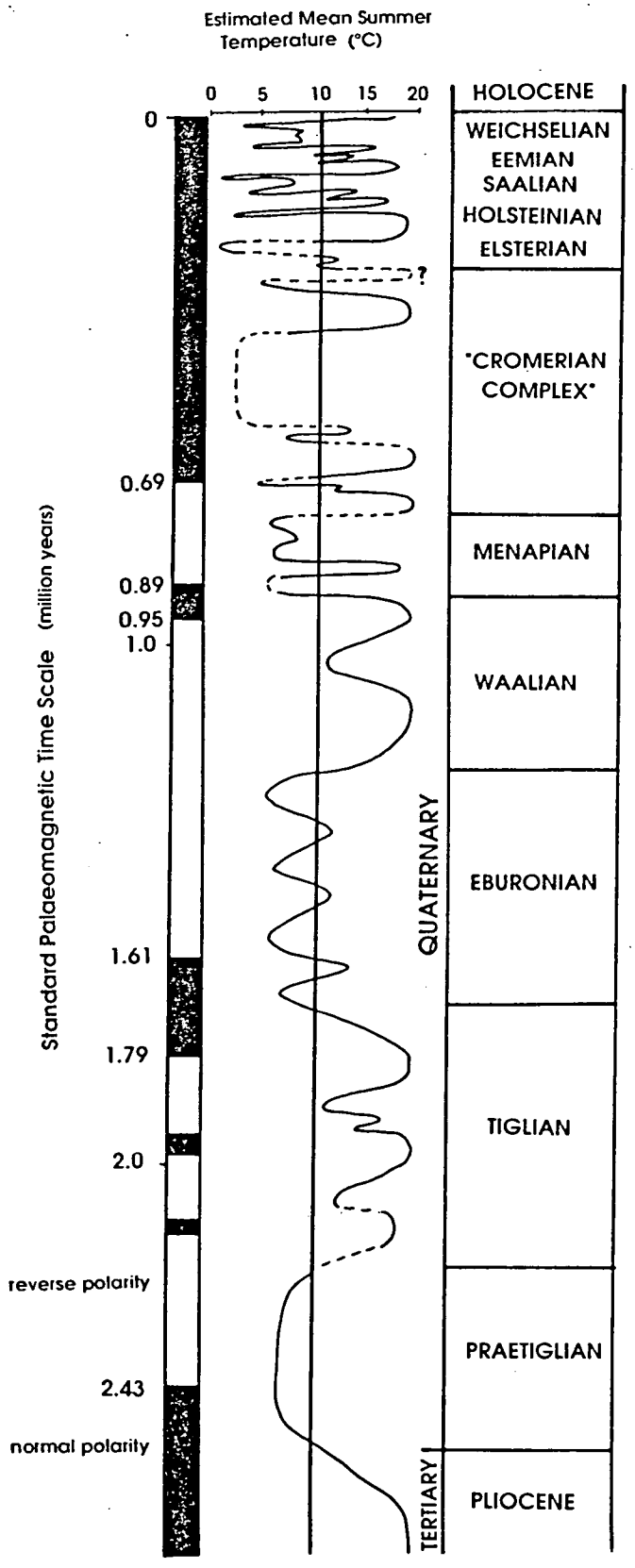

Figure 3.5: Subdivision of the Quaternary in the Netherlands based on climatic changes (modified from Zagwijn, 1974).

The pattern of fluvial sedimentation changed in Middle Pleistocene times when the German rivers stopped discharging into the area. The Meuse then deposited the Veghel Formation in the south eastern Netherlands (correlated as upper 'Cromerian Complex' to Saalian in age), whilst the Rhine deposited the non marine parts of the Urk Formation in the central and northern Netherlands (upper 'Cromerian Complex' to Saalian). During both the last interglacial of the 'Cromerian Complex' and the Holsteinian interglacial, eustatic sea level rose sufficiently to cause major marine incursions across the Netherlands (van Staalduien *et al.*, 1979). The resulting marine deposits intercalated with the fluvial deposits of the Urk Formation. Between these interglacials, during the Elsterian, an ice sheet advanced into the northern Netherlands. Deep erosion channels were formed which, after ice retreat, were infilled with the lacustrine sediments of the Peelo Formation. After the Holsteinian, early Saalian aeolian periglacial deposits formed.

Ice advanced into the northern Netherlands again during the later Saalian reaching its maximum extent in the central part of the country. This affected the topography of the area, forming deep basins and ice pushed ridges. The tills and fluvioglacial sediments related to the Saalian glaciation make up the Drenthe Formation which forms a plateau in the northern Netherlands (shown in figure 3.3). The advancing ice diverted the Rhine, causing it to drain west along the ice margin and join the Meuse, depositing the Kreftenheye Formation. On deglaciation the Rhine regained part of its former course, flowing to the north west (van de Meene and Zagwijn, 1978).

In the Upper Pleistocene, at the end of the Saalian, deglaciation caused sea level to rise. Marine sediments were deposited in the south west, and in glacial depressions (the Eem Formation). Meanwhile fluviatile sedimentation continued depositing the Kreftenheye Formation. Marine deposition ceased completely at the start of the Weichselian as sea level fell in response to glaciation. The Weichselian ice sheet did not reach the Netherlands, terminating to the north east in eastern Denmark and northern Germany. Deposition of aeolian sand was, however, widespread in a dry, poorly vegetated, periglacial environment affected by strong, glacial katabatic winds.

Deglaciation at the beginning of the Holocene caused sea level to rise. This was accompanied by a rise in the groundwater table resulting in widespread peat formation. Continuing sea level rise caused flooding and thus the peat is generally overlain by brackish sediments which pass into marine deposits. Slight regressions resulted in peat intercalations within these clays.

More recently, anthropogenic influence has changed the landscape to a large extent, through dyke building, peat digging and land reclamation.

Ice is thought to have advanced into the northern Netherlands in Elsterian and Saalian times. These two stages are discussed in more detail in the following section.

3.2.2 Elsterian and Saalian Glaciations in the Netherlands

The Quaternary period in the northern hemisphere is characterised by cyclical phases of ice sheet growth and decay. These ice sheets periodically loaded the crust and as a result consolidated their underlying sediments. Glaciations leave distinctive erosive and depositional traces in the sedimentary record. Climate change can also be identified in the palynological record from which Zagwijn (1985) has identified eight glacial periods in the Netherlands during the last 900ky. In two of these cold phases the large ice sheets which spread over north west Europe extended into the Netherlands (Wildenborg *et al.*, 1990).

3.2.2.i The Elsterian Stage

The earliest evidence for glaciation in north west Europe is found in the Elsterian (Ehlers *et al.*, 1984). The southern marginal areas of this ice sheet are characterised by elongate subsurface channels, orientated roughly parallel to the direction of ice movement, forming a broad belt stretching from the U.K. in the west (Woodland, 1970) to Bjelorussia in the east (Stephan, 1983). The distribution of Elsterian channels in the Dutch sector of the North Sea, the Netherlands and Germany is shown in figure 3.6. In the Netherlands and North Sea these channels are overdeepened, have a complex anastomosing form, and are often loosely termed tunnel valleys. Individual channels reach a length of 6 - 20 km and a width of 2.5 - 6 km and have a maximum depth of 450 m in the North Sea (Wildenborg et al, 1990).

Various theories have been put forward to explain the origin of these channels. The majority of workers have assumed that they are subglacial meltwater features (e.g. Kuster and Meyer, 1979). Boulton and Hindmarsh (1987) suggest that they originate through subglacial piping as a result of high pore water pressure in the subglacial sediments, whilst Wingfield (1990) proposes that they are formed during deglaciation as a result of the catastrophic draining of lakes in or at the margins of the ice sheets.

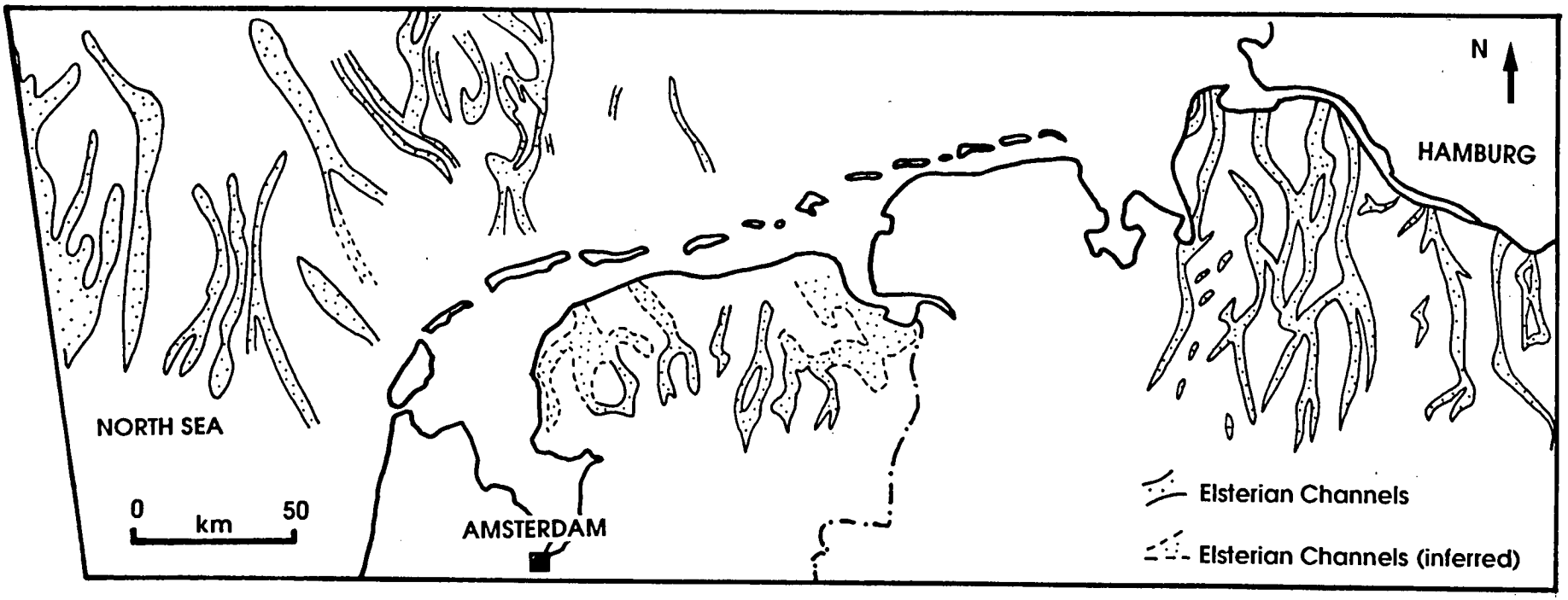

Figure 3.6: Distribution of Elsterian channels in the Netherlands, Germany and the Dutch sector of the North Sea (RGD Report, 1990).

The channels in the Netherlands are filled by sediments dated palynologically as Elsterian (Zagwijn, 1974). The glaciolacustrine, glaciofluvial and periglacial sediments deposited during the Elsterian glacial stage in the Netherlands are assigned to the Peelo Formation (ter Wee, 1983b). In the north, the Peelo Formation occurs largely as tunnel valley infill, comprising large irregular lenses of clay with interbedded fine sands, whereas in the south it occurs as fine sands. Channels up to 350 m deep are found in the north eastern Netherlands, filled in their lower parts by coarse and fine sands which are replaced by clay towards the top. This clay is present in the channels to the west but wedges out in the south where it is replaced by coarse and fine sands. This clay, known as 'potklei', is a dark grey to black, homogeneous clay, although locally it is laminated and resembles a varved clay (ter Wee, 1983b). The distribution of Peelo Formation sediments in the northern Netherlands is shown in figure 3.7.

Similar channel infills are found in northern Germany, consisting of a complex of clays, silts and fine sands, known as the Lauenburg Clay (Ehlers *et al.*, 1984). These sediments form a regular fining up sequence which fines from proximal in the north west to distal in the south east. It is suggested that these were deposited during deglaciation, initially by meltwater, and later in a proglacial lake, reflecting the progressive decay of the Elsterian ice sheet (Ehlers and Linke, 1989).

Elsterian till is only recognised at two locations in the Netherlands. Unlike its German counterparts it contains no Scandinavian material. Ehlers *et al.* (1984) and ter Wee (1983b) are not convinced that this is a true till and suggest that the Elsterian ice sheet did not reach the Netherlands but terminated to the north east.

During the Holsteinian the sea entered what remained of the channels depositing a marine facies. By the early Saalian the channels were completely filled in (Ehlers and Linke, 1989).

3.2.2.ii The Saalian Stage

The Saalian began as a non-glacial cold phase, interrupted by several weakly developed warm phases. Zagwijn (1973) identified two interstadials in the vegetational record of the Netherlands; the Bantega and Hoogeveen. The continental ice sheet developed during the youngest stadial, and was associated with widespread permafrost which formed in non-glaciated areas (ter Wee, 1983a).

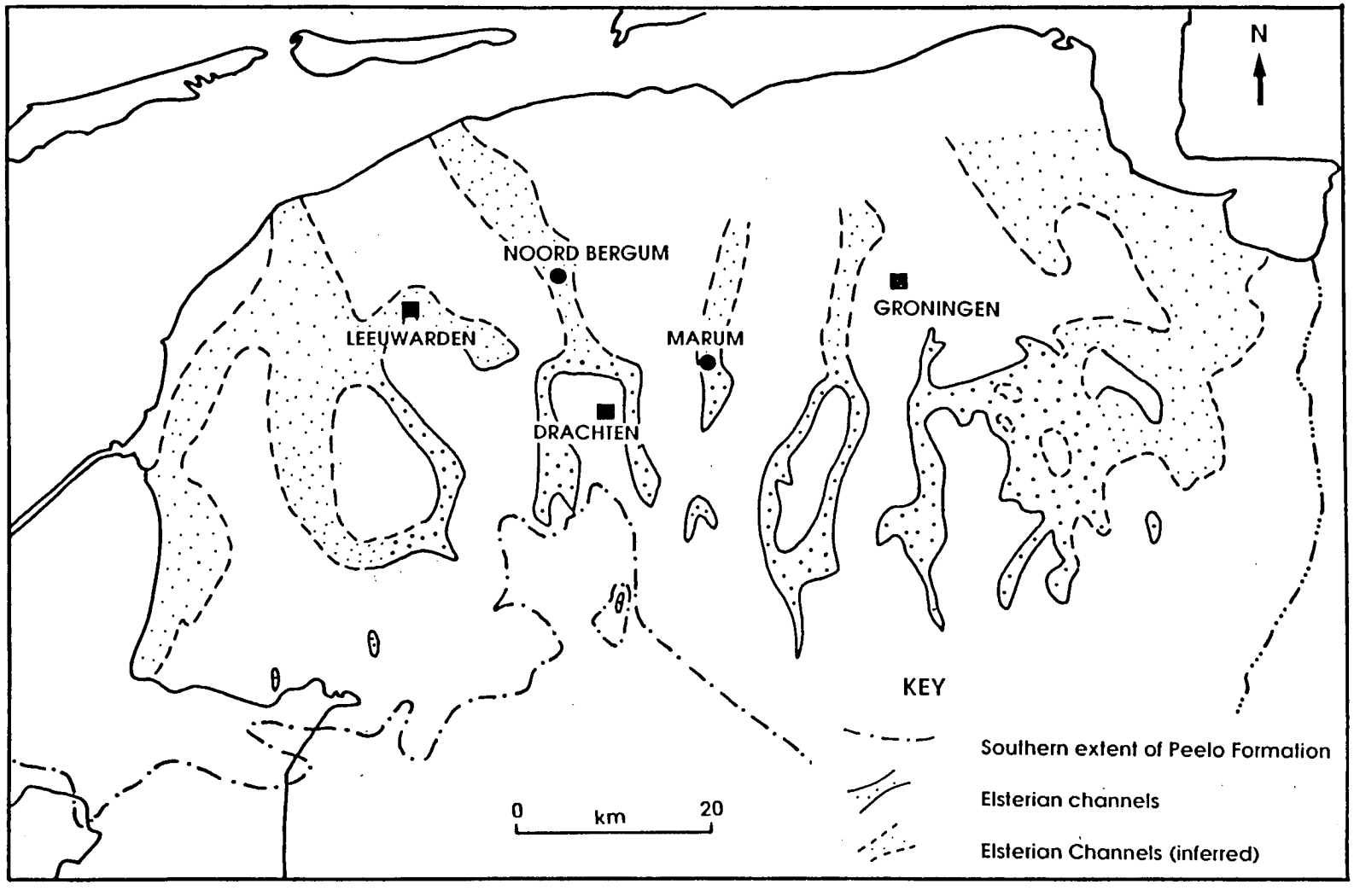

Figure 3.7: Location of Elsterian channels and Peelo Formation sediments in the northern Netherlands (RGD Report, 1990).

Only one till sheet occurs in the Netherlands (Zandstra, 1976). It is fairly continuous and preserves evidence of a major glacial cover during the Saalian (Ehlers *et al.*, 1984). Different till types are recognised within this sheet on the basis of crystalline pebble assemblages, lithological and granulometric properties, and fine gravel and heavy mineral compositions (Rappol *et al.*, 1989; see also Zandstra, 1983; Schuddebeurs and Zandstra, 1983; Rappol and Stoltenberg, 1985; Haldorsen *et al.*, 1989).

The direction of ice movement is inferred from morphological, petrographical and clast-fabric analyses of the till sheet. Two successive flow directions, an older movement towards the south west and a younger movement towards the south east or south south east, have been recognised (Rappol, 1984, 1987; van den Berg and Beets, 1987). The younger movement is petrographically distinguished by east Baltic (Finnish) crystalline indicator pebbles in the till in the north east of the Netherlands and east central Baltic pebbles in the central Netherlands (Rappol *et al.*, 1989). The provenance areas are shown in figure 3.8 (Zandstra, 1987). The older ice movement, towards the south west, can be divided into two phases on the basis of different indicator pebble assemblages (Rappol *et al.*, 1989). The till deposited in the earlier phase is indicated by east Baltic pebbles, whilst a later phase is characterised by south and west Baltic (Swedish) pebbles. Figure 3.9 shows the different directions of ice flow during the Saalian giving rise to the till assemblages found in the northern Netherlands. The resulting till profile is summarised in figure 3.10.

Thus in the northern Netherlands a series of sediments belonging to the Peelo Formation, including pot clay, have been deposited in channels overlying more permeable strata (the lower Pleistocene Dutch aquifer) which is in turn underlain by impermeable marine clays of Tertiary age. This sequence was overridden by an ice sheet during the Saalian glaciation and thus can be used to test the one dimensional drainage model (figure 2.8).

The Peelo Clay is known to be fine grained and homogenous and should therefore preserve a record of its stress history. The sedimentological and geotechnical properties of the pot clay were therefore studied in more detail to confirm its suitability for preconsolidation pressure determination.

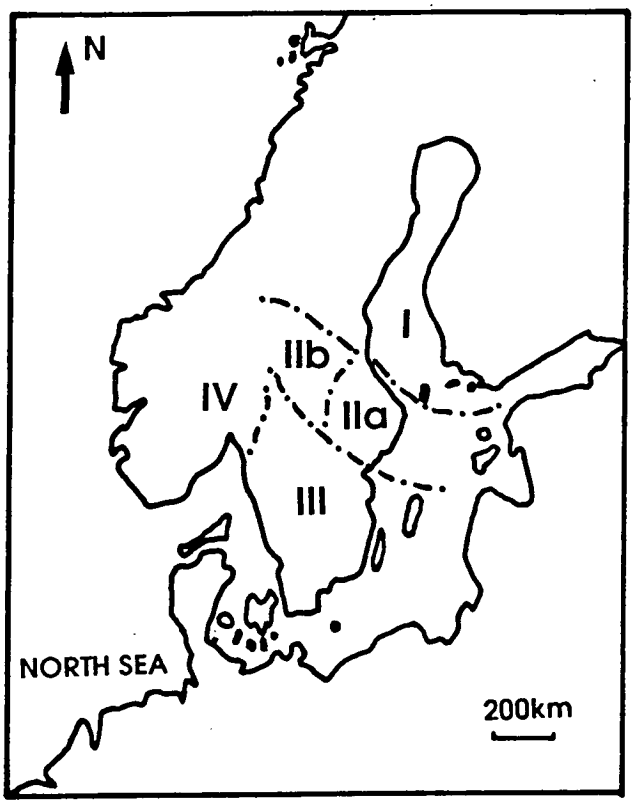

Figure 3.8: Provenance of indicator pebble assemblages (Rappol, 1987):

I	east Baltic
IIa	east central Baltic
IIb	west central Baltic
III	south Baltic
IV	Oslo region.

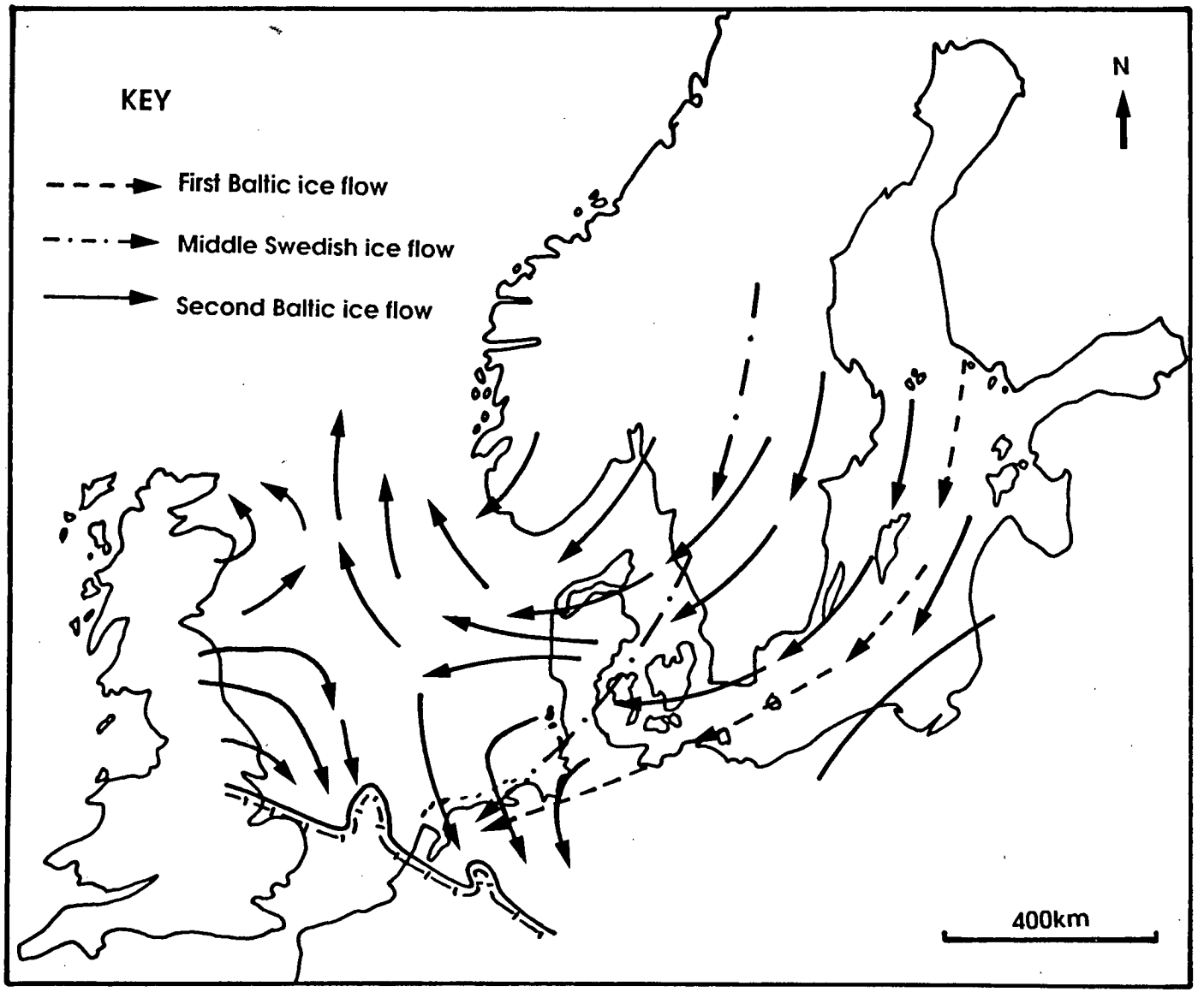

Figure 3.9: Schematic representation of flow lines for the Saalian ice sheet (modified from Rappol *et al.*, 1989)

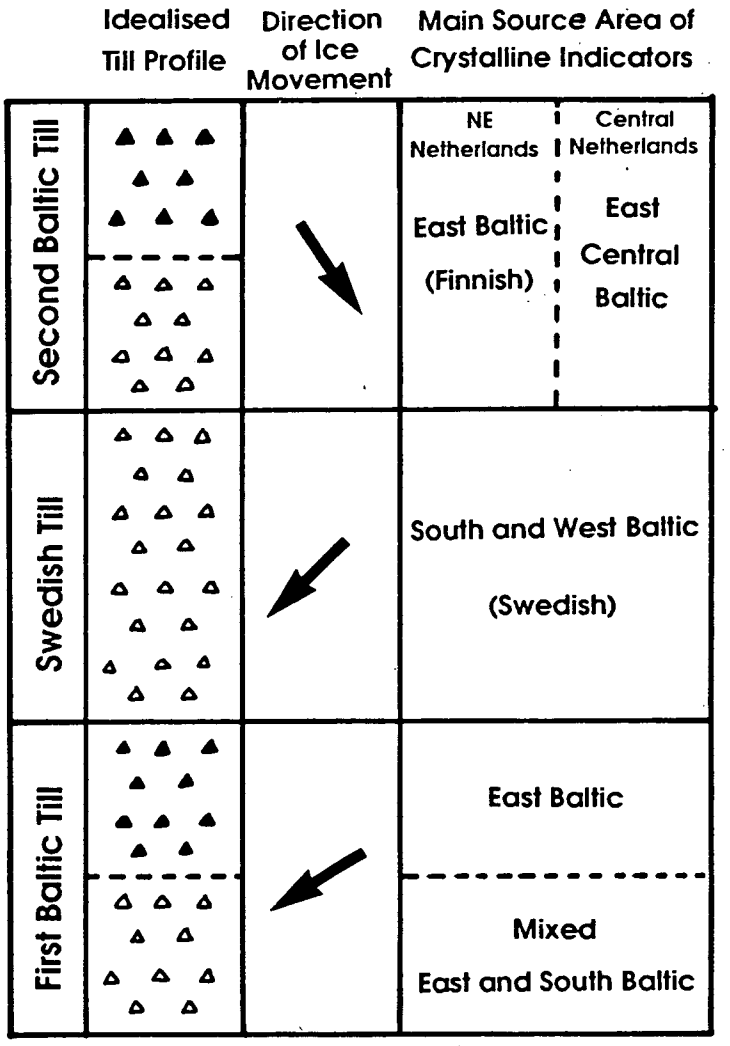

Figure 3.10: Schematic stratigraphic sequence of till types in the Netherlands (modified from Rappol *et al.*, 1989).

3.3 Sedimentological and Geotechnical Analysis of the Pot Clay

Peelo formation sediments, including pot clay, were known from previous drilling to exist in an Elsterian channel near Noord Bergum in the northern Netherlands (figure 3.7). Site investigations, carried out for civil engineering purposes (Schokking, 1984), have shown that this clay is overconsolidated. This has presumably occurred as a result of loading by the Saalian ice sheet. The pot clay has a fine grained and homogeneous nature and should therefore be an ideal medium to preserve a record of preconsolidation. A borehole was therefore drilled near Noord Bergum to allow further investigation of the properties of the former subglacial sediment. (A borehole was drilled through a similar channel near Marum, also in the northern Netherlands, and a series of geotechnical tests carried out on the sediments. The results of these tests are reported by Schokking, 1990a & b).

After completion of the Noord Bergum borehole, geophysical logging was carried out. A natural gamma log was run with the steel casing in place. This was then removed and electrical resistivity and spontaneous potential logs taken. The logs are explained in appendix A and illustrated in figure 3.11.

The geophysical logs (figure 3.11) show that the top 40m of the borehole consists of alternating bands of low permeability, fine grained, argillaceous material and high permeability, coarser, sandy material. This overlies a unit, approximately 70m thick, consisting of uniform, fine grained, argillaceous material of low permeability. An abrupt change to a coarser, sandy unit occurs at about 110m depth and this comprises the bottom 10m of the core.

3.3.1 Sampling Procedure

The borehole, 120m deep, was sampled every 3m, and an undisturbed, orientated 70mm ϕ tube sample, 40 - 50 cm long, was taken. These were sealed and waxed to prevent moisture loss. Forty two samples were taken, thirty of which were split lengthwise along their axis in the laboratory at the Rijks Geologische Dienst (R.G.D.) for visual inspection and geotechnical index testing. The position of the opened samples in the core is shown in figure 3.12.

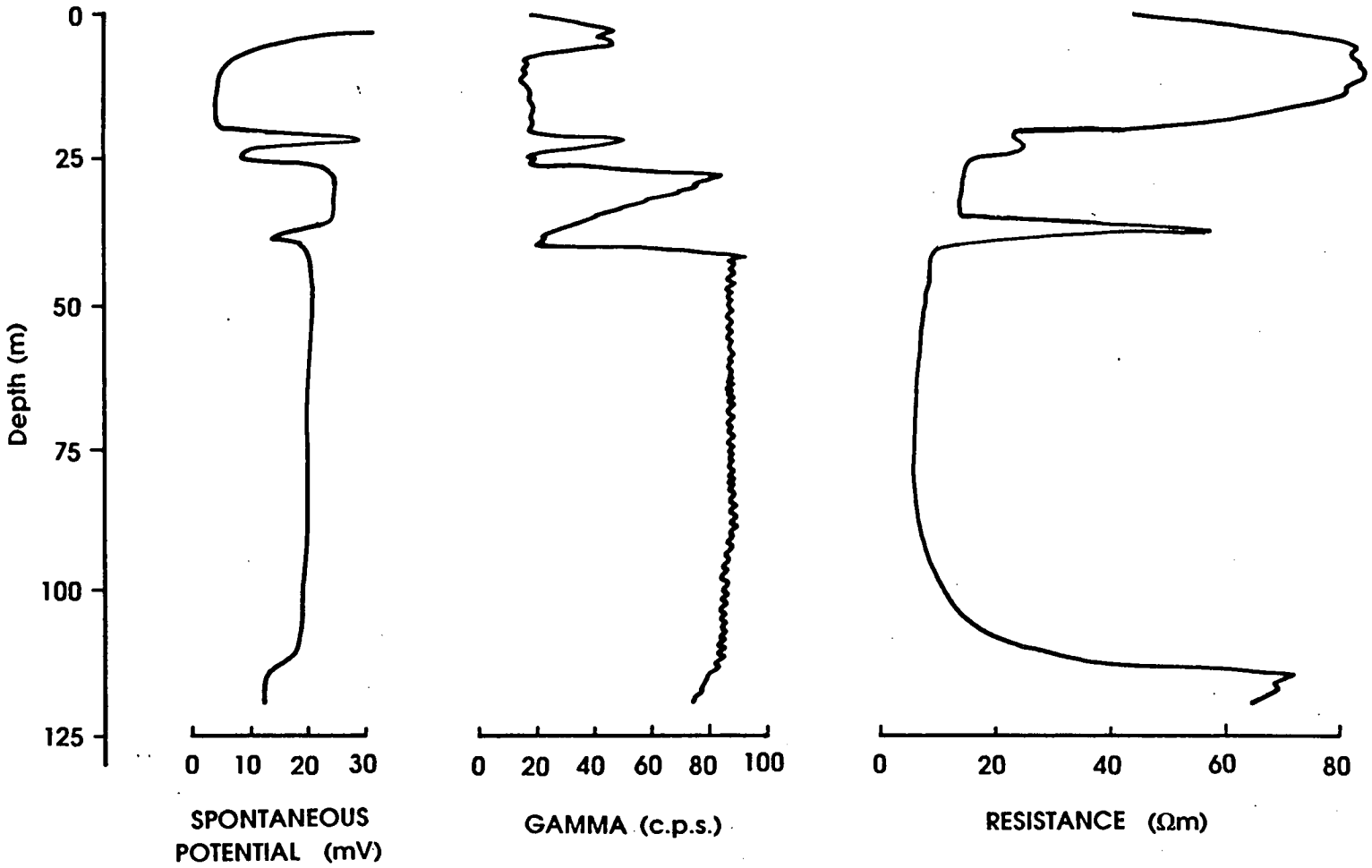

Figure 3.11: Geophysical logs for the Noord Bergum borehole.

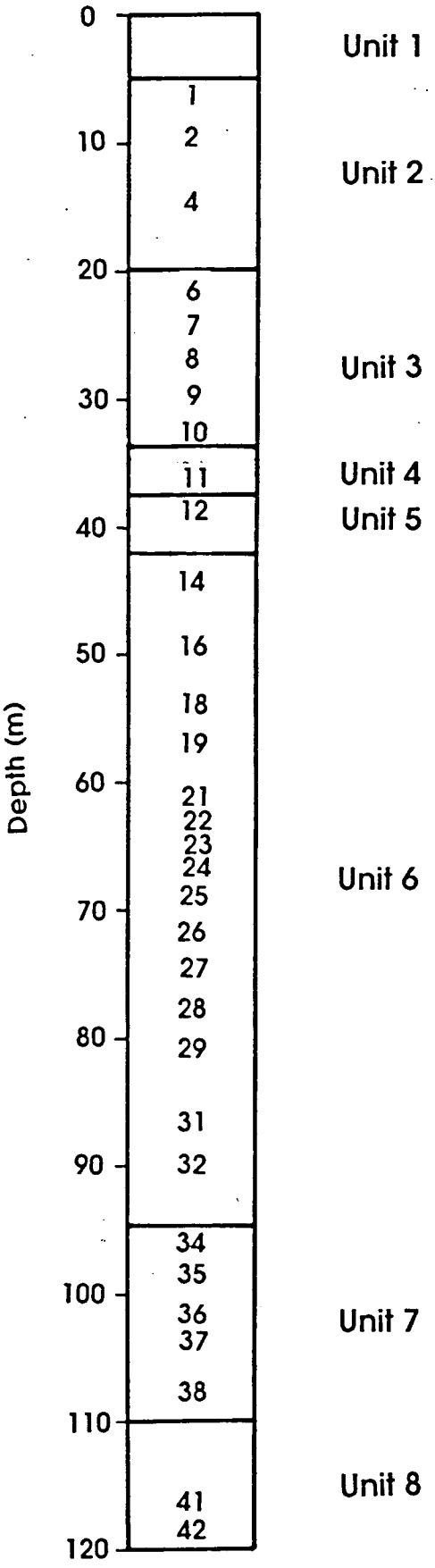

Figure 3.12: Position of the core samples in the Noord Bergum borehole. The lithological units are described in the text and a summary sample description given in table 3.1.

Table 3.1: Description of core samples.

Sample No.	Depth (m)	Summary Sample Description
NB1	5.5	Fining up beige sand.
NB2	9.4	Coarse and fine beige sands.
NB4	14.5	Coarse and fine beige sands with organic matter.
NB6	20.5	Dark olive green silty clay interbedded with fining up beige sand.
NB7	23.5	Olive green silty clay, top of sample rich in organic matter.
NB8	26.4	Homogeneous dark grey clay with shell fragments.
NB9	29.5	Grey green homogeneous clay with shells and sand.
NB10	32.5	10cm beige sand overlying dark grey silty clay with organic material and shells.
NB11	35.5	Brown black silty clay with organic material.
NB12	38.5	Olive green coarse and fine sands.
NB14	44.5	Contorted grey and black clay with areas of coarse sand.
NB16	49.8	Contorted grey and black clay with wispy folds.
NB18	53.5	Homogeneous (?) black clay with silty wispy folds.
NB19	56.5	Dark grey - black clay ; fractured.
NB21	61.0	Fissured black clay.
NB22	62.8	Fissured black clay.
NB23	64.0	Fissured black clay.
NB24	65.5	Fissured black clay.
NB25	68.5	Fissured black clay.
NB26	74.5	Fissured black clay.
NB28	77.5	Black clay with khaki silt rich folds.
NB29	80.5	Black clay with light grey silty clay pockets.
NB32	89.5	Fractured dark grey clay.
NB35	98.5	Silty black clay.
NB36	101.7	Dark grey - black silty clay.
NB37	104.5	Grey - green silty clay.
NB38	107.5	Dark grey - black clayey silt with sandy silt lenses.
NB41	116.5	Interbedded olive green - yellow silts and sands with a complex structure at the base of the sample.
NB42	119.5	Coarse and fine sands and silty sands folded at the base.

3.3.2 Borehole Description

3.3.2.i Lithology of the Borehole

This section is based on information obtained from opened samples, geophysical logs and discussion with F. Schokking at the R.G.D. The core samples are described in table 3.1 and illustrated in figure 3.13.

The borehole was drilled into a channel filled with Pleistocene sediments (Greeuw and Schokking, 1990). It comprises:

UNIT	LITHOLOGY	THICKNESS (m)	AGE
1	till	5	Saalian
2	sand	15	Holstein
3	clay	15	Holstein
4	silty clay	5	Elsterian
5	sand	5	Elsterian
6	clay	50	Elsterian
7	silty clay	15	Elsterian
8	sand	10	Early Pleistocene

Unit 1, interpreted as a till of Saalian age (Schokking, pers. comm.), consists of predominantly grey - green silty clay which becomes more sandy towards the base.

Unit 2, the upper sand layer, is 15m thick and consists of a unit of generally fining upwards beige sand underlain by interbedded coarse and fine beige sands. It is rich in organic matter at the base. These sands are thought to be of fluvial origin (Douma et al., 1989).

Unit 3, the upper clay layer, is also 15m thick. It consists predominantly of homogeneous dark grey - green clay which becomes more sandy towards the base, initially in the form of sand layers in clay, then as clay layers in sand. Shell fragments are found in the lower part of the unit suggesting an estuarine origin (Douma et al., 1989; Greeuw and Schokking, 1990).

Units 2 and 3 are correlated as Urk Formation sediments of Holstein age (Douma et al.,1989).

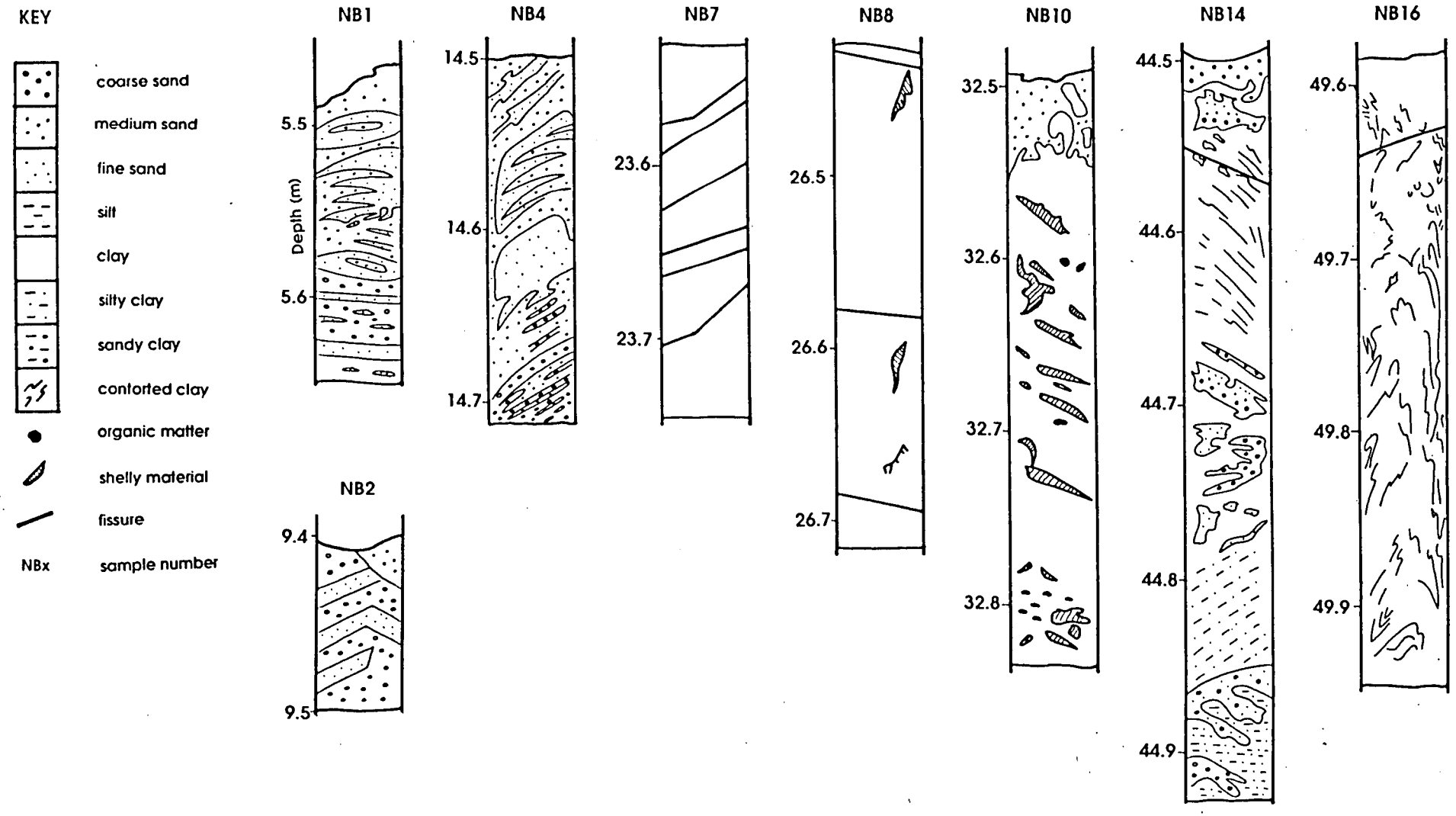

Figure 3.13: Illustrations of the core samples from the Noord Bergum borehole.

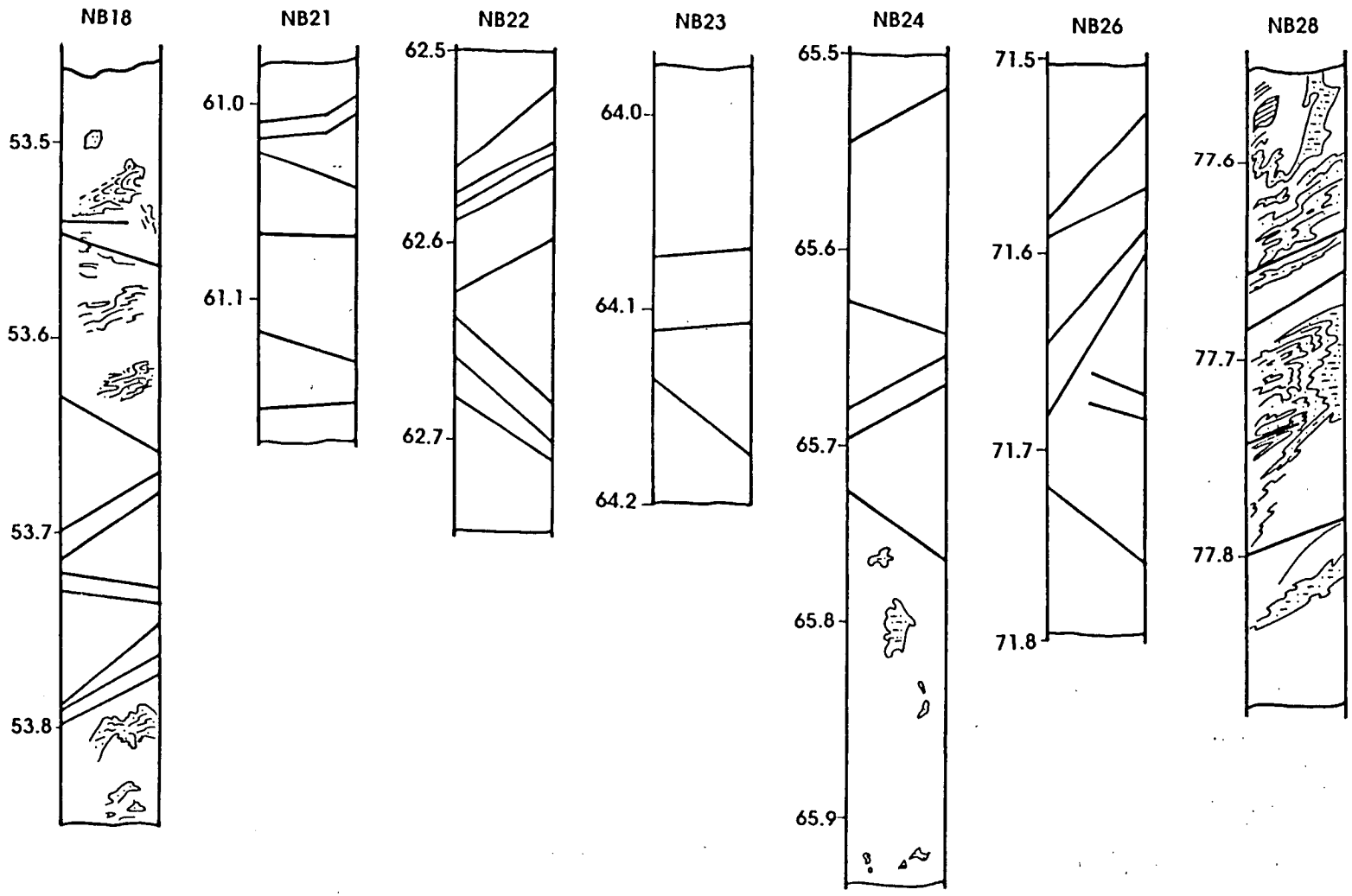

Figure 3.13: (cont). Illustrations of the core samples from the Noord Bergum borehole.

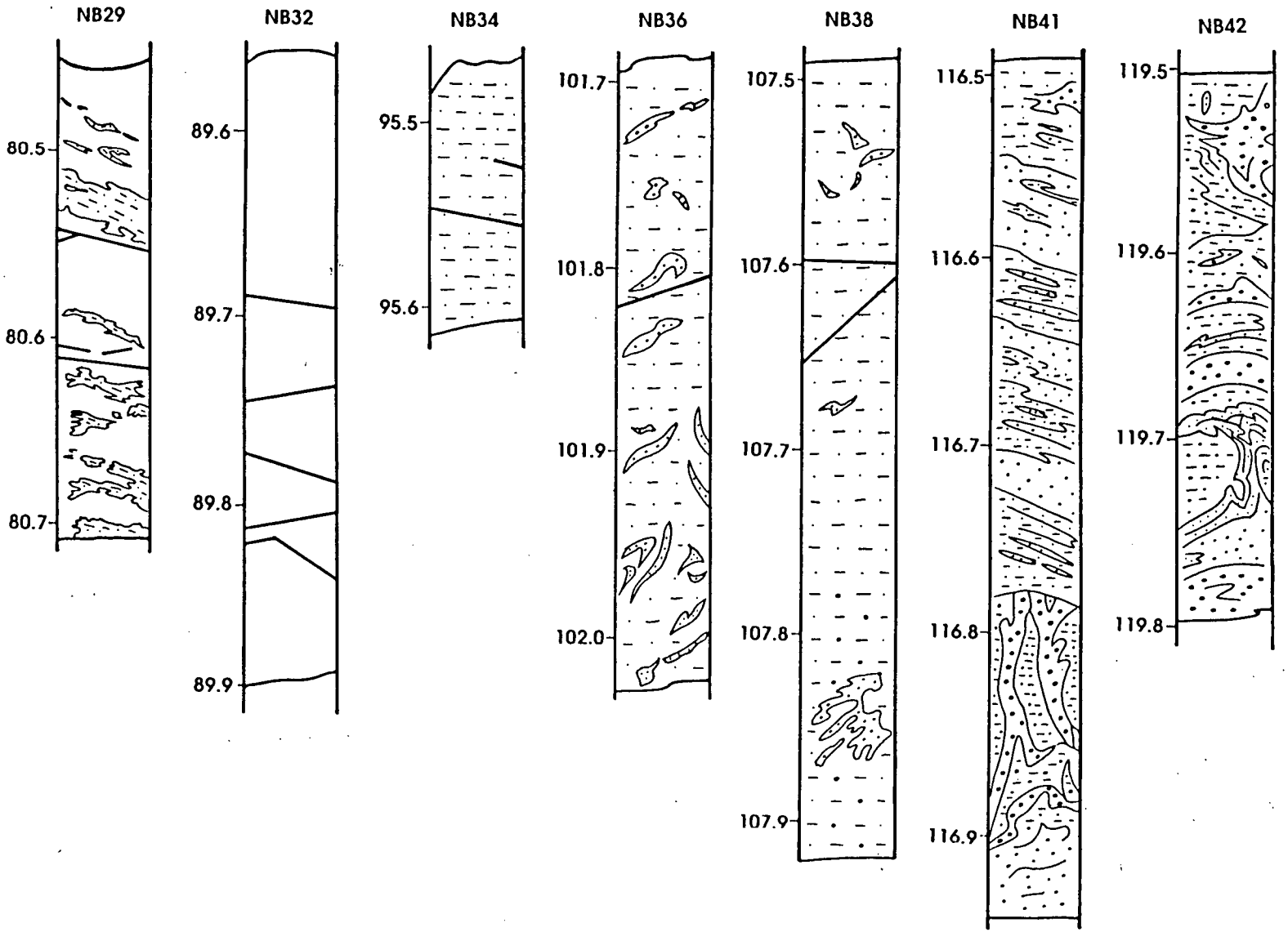

Figure 3.13: (cont). Illustrations of the core samples from the Noord Bergum borehole.

Unit 4 consists of 5m of thick dark brown - black silty clay, rich in organic matter. This is the pot clay of the Peelo Formation, thought to be of glaciolacustrine origin, deposited at the end of the Elsterian glaciation.

Unit 5 is an olive green sand layer, also 5m thick.

Unit 6 is a 50m thick pot clay deposit which is generally homogeneous throughout. The top 15m is a deformed mass of light and dark grey clay with some wispy, silt rich, disrupted fold fragments. This overlies 15m of homogeneous black clay which is very stiff and fractured. 20m of black clay with khaki silt rich folds then occurs with evidence of more deformation towards the base. This unit grades into unit 7.

Unit 7 is a lighter, more silty unit, 15m thick.

Unit 8 forms the bottom 10m of the core and comprises interbedded olive green - beige silts and sands which have a complex structure suggesting water escape has occurred. Deeper boreholes in the same area show that the Peelo clay sits on top of a thick unit of sands and gravels with localised thin silt and clay layers.

The sediments found in the core are interpreted as having been deposited in a channel. A cross section through the channel at Noord Bergum is shown in figure 3.14. The structures observed in the opened core samples are illustrated in figure 3.13 and described below.

3.3.2.ii Structures found in the Borehole

The structures observed in the sediments (figure 3.13) were studied by visual inspection of the open core samples. Examples of folding and fissuring were found suggesting that the sediments have at some stage been deformed.

At a depth of 5.5m in unit 2 (the upper sand layer), the sands are predominantly horizontally bedded. However, with depth, the bedding becomes inclined, dipping around 30° to the north. This is found in a section of core at 14.5m. Fissures occur at 5.5m and at 5.6m, dipping towards the south at 20 - 30°.

Bedding becomes horizontal again at 20.5m where silty clay is interbedded with coarse sand.

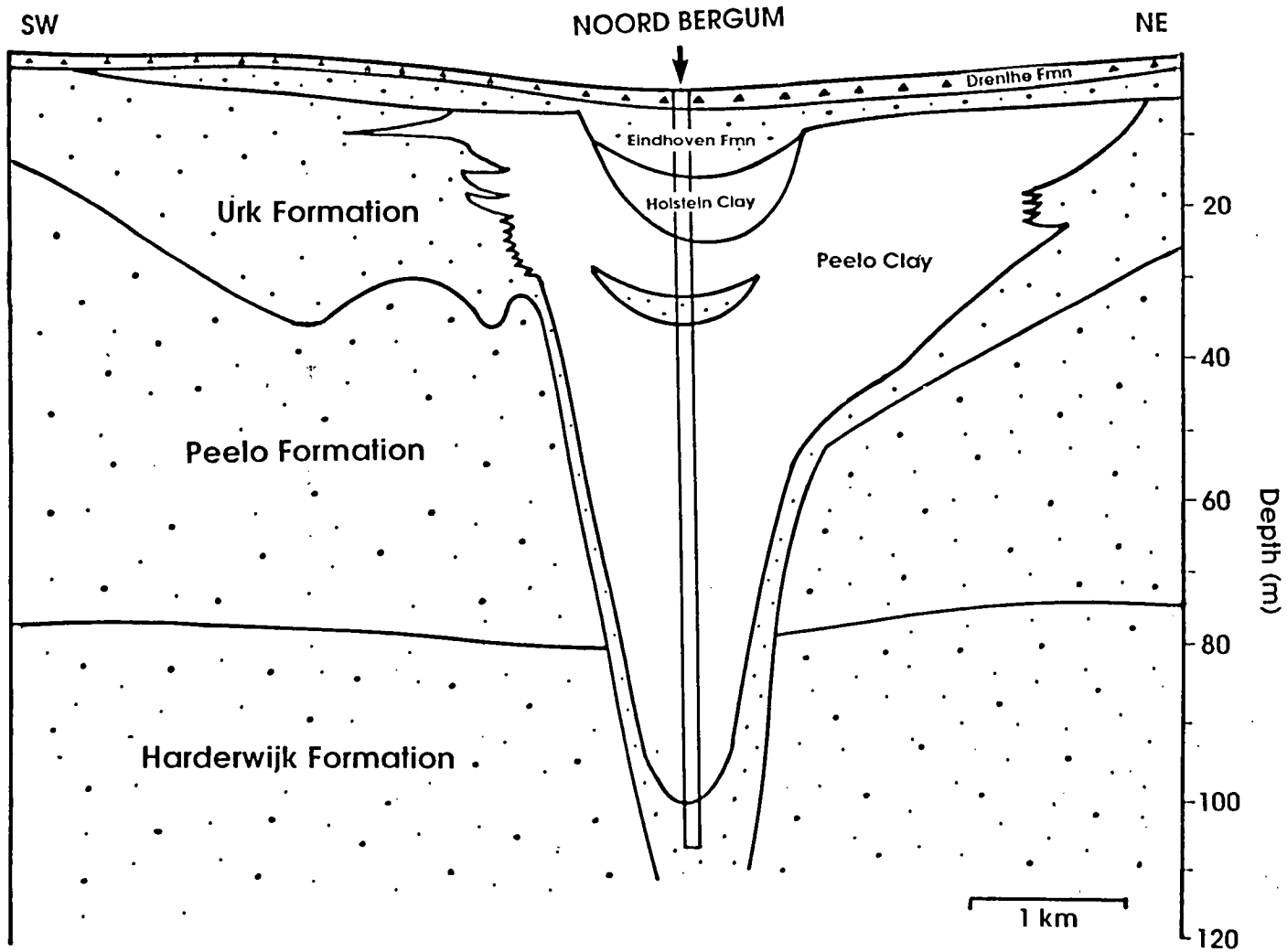

Figure 3.14: Cross section through the Elsterian channel at Noord Bergum.

The clay of unit 3 is fairly homogeneous. There are no folds and no obvious signs of intense deformation, although there are a few fissures. These dip towards the south, steepening with depth from 10 - 30°. Shells occuring in the section at 32.6m are aligned, also dipping at 20 - 30° towards the south.

In the pot clay (unit 6), from 44 - 54 m, there is evidence of deformation and fracturing. The clay is contorted, shown by areas of lighter and darker grey clay which form wispy patterns. At 50m these are vertically inclined and take the form of sinuous areas of different shades of grey. At 53.5m, disrupted silt rich fold fragments are found. One such fragment consists of a fold nose, 3.5cm long and 1.5cm wide, surrounded by black clay. This section is also fractured.

Below this, from 60 - 72 m, the clay again appears to be homogeneous. However there is evidence to suggest it is intensely deformed. An indistinct flow structure is visible suggesting that the clay has been so extremely deformed that the original contortions have been stretched out leaving little trace. This section of the core is intensely fissured.

The lower part of the clay unit, from 77 - 90 m, again contains evidence for deformation in the form of folded silt rich horizons within the clay. At 77.7m the nose of a fold is preserved. At 80.6m, the silt rich horizons may represent the stretched out limbs of a fold. These silt rich bodies look as if they deformed and then remained competent whilst the clay was in a fluid state. Fissures occur in this section, mostly dipping at around 20° to the north.

In unit 7, the silt rich section, from 95 - 108 m, sandy flame like structures occur. These may have been injected into the clay when it was in a fluid state. This unit contains only a few fissures. These dip gently (3 - 6°) towards the north.

The sands of unit 8 at the base of the borehole have a complex structure. From 116.5 to 116.8 m these are interbedded and inclined at 20° towards the north, although at 116.8 - 116.9 m the horizontal bedding is disrupted and a predominantly vertical orientation occurs. This could have been caused by water escaping up through the sediment, perhaps as a result of loading. Below this the bedding is complex and at 119.7m a folded silt layer occurs in the sand. There are no fractures in the sand unit.

Fissures are found in the clay throughout the core (figure 3.13). They are also found in pot clay from other areas in the northern Netherlands (Schokking, 1990a). The fissures have a shiny, slickensided surface, visible when the core is broken up. Study of these fissures under the scanning electron microscope shows that on a microscale there is a preferred orientation of clay particles along the fissures.

The fissures are generally continuous across a sample. In unit 3, they tend to dip towards the south, whereas in the pot clay (unit 6), especially from 53 - 81 m, two sets occur. One dips towards the south at anything from 10 - 40° whilst another dips towards the north again at 10 - 40°. There is no distinct cross cutting relationship between the two sets of fissures. Fewer fissures occur in the silt rich layer and none occur in the sand.

Derbyshire *et al.* (1985) suggest that information can be obtained about the stress history of a glacially deposited sediment from its macrofabric. They identify three post depositional macrofabrics which are illustrated in figure 3.15.

The majority of fissures found in the pot clay have a shiny, slickensided surface, dip at a relatively high angle, and extend across the width of the core. They therefore correspond to the type IV macrofabric of Derbyshire *et al.* (1985) thought to be caused by differential compaction as a result of loading and subsequent unloading of sediment by an ice sheet.

Type II and III macrofabrics (Derbyshire *et al.*, 1985) are formed by an active layer of freeze thawing and permafrost respectively. They tend to have randomly orientated, discontinuous fissures which give an overall blocky appearance to the sediment. However these do not play an important part in the sediments of the Noord Bergum borehole suggesting that any permafrost present before the advance of the ice sheet must have thawed, and its effects overprinted by subsequent shearing and consolidation of the sediment as a result of the stresses imposed by the overriding ice.

More detailed study of the fissures is being carried out by F. Schokking at the R.G.D. to provide further information on the stress history of the sediment.

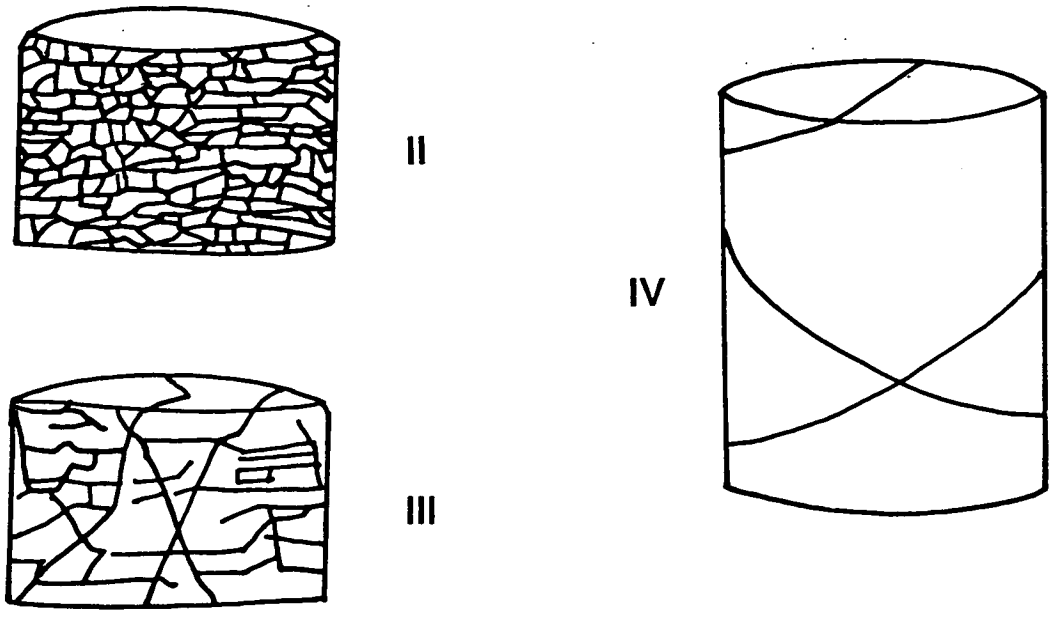

Figure 3.15: Post depositional macrofabric types described by Derbyshire *et al.*, 1985 (Derbyshire *et al.*, 1985).

3.3.2.iii Summary

The information obtained from the visual study of the opened core samples suggests that any permafrost existing before or during the initial stages of ice advance must have thawed before the glacial maximum. The porewater pressure, induced by the weight of the ice and the influx of basal meltwater, decreased the shear strength of the sediment and allowed it to deform in response to the basal shear stress imposed by the advancing ice. A steady state was then reached at the maximum extent of the ice sheet which allowed the sediment to consolidate but still permitted basal meltwater to drain through the sediment. The effective pressure at the base of the ice in the steady state would have been much larger than it was during the ice advance and thus incompatible with shear failure of the sediment as the sediment would have had significant strength. The subsequent retreat of the ice decreased the load acting on the sediment causing fissuring as a result of stress release. Later permafrost is not thought to have affected the clay based on the the absence of cross cutting discontinuous fissures.

3.3.3 Testing Procedure

The geotechnical tests carried out included the determination of unit weight, natural water content, plasticity, undrained shear strength and particle size distribution. The results of these tests (see section 3.3.4) suggested that the clay would be suitable for the determination of preconsolidation pressures and so fifteen samples were taken for one dimensional consolidation testing (described in the following chapter), particle size analysis, x-ray diffraction and scanning electron microscopy analyses.

A glossary of geotechnical definitions and symbols is given in appendix A.

3.3.4 Geotechnical Properties of the Pot Clay

Geotechnical tests were carried out on the pot clay to confirm that it was fine grained and homogeneous and so would be a suitable material for consolidation testing. The results of unit weight, moisture content, Atterberg limits and undrained shear strength tests were provided by the R.G.D. and are plotted in figure 3.16. Particle size analysis results are plotted in figure 3.17. Tables of results are presented in appendix A.

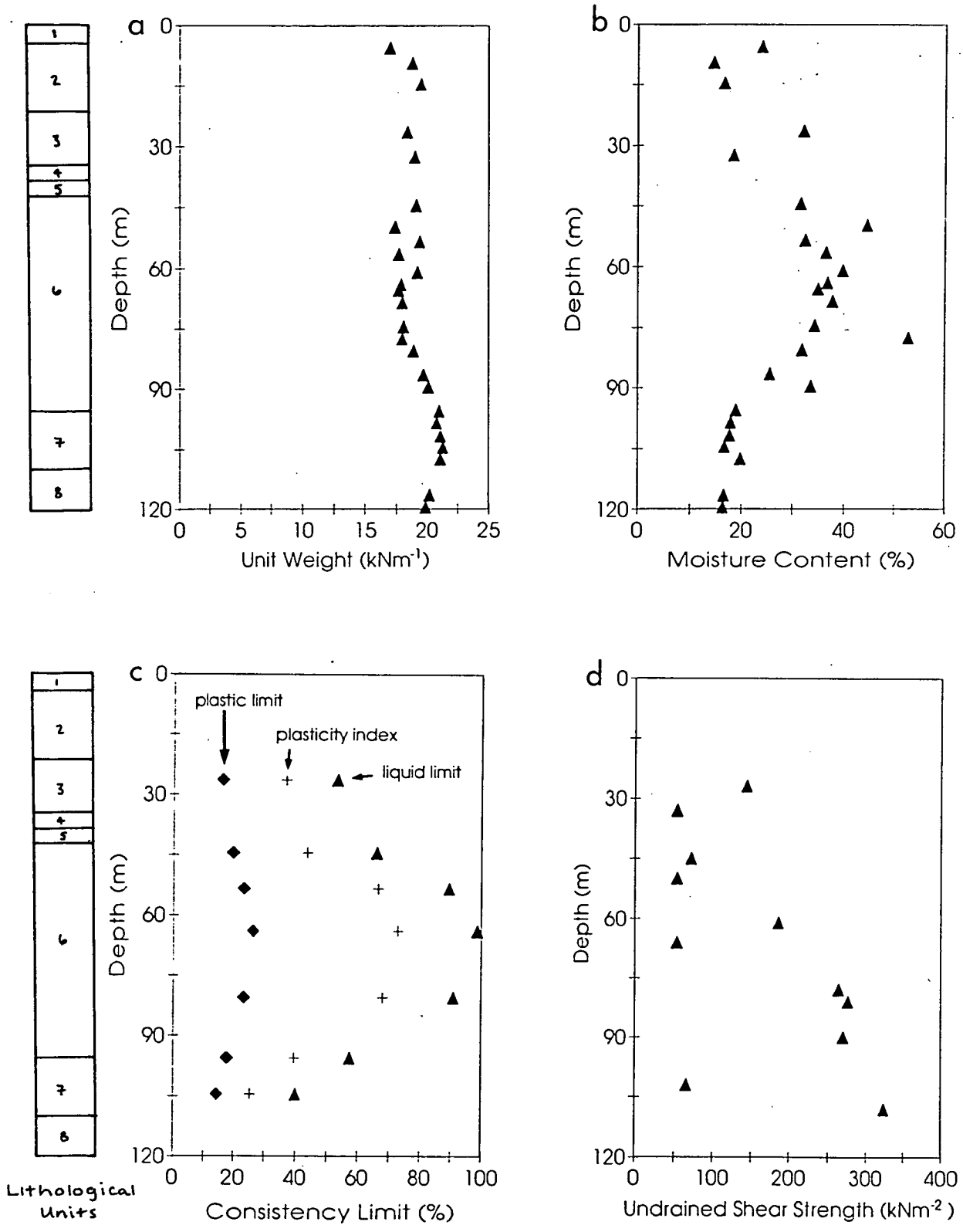

Figure 3.16: Vertical Distribution of geotechnical properties of the sediment in the Noord Bergum borehole: **(a)** unit weight; **(b)** moisture content; **(c)** Atterberg limits; **(d)** undrained shear strength.

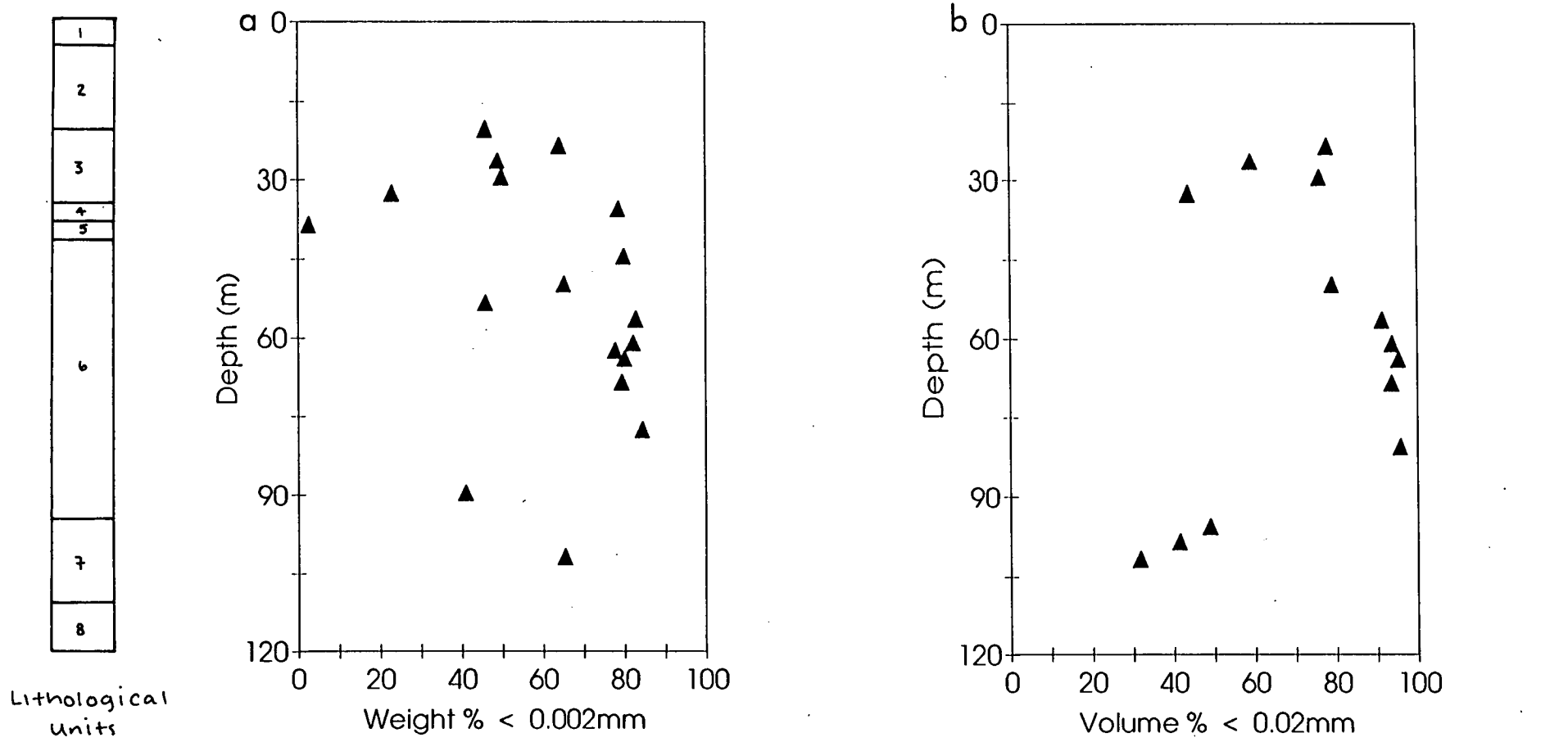

Figure 3.17: Vertical distribution of the clay fraction in the Noord Bergum borehole: **(a)** weight percent; **(b)** volume percent.

3.3.4.i Unit Weight (Figure 3.16a)

The saturated unit weight varies between 17.2 and 19.4 kN/m in the pot clay (unit 6) which, after an initial decrease in the top 20m, generally increases with depth. In the lower silty clay section (unit 7) the unit weight continues to increase with depth from 19.7 - 21.3 kN/m. Greeuw and Schokking (1990) suggest that the presence of fissures effectively lowers the unit weight as when the cores are opened, the fissures expand, releasing stress and increasing the total volume of the sediment. Thus the area of most intense fissuring has an artificially lower unit weight as is found in the centre of the clay unit. Below 75m, the unit weight increases more rapidly with depth.

3.3.4.ii Moisture Content (Figures 3.16b)

The natural moisture content shows almost a mirror image of this trend, being about 30% at the top of the pot clay and reaching a maximum of around 40% in the middle of the pot clay unit. This drops to around 20% in the lower silt rich layer.

3.3.4.iii Atterberg Limits (Figure 3.16c)

The liquid and plastic limits increase with depth in the upper half of the pot clay then decrease in the lower half. The plasticity index therefore increases from 45 at the top of the pot clay to about 70 at the centre, before decreasing to around 40 at the top of the silt rich band. It then decreases to around 25 at the base of the silty unit (unit 7). This follows the general trend of the clay fraction and the natural water content.

3.3.4.iv Undrained Shear Strength (Figure 3.16d)

The undrained shear strength, measured by the laboratory vane apparatus, again increases with depth from 50 to 270 kN/m^2. The lowest values correspond to areas where fissures occur as a result of the fissures acting as shear planes at low stresses.

3.3.4.v Particle Size Analysis

Particle size analysis was carried out using a sedimentation technique at the R.G.D. and a laser diffraction method in the Department of Geology and Geophysics at the University of Edinburgh. These methods are described in detail in appendix A.

The clay fraction, determined by the pipette method (figure 3.17a), reaches a maximum of 80%, again in the centre of the clay unit, before decreasing to 40% in the silt rich layer.

The graphical output from the Coulter LS100 particle size analyser showing the distribution of particle size against volume percent (figure 3.18) cannot be directly compared to the weight percent values obtained from the Dutch pipette analysis. However the trends obtained from the two tests can, and these are found to be similar.

Study of the particle size versus volume percent graphs for the pot clay suggests that the < 2μm fraction is not the best size population to study, since the 2μm point is usually found on the shoulder of a population and itself does not contain a population (figure 3.18). The 20μm point does however appear to contain a definite population and was therefore chosen as a cut off point. The percentage of the sample < 20μm (medium silt, fine silt and clay) was calculated and plotted against depth in the core (figure 3.17b).

In the upper clay layer (unit 3), the fraction < 20μm makes up between 75 and 80% of the sample whilst in the pot clay (unit 6) it is between 90 and 95%. This drops dramatically in the silt rich unit (unit 7) where < 50% of the particles are < 20μm.

Statistical analysis carried out reflects the extreme homogeneity of the clay between 20 - 80 m (unit 6). The modal class (figure 3.19c), that is the size class in which the greatest percentage of grains is represented, is fairly constant within each unit, being around 7.5μm in unit 3, 5μm in unit 6 (the pot clay) and 200μm in unit 7. The mean and median (figures 3.19 a & b) show similar trends. The mean grain size being around 20μm in unit 3, 7μm in unit 6 and 60 to 150 μm in unit 7 whilst the median is 12μm in unit 3, 4μm in unit 6 and increases from 40 to 150 μm with depth in unit 7. The clay units are unimodal (figure 3.18 a & b) whereas the silt rich unit is bimodal (figure 3.18c), having a clay/fine silt fraction and a fine sand fraction.

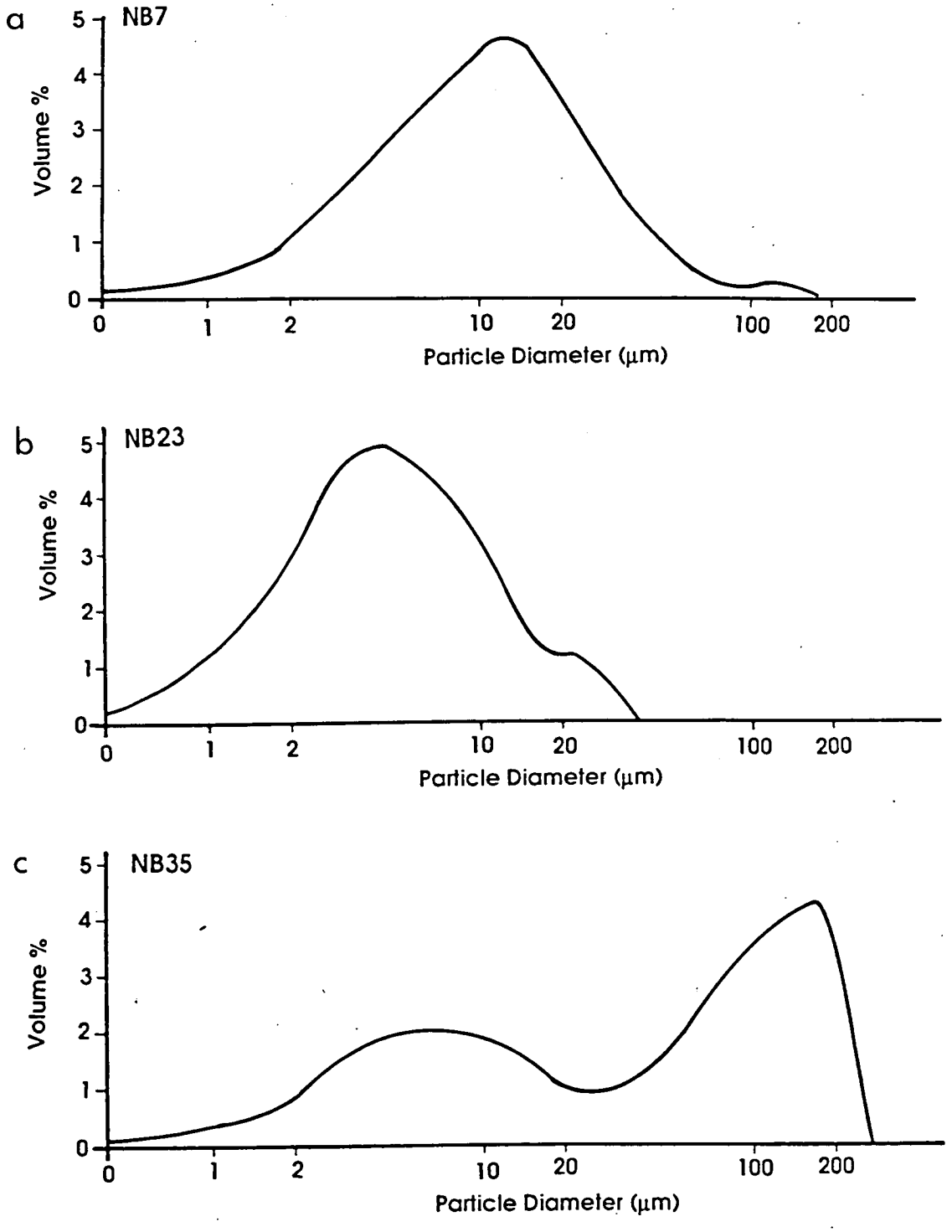

Figure 3.18: Particle size distribution in sediment from the Noord Bergum borehole determined in the Coulter LS 100 analyser: **(a)** sample NB7, unit 3; **(b)** NB23, unit 6; **(c)** NB35, unit 7.

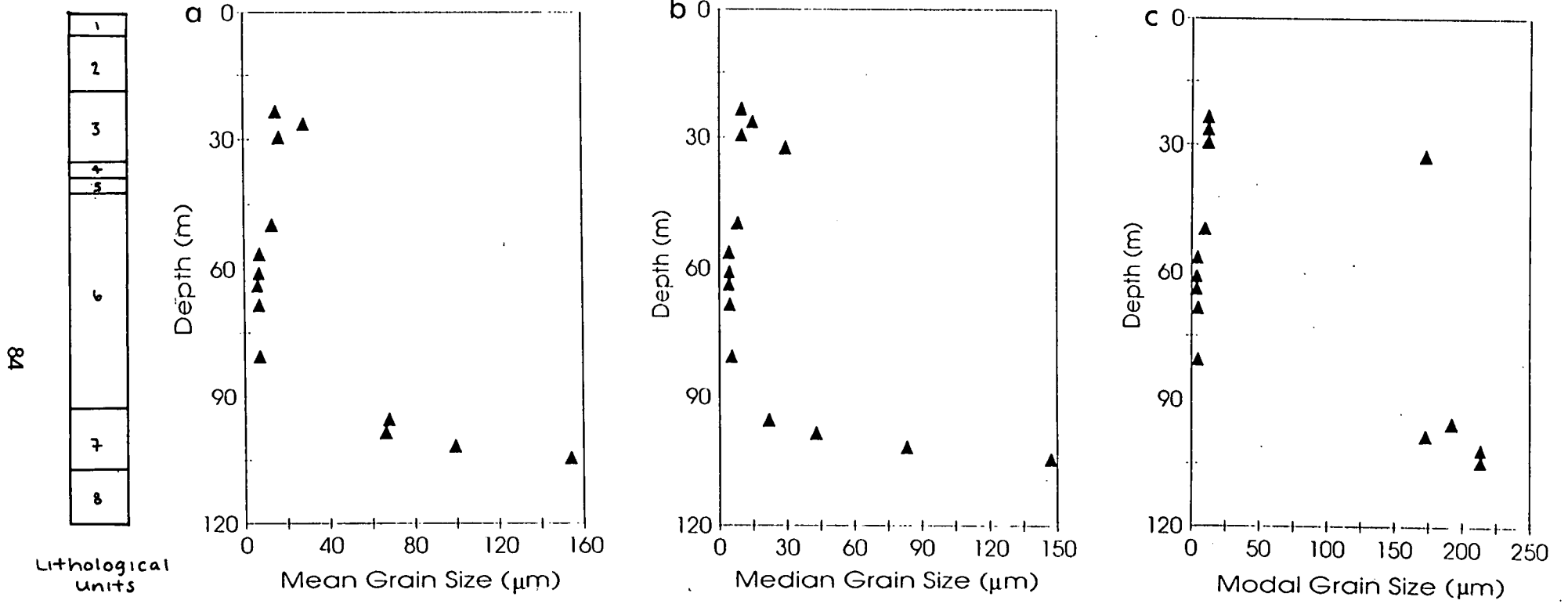

Figure 3.19: Mean, median and modal grain size in the Noord Bergum borehole.

3.3.4.vi X-Ray Diffraction Analysis

X-ray diffraction analysis was carried out on the APD 1700 diffractometer in the Department of Geology and Geophysics at the University of Edinburgh. The technique is described in appendix A.

X-ray diffraction traces of the whole sample show that all the sections contain quartz, calcite and varying amounts of clay minerals and mica (figure 3.20).

After allowing the larger particles to settle out, the samples from the upper clay (unit 3) consist of kaolinite, illite, chlorite, smectite and some quartz and calcite (some of which has been altered to gypsum). The upper half of the pot clay (unit 6) is mineralogically very similar to unit 3, however the lower half has much more material with diffraction peaks of $2\theta < 10°$. The silty clay (unit 7) is also mineralogically similar to unit 3. These are illustrated in figure 3.21.

Treatment of the lower pot clay samples with ethylene glycol resulted in a more pronounced peak occurring at 2θ of 5° (shifting from 6°) (figure 3.22). This is what would be expected from a sediment containing smectite group minerals such as montmorillonite. Treatment of samples from the upper half of the pot clay had a similar effect.

3.3.4.vii Relationships Derived from the above Parameters

If the plasticity index is plotted against the liquid limit on a conventional plasticity chart (figure 3.23) the points fall on a line parallel to, but above, Casagrande's A line (Casagrande, 1948) and Skempton's line for marine clays (Skempton, 1970). The trend and position of this line is controlled by the dilution effect of an increasing coarse fraction on the liquid and plastic limits of the clay end member. For example, Boulton and Paul (1976) define a T line for glacial tills which lies in much the same position as the pot clay line. However the pot clay is not as coarse grained as these tills and so there must be another reason for the displacement of the line. The liquid limit of a clay is governed by the relative proportions of the clay species present. Increasing amounts of montmorillonite within the clay fraction would significantly increase the plasticity index, by increasing the clays' ability to absorb water without deforming plastically. This would displace the A line.

The A line represents the empirical boundary between typical inorganic clays, which are generally above the A line, and plastic soils containing organic colloids which lie

below it (Casagrande, 1948). Pot clay is a highly plastic inorganic clay in this classification scheme whilst the lower silt rich unit plots as a low to medium plasticity, inorganic silty clay (figure 3.23).

The relative consistency of the clay, defined by the liquidity index, generally decreases with depth, as the clay becomes stiffer (figure 3.24).

The activity of the clay is a function of the mineral species present (Skempton, 1953). It varies from 0.5 to 1.5 in the pot clay (figure 3.25). The high values in the centre of the unit could again be a result of the high montmorillonite content (Greeuw and Schokking, 1990) whilst the lower values in the silt rich unit may be due to the higher proportions of inert quartz and calcite. Montmorillonite is an important constituent of pot clay and is found in samples from other locations (Breeuwsma, 1984).

3.3.4.viii Summary

The geotechnical tests show that the pot clay is a fine grained, plastic, inorganic clay and as such should be an ideal medium to preserve information about its stress history.

3.3.5 Conclusions

The sequence of sediments found in the Elsterian channels of the northern Netherlands are an example to which the one dimensional drainage model can be compared. A borehole was therefore drilled through such a sequence at Noord Bergum and the sediments studied to establish their suitability for consolidation testing.

The results obtained from the above experiments suggest that the Peelo clays are generally fine grained and homogeneous and hence should preserve information about the past maximum pressure to which they were subjected. One dimensional consolidation tests were carried out to obtain the preconsolidation pressure recorded in the clay thus allowing the conditions under the Saalian Ice Sheet at Noord Bergum to be established. This is discussed in the following chapter.

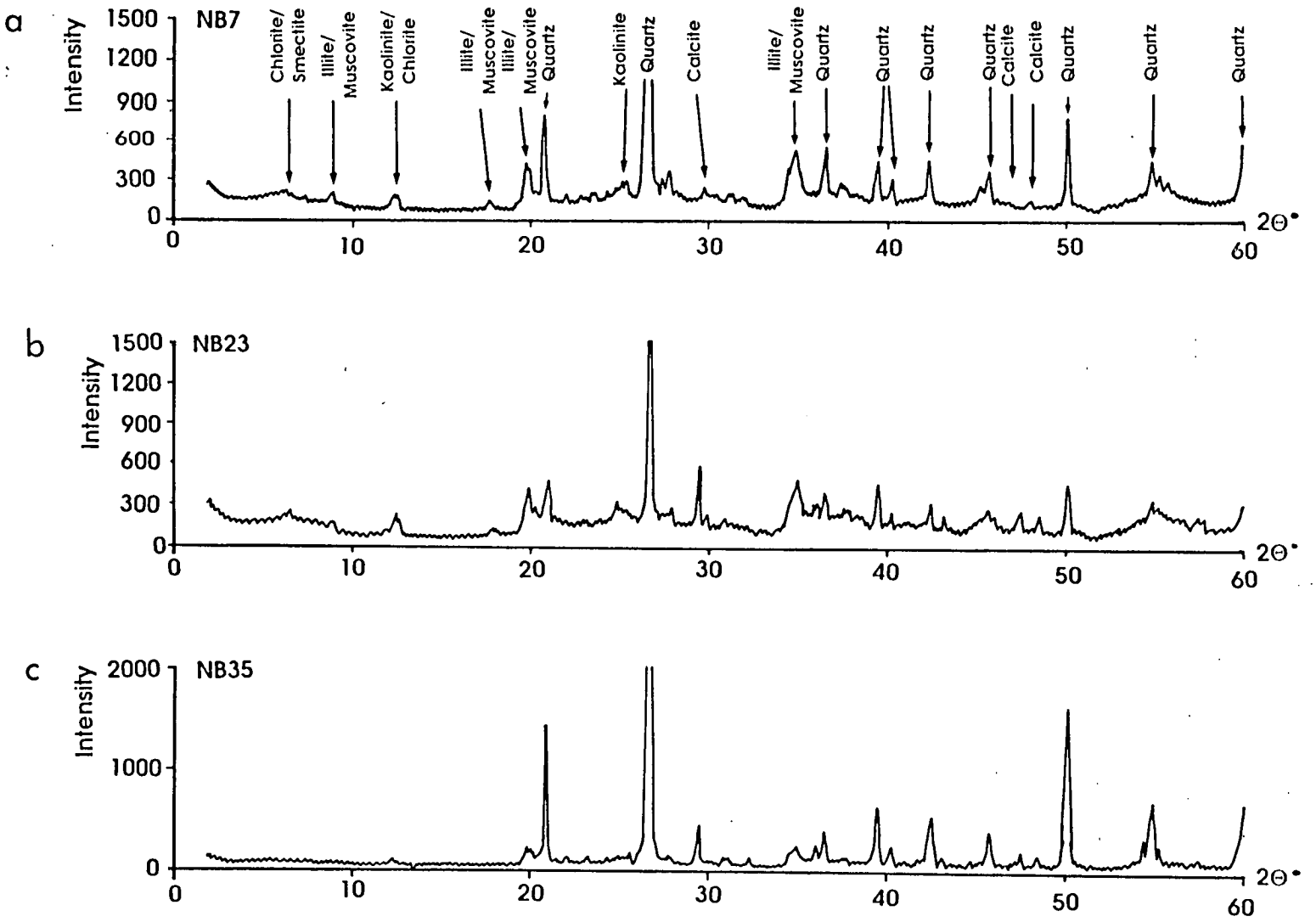

Figure 3.20: X - ray diffraction analysis of the whole sediment sample:. **(a)** sample NB7, unit 3; **(b)** NB23, unit 6; **(c)** NB35, unit 7.

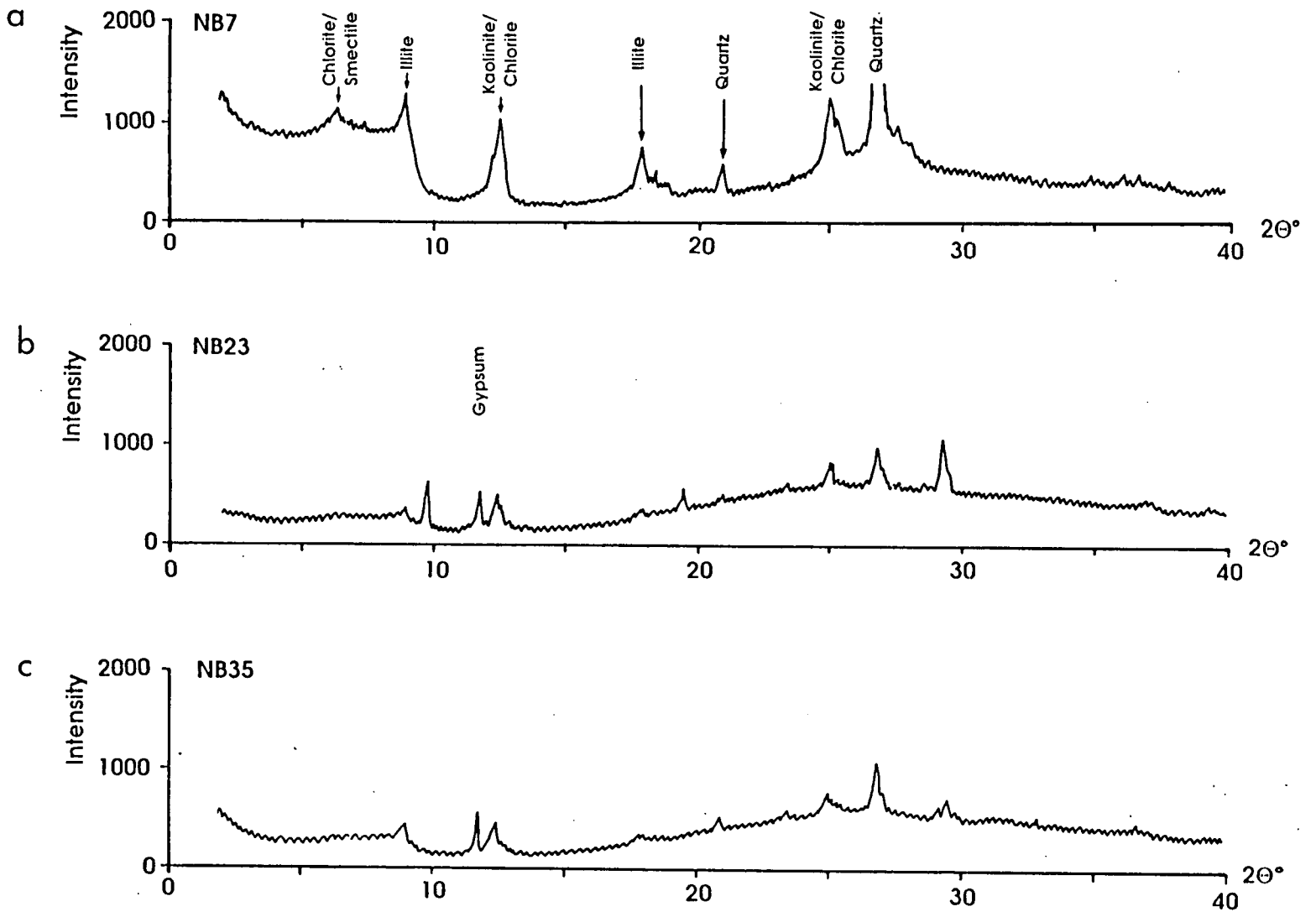

Figure 3.21: X - ray diffraction analysis of the clay fraction of the sediment: **(a)** sample NB7, unit 3; **(b)** NB23, unit 6; **(c)** NB35, unit 7.

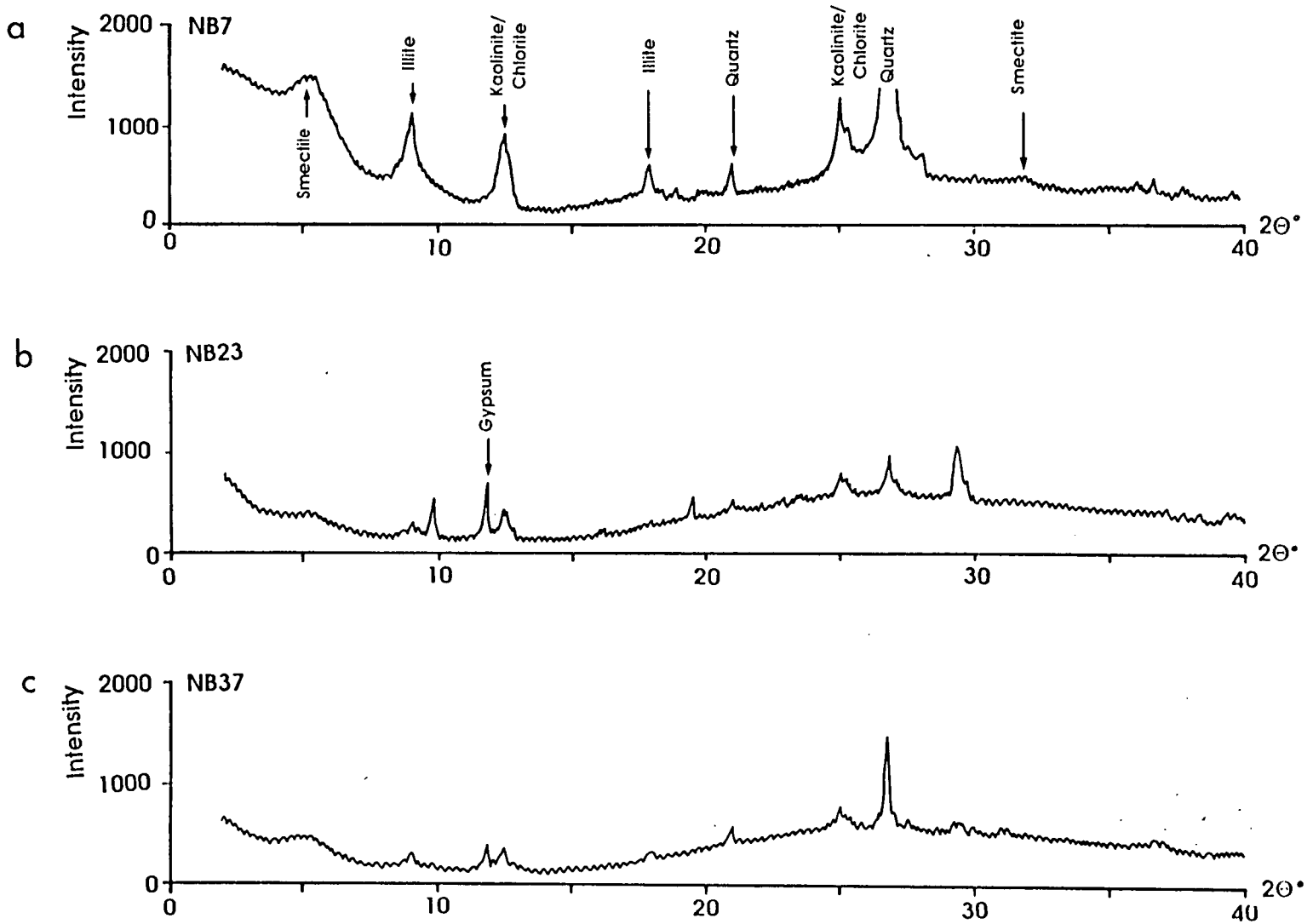

Figure 3.22: X - ray diffraction analysis of the clay fraction of the sediment after treatment with ethylene glycol: **(a)** sample NB7, unit 3, **(b)** NB23, unit 6; **(c)** NB35, unit 7. Note the more pronounced peak at 5° compared with the xrd traces of figure 3.21.

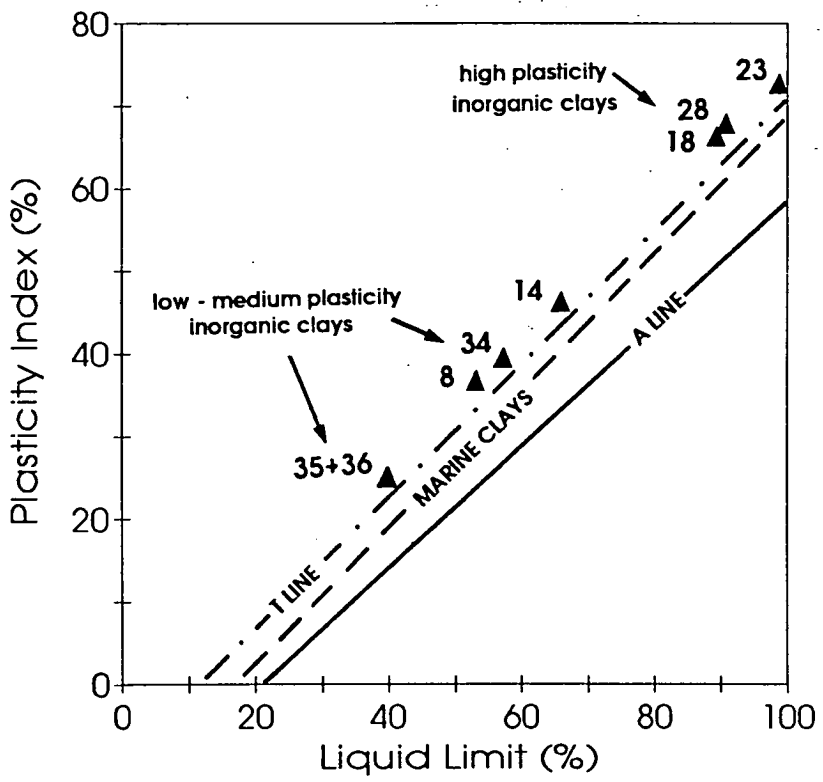

Figure 3.23: Plasticity chart showing the location of the Noord Bergum samples in relation to Casagrande's A line (Casagrande, 1948), Skempton's line for marine clays (Skempton, 1970) and Boulton and Paul's T line (Boulton and Paul, 1976).

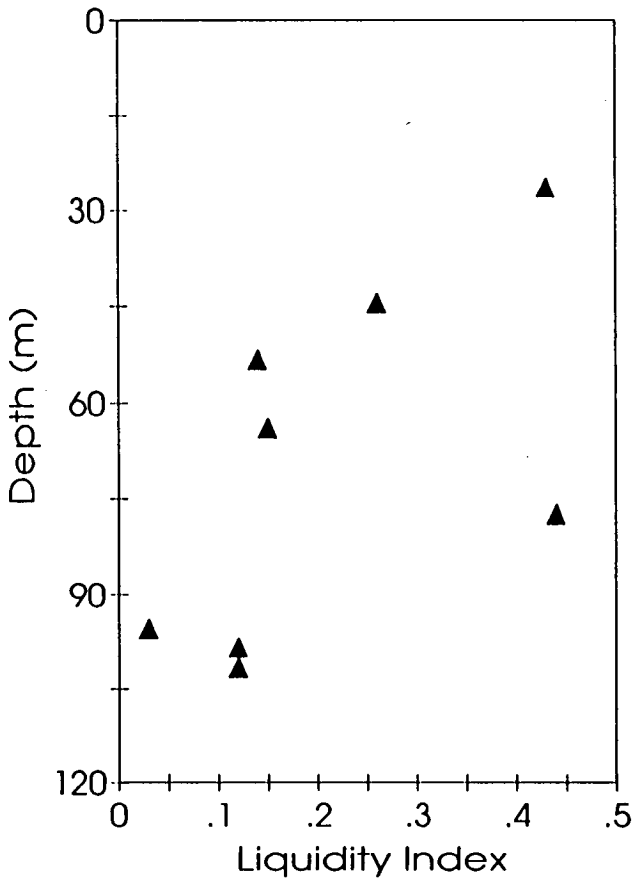

Figure 3.24: Vertical profile of liquidity index in the Noord Bergum borehole.

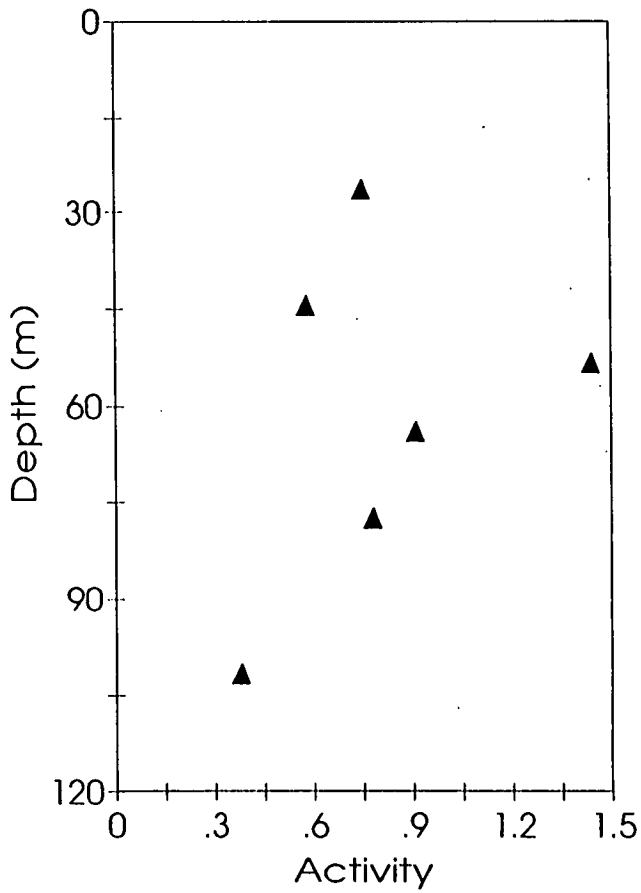

Figure 3.25: Vertical profile of activity in the Noord Bergum borehole.

CHAPTER 4

CONSOLIDATION OF SUBGLACIAL SEDIMENTS: DETERMINATION OF PRESSURE CONDITIONS AT THE BASE OF AN ICE SHEET

4.1 Introduction

An advancing ice sheet causes an additional load to act on the underlying sediment. The resulting effective pressure acting on the sediment is assumed to be greatest at the maximum extent of the ice sheet. On retreat of the ice the effective pressure is reduced and the sediments become overconsolidated. The past maximum pressure to which the sediments were subjected can be determined experimentally in the one dimensional consolidation test. The effective pressure obtained from the test however is not a simple consequence of the overburden of sediments and ice but contains a potential pressure component due to the meltwater flux.

A vertical profile of preconsolidation pressures is determined for the Peelo Clay in the Noord Bergum borehole. This is equated to the effective pressure gradient in the clay at the glacial maximum when the ice sheet was in a steady state. Using the theory outlined in chapter 2 it is possible to obtain the potential pressure gradient in the clay from which a minimum basal melt rate can be determined.

The effective pressure and potential pressure at the base of the ice can also be determined from the preconsolidation data and thus the pressure due to the weight of the overlying ice calculated. The ice sheet thickness at Noord Bergum at the glacial maximum can therefore be inferred and the steady state Saalian Ice Sheet surface profile reconstructed.

4.2 Previous Attempts at Determining Ice Sheet Thickness

Previous attempts have been made to establish ice sheet thickness from preconsolidation pressure measurements in glacial deposits as these reflect the past maximum effective pressure to which the sediments were subjected. Values obtained however are generally less than estimates of ice sheet thickness from independent geological evidence.

Initially it was assumed that the preconsolidation pressure preserved in former subglacial sediments was a result of the overburden of sediments and ice alone at the glacial maximum. Preconsolidation pressures were therefore determined from a number of sites within a study area to obtain ice thicknesses and allow reconstruction of the ice sheet profile.

Harrison (1958) contoured ice thickness, using preconsolidation measurements from silty sediments, near the margin of Champaign glacier in Indiana, but had no direct geological evidence to verify his thickness values.

MacDonald and Sauer (1970) found preconsolidation pressures from a site in Saskatchewan were much less than expected from the estimated thickness of the continental Laurentide ice sheet. Khera and Schulz (1984) also found that preconsolidation pressures from northern Germany gave ice thicknesses much less than glaciological estimates. They suggested that this was due to inadequate testing methods.

The above examples assume that all excess pore water pressure induced in the sample by loading of the sediment by ice has dissipated and that the sediment has fully consolidated. However the theory outlined in chapter 2 suggests that where an ice sheet advances over low permeability sediments an excess pore water pressure may be retained in the sediment thus reducing the effective pressure acting on the sediment.

One area in which the determined preconsolidation loads were comparable with estimates of ice sheet thickness from other geological measurements was in East Anglia where Kazi and Knill (1969) obtained preconsolidation pressures in till from sites thought to be near the terminus of the ice sheet. In such areas, close to the terminus, drainage paths would be short and thus drainage would allow all the initial excess pore water pressure to dissipate. The resulting pressure acting on the sediment would be equal to the applied pressure.

Boulton and Paul (1976) suggested that in cases where unlithified low permeability material lay beneath an ice sheet, there may be insufficient time for the excess pore water pressure to dissipate. They also noted that the presence of a water pressure gradient in the underlying sediment would have an effect on the effective pressure. They concluded that there was no obvious relationship between ice thickness and effective pressure and that the hydrogeology of the bed was an important variable.

Sauer and Christiansen (1988) determined preconsolidation pressures from a site in Saskatchewan and obtained values of less than 20% of the expected overburden. They suggested that this was due to insufficient time available for the relief of excess pore water pressure created by glacial loading. These measurements are compatible with Mathews (1974) conclusions from geomorphological evidence that the low glacier profiles in the south western regions of the Laurentide Ice Sheet were a response to the slow dissipation of high pore water pressures in the subglacial sediments at the advancing ice front. It is noted therefore that the Laurentide Ice Sheet was not in a steady state as the pore water pressure had not equilibrated. Sauer and Christiansen (1988) also suggested that this mechanism could account for the low values of preconsolidation obtained by MacDonald and Sauer (1970) and Khera and Schulz (1984).

In an attempt to quantify the effects of pore water pressure on the effective pressure, Schokking (1990b) used preconsolidation measurements to reconstruct the vertical effective pressure profile in the Peelo Clay from a site near Marum in the northern Netherlands. He assumed that the effective pressure would have reached a maximum during loading and that consolidation would have occurred in the centre of the clay body due to the subglacial distribution of pore water pressure (Schokking, 1990b). The resulting preconsolidation load in the centre of the clay unit therefore corresponded to the ice load. He constructed a pressure gradient due to the overburden of ice and sediments and compared this to the effective pressure gradient obtained from the preconsolidation measurements to obtain the distribution of pore water pressure with depth. However he did not take into account the effects of meltwater draining through the system.

Whilst Sauer and Christiansen (1988) noted that an excess pore water pressure could explain the low preconsolidation load and Schokking (1990b) attempted to determine the distribution of excess pore water pressure with depth, no one has previously considered the effects of the meltwater flux through the sediment at a steady state.

In chapter 2 it is noted that a basally melting glacier consolidates the underlying sediments but that the final steady state must still allow meltwater to drain through the sediment. There is thus a potential pressure component in the system that will affect the magnitude of the effective pressure. This will be much more pronounced if the subglacial sediment is of low permeability as the potential pressure gradient will be relatively large (section 2.11.2). Preconsolidation pressures cannot therefore be interpreted simply as indices of ice pressure.

In the one dimensional model outlined in chapter 2, water is assumed to drain vertically through a sediment of low permeability. If preconsolidation pressures are determined through a vertical section of a suitable sediment (i.e. the Peelo Clay) and equated to the effective pressure gradient, using the theory of chapter 2 (equation 2.30) it is possible to calculate the potential pressure gradient from which more realistic values of ice sheet parameters, including ice thickness, can be determined.

4.3 Preconsolidation Pressure Determination

4.3.1 Experimental Method

The past maximum pressure to which a sediment was subjected can be obtained from the results of the one dimensional consolidation test. The experimental method is described in appendix B. The results of the consolidation test are presented in the form of a graph of voids ratio against the log of the applied pressure, known as the e/logp curve (described below in section 4.3.2). From this it is possible to determine the preconsolidation pressure using the Casagrande (1936) construction (discussed below in section 4.3.3).

4.3.2 Nature of the e/logp Curve for Overconsolidated Clays

The e/logp curve shown in figure 4.1 illustrates the overconsolidation process.

After deposition, the clay consolidates naturally under the sediment load following the line AB in figure 4.1. During glaciation, it further consolidates, continuing along the line AB until the maximum effective pressure is reached at point C. The line ABC is known as the virgin consolidation curve. On deglaciation, the effective pressure is reduced and the sediment swells, as water is drawn into the voids, following the unloading curve CDE. Consolidation, however, is not a completely reversible process and the initial compression due to consolidation is never fully recovered on unloading and thus the voids ratio remains lower.

Reloading the sediment in the laboratory consolidation test causes it to reconsolidate along the line EFG. This curve is initially flatter than the original consolidation line ABC as the clay is less compressible than before. However the curve becomes steeper as it approaches the original maximum pressure as the clay becomes more compressible again. The curve continues steeply beyond the point

of maximum pressure, approaching the virgin curve when the preconsolidation pressure is exceeded.

4.3.3 Determination of the Preconsolidation Pressure

Casagrande (1936) suggested that it should be possible to estimate the load under which the sediment was consolidated in the ground from a consolidation test. He carried out a large number of tests on different soil types and found that, for the majority of clays, the preconsolidation pressure could be derived with a satisfactory degree of accuracy by an empirical method. This procedure is illustrated in figure 4.2.

The point of maximum curvature P on the laboratory loading curve is estimated and a tangent PS drawn at that point. A horizontal PQ is also drawn through that point and the angle QPS between the tangent and the horizontal is bisected. The point T where this bisector PR cuts the virgin compression curve AB represents the preconsolidation pressure.

Schmertmann's (1953) method of determining preconsolidation pressure was also considered, but was found not to give as clear an indication of preconsolidation results as Casagrande's (1936) method.

4.3.4 Verification of the Casagrande (1936) Technique

To verify this method, a sample of material from Noord Bergum was air dried, ground and remoulded to the original water content. It was then compacted to its original density and a sample prepared for consolidation. The one dimensional consolidation test was carried out as described in appendix B, loading the sample incrementally to 1200kPa. The sample was then unloaded and reloaded until the virgin curve was obtained. An e/logp curve was plotted, shown in figure 4.3, from which the preconsolidation pressure was determined using the Casagrande (1936) technique, outlined above (section 4.3.3) and illustrated in figure 4.3. The value of approximately 1200kPa obtained agreed well with the original past maximum of 1200kPa and so the method was assumed to be suitable for the determination of the preconsolidation pressure.

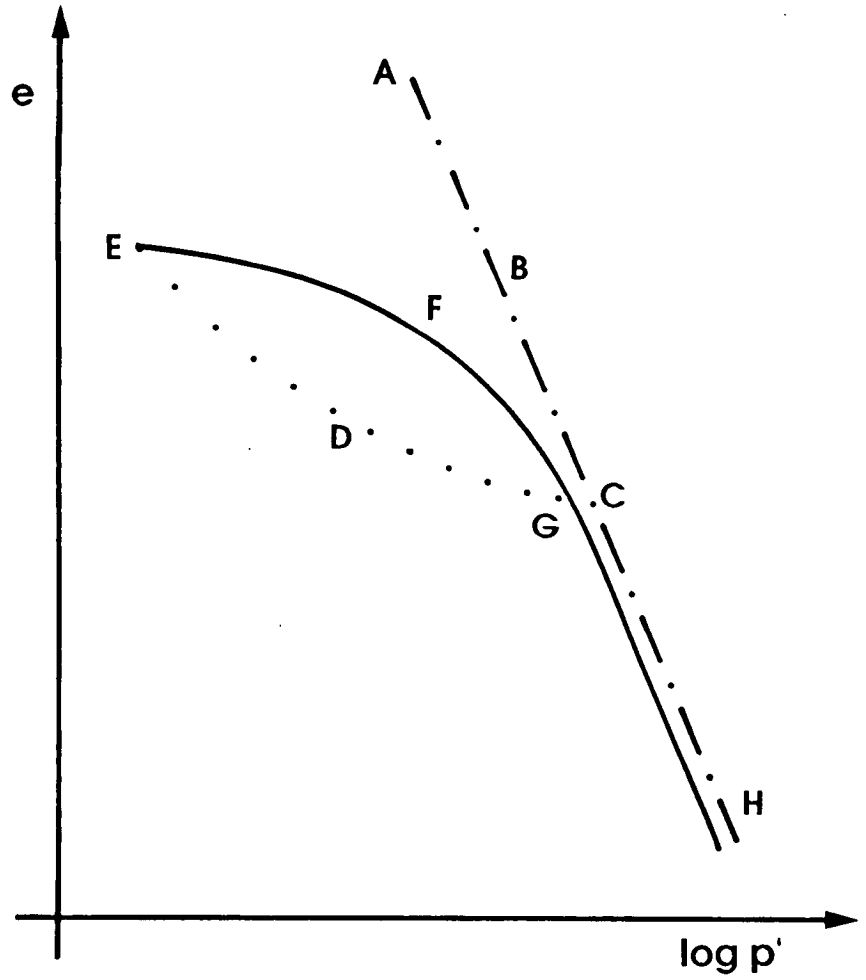

Figure 4.1: An e/logp curve illustrating the overconsolidation process as described in the text.

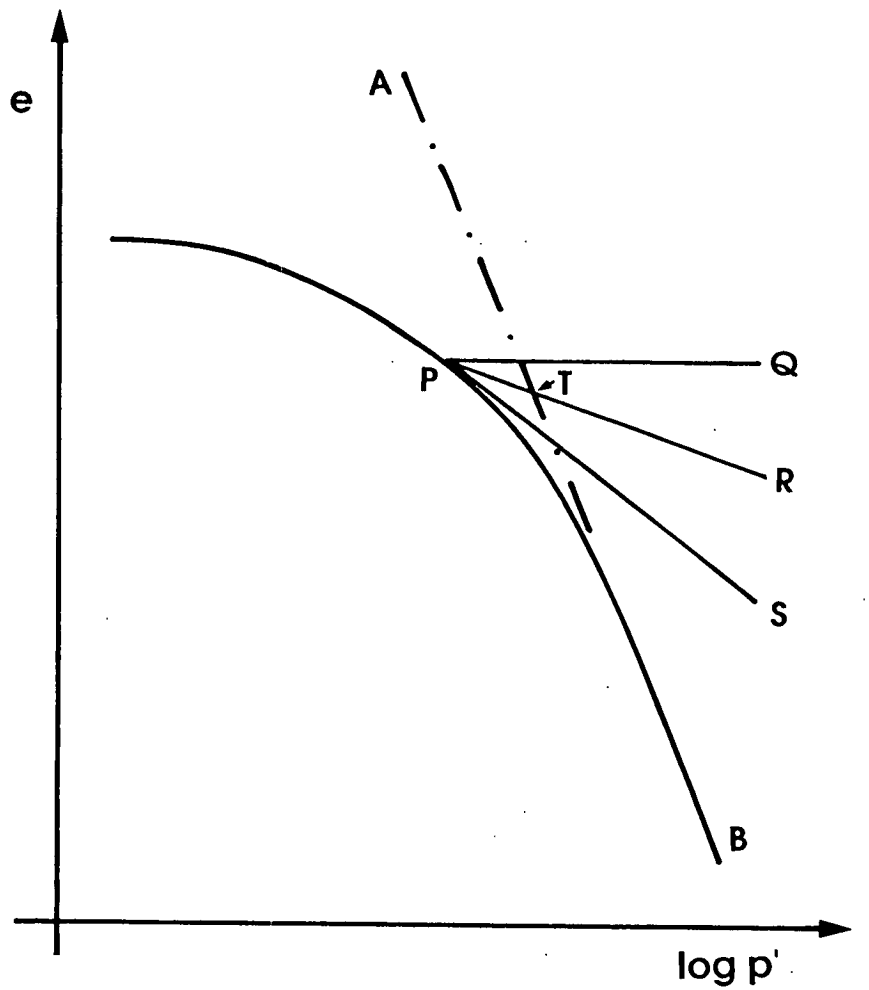

Figure 4.2: The Casagrande (1936) construction for the determination of the preconsolidation pressure described in the text.

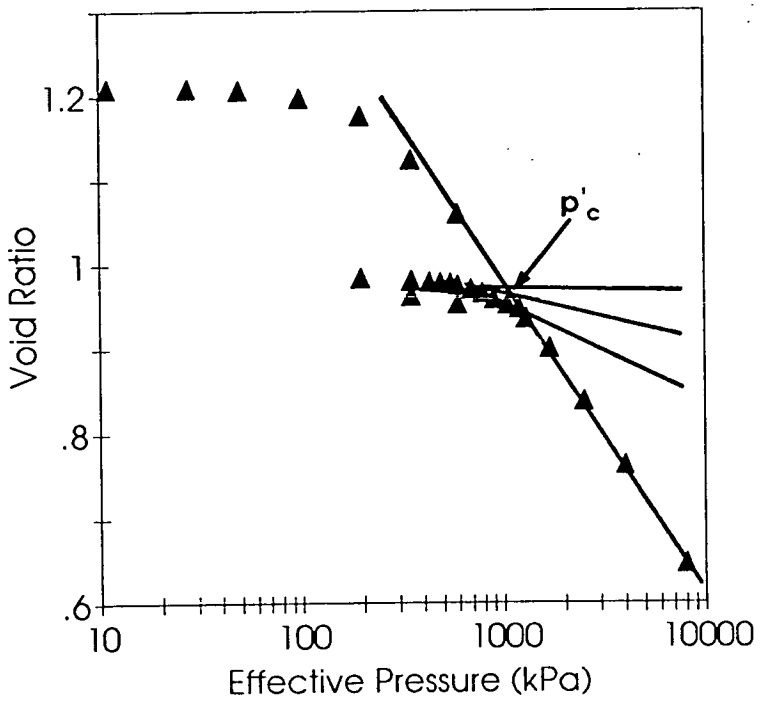

Figure 4.3: Determination of the preconsolidation pressure on a remoulded sample of Peelo Clay from the Noord Bergum borehole (NB18).

4.3.5 Testing Procedure

One dimensional consolidation tests were therefore carried out, as described in appendix B, on thirteen samples from different depths in the Noord Bergum borehole. Corresponding values of void ratio and effective pressure for the tests are tabulated in appendix B and presented as e/logp graphs in figure 4.4. Preconsolidation pressures were determined from the e/logp curves for each sample using the Casagrande (1936) technique outlined above and tabulated in appendix B. A plot of preconsolidation pressure against depth was constructed and is shown in figure 4.5.

4.3.6 Discussion of Preconsolidation Results

The vertical profile of past maximum pressure in the Noord Bergum borehole is shown in figure 4.5.

In the upper clay (unit 3) the preconsolidation pressure generally increases with depth. (The NB 10 sample is ignored as it contained shells and thus its consolidation properties are unlikely to reflect overconsolidation).

In the pot clay (unit 6) the preconsolidation pressure increases with depth until about 70m. Below 80m however preconsolidation pressures decrease. This trend of decreasing preconsolidation pressure with depth continues into the silty clay of unit 7.

The upper zone of preconsolidation pressures increasing with depth coincides with a zone of relatively uniform grain size distribution with a mean grain size of 6 - 8 μm and a modal class of 3 - 5 μm (figure 3.19). The lower zone of decreasing preconsolidation pressures with depth corresponds to an increasing mean grain size from 65 - 150 μm and a modal class increasing from 175 - 220 μm.

The coarse grained, silt - fine sand rich samples of unit 7 do not (figure 4.4) record preconsolidation loads as well as the clay rich samples of unit 6. Moreover, it is more difficult to determine preconsolidation pressures as the silt rich samples have much flatter loading curves and thus it is difficult to estimate the point of maximum curvature. It is therefore suggested that these samples have responded differently to loading and that the reduction in preconsolidation values in unit 7 may reflect the decreasing capacity of the sediment to reflect their stress history.

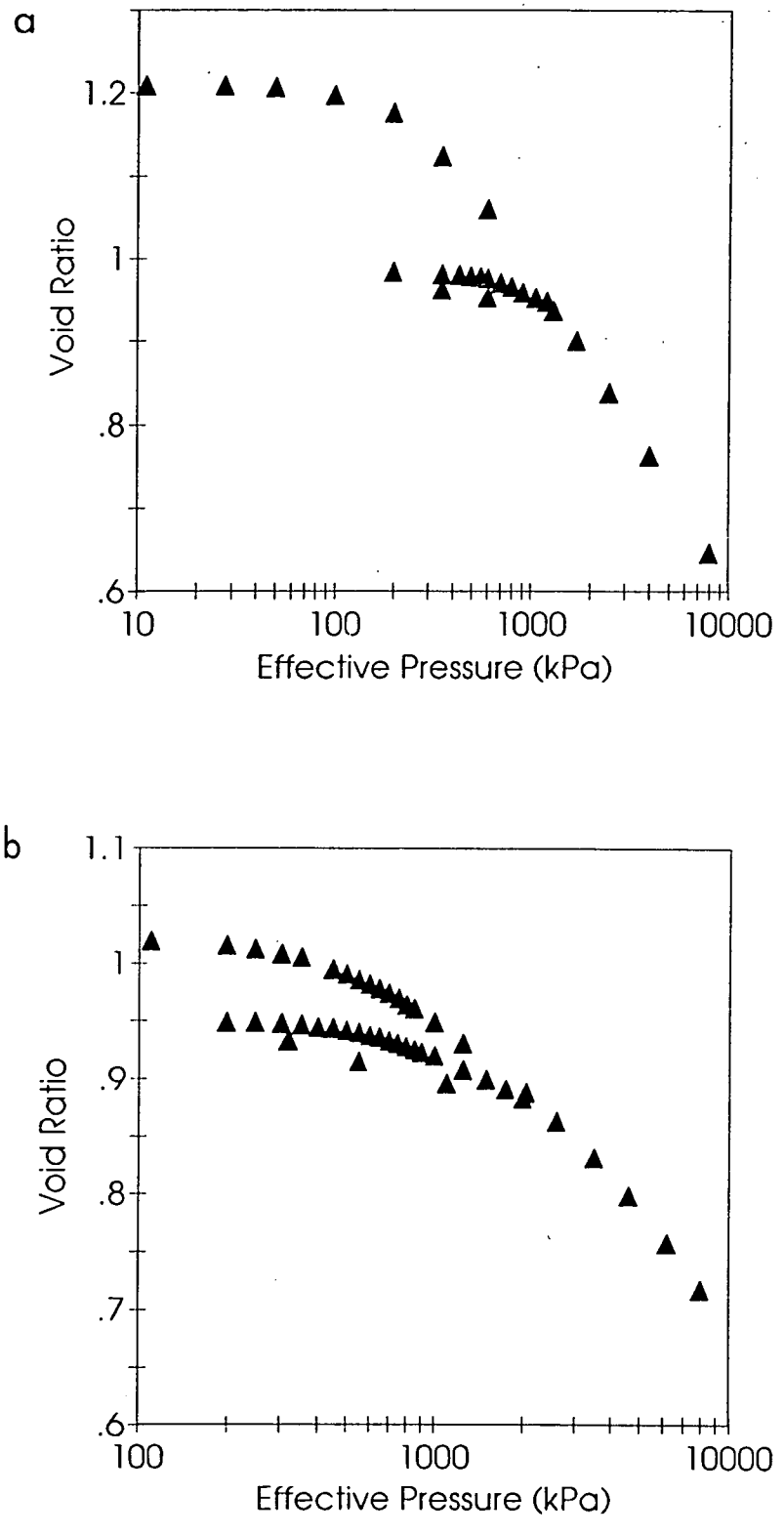

Figure 4.4: e/logp plots for the Noord Bergum core samples: **(a)** remoulded sample of NB18; **(b)** undisturbed sample of NB18.

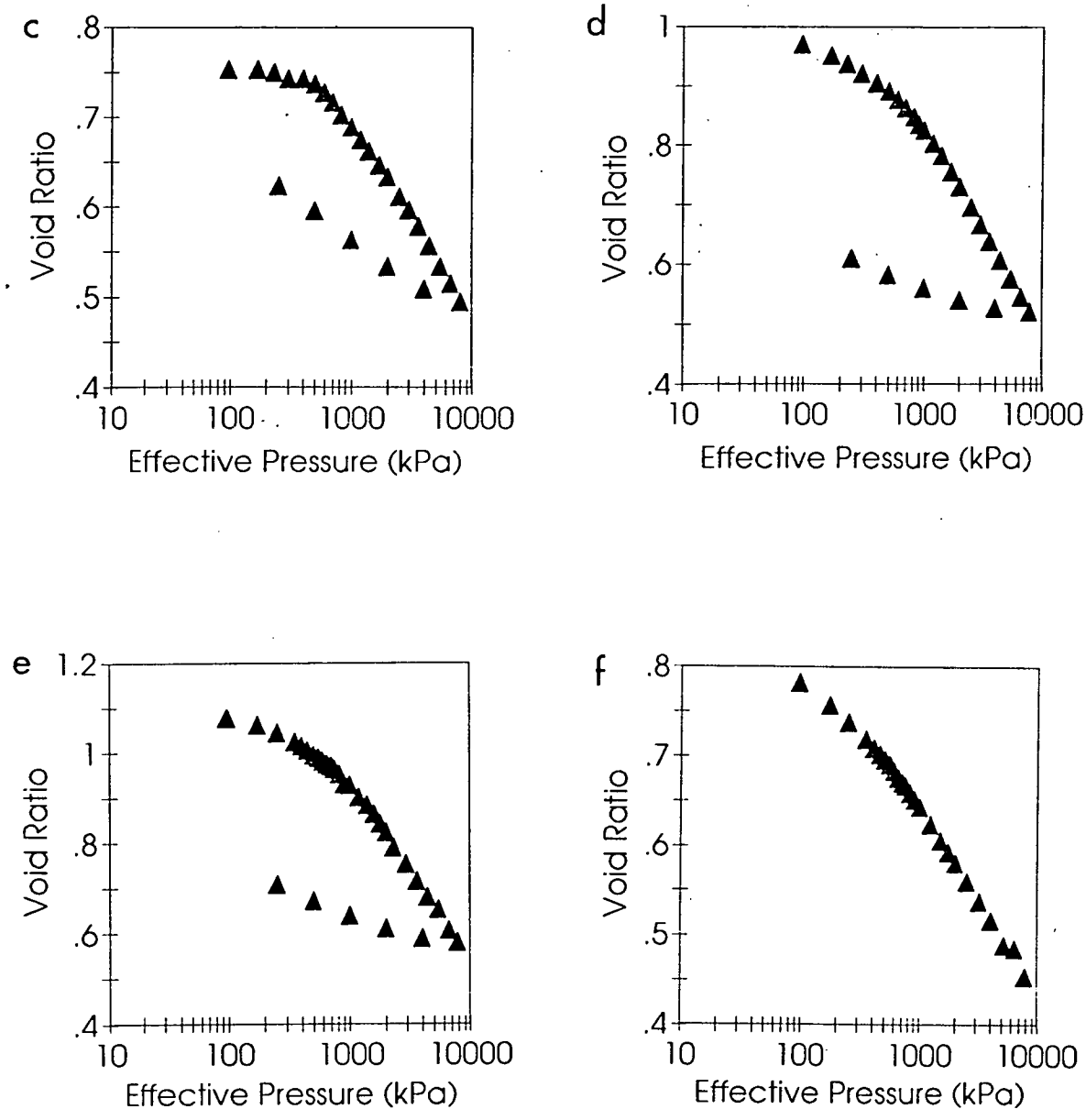

Figure 4.4 (cont): e/logp plots for the Noord Bergum core samples: **(c)** NB7; **(d)** NB8; **(e)** NB9; **(f)** NB10.

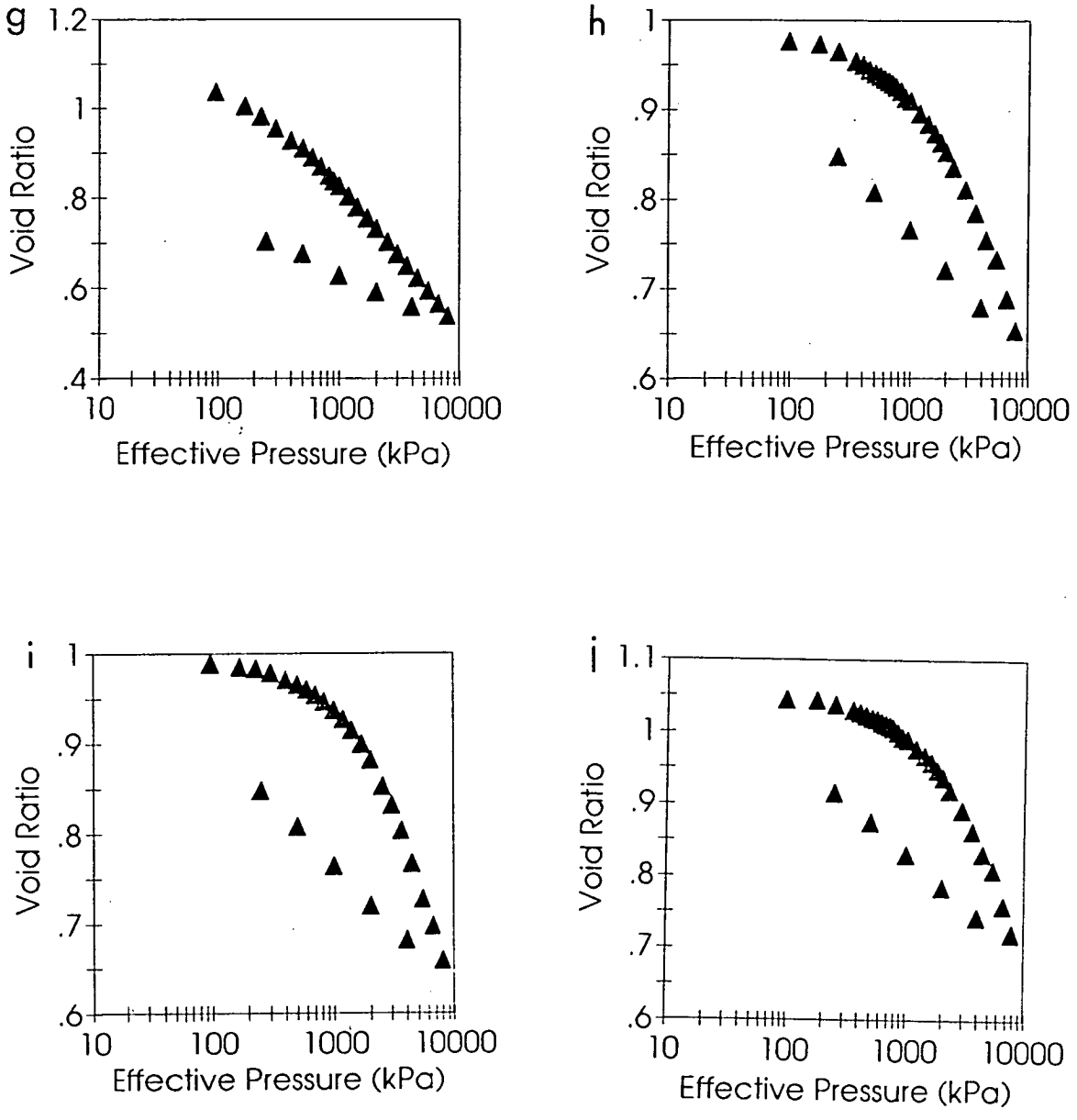

Figure 4.4 (cont): e/logp plots for the Noord Bergum core samples: **(g)** NB16; **(h)** NB19; **(i)** NB21; **(j)** NB23.

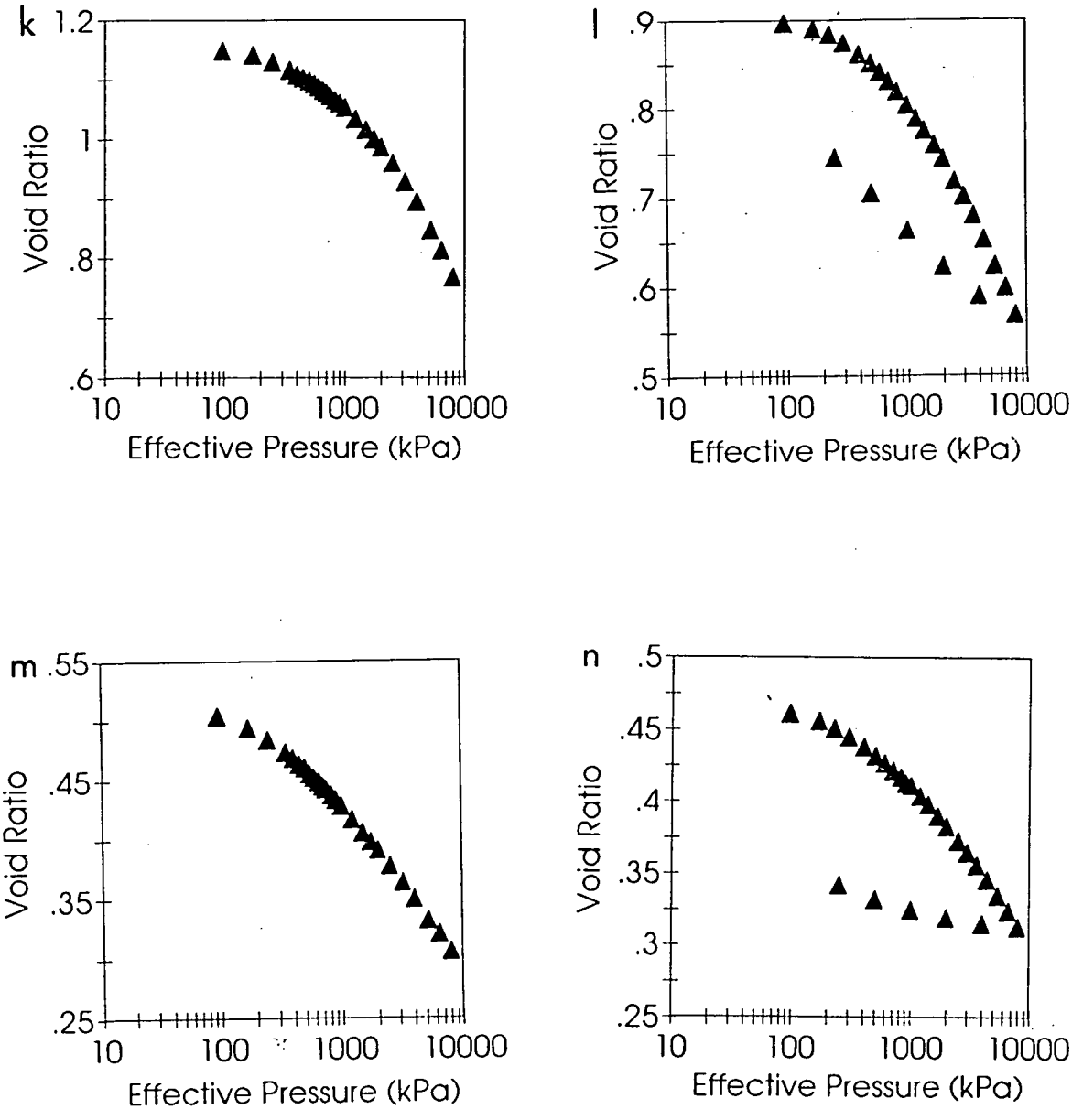

Figure 4.4 (cont): e/logp plots for the Noord Bergum core samples: **(k)** NB25; **(l)** NB29; **(m)** NB35; **(n)** NB36.

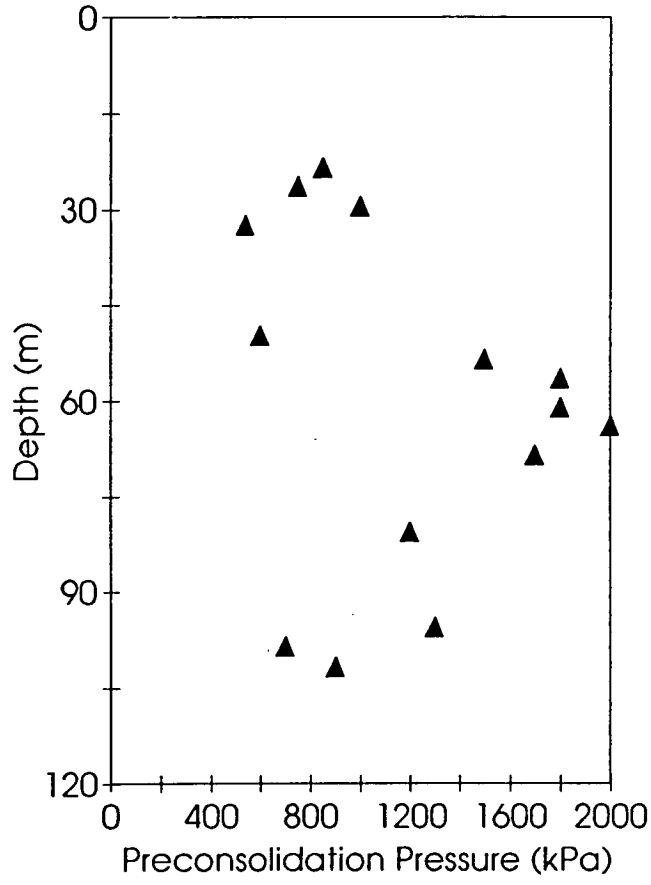

Figure 4.5: Vertical profile of preconsolidation pressures preserved in the Peelo Clay.

Due to the time consuming nature of the consolidation test (six weeks to determine the preconsolidation pressure for each sample), it was impractical to carry out further testing and so a proxy method was required. It has been suggested by Schokking (pers. comm.) that the results obtained from cone penetration tests reflect preconsolidation. A cone penetration test was therefore undertaken to explore the relationship between cone resistance and preconsolidation pressure.

4.4 The Cone Penetration Test

4.4.1 Principle of the Cone Penetration Test

A cone with a built in load cell is pushed into the ground by a hydraulic jacking system. A thrust is exerted on high tensile steel rods attached to the cone and the resistance of the cone to movement recorded. The penetrometer also contains a probe which measures the pore pressure generated by the cone during penetration. The resistance to penetration yields information on the lithology and geotechnical properties of the sediment.

The cone penetration test was carried out in this study principally to establish if there was a relationship between cone resistance and the preconsolidation pressure retained in the sediment, however it also provides information about the lithology of the sediment tested. A Delft Geotechnics standard $10cm^2$ piezocone, with an apex angle of 60° was used in the test. The experimental method is outlined in appendix B.

4.4.2 Discussion of Results

Graphs showing the relationships between cone resistance, friction ratio (the ratio of frictional shear stress on the cone to the cone resistance) and excess pore pressure with depth are shown in figure 4.6. These profiles give an indication of the type of sediment encountered in the borehole.

4.4.2.i Lithology of the Borehole

In this test, a high cone resistance indicates a dense sand layer whilst a high pore pressure value indicates an impermeable clay layer and a high friction value indicates a clay or peat (Greeuw and Schokking, 1990).

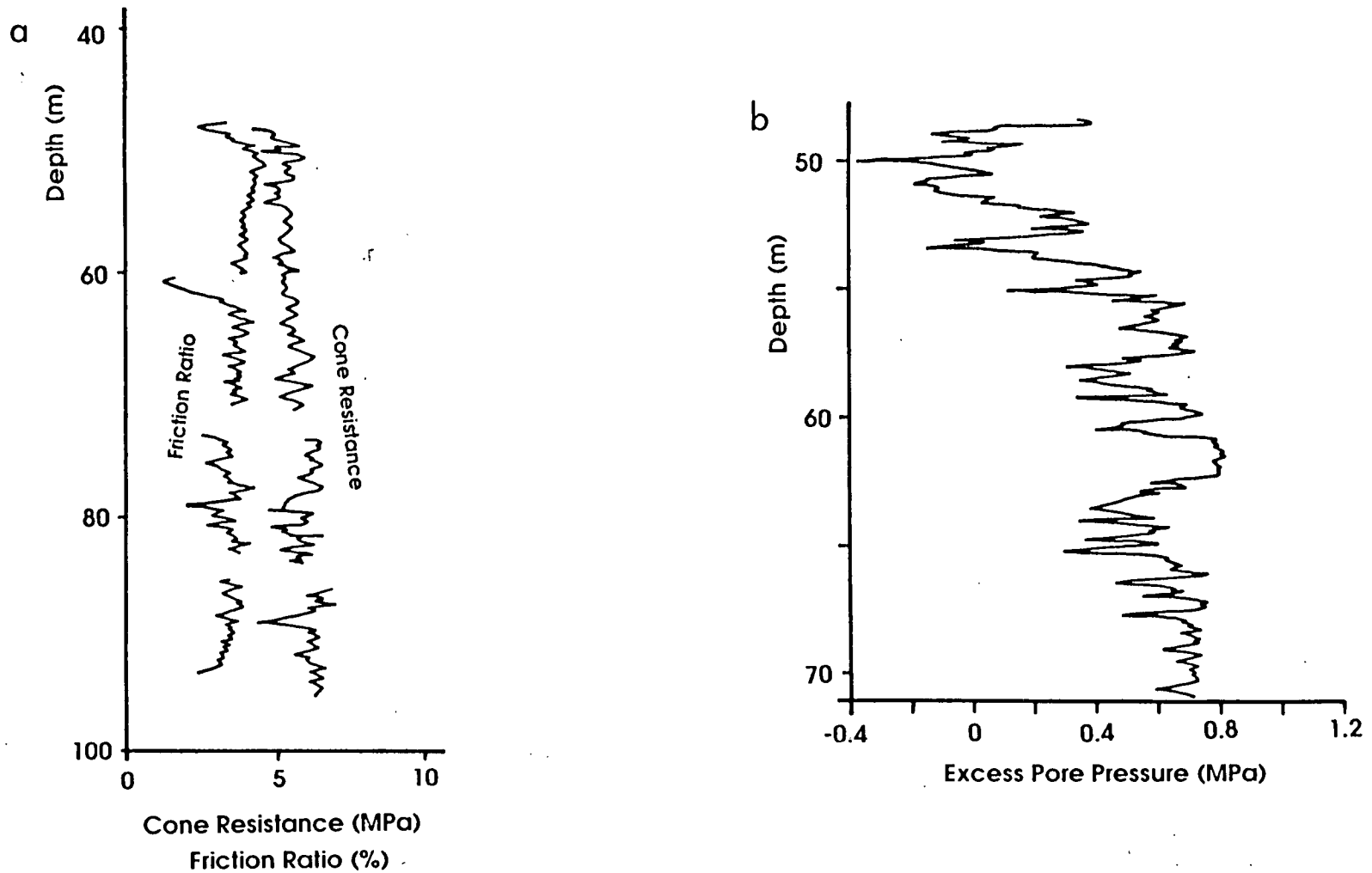

Figure 4.6: **(a)** Cone resistance and friction ratio plotted against depth for a cone penetration test carried out next to the Noord Bergum borehole; **(b)** excess pore pressure plotted against depth for the same test.

In the pot clay of unit 6, the cone resistance increases from around 5 to 7MPa at a rate of 0.03MPam^{-1}, whereas the friction ratio decreases from 4 to 3% at a rate of 0.035%m^{-1} (figure 4.6). These results plotted on a general graph of cone resistance against friction ratio (figure 4.7) show that the lithology of the pot clay changes with depth gradually from a hard insensitive inorganic clay to a more silty then sandy clay, thus agreeing with the previous tests of particle size and plasticity in chapter 3.

The excess pore pressure steadily increases with depth in the pot clay, from negative values initially to more positive values (figure 4.6). Greeuw and Schokking (1990) suggest the negative excess pore pressures are due to extensive fissuring of the samples and that the increase in depth is due to a decrease in the number of fissures. A similar effect is found in the Marum borehole (Schokking, 1990a).

4.4.2.ii Relationship Between Cone Resistance and Preconsolidation Pressure

A graph of preconsolidation pressure against cone resistance, presented in figure 4.8, suggests that the cone resistance is virtually independent of the preconsolidation pressure. The cone resistance increases steadily with depth whereas the preconsolidation pressure increases then decreases with depth. There is not enough information available to make further comment on the nature of the relationship.

Measurement of pore pressure generation during penetration allows analysis of cone resistance and friction in terms of effective stress (de Ruiter, 1982). This, however, is outwith the scope of this study.

4.5 Implications of the Preconsolidation Results

4.5.1 Determination of the Effective Pressure Gradient

The preconsolidation pressure is the past maximum pressure to which a sediment was subjected. The maximum loading of a sediment is assumed to have occurred when the ice sheet was at its maximum extent and thus the vertical preconsolidation pressure preserved in the Peelo Clay can be equated to the effective pressure gradient in the clay at the glacial maximum.

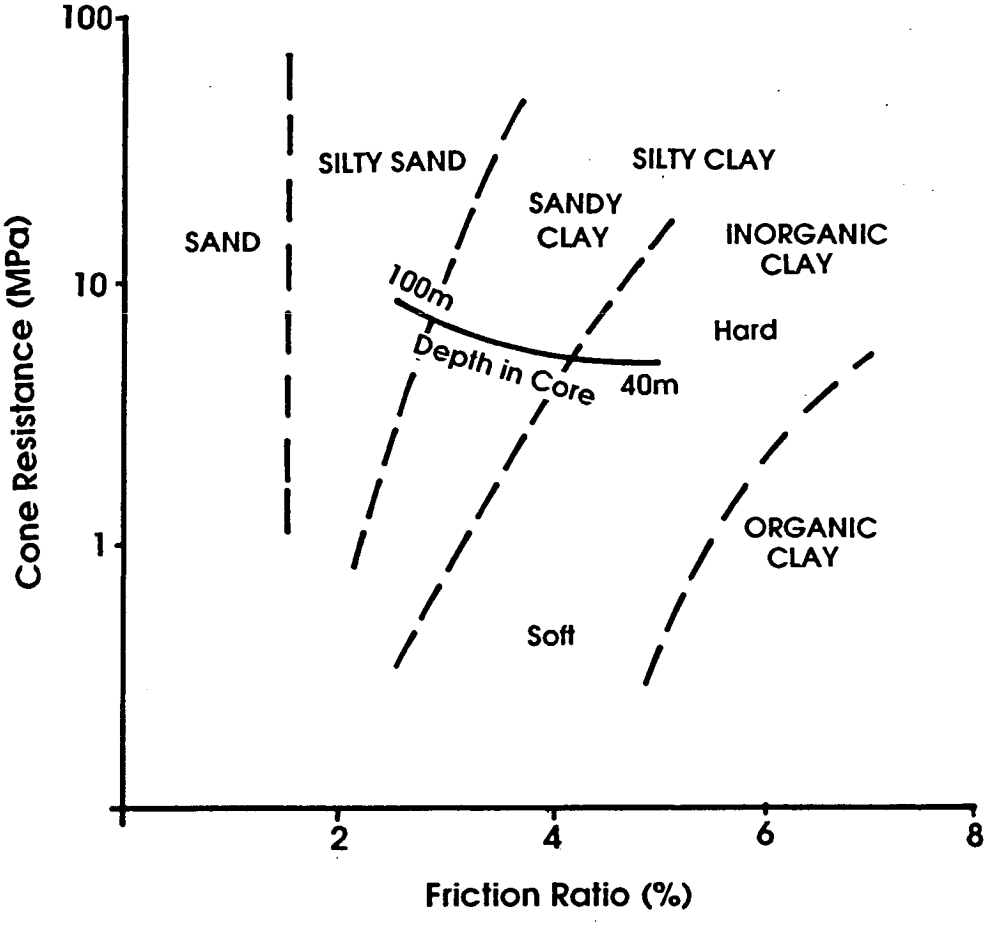

Figure 4.7: Sediment type as a function of cone resistance and friction ratio showing the position of the Noord Bergum sediments. The pot clay changes from a hard, inorganic clay to a silty clay then a sandy clay with depth in the borehole.

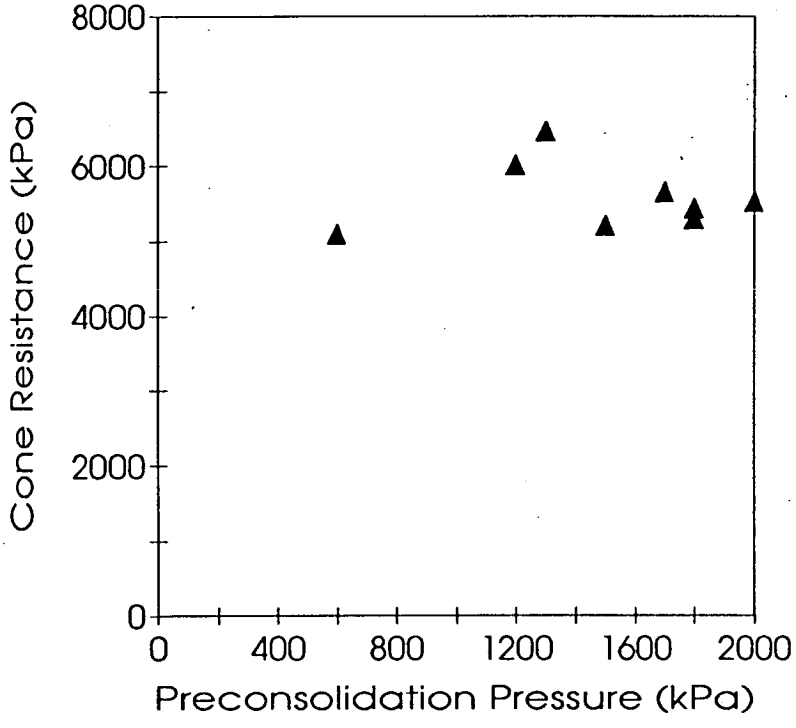

Figure 4.8: Cone resistance plotted against preconsolidation pressure showing that the cone resistance is virtually independent of preconsolidation pressure.

The sequence of sediments in the Noord Bergum borehole is an example to which the one dimensional drainage model outlined in chapter 2 can be compared. The vertical effective pressure gradient in the Peelo Clay resulting from loading by a basally melting ice sheet, the melt water from which is assumed to drain vertically through the clay, is thus given by equation 2.30:

$$\frac{dp'}{dz} = \left(\frac{dp'}{dz}\right)_g - \frac{d\psi}{dz} \qquad 4.1$$

where dp'/dz is the vertical effective pressure gradient,
$(dp'/dz)_g$ is the vertical gravitational gradient,
$d\psi/dz$ is the vertical potential pressure gradient.

The vertical effective pressure gradient is determined from the preconsolidation pressure profile preserved in the Peelo Clay (figure 4.5). Only values from the top 20m of clay are considered in the determination since the samples taken from this horizon have similar properties (chapter 3). The results from the 80m sample are not considered, since its grain size, moisture content and void ratio properties are different to those of the Peelo Clay in general. A linear regression line is drawn through the relevant points and an effective pressure gradient of 52 $kPam^{-1}$ is obtained, illustrated in figure 4.9.

4.5.2 Determination of the Gravitational Gradient

The vertical gravitational gradient is obtained from equation 2.24;

$$\left(\frac{dp'}{dz}\right)_g = (\rho_s - \rho_w)(1-n)\,g \qquad 4.2$$

where $\rho_S - \rho_W$ is the dry density (determined for the sample by the R.G.D.), and n is the porosity.

The porosity of a sediment is related to its void ratio (e) by the following equation;

$$n = \frac{e}{1+e} \qquad 4.3$$

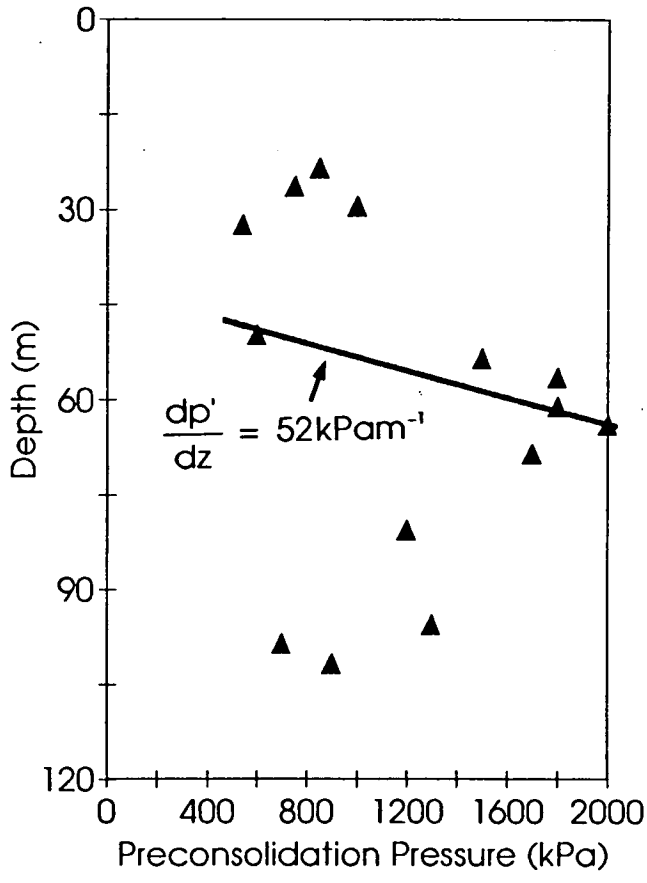

Figure 4.9: Distribution of preconsolidation pressure with depth in the Noord Bergum borehole, showing the determination of the effective pressure gradient in the Peelo Clay.

and thus it is possible to calculate the sediment porosity from the void ratio values obtained in the one dimensional consolidation test.

Dry density and porosity at the preconsolidation pressure are plotted against depth in the core and shown in figure 4.10 (values of porosity and dry density are given in appendix B). Substituting these values into equation 4.2 results in a gravitational gradient of 7 $kPam^{-1}$ in the clays whilst a gradient of 10 $kPam^{-1}$ is found in the sands.

4.5.3 Reconstruction of the Potental Pressure Gradient

The vertical potential pressure gradient causing the melt water to flow down through the clay can be obtained by rearranging equation 4.1:

$$\frac{d\psi}{dz} = \left(\frac{dp'}{dz}\right)_g - \frac{dp'}{dz} \qquad 4.4$$

Substituting the above values of vertical effective pressure gradient and vertical gravitational gradient into equation 4.4 gives a vertical potential pressure gradient in the clay of -45 kPa/m.

4.5.4 Determination of the Melt Rate

The potential pressure gradient drives water through the sediment at a rate given by Darcy's Law (section 2.4.3, equation 2.14). This, in terms of a vertical drainage path and a potential pressure gradient, states that

$$q = \frac{-k}{\rho_w g}\frac{d\psi}{dz} \qquad 4.5$$

where q is the rate of water flow per unit area of the sediment column.

If it is assumed that all the meltwater produced at the base of the ice flows vertically down through the underlying sediment and out into the aquifer and that an equilibrium is maintained, then the rate of water flow through the sediment must equal the basal melt rate of ice. The melt rate (m) can therefore be calculated from Darcy's Law, substituting the value of the potential pressure gradient calculated in section 4.5.3 above into equation 4.5:

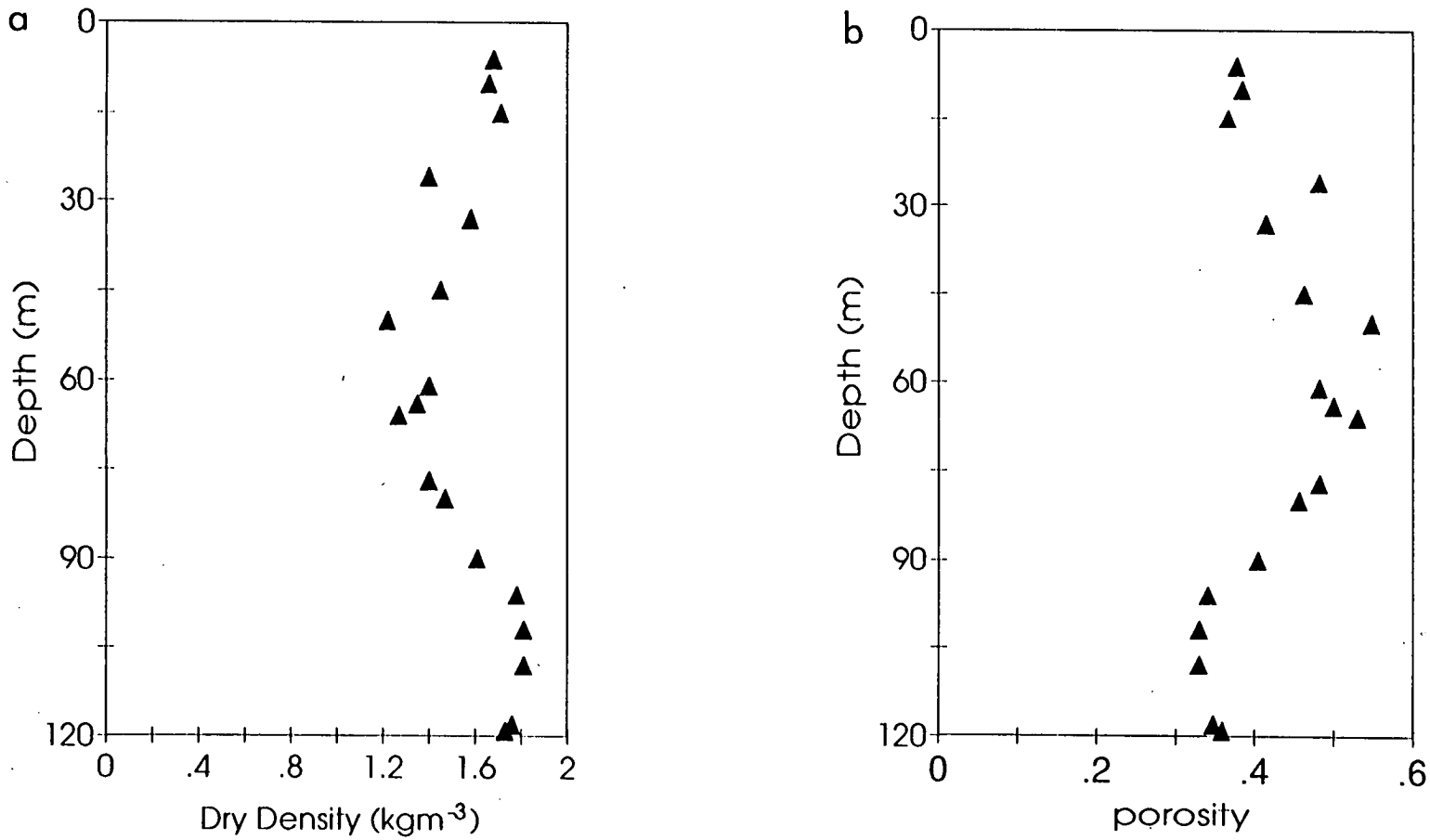

Figure 4.10: Graphs showing the distribution of **(a)** dry density and **(b)** porosity with depth in the sediment column at Noord Bergum.

$$m = \frac{-k_c}{\rho_w g} \frac{d\psi}{dz} \qquad 4.6$$

The permeability of the Peelo Clay (k_c) is determined from the consolidation tests and found to be of the order of 10^{-11} ms^{-1}. The melt rate of ice at Noord Bergum is therefore 1.4 mmy^{-1}.

As mentioned above, this calculation assumes that all the basal meltwater drains vertically through the upper low permeability stratum. For this to occur the transmissibility of the underlying aquifer must be large enough to ensure that the potential pressure at the top of the aquifer is significantly lower than that occurring at the base of the ice. Under these circumstances, melt water will drain freely through the sediment and not accumulate at the glacier sole. If, however, the potential drop across the low permeability stratum is not large enough to drive all the melt water through it, water will collect at the base of the ice where it must be discharged in channels or by sheet flow. If either of these processes occur, then the above calculation yields a minimum value for the melt rate.

The basal melt rate obtained for the ice at Noord Bergum lies within the relatively narrow range of values typical of non surging glaciers (G.S. Boulton, pers. comm.).

A similar calculation, carried out for the site at Marum, using preconsolidation data presented by Schokking (1990b), gives a melt rate of 1.7 mmy^{-1}. This agrees very well with the Noord Bergum calculation and is thus taken as confirmation of the result.

4.5.5 Determination of Effective Pressure at the Glacier Sole

Above the Peelo Clay, the sedimentary sucession at Noord Bergum consists of two sandy units separated by a clay unit (section 3.3.2). The permeability in the sandy units is assumed to be sufficiently high to have permitted vertical drainage without requiring a significant potential gradient and thus the resulting vertical effective pressure gradient in these units will be gravitational (from equation 4.1). In the upper clay (the Holstein Clay), the effective pressure gradient is calculated as above for the Peelo Clay (section 4.5.1) and found to be 26 $kPam^{-1}$ indicating that the Holstein clay is more permeable than the Peelo Clay resulting in a smaller potential pressure gradient. It is therefore possible, using these gradients, to extrapolate up through the sediment column from the known values of effective pressure in the Peelo Clay and calculate the effective pressure at the base of the ice sheet at the time of

maximum consolidation. This is demonstrated in figure 4.11. A resulting effective pressure of 150 kPa is found at the glacier sole at Noord Bergum. The errors on the gradient determination were calculated and the range of possible effective pressure values at the base of the ice determined. At Noord Bergum, the effective pressure at the base of the ice could therefore lie in the range 0 - 700 kPa.

At Marum, the sedimentary sequence is much simpler, with only one sandy unit overlying the Peelo Clay. Extrapolating the gravitational effective pressure gradient up through the sand gives an effective pressure at the glacier sole of 730 kPa (figure 4.12). The errors on the gradient determination were calculated resulting in a range of effective pressures at the glacier sole of 690 - 760 kPa.

The large value of effective pressure found at Marum suggests that all the basal melt water could have been discharged through the Peelo Clay. The effective pressure at Noord Bergum is less, however the values of melt rate are so similar for both sites, it is suggested that all or most of the basal melt water produced is also likely to have been discharged through the clay at Noord Bergum.

Since the effective pressure at the glacier sole is the difference between the pressure due to the overlying ice mass and the water pressure at the base of the ice (equation 2.10), if the water pressure can be calculated, the pressure due to the ice overburden and thus the ice thickness can be determined. The water pressure at the base of the ice will be the potential pressure which can be determined by studying the groundwater flow in more detail.

4.5.6 Subglacial Groundwater Flow

Groundwater flow in the subglacial aquifer is determined by the vertical discharge of water into the aquifer and the transmissibility of the aquifer, as the aquifer then discharges the water horizontally into the proglacial zone. A simplified model representing the Dutch situation is presented in figure 4.13.

In the model illustrated in figure 4.13, water is assumed to drain from a basally melting ice sheet vertically through a 50m thick unit of pot clay with a vertical permeability of $10^{-11}ms^{-1}$. The water then discharges horizontally in an aquifer, 100m thick, with a horizontal permeability of $10^{-4}ms^{-1}$. The model is therefore an example of the one dimensional drainage situation discussed in chapter 2. The values of permeability and thickness used in the model are based on information given by the R.G.D.

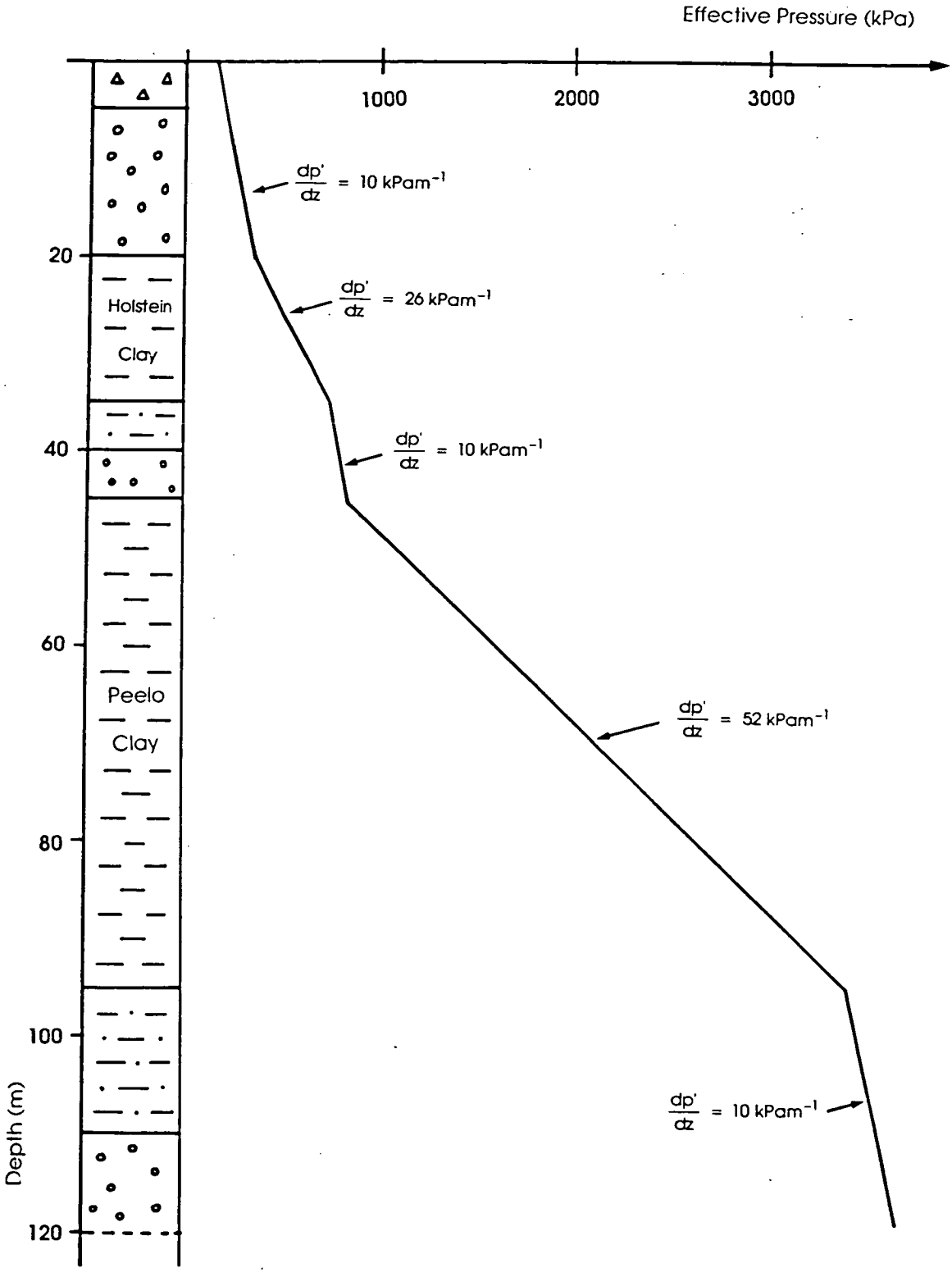

Figure 4.11: Extrapolation of effective pressure up through the sediment column, inferred from preconsolidation data, to determine the effective pressure at the base of the ice at Noord Bergum.

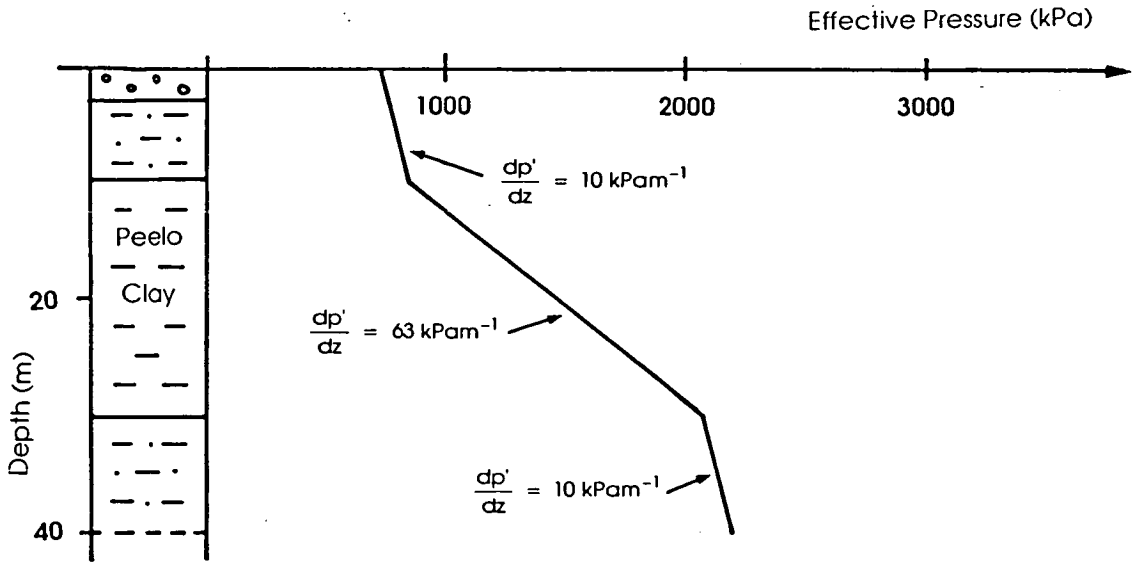

Figure 4.12: Extrapolation of effective pressure up through the sediment column inferred from preconsolidation data to determine the effective pressure at the base of the ice at Marum.

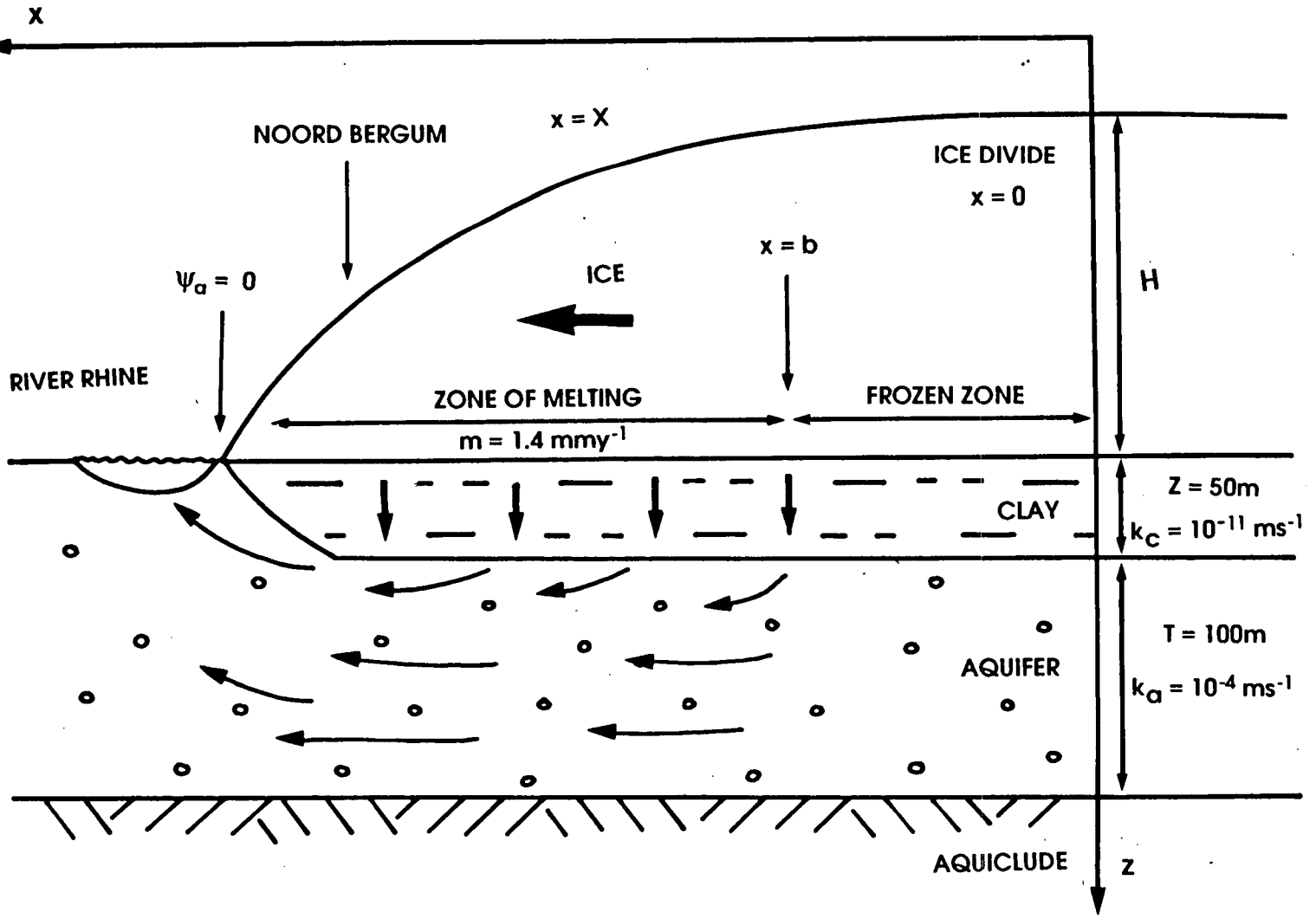

Figure 4.13: The one dimensional drainage model as found in the northern Netherlands showing the various parameters, defined in the main text, used in the model calculations

Assuming a constant basal melt rate (m), a vertical potential pressure gradient develops in the clay such that (rearranging equation 4.6):

$$\frac{d\psi}{dz} = \frac{-m\rho_w g}{k_c} \qquad 4.7$$

The magnitude of the potential pressure at the base of the ice (ψ_x) can be obtained by integrating the above equation (4.7) over the length of the drainage path (effectively the thickness of the clay unit, Z) to obtain;

$$\psi_x = \psi_a + \frac{m\rho_w g Z}{k_c} \qquad 4.8$$

where ψ_a is the potential pressure at the top of the aquifer at a point x.

The potential pressure at the top of the aquifer can be obtained by considering a zone of melting, initiating at the point x = b. Water discharge in the aquifer per unit width at any point x will then be:

$$Q = m(x-b) \qquad 4.9$$

where Q is the discharge per unit width.

The rate at which water flows in the aquifer (i.e. the discharge per unit area) is:

$$q = \frac{m(x-b)}{T} \qquad 4.10$$

where q is the velocity of flow

T is the aquifer thickness.

Water flows horizontally in the aquifer according to Darcy's Law:

$$q = \frac{-k}{\rho_w g}\frac{d\psi}{dx} \qquad 4.11$$

where $d\psi/dx$ is the horizontal potential pressure gradient.

Substituting equation 4.10 into equation 4.11, and rearranging, gives the horizontal potential pressure gradient in the aquifer at any point x as:

$$\frac{d\psi}{dx} = \frac{-m\,(x-b)\,\rho_w\,g}{k_a\,T} \qquad 4.12$$

where k_a is the horizontal permeability in the aquifer.

The magnitude of the potential pressure at the top of the aquifer (ψ_a) at the point x = X can therefore be obtained by integrating equation 4.12 between X and b resulting in the expression:

$$\psi_a = \psi_b - \frac{m\,\rho_w\,g\,(X-b)^2}{2\,k_a\,T} \qquad 4.13$$

where ψ_b is the potential pressure at the top of the aquifer at the point x = b.

The potential pressure at the base of the ice at a point x = X is therefore given by

$$\psi_x = \psi_b - \frac{m\,\rho_w\,g\,(X-b)^2}{2\,k_a\,T} + \frac{m\,\rho_w\,g\,Z}{k_c} \qquad 4.14$$

where ψ_x is the potential pressure at the base of the ice.

Assuming the system is in equilibrium, the water pressure at the glacier sole is entirely due to the potential pressure component (i.e. $p_w = \psi_x$) and represented by the above equation (4.14). Since the effective pressure at the base of the ice is already known from the consolidation experiments, it is possible to calculate the pressure applied by the overriding ice sheet at x = X by rearranging equation 2.10 and substituting in the relevant terms:

$$p_i = p' + \psi_x \qquad 4.15$$

where p_i is the pressure of ice

p' is the effective pressure.

Hence the thickness of the ice sheet giving rise to this overburden can be calculated.

4.5.7 Determination of the Ice Overburden

The pressure applied to the sediments by the overlying ice at Noord Bergum at the time of maximum effective pressure is obtained by substituting equation 4.14 into 4.15:

$$p_i = p' + \psi_b - \frac{m \rho_w g (X-b)^2}{2 k_a T} + \frac{m \rho_w g Z}{k_c} \qquad 4.16$$

The effective pressure at the base of the ice and the potential difference across the clay unit are calculated from existing information whilst the potential pressure at the top of the aquifer can be estimated.

4.5.7.i Determination of the Potential Pressure at the Top of the Aquifer

A number of assumptions are required before an estimation of the potential pressure at the top of the aquifer can be made. The most important of these are:

(i) the melt rates calculated for Noord Bergum and Marum are typical of the Saalian ice sheet;

(ii) the pattern of subglacial melting is similar to that determined by Hindmarsh et al (1989) for a mid-latitude ice sheet. This involves a stable condition in which basal temperatures are at the melting point of ice for a distance of over 300 - 400 km from the ice sheet margin, behind a narrow frozen zone, for an ice sheet of similar dimensions to that which covered northern Europe during the Saalian. Recent sensitivity tests by Payne and Boulton (pers. comm.) confirm a melting zone width of this magnitude;

(iii) the melt water was discharged primarily within the sandy aquifer underlying the Peelo Clay and that its horizontal permeability was similar to that found today ($k_a = 10^{-4}$ ms^{-1}). This aquifer extends into northern Germany and may well have been the principal means of melt water discharge for as much as 800 km from the margin of the Saalian ice sheet;

(iv) the permeability of the sandy sediments is relatively insensitive to the changes in pressure considered here.

The inner zone of the ice sheet near the ice divide, and the terminal zone, are normally assumed to have been frozen and thus zones of zero water input to the aquifer. Beneath the inner frozen zone there will be no groundwater discharge within the aquifer and thus there will be a constant potential pressure at the top of the aquifer (ie $d\psi/dx = 0$). Meanwhile beneath the terminal frozen zone, or beneath any zone of proglacial permafrost, there will be a constant groundwater discharge out of the system and thus the horizontal potential pressure gradient in the aquifer will be constant. In the case of the northern Netherlands, the Saalian ice sheet reached its maximum extent at the River Rhine. This will have prevented permafrost development and therefore it is assumed that at the terminus the melt water would have discharged from the aquifer into the river where the potential pressure at the top of the aquifer was zero, and that the length of the terminal frozen zone would have been negligible.

From the above assumptions, ψ_a is zero at the terminus ($x = 0$) and thus ψ_b can be calculated (rearranging equation 4.13):

$$\psi_b = \frac{m \rho_w g (-b)^2}{2 k_a T} \qquad 4.17$$

Melting zones of 400 and 800 km from the ice sheet margin are considered giving rise to potential pressure profiles (using equation 4.13 and substituting in values of ψ_b from equation 4.17) for the top of the aquifer at Noord Bergum and Marum. These potential pressure profiles are illustrated in figure 4.14.

4.5.7.ii Determination of the Potential Pressure at the Base of the Ice

The potential pressure at the base of the ice can be determined from equation 4.14 for any point $x = X$ along the flow line. However the sedimentary sequence at Noord Bergum is more complicated than suggested by the simple model shown in figure 4.13. A more accurate value for the potential pressure at the base of the ice at this point can be determined by assuming the potential pressure at the top of the aquifer is as established in section 4.5.7.i above and extrapolating up through the sediment column using the potential pressure gradients calculated in the overlying sediments. The potential pressure gradient in the Peelo Clay is obtained in section 4.5.3, the potential pressure gradient in the Holstein Clay is calculated in a similar manner, and the potential pressure gradient in the sandy sediment is assumed to be negligible. The determination of the potential pressure at the base of the ice is shown in figure 4.15. Thus for a melt rate of 1.4 mmy^{-1}, the potential pressure at the

base of the ice at Noord Bergum is found to be 4390 and 6670 kPa for melt zones of 400 and 800 km respectively.

The potential pressure at the base of the ice at Marum is calculated in the same way (figure 4.16) and found to be 3640 and 6720 kPa for melt zones of 400 and 800 km respectively.

(If the model sediment column (figure 4.13) is considered, the potential pressures at the base of the ice at Noord Bergum from equation 4.14 are 4270 and 6550 kPa for melt zones of 400 and 800 km respectively.)

4.5.7.iii Determination of the Ice Overburden

The pressure acting at the glacier sole due to the overlying ice is determined from equation 4.15 by substituting in the effective pressure and potential pressures at the base of the ice determined above. This results in applied pressures at Noord Bergum in the range 4540 to 6820 kPa for melt zones of 400 and 800 km, whilst at Marum, ice pressures of 4370 and 7450 kPa are obtained.

4.5.8 Determination of the Ice Sheet Thickness

If the pressure due to the overlying mass of ice is known, the ice sheet thickness can be calculated by dividing the applied pressure by the density of the ice and the acceleration due to gravity. This results in ice thicknesses of 495 and 745 m at Noord Bergum and 477 and 812 m at Marum, for respective melt zones of 400 and 800 km.

4.5.9 Determination of the Ice Sheet Profile

Assuming that the above values represent the thickness of the ice at its maximum extent allows the longtitudinal ice sheet profile to be reconstructed. This is achieved by using equation 1.3 which states that;

$$\left(\frac{h}{H}\right)^2 + \frac{x}{L} = 1 \qquad 4.18$$

where H is the thickness of ice at the divide

L is the distance from the terminus to the ice divide

h is the ice thickness at a point x along the flow line.

Assuming the ice sheet was perfectly plastic (Orowan, 1949), and its span from the ice divide to the terminus was 1000 km (the distance between the assumed terminus in the central Netherlands and the assumed ice divide in central Sweden), H can be calculated for the ice sheet which advanced over the northern Netherlands during the Saalian since h and x are known for Noord Bergum. This allows the ice sheet profile to be constructed using equation 4.18. The reconstructed profiles based on the data obtained at Noord Bergum and Marum are illustrated in figure 4.17.

4.5.10 Determination of the Basal Shear Stress

For a perfectly plastic ice sheet, Orowan (1949) showed that

$$h^2 = \frac{2\tau_o}{\rho_i g}(L - x) \qquad 4.19$$

where τ_o is the yield strength of ice.

Rearranging this equation to obtain τ_o gives

$$\tau_o = \frac{\rho_i g h^2}{2(L - x)} \qquad 4.20$$

If it is assumed that the Saalian ice sheet was perfectly plastic, it is possible to determine the basal shear stress by substituting the relevant parameters for Noord Bergum and Marum into equation 4.20.

Values of basal shear stress of 9 - 20 kPa are obtained at Noord Bergum whilst at Marum values of 8 - 22 kPa are found. These are very much less than typical values of basal shear stress for modern ice sheets resting on rock beds which are normally assumed to be 50 - 150 kPa (Paterson, 1981).

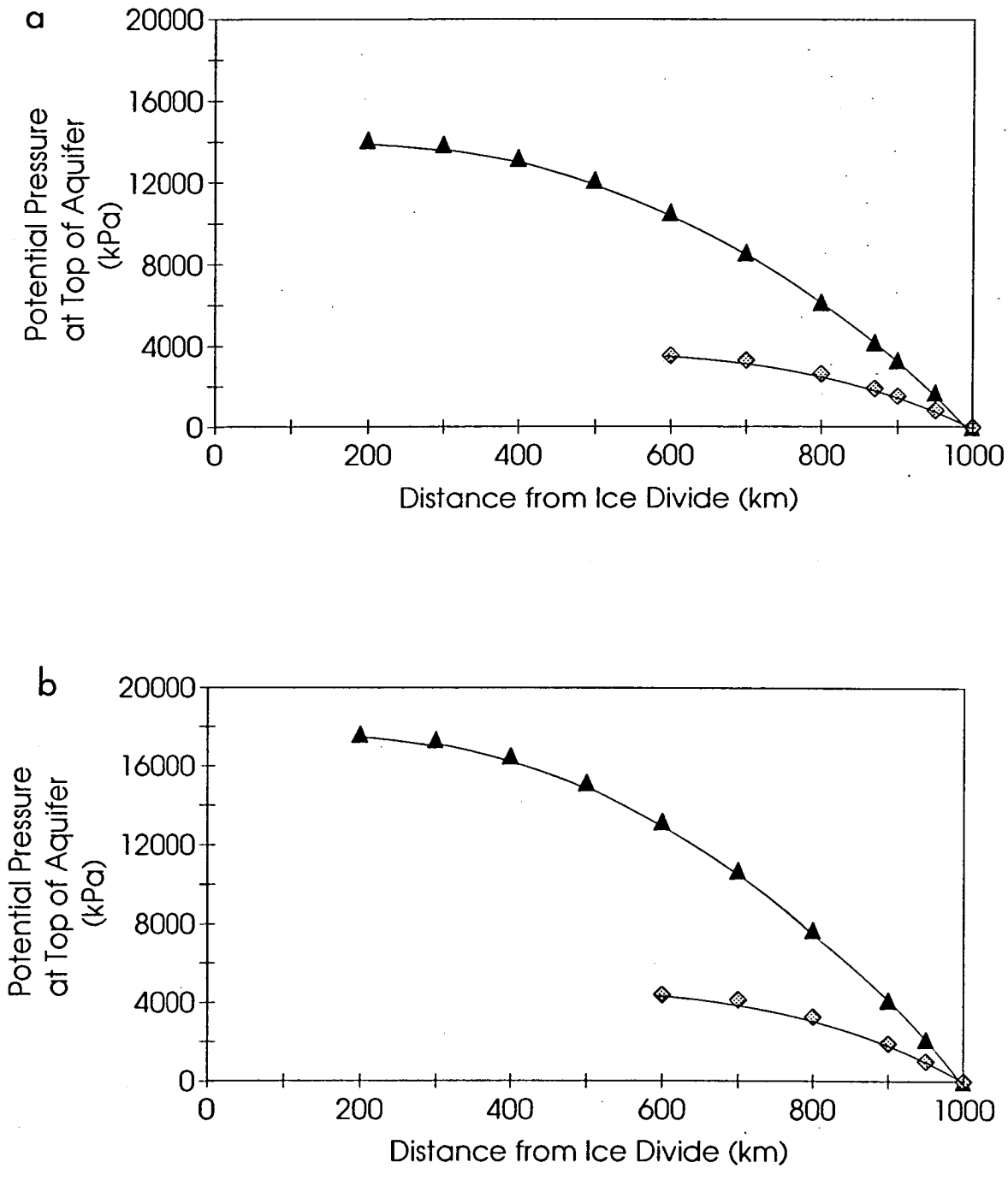

Figure 4.14: The distribution of potential pressure at the top of the aquifer with distance along the flow line **(a)** at Noord Bergum and **(b)** at Marum.

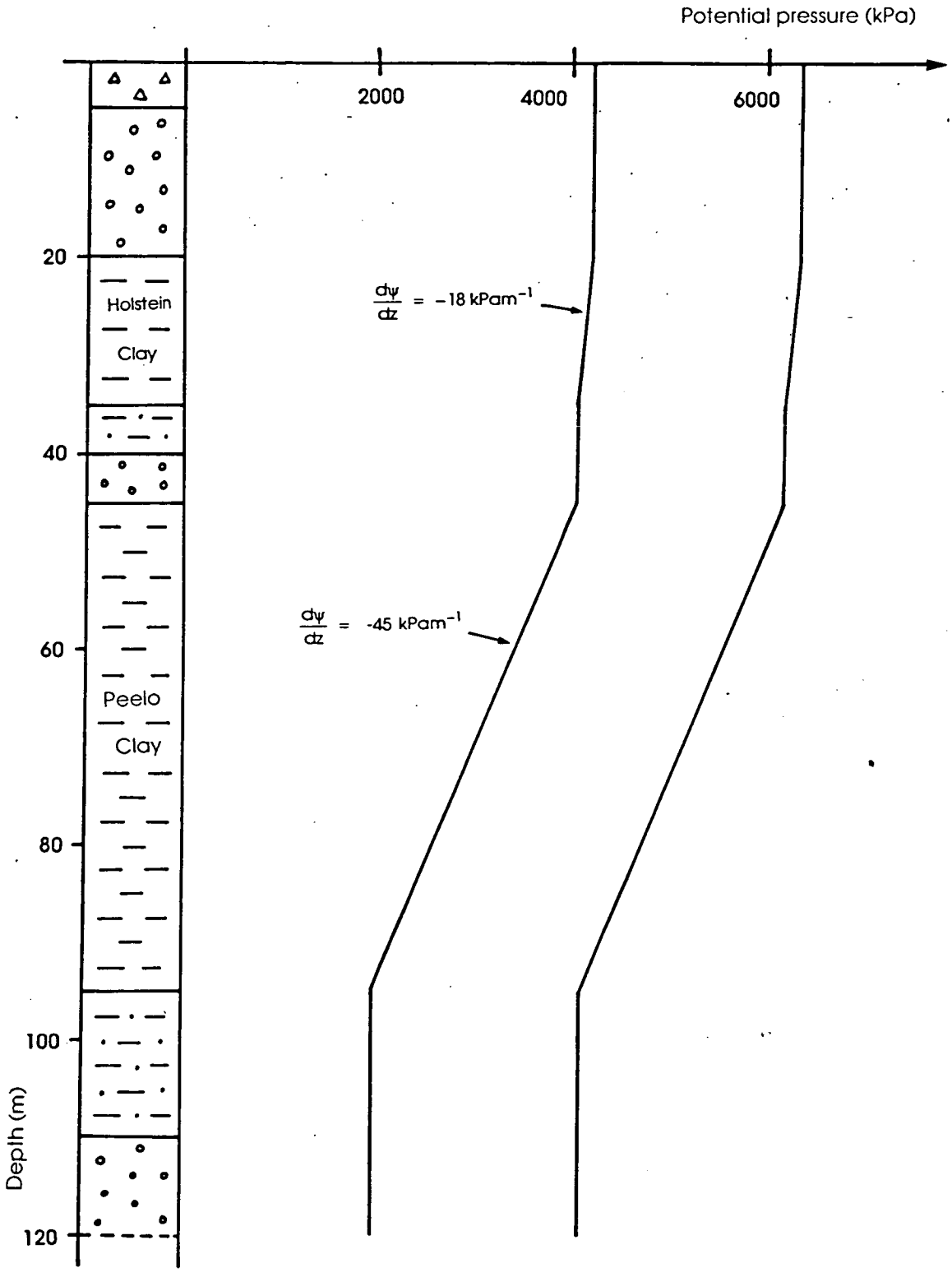

Figure 4.15: Extrapolation of potential pressure up through the sediment column at Noord Bergum from the value of the potential pressure inferred at the top of the aquifer from groundwater modelling.

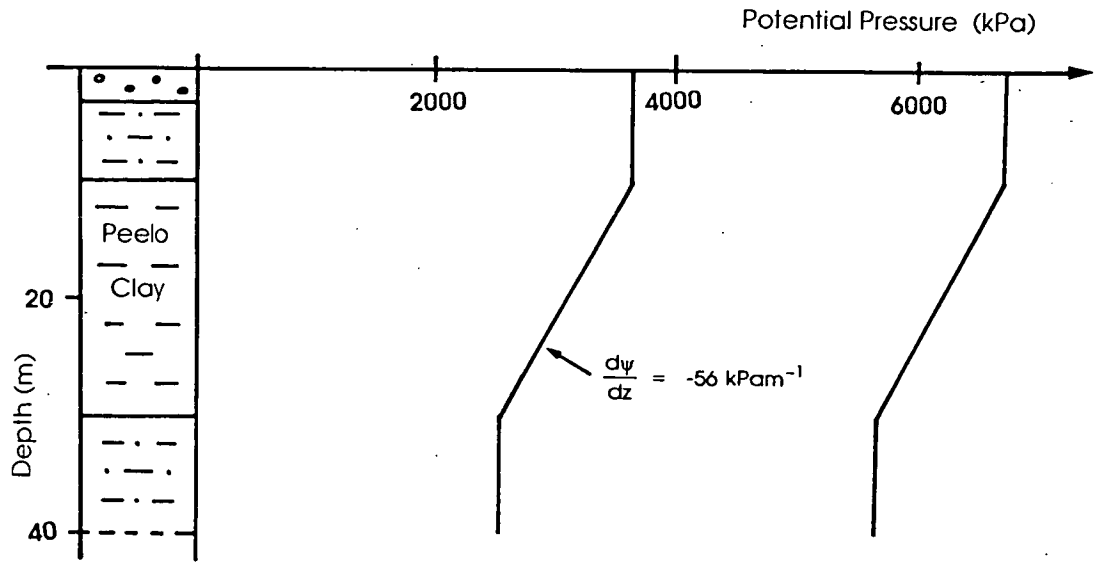

Figure 4.16: Extrapolation of potential pressure up through the sediment column at Marum from the value of the potential pressure inferred at the top of the aquifer from groundwater modelling.

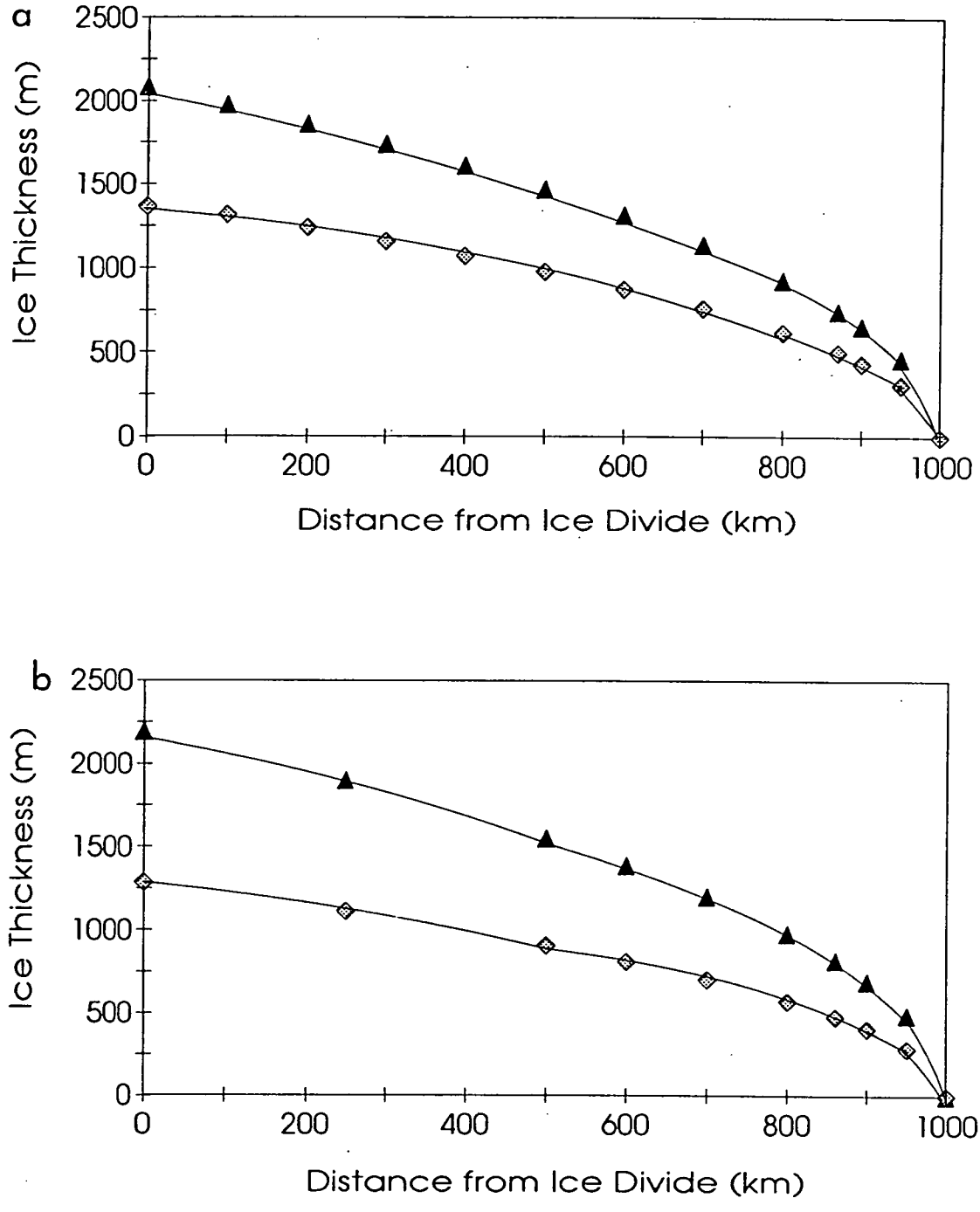

Figure 4.17: The reconstructed ice sheet profiles for **(a)** Noord Bergum and **(b)** Marum.

4.6 Conclusions

The results obtained in this chapter are summarised in tables 4.1 and 4.2.

A minimum basal melt rate of 1.4mmy^{-1} was calculated from the palaeopotential gradient inferred in the Peelo clay for the steady state glacial maximum. This is an important determination as melt rates of former ice sheets resting on soft sediments have previously been impossible to determine. This result can therefore be used as a constraint in ice sheet modelling.

Reconstruction of pressure gradients in the Peelo clay, constrained by experimentally determined effective pressure values, allow the ice overburden at the maximum extent of the ice sheet to be calculated. This results in an ice thickness at Noord Bergum of 495 - 745 m. The Saalian ice sheet profile in the northern Netherlands could therefore be reconstructed.

A basal shear stress of 9 - 20 kPa is consistent with this ice sheet profile. The basal shear stress is lower than expected for a perfectly plastic ice sheet flowing over a rigid substratum, which could indicate that subglacial sediment deformation contributed to the forward motion of the ice.

The relationship between the effective pressure and shear strength of subglacial sediments and the possibility that the forward motion of the ice sheet was a result of shear deformation in the underlying sediments are explored further in the following chapter.

Table 4.1: Calculated and inferred properties of the ice sheet and sediment at Noord Bergum.

Calculated Physical Properties of the Pot Clay at Noord Bergum

Vertical Effective Pressure Gradient	Vertical Gravitational Gradient	Coefficient of Permeability	Vertical Potential Pressure Gradient
52 $kPam^{-1}$	7 $kPam^{-1}$	10^{-11} ms^{-1}	-45 $kPam^{-1}$

Inferred Groundwater and Ice Sheet Characteristics

Potential Difference In Clay	Potential at Top of Aquifer	Effective Pressure at Glacier Sole	Melt Rate of Ice	Pressure due to Ice	Ice Thicknesss
2200 kPa	1920 - 4200 kPa	150 kPa	1.4 mmy^{-1}	4540 - 6820 kPa	495 - 745 m

Table 4.2: Calculated and inferred properties of the ice sheet and sediment at Marum

Calculated Physical Properties of the Pot Clay at Marum

Vertical Effective Pressure Gradient	Vertical Gravitational Gradient	Coefficient of Permeability	Vertical Potential Pressure Gradient
63 $kPam^{-1}$	8 $kPam^{-1}$	10-11 ms^{-1}	-55 $kPam^{-1}$

Inferred Groundwater and Ice Sheet Characteristics

Potential Difference in Clay	Potential at Top of Aquifer	Effective Pressure at Glacier Sole	Melt Rate of Ice	Pressure due to Ice	Ice Thicknesss
1100 kPa	2540 - 5620 kPa	760 kPa	1.7 mmy^{-1}	4370 - 7450 kPa	477 - 812 m

CHAPTER 5

DEFORMATION OF SUBGLACIAL SEDIMENTS: DETERMINATION OF A FLOW LAW FOR THE DRENTHE TILL

5.1 Introduction

In the previous chapter, probable ranges of basal meltwater production, effective pressures and shear stresses for the ice sheet which advanced over the northern Netherlands during the Saalian are established. It is concluded that the resulting ice sheet profile is much lower than would be expected if the ice sheet behaved as a perfectly plastic solid, and its advance was a result of internal deformation of the ice alone. The magnitudes of shear stress and effective pressure are less than values typical of ice sheets flowing over hard beds suggesting that subglacial sediment deformation could have played an important role in the dynamics of the ice sheet.

Various deforming bed models have been proposed (e.g. Alley *et al.*, 1986, 1987a & b, 1989, Boulton and Hindmarsh, 1987, Clarke, 1987, Alley, 1989a & b). However the mechanical properties of subglacial till, a fundamental component of the deforming bed model, are as yet not well defined. A realistic flow law for subglacial sediment is therefore required before the deforming bed mechanism can be fully understood. The flow law should relate shear strain rate in the till to the shear stress and effective pressure at the base of the ice, allowing predictions to be made about the nature and extent of sediment deformation and its effect on ice sheet dynamics.

This chapter considers how sediments will deform under subglacial conditions. Firstly, previous attempts at determining a flow law for till are outlined and their limitations discussed. Shear tests in general are then examined and the choice of test employed in this study, the ring shear test, substantiated. The residual strength of till from the northern Netherlands is measured for a range of effective pressures and shear strain rates and from the results a flow law for the till is determined. This flow law is then compared with those already established and suggestions made as to why they differ. The implications for stable sediment deformation are discussed.

Ice sheet motion in the northern Netherlands is then modelled using the experimentally determined flow law and applying the shear stress and effective pressure conditions established for the predicted ice sheet. It is found that stable

sediment deformation can occur but within a narrow range of effective pressure values, thus reflecting the sensitivity of the flow law established for the Dutch till.

5.2 Previous Attempts to Determine a Flow Law for Till

Quantitative flow laws are difficult to derive from laboratory experiments because of the problems of sustaining steady conditions for large strains. Previous attempts to establish a flow law for till have therefore concentrated on field observations of the deformation of subglacial till. The majority are based on the flow law determined by Boulton and Hindmarsh (1987) and have assumed the form

$$\dot{\varepsilon} = K \frac{\tau^n}{p'^m} \qquad 5.1$$

where $\dot{\varepsilon}$ is the strain rate

τ is the shear stress

p' is the effective pressure

K, n and m are constants.

5.2.1 The Boulton and Hindmarsh Flow Law

Boulton and Hindmarsh (1987) established a flow law for till from field experiments on subglacial shearing carried out near the terminus of Breidamerkurjökull in Iceland. Their experiments monitored the deformation process and its relation to glacier movement using a series of strain markers and piezometers inserted into subglacial till from tunnels excavated in the ice. The strain rate and effective pressure were averaged over the thickness of the deforming layer and plotted along with the calculated shear stress. Two rheological models were fitted to these data by direct mathematical modelling, a nonlinear viscous material and a nonlinear Bingham material. Boulton and Hindmarsh (1987) suggest that in most circumstances the nonlinear viscous model is the more useful. It takes the form

$$\dot{\varepsilon} = 3.99 \left(\frac{\tau}{10^5}\right)^{1.33} \left(\frac{p'}{10^5}\right)^{-1.8} \qquad 5.2$$

where τ and p' are in Pa and $\dot{\varepsilon}$ is in y^{-1}.

The majority of subsequent models for the deforming bed have assumed a flow law of this form with a linear or weakly non-linear rheology (e.g. Alley *et al.*, 1987b; Alley, 1989b; Alley *et al.*, 1989; MacAyeal, 1989). The one exception is the flow law proposed by Kamb (1991).

5.2.2 Kamb's Flow Law

Kamb (1991) states that the flow law required to model the deforming bed mechanism must describe steady state creep at large strains with the till at failure (the residual state, defined in section 5.3.2). He carried out direct shear tests on till from the base of Ice Stream B, Antarctica, but did not achieve the residual state. The tests were therefore inadequate for the determination of residual shear strength. He claimed nevertheless that the mechanical properties of till observed in the tests were similar to those of clay rich soils in similar tests, and hence assumed that, at large strains, subglacial till would behave in a similar manner to clay rich soils. He consequently calculated equivalent values of n and m from soil mechanics studies of clay rich soils (Skempton, 1985; Bishop *et al.*, 1971).

Kamb (1991) proposes values of n in the range 18 - 115. As n becomes larger the sediment behaves increasingly like a perfectly plastic material, as might a pure clay. He assumes a value of n = 100 in his flow law. Kamb (1991) also obtains an equivalent value of m = 100 arguing that existing models that assume values of m of 0 - 5 (e.g. Boulton and Hindmarsh, 1987; Alley *et al.*, 1987b; Alley, 1989b; Alley *et al.*, 1989; MacAyeal, 1989) do not adequately describe ice sheet motion as they underestimate the sensitivity of the system.

Kamb's flow law *is* of the form;

$$\dot{\varepsilon} = c \left(\frac{\tau^{100}}{p'^{100}} \right) \qquad 5.3$$

where c is an unspecified constant.

5.2.3 Limitations of the Flow Laws

The flow law of Boulton and Hindmarsh (1987) is based on values of shear strain rate and effective pressure averaged over the deforming layer. The averaging process, however, ignores the vertical distribution of effective pressure thus masking the

effects of any non-linearity. A more accurate relationship between shear strain rate, shear stress and effective pressure is therefore required.

Kamb's (1991) flow law is based on the behaviour of clay rich soils and thus may not be directly applicable to tills. This point is discussed in more detail below (section 5.8). Furthermore the direct shear test employed by Kamb (1991) is not the best method of determining shear strength under subglacial conditions (discussed in section 5.3) so the behaviour found may not reflect the true behaviour of till in this environment.

It is therefore necessary to determine more accurately how till will deform under subglacial conditions before comments can be made about the nature of subglacial sediment deformation and its application to deforming bed models. A suitable test to determine the relationship between shear strain rate, shear stress and effective pressure is therefore required.

5.3 Shear Strength of Sediments

The threshold for till deformation is achieved when the basal shear stress exerted by the ice sheet equals the shear strength of the till. Beyond this threshold the rate of deformation may also depend upon effective pressure and shear stress. There are a variety of tests that measure the shear strength of sediments, including the direct shear test, the triaxial shear test and various torsion shear tests (e.g. Smith, 1982).

5.3.1 Methods of Determining Shear Strength

According to Hvorslev (1939), the principal objectives of shear tests are the determination of:

(i) the maximum shearing resistance,
(ii) the bond resistance and the velocity of slow plastic flow before failure,
(iii) the temporary or permanent decrease of shearing resistance after failure,
(iv) the stress-strain relationships and volume change characteristics as a result of shearing stresses.

Hvorslev (1939) studied the various tests available and concluded that whilst objectives (i), (ii) and (iv) could best be achieved by using the triaxial test, the best method for determining (iii) the decrease in shearing resistance after failure, is a

torsion shear test on a ring shaped sample. Subsequent research has confirmed this (Bishop *et al.*, 1971). A full description of the different types of torsion apparatus appears in Hvorslev (1939) and Bishop *et al.* (1971), and a comprehensive discussion on the findings of different authors can be found in Lupini (1980).

5.3.2 Shear Strength of Subglacial Sediments

In chapter 2 the critical state is discussed in which the sediment strength is said to be at its lowest value. However very large displacements may reduce the sediment strength even further, as a result of continuous slip surfaces forming within the sediment mass as it continues to shear beyond failure. This is known as the residual strength (Skempton, 1964) and defined in objective (iii) above.

In subglacial sediments, shearing rates are likely to be slow and displacements large, hence in the subglacial environment sediments are assumed to be in their residual state. Following the conclusions of Hvorslev (1939), it was decided that for this study the best means of determining the shear strength of subglacial sediments would be in a ring shear device in which it is possible to shear the sample through an uninterrupted displacement of any magnitude.

5.4 The Ring Shear Test

Ring shear tests were carried out using the Armfield ring shear apparatus in the Department of Civil Engineering at the University of Edinburgh. As this apparatus was not in general use, a control experiment was initially undertaken to ensure that the apparatus measured the residual shear strength correctly. A sample of kaolin was tested, the residual angle of friction for which is well documented (e.g. Lupini, 1980).

5.4.1 Ring Shear Test on Kaolin

The ring shear test applies a vertical load to a thin, annular sediment sample, clamped between two discs. The sample is then sheared radially at a constant rate to determine the shear strength of the sediment at large strains. The ring shear apparatus used in the test is illustrated and described in appendix C.

Method: 3kg of Speswhite kaolin was mixed thoroughly with 3000cm^3 of distilled water into a smooth slurry which was then transferred to a Rowe cell where it was consolidated under a hydrostatic pressure of 6kgcm^{-3}. The moisture loss from the cell

was monitored until no further water was expelled, at which point maximum consolidation was assumed to have occurred.

The kaolin was extruded from the Rowe cell and a sample of the required dimensions obtained using the sample cutter illustrated in appendix C. The annular sample was then placed in the ring shear cell and the apparatus assembled as described in appendix C.

An initial load was placed on the hanger and the sample left to consolidate for approximately 24 hours to ensure that any excess pore water pressure had dissipated. The sample was then sheared and the angular displacement and shear load monitored throughout the test until the shear load became constant. A further load was then added and the sample allowed to consolidate. This procedure was repeated for increasing load increments allowing a residual shear envelope to be defined.

The test was carried out at the slowest possible shearing rate (a gear ratio of 1000:1, equivalent to a displacement rate of 5×10^{-8} ms^{-1}).

Results: at the end of the test the sample split easily into two sections along a distinct, smooth shear plane suggesting that the sample had failed by the sliding shear process (Lupini, 1980). The sliding shear mechanism is discussed further in section 5.7.1.

For each increment of normal effective stress, readings of shear load (recorded as the number of divisions moved on the proving ring) and the corresponding angular displacement, are tabulated in appendix C and presented graphically in figure 5.1.

The constant value of shear load is interpreted as reflecting the residual shear strength of the material, which is calculated as described in appendix C. Table 5.1 shows the residual shear strength for each normal effective stress. The residual shear envelope is defined by plotting residual shear strength against normal effective pressure (figure 5.2), from which the residual shear strength parameters for kaolin can be determined using the Mohr-Coulomb equation (see section 2.8.2).

The residual angle of friction for kaolin was found to be 11.86° which agrees very well with the range of values obtained by Lupini (1980) of 11.3 - 12° in his study of residual strength of soils.

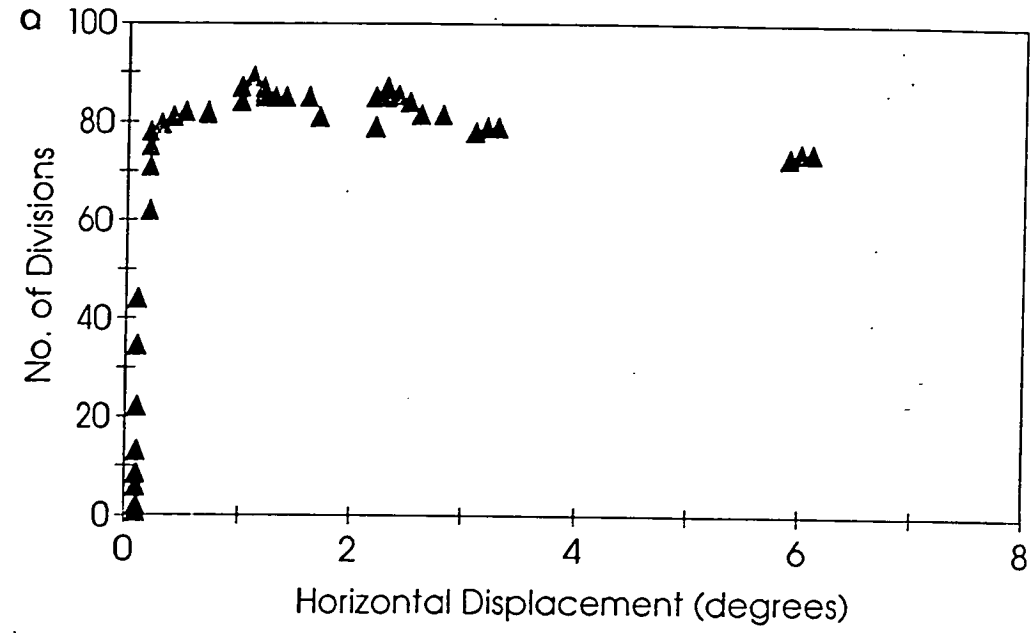

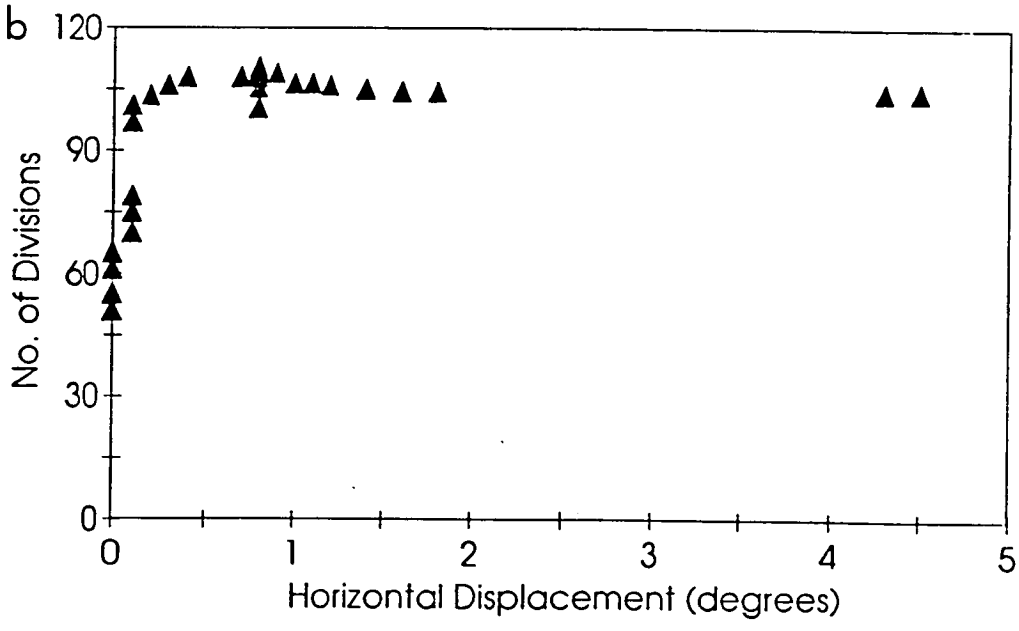

Figure 5.1: Graphs of shear load (illustrated as the number of divisions recorded on the proving ring) against angular displacement in the kaolin sample at a displacement rate of 5 x 10^{-8} ms^{-1} for an effective pressure of: **(a)** 20 and **(b)** 40 kPa (ring shear test 3).

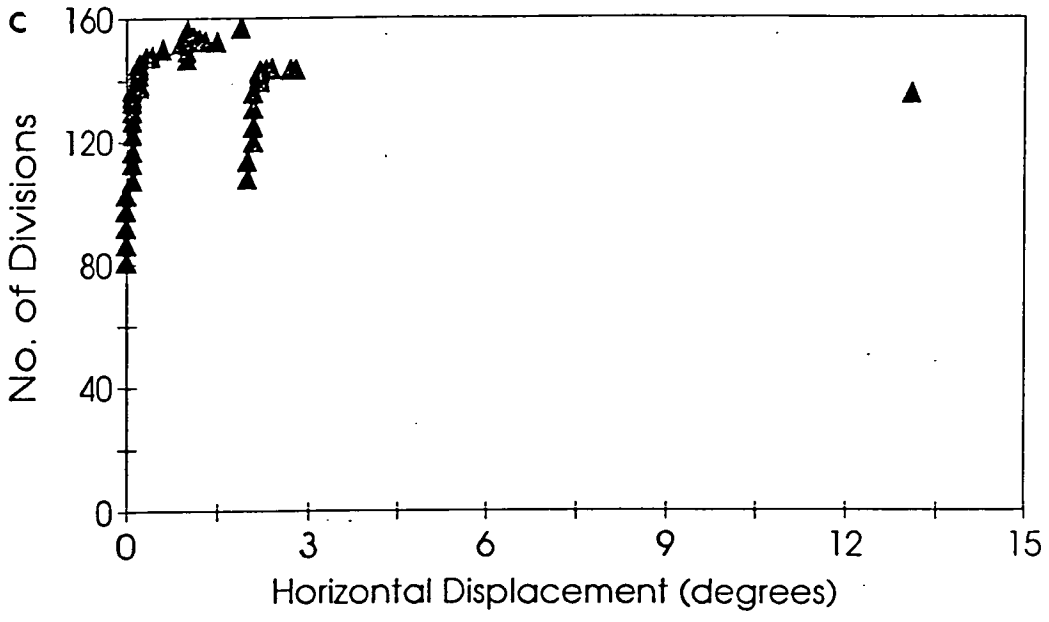

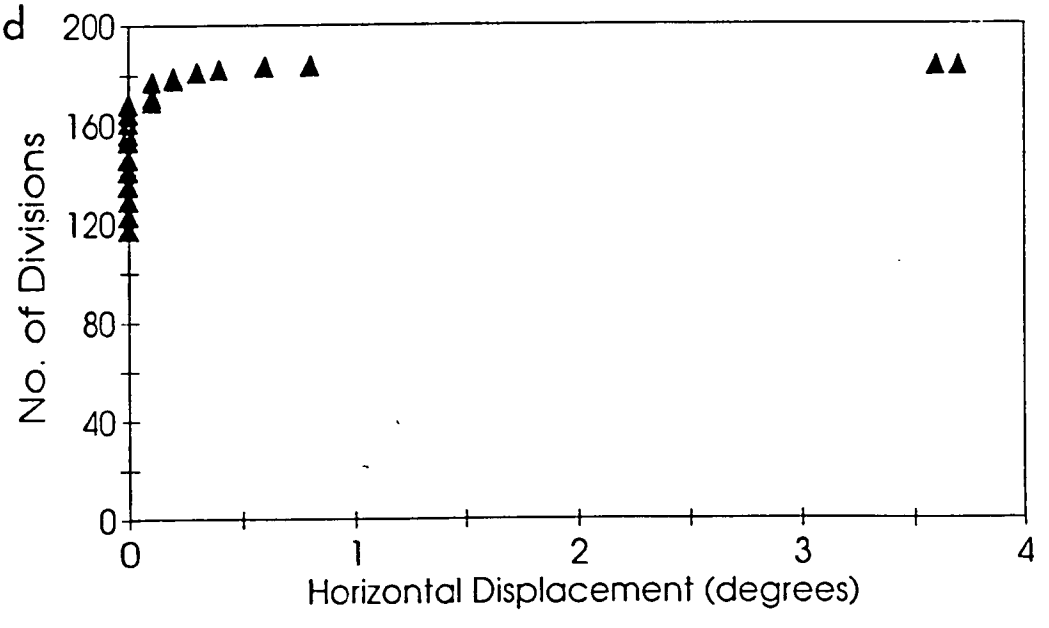

Figure 5.1 cont: Graphs of shear load against angular displacement for the kaolin sample at a displacement rate of 5 x 10^{-8} ms^{-1} for an effective pressure of: **(c)** 60 and **(d)** 80 kPa.

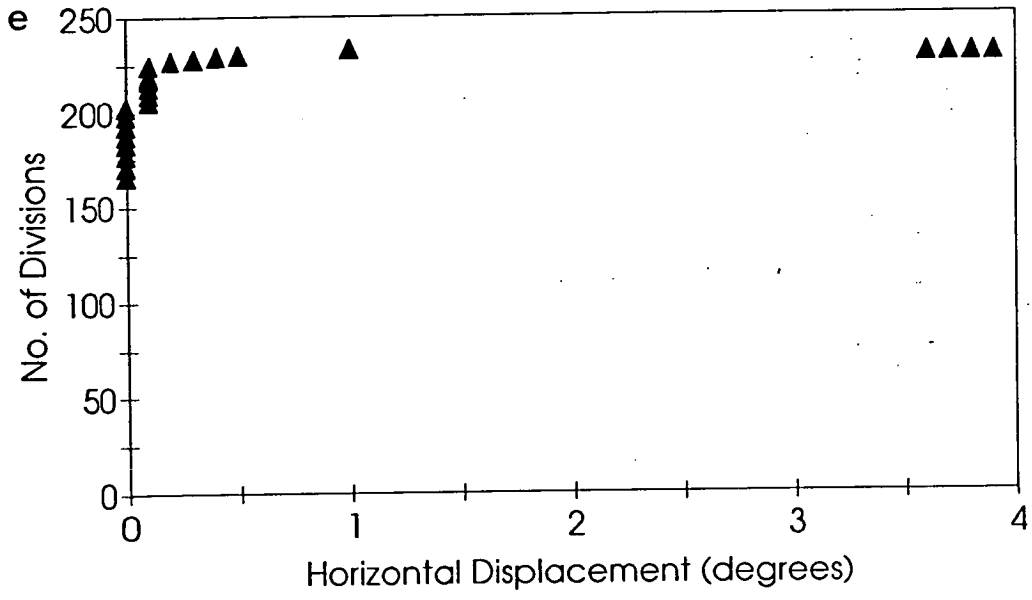

Figure 5.1 cont: Graph of shear load against angular displacement for the kaolin sample at a displacement rate of 5 x 10^{-8} ms^{-1} for an effective pressure of: **(e)** 100 kPa.

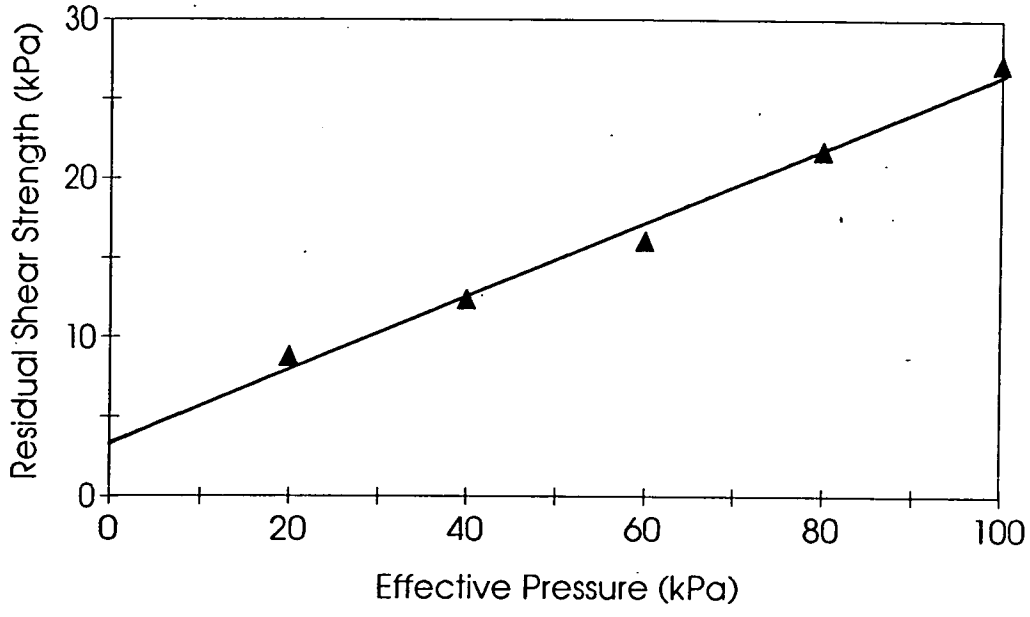

Figure 5.2: Graph of residual shear strength plotted against effective pressure for the kaolin sample, showing the residual shear envelope.

Table 5.1: Corresponding values of residual shear strength and effective pressure for the ring shear test on kaolin (ring shear test 3).

Displacement Rate (ms^{-1})	Effective Pressure (kPa)	Residual Shear Strength (kPa)
4.7×10^{-8}	20	8.8
4.7×10^{-8}	40	12.4
4.7×10^{-8}	60	16.1
4.7×10^{-8}	80	21.8
4.7×10^{-8}	100	27.3

Discussion: the close agreement of the residual friction angle determined in the above test with the values found in the literature was taken as confirmation that the test was a suitable means of determining residual shear strength. Tests were therefore carried out on till from the northern Netherlands to determine its residual shear strength and dependence on shear strain rate and effective pressure.

5.4.2 Ring Shear Test on Till

Method: a test was carried out initially on a till sample from Noord Bergum in its natural state. The sample, block was cut into strips and was kneaded into the rings using thumb pressure, the apparatus assembled as described in appendix C, and an initial mass of 10kg placed on the weight hanger. The slowest speed was chosen (a gear ratio of 1000:1) and the test carried out as before (section 5.4.1), recording the angular displacement and applied shear load throughout.

At the end of the test the apparatus was dismantled and the till remoulded. Both La Gatta (1970) and Bishop et al. (1971) demonstrate that the residual friction angle is unaffected by the initial structure of the sediment and thus the results from the original and remoulded specimens can be directly compared.

The apparatus was then reassembled and the remoulded till pressed into the confining rings as described above. A gear ratio of 100:1 was chosen and the test run as before for different normal stresses. This procedure was repeated for gear ratios of 10:1 and 1:1.

Results: at the end of the test, a shear zone of increased water content, 2 - 3mm thick, was observed. The sample split along this zone revealing a very irregular surface, indicating that the turbulent mechanism of shearing was involved (Lupini, 1980). The significance of this is discussed in section 5.7.1.

The results, tabulated in appendix C, are presented for each displacement rate in figures 5.3, 5.4, 5.5 and 5.6 as plots of shear load against angular displacement for each normal stress. The residual shear strength was calculated for each test and graphs of residual shear strength against normal effective pressure plotted for each displacement rate, thus defining the residual strength envelopes, shown in figures 5.7, 5.8, 5.9 and 5.10.

Triplets of values of x, τ and p' obtained (table 5.2), from which it was possible to determine a flow law for the till.

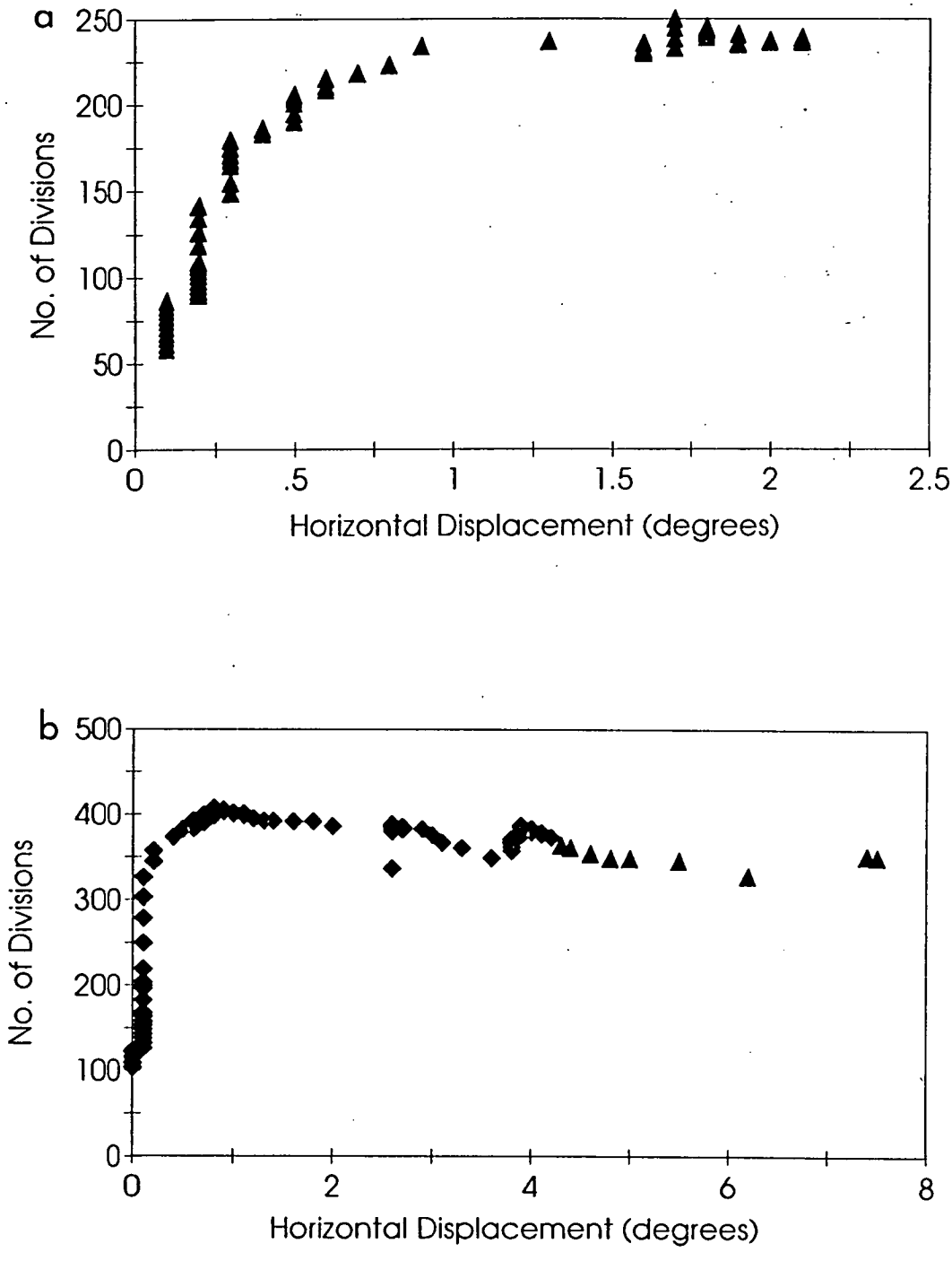

Figure 5.3: Graphs of shear load (illustrated as the number of divisions recorded on the proving ring) against angular displacement in the till sample at a displacement rate of 5×10^{-8} ms^{-1} for an effective pressure of: **(a)** 100 and **(b)** 120 kPa.

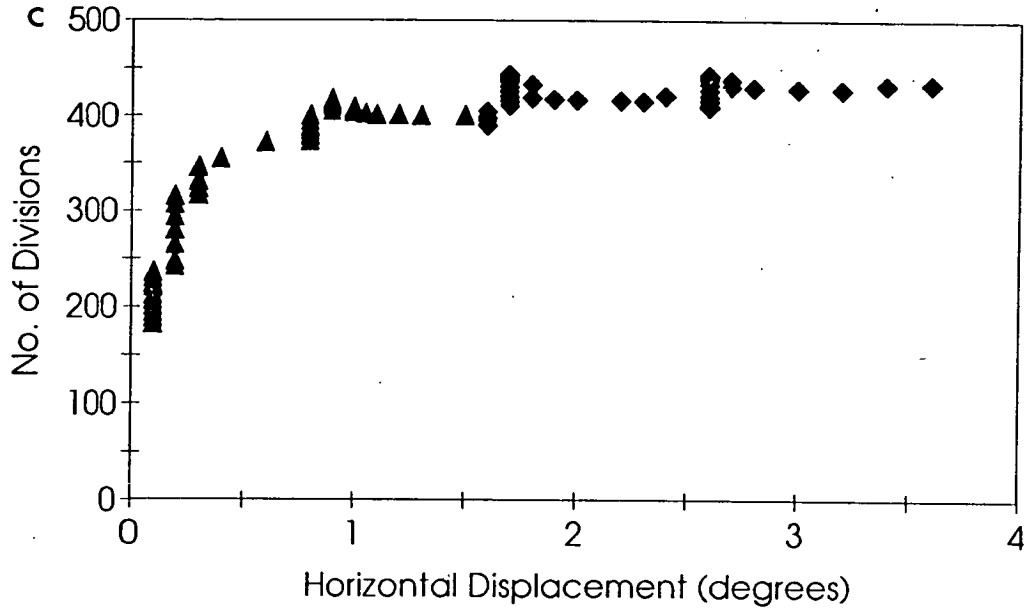

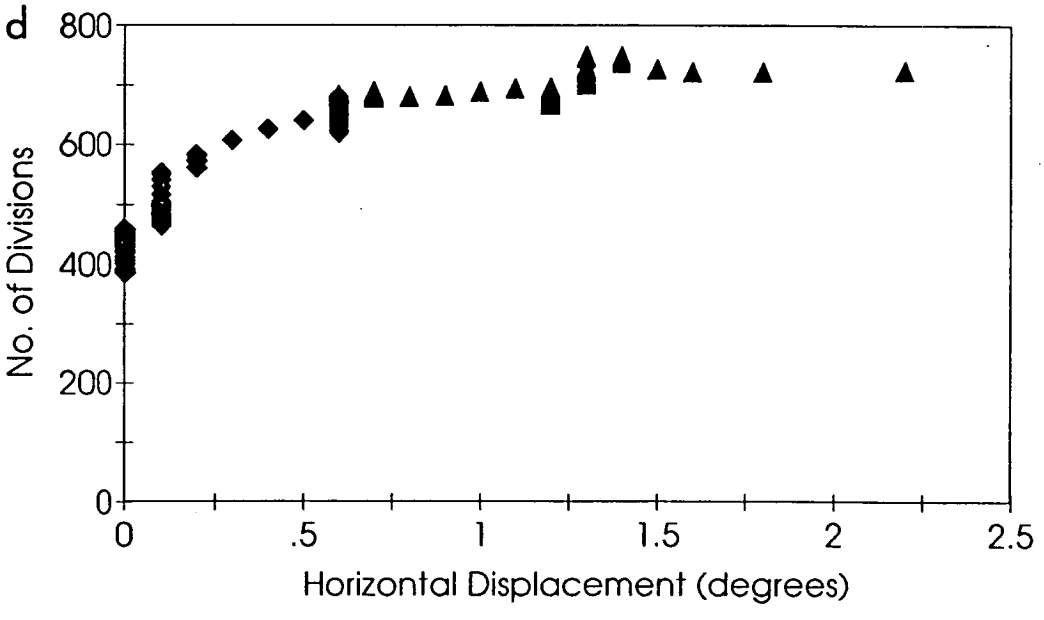

Figure 5.3 cont: Graphs of shear load against angular displacement for the till sample at a displacement rate of 5 x 10^{-8} ms^{-1} for an effective pressure of: **(c)** 140 and **(d)** 200 kPa.

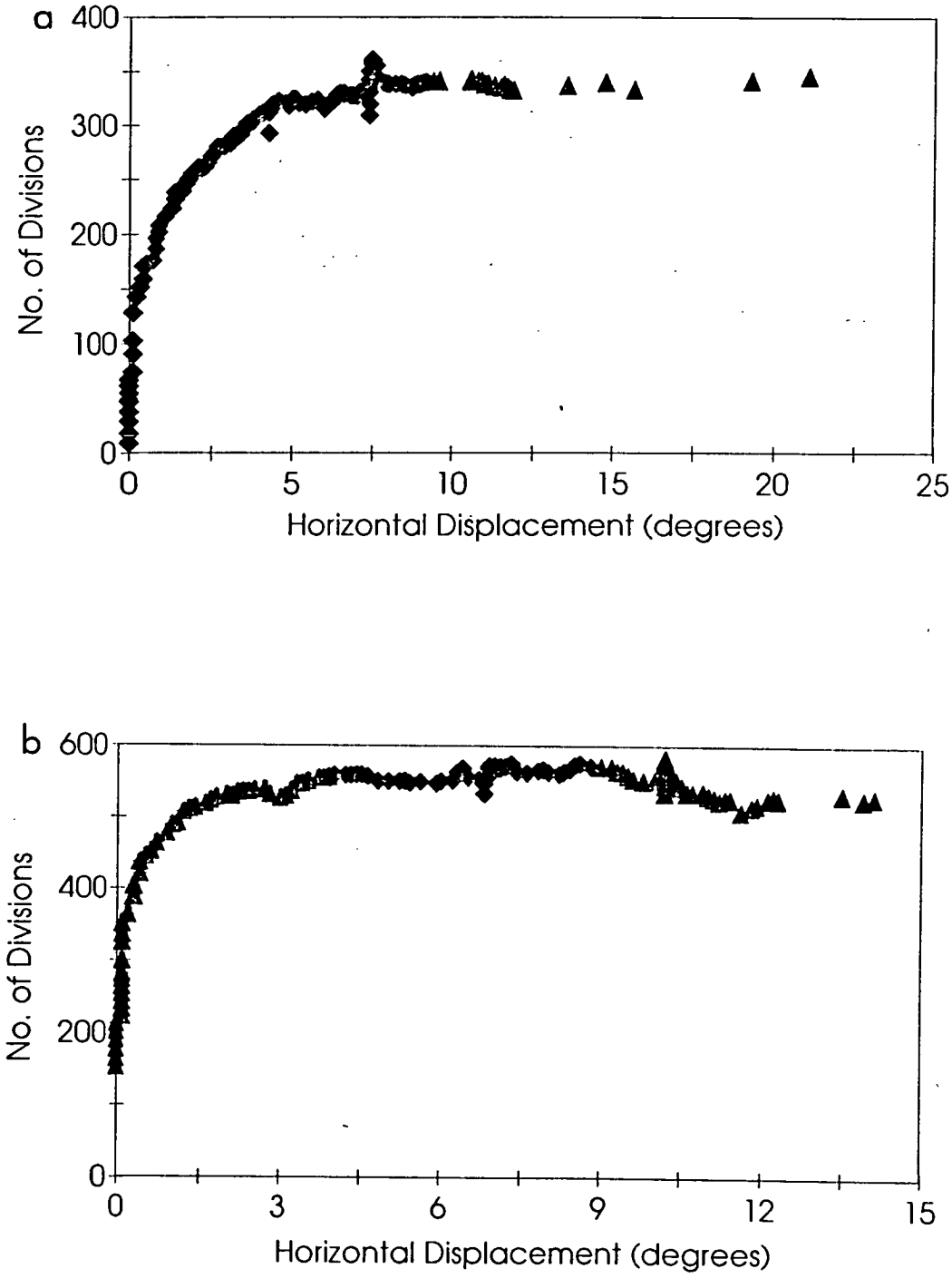

Figure 5.4: Graphs of shear load (illustrated as the number of divisions recorded on the proving ring) against angular displacement in the till sample at a displacement rate of 5×10^{-7} ms^{-1} for an effective pressure of: **(a)** 100 and **(b)** 140 kPa.

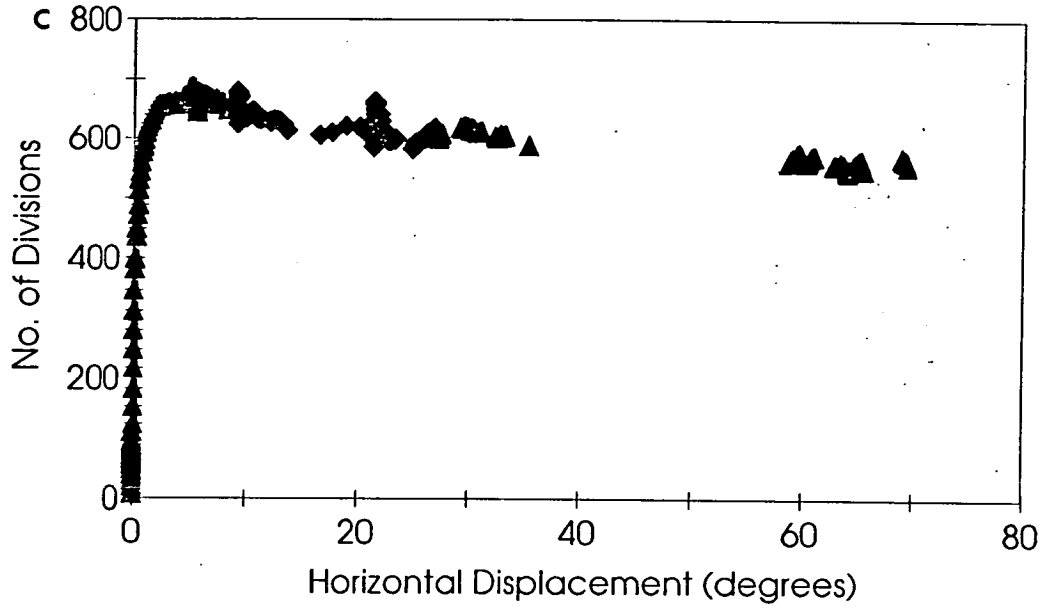

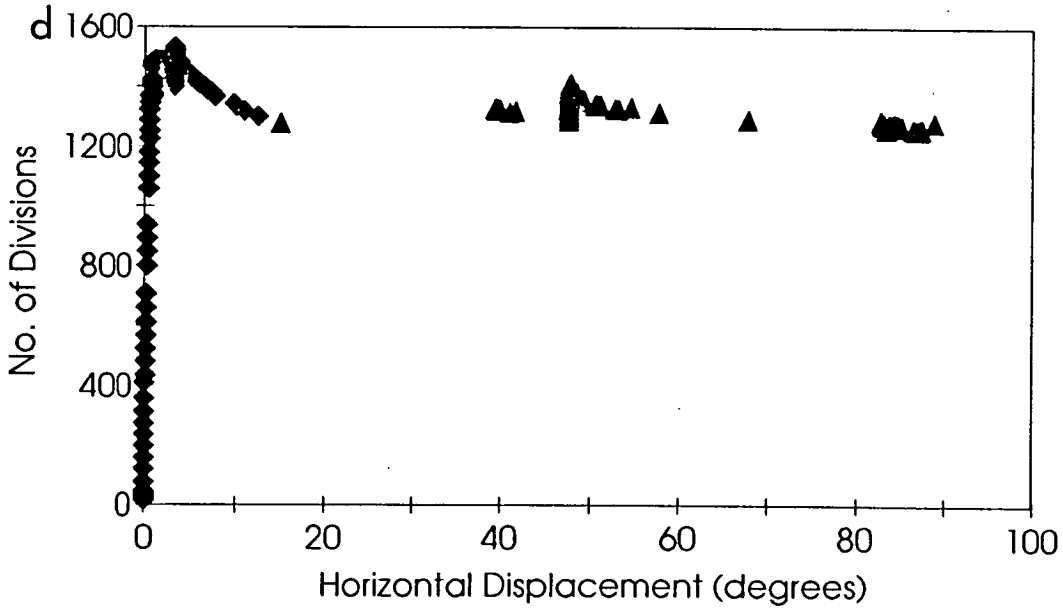

Figure 5.4 cont: Graphs of shear load against angular displacement for the till sample at a displacement rate of 5 x 10^{-7} ms^{-1} for an effective pressure of: **(c)** 150 and **(d)** 300 kPa.

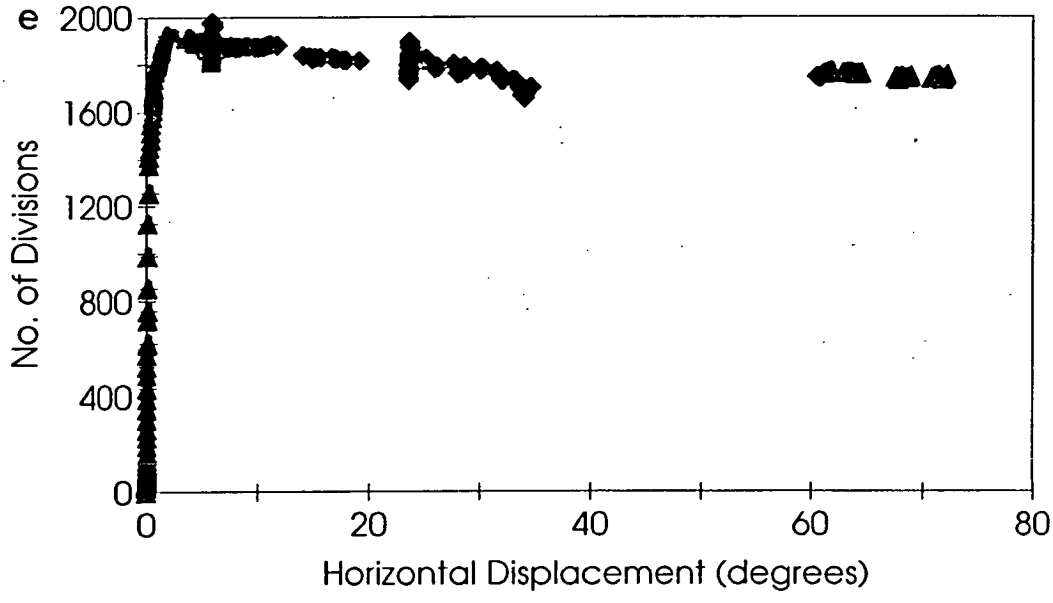

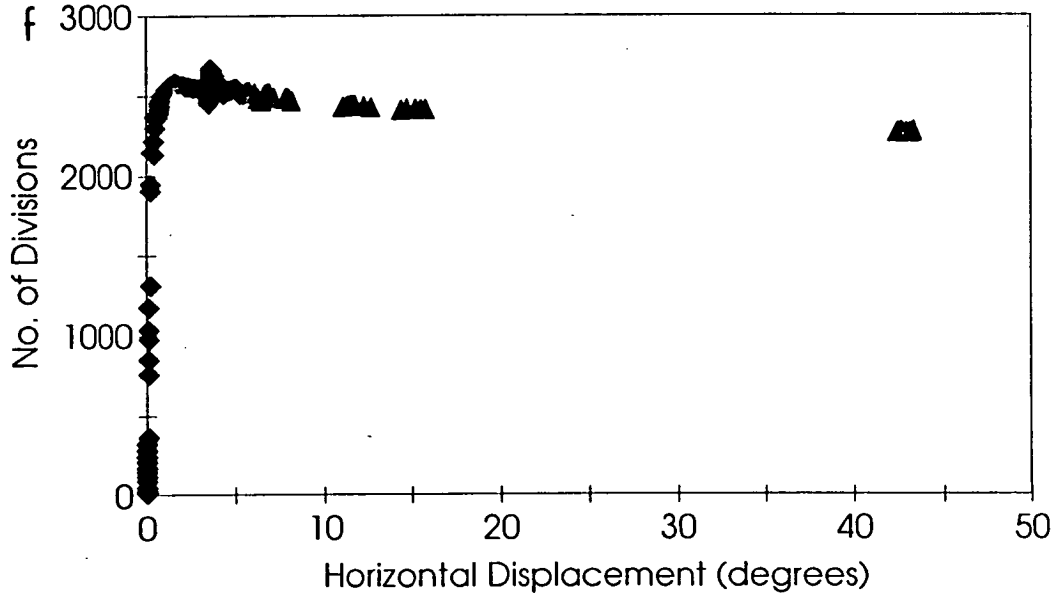

Figure 5.4 cont: Graph of shear load against angular displacement for the till sample at a displacement rate of 5 x 10^{-7} ms^{-1} for an effective pressure of: **(e)** 400 and **(f)** 600 kPa.

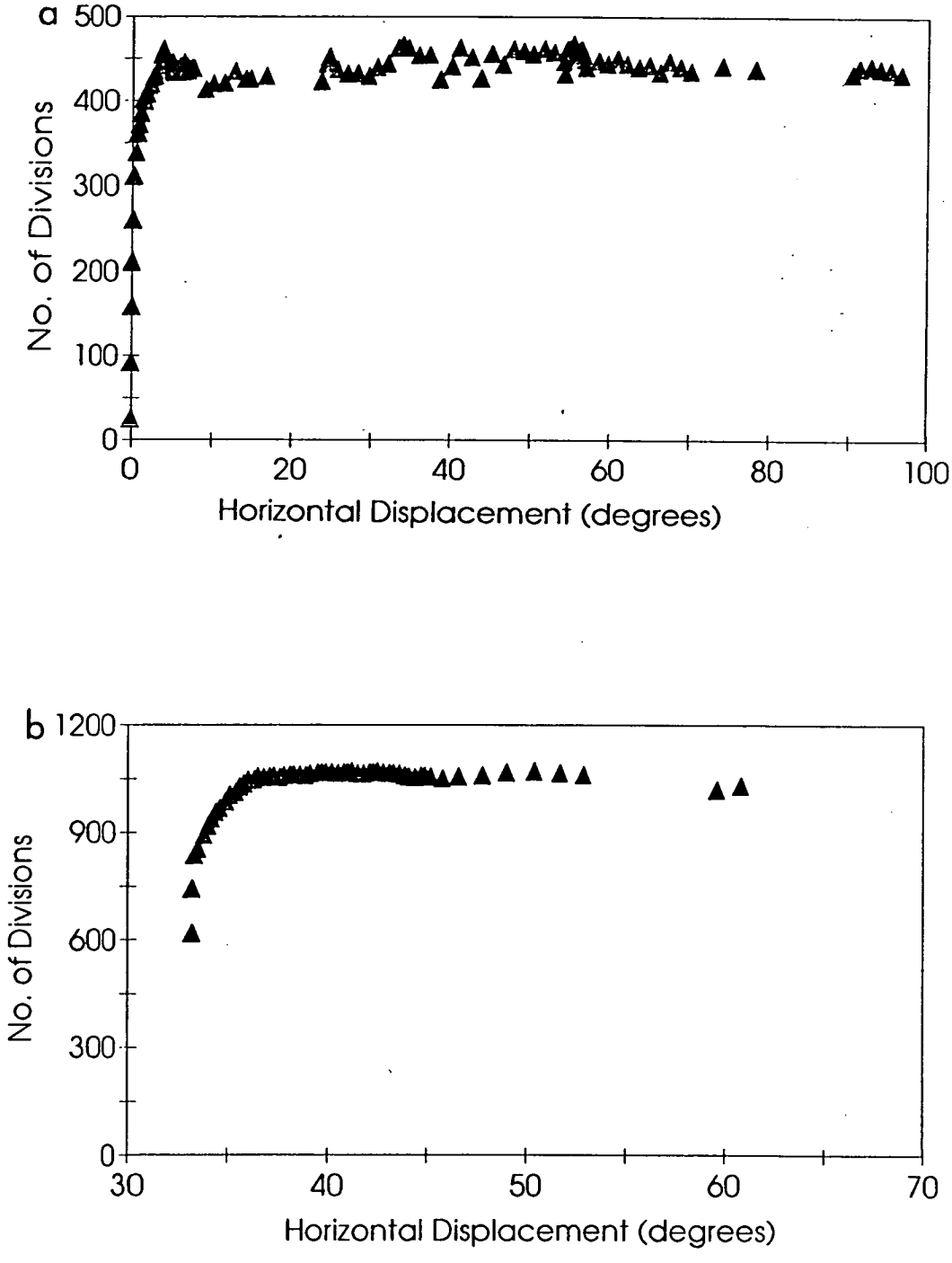

Figure 5.5: Graphs of shear load (illustrated as the number of divisions recorded on the proving ring) against angular displacement in the till sample at a displacement rate of 5×10^{-6} ms^{-1} for an effective pressure of: **(a)** 100 and **(b)** 200 kPa.

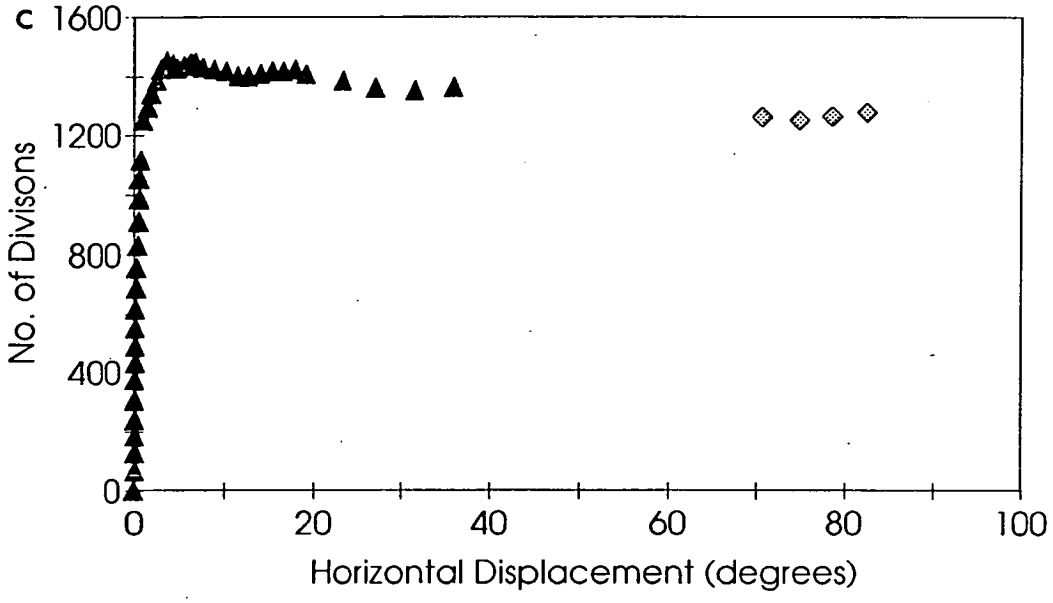

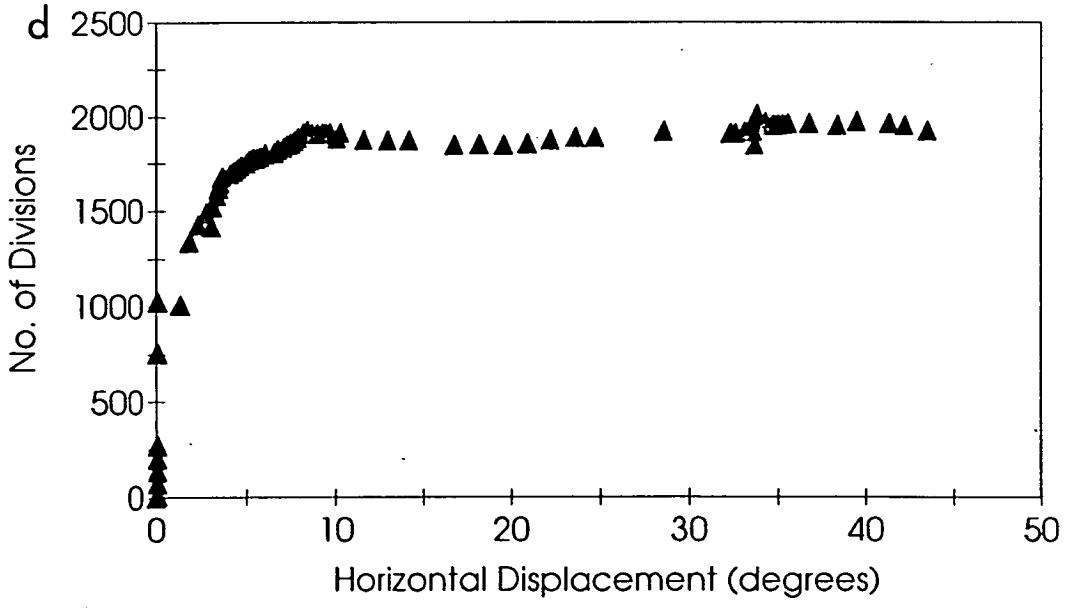

Figure 5.5 cont: Graphs of shear load against angular displacement for the till sample at a displacement rate of 5 x 10^{-6} ms^{-1} for an effective pressure of: **(c)** 300 and **(d)** 400 kPa.

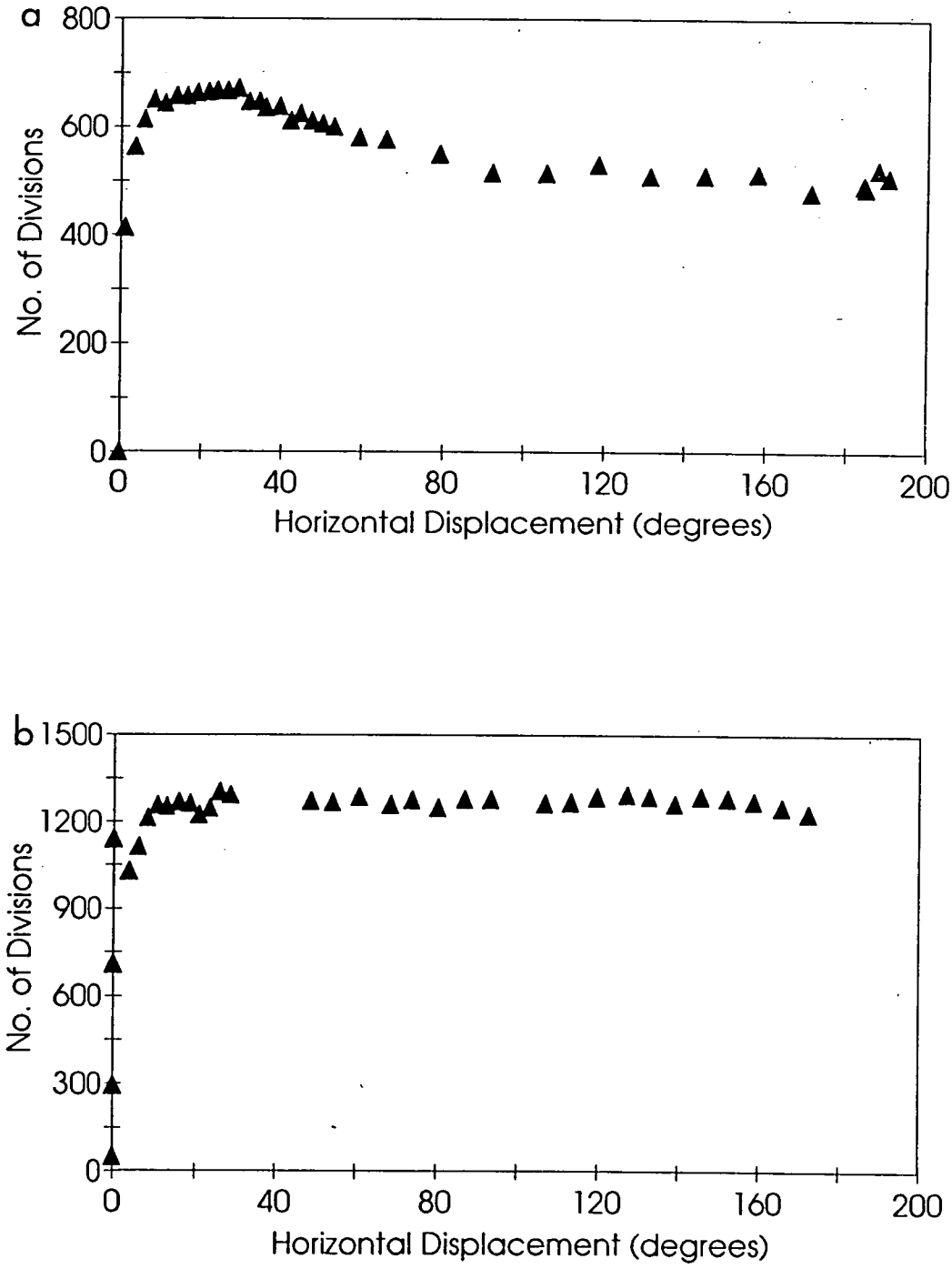

Figure 5.6: Graphs of shear load (illustrated as the number of divisions recorded on the proving ring) against angular displacement in the till sample at a displacement rate of 5×10^{-5} ms^{-1} for an effective pressure of: **(a)** 100 and **(b)** 300 kPa.

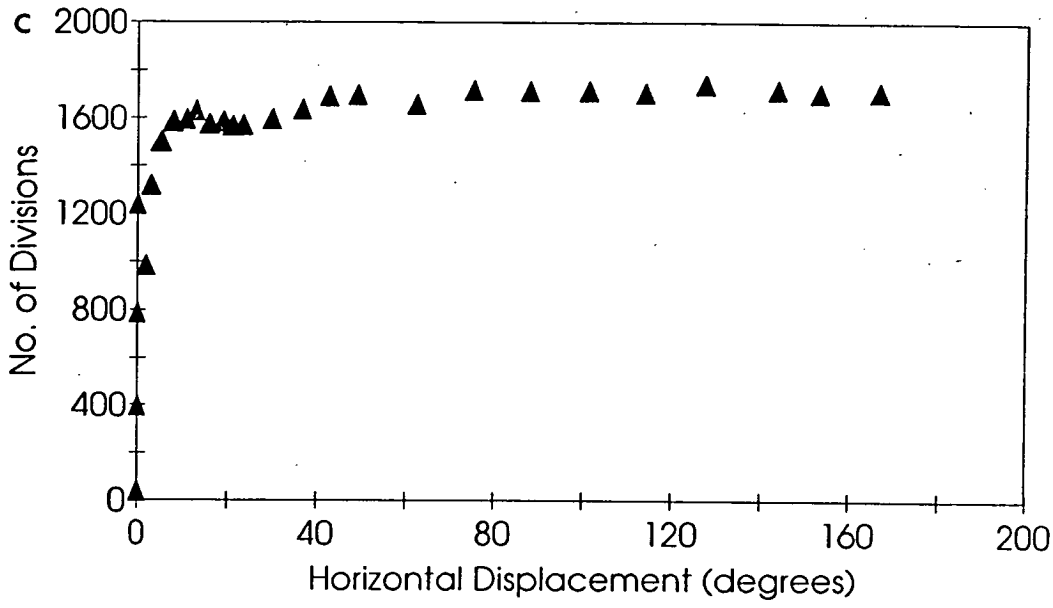

Figure 5.6 cont: Graph of shear load against angular displacement for the till sample at a displacement rate of 5×10^{-5} ms^{-1} for an effective pressure of: **(c)** 400 kPa.

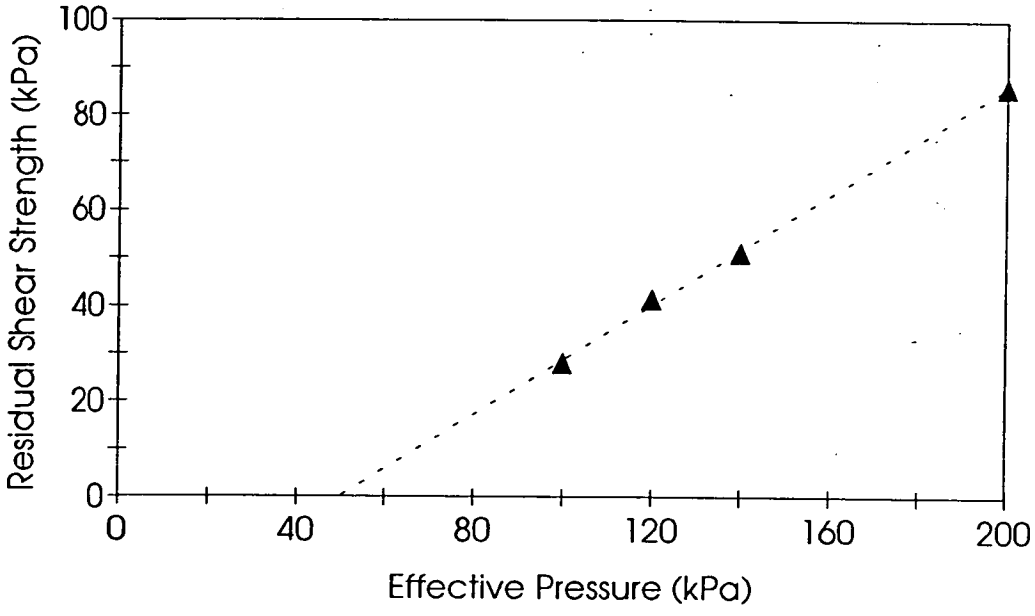

Figure 5.7: Graph of residual shear strength in the till against effective pressure for a displacement rate of 5×10^{-8} ms^{-1}. The residual shear envelope is outlined.

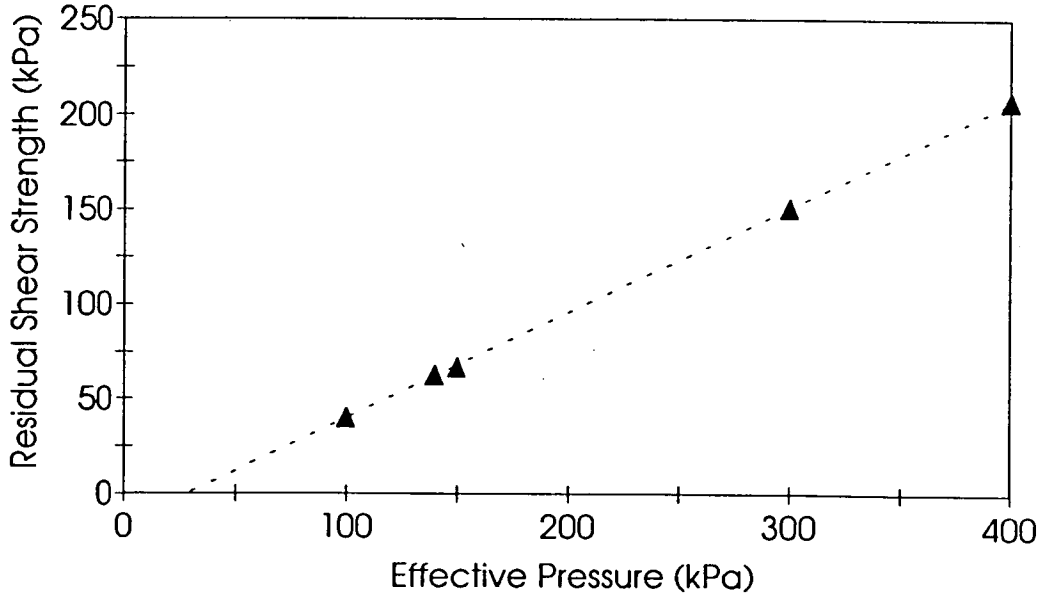

Figure 5.8: Graph of residual shear strength in the till against effective pressure for a displacement rate of 5×10^{-7} ms^{-1}. The residual shear envelope is outlined.

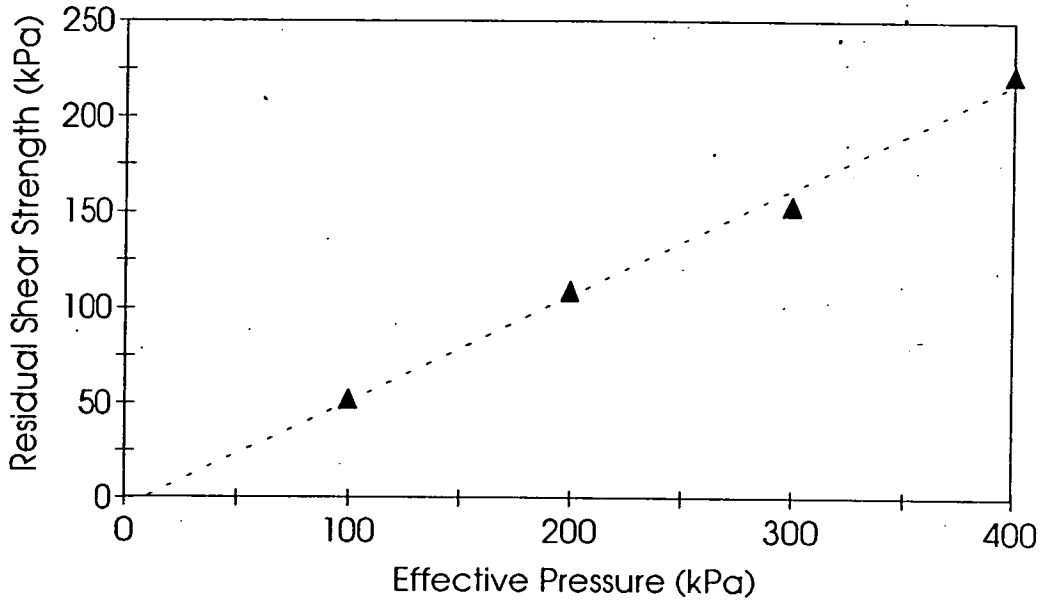

Figure 5.9: Graph of residual shear strength in the till against effective pressure for a displacement rate of 5×10^{-6} ms^{-1}. The residual shear envelope is outlined.

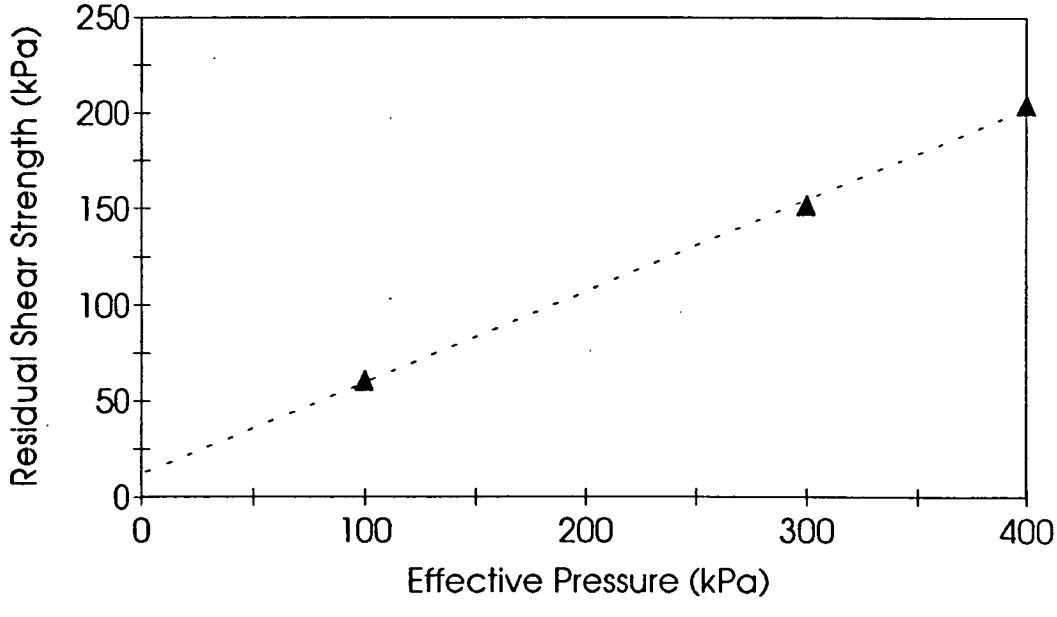

Figure 5.10: Graph of residual shear strength in the till against effective pressure for a displacement rate of 5×10^{-5} ms^{-1}. The residual shear envelope is outlined.

Table 5.2: Values of strain rate, effective pressure and residual shear strength from which the flow law for the Dutch till is determined.

Gear Ratio	Displacement Rate (ms^{-1})	Strain Rate (y^{-1})	Effective Pressure (kPa)	Residual Shear Strength (kPa)
1000:1	4.7×10^{-8}	150	100	28.1
1000:1	4.7×10^{-8}	150	120	41.5
1000:1	4.7×10^{-8}	150	140	51.2
1000:1	4.7×10^{-8}	150	200	86.0
100:1	4.7×10^{-7}	1500	100	40.3
100:1	4.7×10^{-7}	1500	140	62.8
100:1	4.7×10^{-7}	1500	150	66.9
100:1	4.7×10^{-7}	1500	300	151.1
100:1	4.7×10^{-7}	1500	400	207.3
10:1	4.7×10^{-6}	15000	100	52.2
10:1	4.7×10^{-6}	15000	200	109.0
10:1	4.7×10^{-6}	15000	300	153.6
10:1	4.7×10^{-6}	15000	400	222.5

Discussion: the ring shear tests are very time consuming. The initial test was carried out at a gear ratio of 1000:1 corresponding to a displacement rate of 0.18mm per hour. As a result, the tests carried out at this speed, although continued until a constant shear load was attained (approximately 4 - 5 days), may not have been left long enough to achieve the true residual state. However, in sediments in which turbulent shear is the dominant shearing mechanism, the residual state is generally reached at small shear displacements (Lupini, 1980) and so the shear strength determined may well reflect the residual value. The angle of friction for the steady state achieved was found to be 29.7°.

The tests carried out at gear ratios of 100:1 and 10:1 were allowed to run for displacements of greater than 100° and the residual angle of friction obtained was 29.2° in both cases. This is not too dissimilar to the value of 29.7° obtained in the slow test and thus it was assumed that the slow test did reflect residual conditions.

The tests carried out at a gear ratio of 1:1 gave a much lower friction angle of 24.7°. This is thought to be due to the development of excess pore water pressures which are unable to dissipate at such a fast displacement rate. The effect of this excess pore water pressure would be to mask the true values of the effective pressure and thus of the residual strength. The results of the fast test were therefore not included in the following flow law determination.

The cohesion values obtained from the residual shear envelopes in the ring shear tests vary with the rate of shearing and are found to be negative for the slow tests. This feature has been noted by other researchers of till properties (M. Paul, pers. comm.). Nevertheless the gradient of the residual shear envelope, and thus the angle of internal friction, is very similar in each case and thus the tests are assumed to be comparable and cohesion is ignored.

Conclusions: the above experiments yielded corresponding values of x, τ and p', (table 5.2), from which a flow law for the Dutch till could be determined.

5.5 Determination of a Flow Law for the Dutch Till

The above experiments allow the determination of residual strength and corresponding values of effective pressure and displacement rate along the shear zone. The results are therefore better suited to a flow law determination than those of Boulton and Hindmarsh (1987) or Kamb (1991).

To allow comparison with the existing flow laws, the shear displacement rates measured in the ring shear tests were converted into shear strain rate values. Shear strain is defined as the deformation caused by a shear stress, as illustrated in figure 5.11. The shear strain is given by

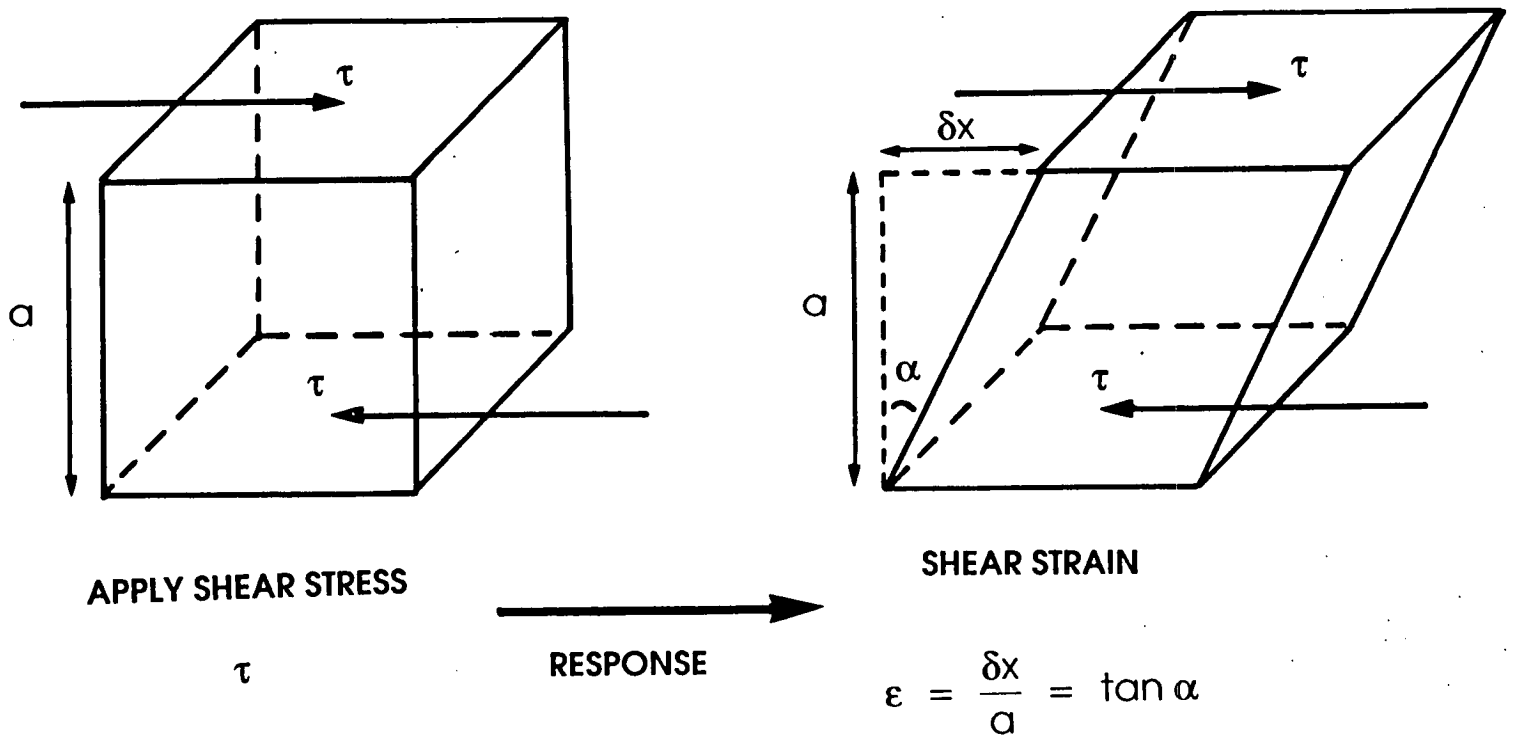

Figure 5.11: The definition of shear strain as a response to an applied shear stress.

$$\varepsilon = \frac{\delta x}{a} \qquad 5.4$$

where ε is the average shear strain,

δx is the horizontal displacement along the shear surface

a is the sample height.

The shear strain rate ($\dot{\varepsilon}$) is therefore;

$$\dot{\varepsilon} = \frac{d\varepsilon}{dt} \qquad 5.5$$

where t is time.

Strain rate values calculated for the various gear ratios on the ring shear apparatus used above are presented in table 5.2.

The resulting shear strain rates and their corresponding shear stress and effective pressure values, presented in table 5.2, were then analysed using a standard multiple regression package, resulting in the following relationship;

$$\log \tau = -0.955 + 0.073 \log \dot{\varepsilon} + 1.164 \log p' \qquad 5.6$$

where τ and p' are in kPa and $\dot{\varepsilon}$ in y^{-1}.

Rearranging this to obtain a flow law in the form of equation 5.1 gives;

$$\dot{\varepsilon} = 10^{13.1}\left(\frac{\tau^{13.7}}{p'^{15.9}}\right) \qquad 5.7$$

This is very different to the weakly non-linear rheology found by Boulton and Hindmarsh (1987) and adopted by most authors (e.g. Alley *et al.*, 1987b; Lingle and Brown, 1987; Alley, 1989b; Alley *et al.*, 1989; MacAyeal, 1989). The larger values of the exponents n and m indicate that the system is more sensitively dependent on shear stress and effective pressure than previously thought. It is however not as extreme as the nonlinearity suggested by Kamb (1991).

5.6 Comparison of Flow Laws

The flow laws of Boulton and Hindmarsh (1987) and Kamb (1991) can be compared with the flow law determined for the Dutch till by plotting effective pressure against shear stress for each law (figure 5.12), bearing in mind the lack of a constant in Kamb's law. This graph illustrates the sensitivity of the various systems. The introduction of a constant to Kamb's Law would mean that the gradients of the effective pressure/shear stress curves, at constant shear strain rates, would remain the same but their relative position in effective pressure/shear stress space would change.

The differences between the flow laws is also illustrated by plotting shear strain rate against depth in a sediment column (figure 5.13), where the effective pressure at the top of the bed is 50kPa and the basal shear stress is 10kPa. Boulton and Hindmarsh's (1987) flow law results in strain rates which decrease with depth, but not as rapidly as the flow law for the Dutch till, whereas Kamb's (1991) law, plotted at the same scale, predicts that the strain rate under these conditions is negligible.

The differences between the flow laws could be due to differences in grain size distribution of the materials considered. Boulton and Hindmarsh (1987) comment that their flow law is applicable to materials of similar granulometry, whilst Alley *et al.* (1987a) note that the rheological properties of till probably vary with grain size. The dependence of the flow law on grain size distribution is discussed in more detail in the following section.

5.7 Dependence of the Flow Law on Grain Size

The variations in the above three flow laws could be a result of the differences in grain size distribution between the three materials considered. The Boulton and Hindmarsh (1987) law was determined by observations on till from Breidamerkurjökull which has a clay sized particle component of around 10% (Boulton and Paul, 1976). Kamb's (1991) flow law is based on clay rich soils, for example London Clay, which has a clay sized fraction of around 50% (Lupini, 1980). The Drenthe Till has a clay content of around 25% (this thesis figure A.1). The clay fraction varies considerably between each sediment and therefore may be a significant factor in the final expression of the flow law.

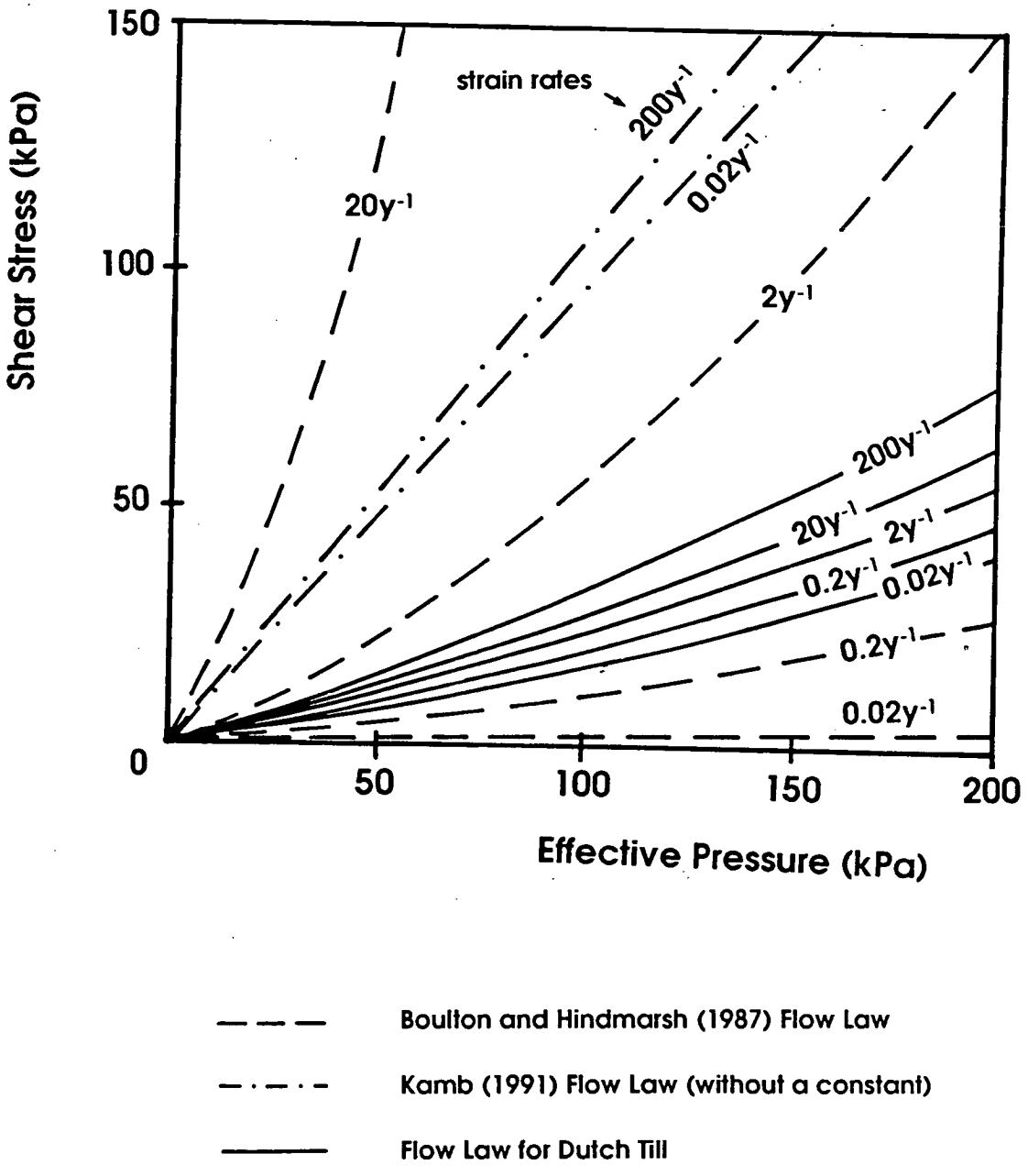

Figure 5.12: Comparison of the three flow laws; a plot of shear stress against effective pressure for different strain rates for each law.

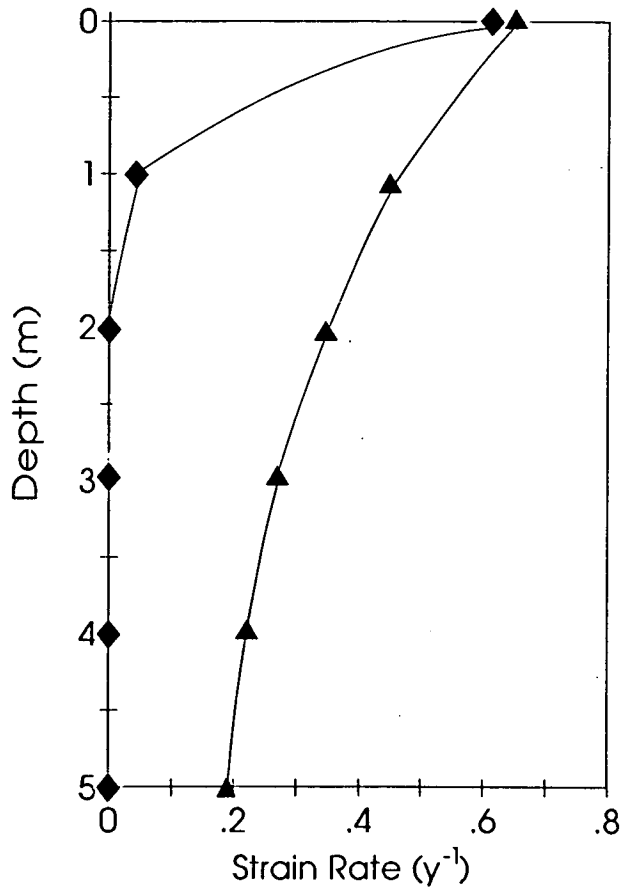

▲ **Boulton and Hindmarsh (1987) Flow Law**

◆ **Flow Law for Dutch Till**

Kamb's (1991) Flow Law results in very small strain rates under these conditions and thus plots on the y axis of the graph.

Figure 5.13: Comparison of the three flow laws; a plot of shear strain rate against depth in a subglacial till bed. The effective pressure at the top of the layer is assumed to be 50kPa, the basal shear stress, constant with depth, assumed to be 10kPa and the effective pressure gradient in the till 10kPam^{-1}.

5.7.1 Dependence of Shearing Mechanism on Grain Size Distribution

Lupini (1980) carried out experiments to determine the relationship between the residual shearing mechanism and the clay content of sediments using samples with known proportions of sand and clay. He identified three basic mechanisms of residual shear; turbulent, sliding and transitional which are illustrated in figure 5.14. The mode of shear was found to depend on the proportion of massive, non-platey minerals to platey, low frictional minerals.

5.7.1.i Turbulent Shearing Mechanism

Sediments exhibit turbulent shear behaviour when the proportion of massive, non-platey particles is dominant. These sediments typically have relatively high residual shear strength. If a shear zone forms it will exist as an area of different porosity.

5.7.1.ii Sliding Shear Mechanism

A sliding shear mechanism occurs when the platey, low friction mineral content is sufficiently high that a shear surface consisting of strongly orientated clay particles develops (figure 5.14c). The residual shear strength in this case varies depending on the clay mineralogy and the pore water chemistry (Kenney, 1977).

5.7.1.iii Transitional Shearing Mechanism

When there is no dominant particle shape, a thick shear zone forms which contains discontinuous sliding surfaces and pockets of sediment behaving in a turbulent fashion (figure 5.14b). The residual strength in this case varies sensitively with the grain size distribution of the sediment.

5.7.2 Dependence of Shearing Mechanism on Clay Mineralogy

Figure 5.15 summarises the relationship between the clay size fraction of a sediment and its residual friction angle (after Skempton, 1985). Skempton (1985) states that clay minerals have very little effect on the residual strength of a sediment when its clay fraction is less than 20% as its strength is controlled by the sand and silt particles. Conversely, if the clay fraction exceeds 50%, the residual strength depends almost entirely on sliding friction between the clay particles and thus on their character.

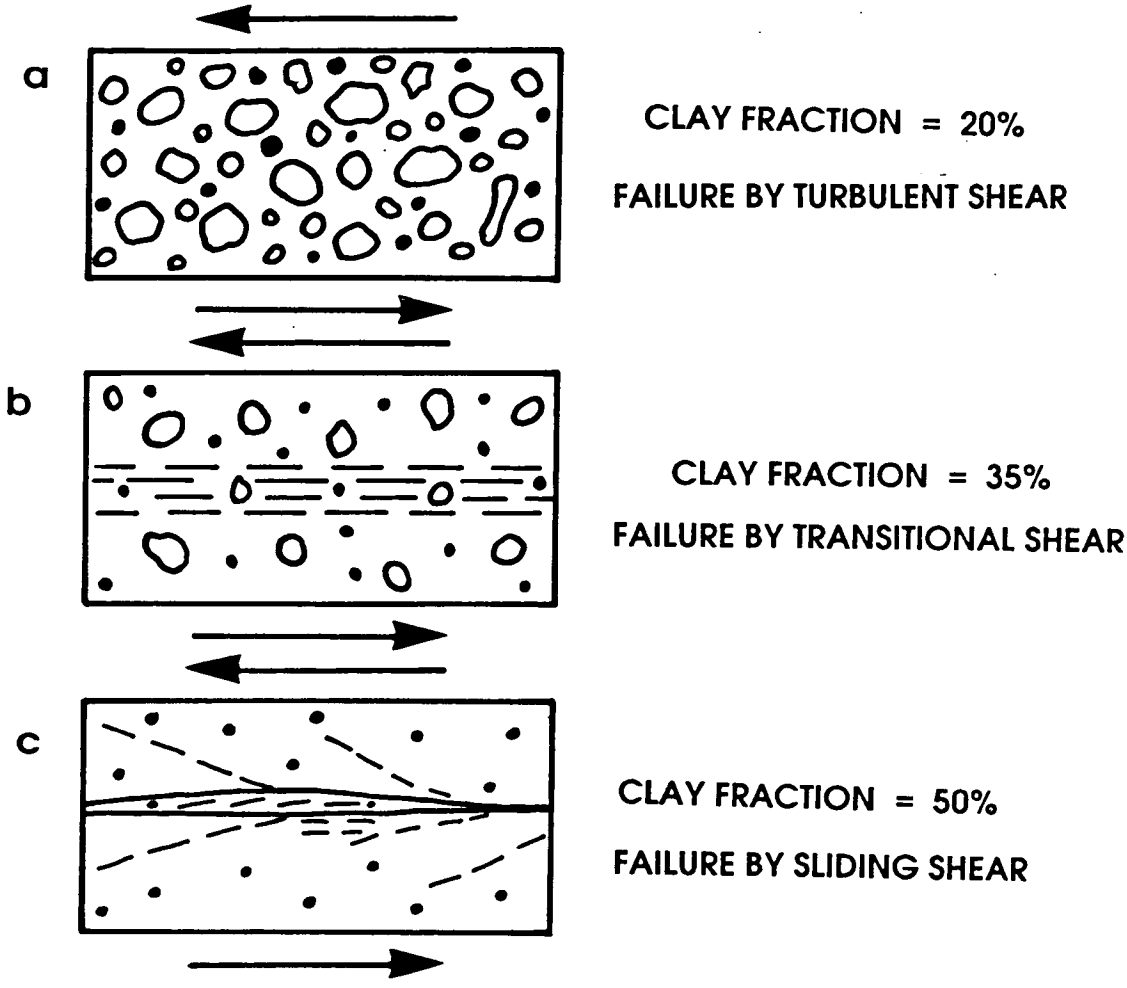

Figure 5.14: Post-failure structures found in thin sections of till/clay mixtures; (a) is a sample with a 20% clay fraction in which no shear zone or preferred orientation of clay particles is found; (b) is a sample with a clay fraction of 35% in which a shear zone about 1.5mm thick containing discontinuous shear surfaces parallel to the direction of shear is found and (c) is a sample with a clay fraction of 50% in which separation occurred along a polished shear surface, with clay particles oriented to the direction of shear (modified from Lupini, Skinner and Vaughn (1981).

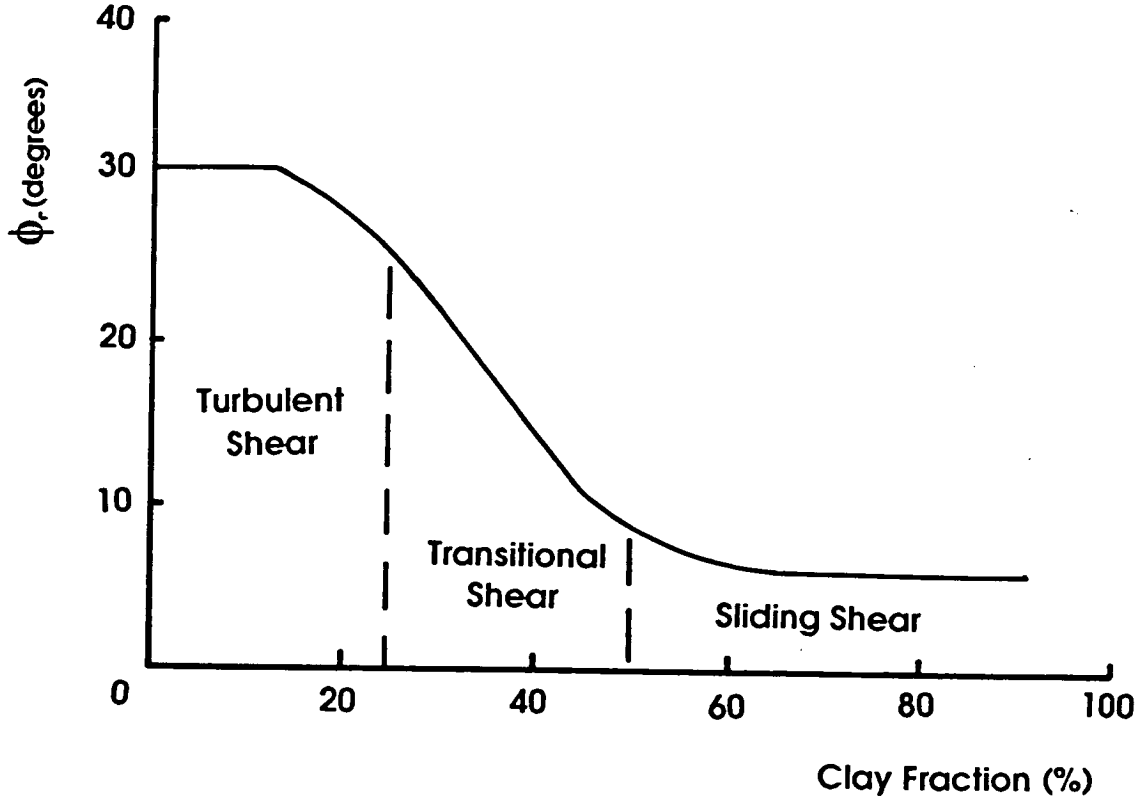

Figure 5.15: A graph showing the relationship between the clay fraction of a sediment and its residual angle of friction. The sediment considered is a mixture of sand and bentonite (modified from Skempton, 1985).

5.7.3 Relationship between Residual Shear Strength and Shear Strain Rate

Lupini (1980) also suggests that sediments which exhibit the sliding mode of shear show a slight increase in residual strength with shear strain rate whereas a till which shears in a turbulent manner tends to decrease in residual strength with increasing shear strain rate.

5.7.4 Conclusions

The above observations suggest that the mechanism of shear failure in a sediment and its response to strain rate variations are dependent on the proportion of clay sized particles in the sediment. Thus the nature of the flow law for a sediment will depend on the clay fraction, implying that Kamb's (1991) flow law cannot be applied to tills in general.

The Boulton and Hindmarsh (1987) law was determined from field observations and thus the sediment included boulders, whereas the flow law established in this study was determined in the laboratory on a sample from which all the large clasts had been removed. This could also be a significant factor in the differences between the flow laws.

5.7.5 Implications of Grain Size Distribution

If the three flow laws discussed above are considered with respect to their clay fractions, it is found that an increasing proportion of clay sized particles corresponds to an increase in the exponents of the effective pressure and shear stress parameters of the flow law. Hence an increasing proportion of clay in the sediment should correspond to a decrease in the range of effective pressures over which the system is stable.

5.8 Implications of the Flow Laws for Stable Sediment Deformation

The results of Boulton and Hindmarsh (1987) imply that if ice sheet velocity is determined by subglacial sediment deformation then stable deformation (velocities of 1 - 100 my^{-1}) can occur under a wide range of effective pressures for a constant basal shear stress. Kamb's (1991) results however, suggest that stable deformation can only occur under an extremely narrow range of effective pressures. If the effective pressure drops below a critical value, an infinite strain rate ensues, resulting

in instability. The flow law determined in this study suggests that stable deformation can occur but in a narrower range of effective pressures than proposed by Boulton and Hindmarsh (1987). Figure 5.12 illustrates the range of basal effective pressures and shear stresses over which stable sediment deformation can occur.

5.8.1 Factors Influencing Stability

The capacity of subglacial sediments to drain all the water supplied to the bed is limited by the permeability of the sediment and the length of the flow path (i.e. the transmissibility of the sediment). If the transmissibility of the sediment is high compared to the amount of meltwater then the basal water pressure will be low and the effective pressure high, in which case the shear strength of the sediment will be high and therefore sediment deformation likely to be negligible.

Previous analyses, however, have shown that the transmissibility of a subglacial aquifer may not always be sufficient to allow all the meltwater to escape (e.g. Boulton and Hindmarsh, 1987; Alley, 1989a). Water pressure will therefore build up at the ice/bed interface until it exceeds the ice pressure at which point the system will become unstable. Hence to maintain stability, for an ice sheet flowing over a sediment of given grain size, there must be some mechanism whereby the effective pressure will be contained within the range of values that permit stable deformation for that grain size.

Boulton and Hindmarsh (1987) suggest two possible responses to an effective pressure perturbation. Either (i) there is a negative feedback mechanism which will inhibit instability by maintaining the effective pressure within the narrow stable band, or return it to that band; for example drainage along the ice/bed interface, or (ii) there is an automatic instability, for example a surge mechanism.

On the other hand
Kamb (1991) suggests that there will be a positive feedback which results in the deforming bed being unstable, and thus that the deforming bed mechanism cannot account for ice stream motion at the present day.

5.9 The Boulton and Hindmarsh Model

Boulton and Hindmarsh (1987) develop a one dimensional drainage model and establish the conditions under which steady state deformation of subglacial sediments can occur. They also consider the time-dependent response of

subglacial deformation to changing external conditions and conclude that although the nature of subglacial deformation and the deformation velocity of an ice sheet can be very sensitive to small changes in glacier stress, basal melt rates or subglacial aquifer pressure, there are important negative feedbacks which control the system allowing it to remain in a relatively stable state. In such a state, sediment deformation is maintained at the level required to sustain the basal velocity necessary to discharge the flux of ice through the glacier system. They suggest that stability is achieved by the formation of subglacial channels.

Boulton and Hindmarsh (1987) show that when effective pressure in subglacial sediment tends towards zero, the frictional resistance to glacier flow is reduced and high basal velocities ensue. Basal shear stress decreases and thus the water flux due to shear heating decreases. The effective pressure therefore increases, reducing the amount of sediment deformation, causing the ice sheet to decelerate. Meanwhile a reduction in deformation means that the ice sheet can no longer discharge the required amount of ice with the shear stress available. The ice sheet therefore thickens, increasing the surface slope which in turn increases the basal shear stress. This results in increased melting due to friction thus increasing deformation of the bed as the system tends towards its original state. A large ice sheet may absorb such adjustments and remain in an equilibrium state whereas much smaller systems may be unable to equilibrate quickly enough and the increased acceleration could generate a catastrophic flow event, i.e. a surge.

5.9.1 Formation of Subglacial Tunnels

As water pressure in the subglacial sediments increases, the effective pressure decreases, decreasing the strength of the sediment which may liquefy and flow towards the terminus, forming subglacial pipes. These act as drainage conduits allowing any excess meltwater to dissipate thus reducing the basal water pressure, allowing the ice sheet to regain a stable state and for sediment deformation to occur.

Whilst Boulton and Hindmarsh (1987) conclude that stability is achieved by the formation of subglacial channels which permit the drainage of excess meltwater and control the magnitude of the effective pressure allowing sediment deformation to occur, Shoemaker (1986) suggests that channels will develop which will drain the sediment to such an extent that will prevent deformation occurring altogether.

5.9.2 The Surge Mechanism

A number of theories have been proposed for the sudden rapid advance of ice sheets. Paterson (1981) considers various possible mechanisms for an ice sheet resting on a hard bed. In the soft bed case, an increase in water pressure in the sediment at the base of the ice decreases the effective pressure acting on that sediment. This increases the strain rate (from equation 5.1) and thus increases the ice sheet velocity, which may be of sufficient magnitude to cause a surge. During the quiescent period following the surge, the ice sheet regains an equilibrium profile, decreasing its surface slope and basal shear stress, which in turn decreases the strain rate and velocity of flow. The water pressure builds up again and the process is repeated. This is thus an example of a cyclical instability.

A surge may also occur if there is a barrier to channel flow. If for example the sediment becomes impermeable down glacier or there is an area of frozen sediment, the water pressure will increase and a major instability may develop. Such an instability cannot be relieved by tunnel formation and thus meltwater may pond behind the barrier until it fails resulting in a catastrophic outburst such as a jokulhlaup and/or a surge (e.g. Schytt, 1969; Nye, 1976).

5.10 Kamb's Model

The highly non-linear flow law proposed by Kamb (1991) (equation 5.3) assumes that meltwater gathering at the ice/bed interface of Ice Stream B in Antarctica drains through a system comprising a discontinuous, interconnected water layer of varying spatial thickness, in a gap between the base of the ice and the top of the till. Water can thus be transported out of the system.

This flow law predicts that the reciprocal dependence of flow on effective pressure, itself directly related to the non-linear shear stress dependence, will couple the flow sensitively to the basal water pressure. Kamb considers a positive feedback mechanism and shows that above a certain degree of non-linearity in the flow law, the deforming bed mechanism for ice stream motion is unstable.

As the pore water pressure in the sediment increases, the effective pressure decreases, increasing the strain rate and thus the till deformation rate. This results in an increase in the basal melt rate due to shear heating, and a further increase in the

basal water pressure, setting up a positive feedback loop which can induce instability depending on the rheology of the subglacial sediment.

Kamb proposes that the critical value of n in equation 5.3, above which instability occurs, is likely to be in the range 5 - 20. Hence if the till rheology controls the rate of ice sheet motion through the deforming bed mechanism, the system will be unstable if the till behaves mechanically like a clay rich soil at its residual strength (i.e. with n = 100).

Kamb concludes that the motion of ice stream B is not presently being controlled by till rheology as this would not provide the stabilisation required for sediment deformation and thus that some other mechanism must control the ice stream motion. However as discussed earlier, this law may only be valid for a clay rich till.

5.11 Ice Sheet Motion in the Northern Netherlands

In the northern Netherlands, an example of the one dimensional drainage system, the ice sheet flowed over unlithified till which under certain conditions could have deformed and contributed to the forward motion of the ice sheet.

If it is assumed that ice sheet velocity is dominated by the pervasive deformation of its bed, as suggested by the observations of Boulton and Jones, 1979 (also Boulton and Hindmarsh, 1987; Engelhardt *et al.*, 1978), the ice sheet velocity should reflect that of the basal till. The velocity/depth profile in the till and thickness of the deforming layer are important in determining ice and till fluxes, and may be used in some cases to constrain the flow law for till (Alley, 1989b).

Using the flow law established for the Dutch till (equation 5.7), and substituting values for effective pressure and basal shear stress calculated from information obtained in the one dimensional consolidation tests (chapter 4), gives the range of shear strain rates likely to have been encountered during the advance of the Saalian ice sheet. Integrating these strain rates over the thickness of the deforming layer gives values of till velocity at the base of the ice, thus allowing estimates of ice sheet velocity to be made.

5.11.1 Determination of Shear Strain Rate

The consolidation experiments on clay from Noord Bergum yield an effective pressure at the base of the ice of 150kPa and a basal shear stress of 15kPa. Substituting these values into the flow law for Dutch till (equation 5.7) gives a shear strain rate of the order of 10^{-6} y^{-1} in the till at the top of the deforming layer.

The value of effective pressure obtained from the consolidation tests is the maximum effective pressure to which the sediments were subjected. It is assumed to occur at the maximum extent of the ice sheet, when the ice was in a steady state. However, sediment deformation will presumably have occurred when the ice sheet was moving and not in the steady state. Excess pore water pressures resulting from the ice advance would not therefore have time to dissipate and thus the effective pressure acting on the sediments would be less than the maximum. For this reason, a range of effective pressure values of 50, 100, 150 and 200 kPa and a range of basal shear stresses of 10, 15, 20, 50 and 100 kPa are considered in the model.

These values, when substituted into equation 5.7, result in the strain rates presented in table 5.3. A wide range of possible strain rates is obtained reflecting the sensitivity of the flow law. At smaller effective pressures, the sediment is weaker and thus more easily deformed. Hence small effective pressures and large basal shear stresses result in very large strain rates. At higher effective pressures, sediments are stronger and consequently larger basal shear stresses are required before deformation occurs. Thus large effective pressures and small basal shear stresses result in very small strain rates.

5.11.2 Distribution of Strain Rate with Depth

Vertical profiles of strain rate can be determined, assuming the vertical effective pressure gradient in the till is 10 $kPam^{-1}$ and shear stress is constant with depth, by substituting into the flow law relevant values of effective pressure at varying depths in the deforming layer. Examples of the resulting profiles are given in figure 5.16 and the full data set in appendix D. Figure 5.16 shows plots of strain rate against depth for three different effective pressures at a constant basal shear stress (5.16a), and three different shear stresses at constant effective pressure (5.16b). In each case strain rate is found to be greatest at the surface of the till and to decrease rapidly with depth.

Table 5.3: Strain rates obtained from the flow law determined for the Dutch till for the model values of strain rate and effective pressure.

τ (kPa)	p' (kPa)	$\dot{\varepsilon}$ (y^{-1})	τ (kPa)	p' (kPa)	$\dot{\varepsilon}$ (y^{-1})	τ (kPa)	p' (kPa)	$\dot{\varepsilon}$ (y^{-1})
10	50	0.61	15	50	158.20	20	50	8144.39
10	100	1E-05	15	100	0.0025	20	100	0.13
10	150	1.59E-08	15	150	4.1E-06	20	150	0.0002
10	200	1.64E-10	15	200	4.23E-08	20	200	2.18E-06
50	50	2.3E+09	100	50	3.07E+13			
50	100	37692.9	100	100	5.02E+08			
50	150	59.76	100	150	795279			
50	200	0.62	100	200	8203.40			

Table 5.4: Till velocity at the top of the deforming layer obtained by integrating the flow law with respect to effective pressure for the model values of strain rate and effective pressure.

τ (kPa)	p' (kPa)	v (my^{-1})	τ (kPa)	p' (kPa)	v (my^{-1})	τ (kPa)	p' (kPa)	v (my^{-1})
10	50	0.21	15	50	53.04	20	50	2730.54
10	100	6.7E-06	15	100	0.0017	20	100	0.09
10	150	1.57E-08	15	150	4.07E-06	20	150	0.0002
10	200	2.12E-10	15	200	5.07E-08	20	200	2.72E-06
50	50	7.73E+08	100	50	1.03E+13			
50	100	23215.08	100	100	3.36E+08			
50	150	59.28	100	150	494132.2			
50	200	0.80	100	200	10605.84			

a

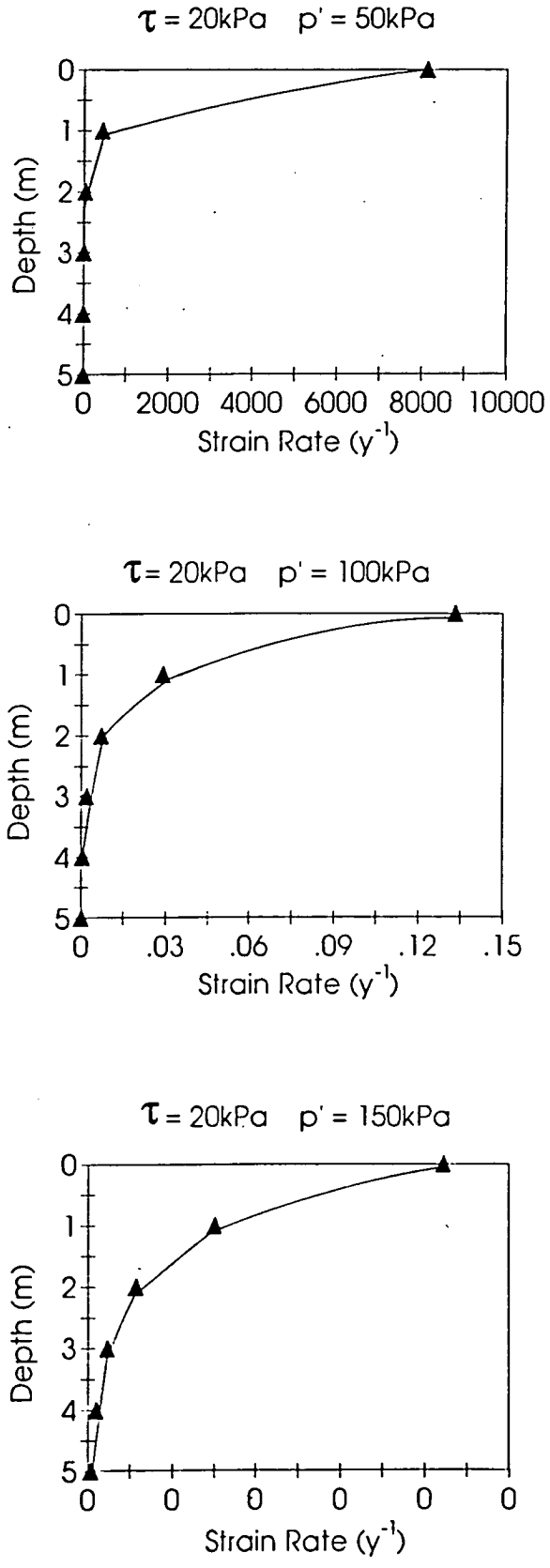

Figure 5.16 (a): The distribution of strain rate with depth in a 5m thick bed of till for a constant basal shear stress of 20kPa at effective pressures at the top of the bed of 50, 100 and 150kPa.

b

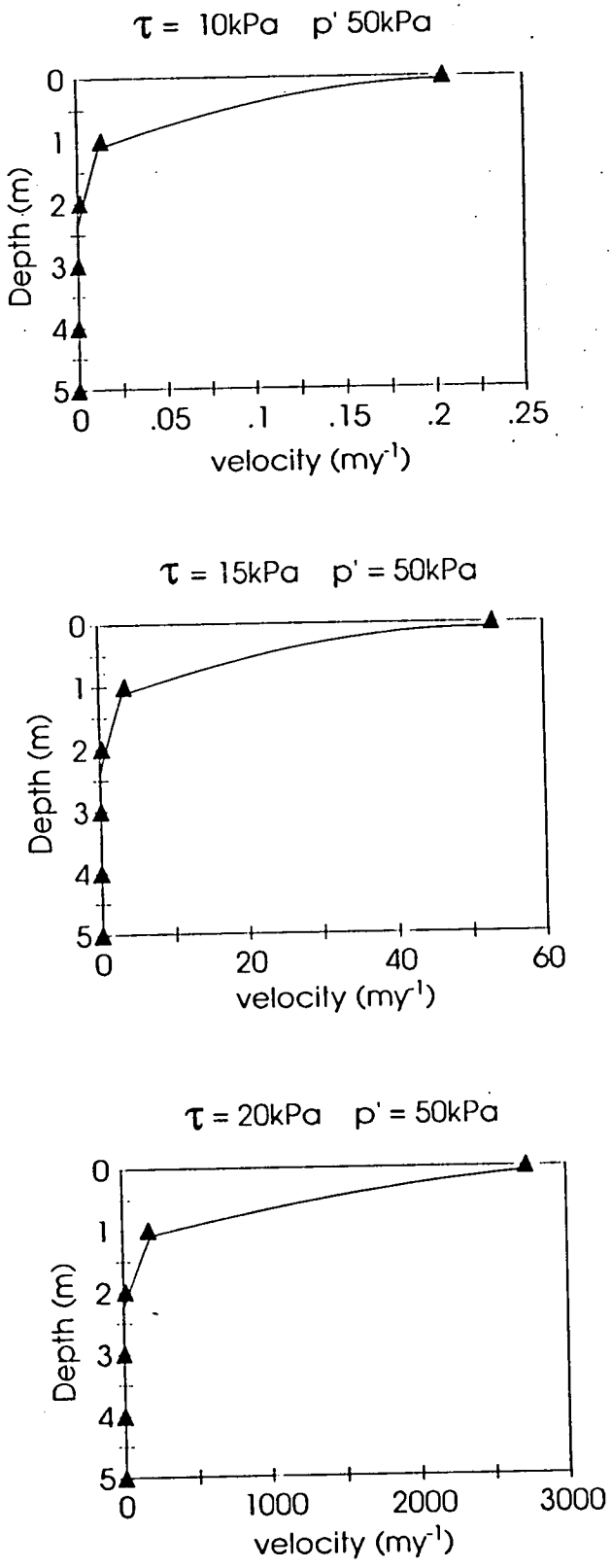

Figure 5.16 (b): The distribution of strain rate with depth in a 5m thick bed of till for a constant effective pressure at the base of the ice of 50kPa at basal shear stresses of 10, 15 and 20kPa.

At a constant basal shear stress, the strain rate at the surface of the deforming layer decreases with increasing effective pressure. For the example shown in figure 5.16 for a constant basal shear stress of 20kPa, the strain rate at the top of the till is $8000y^{-1}$ at an effective pressure of 50kPa, whereas an effective pressure of 150kPa results in a strain rate of $0.0002y^{-1}$.

For a constant effective pressure at the top of the till, strain rate increases with increasing basal shear stress. The example in figure 5.16, for a constant effective pressure of 50kPa, has a strain rate of $0.6y^{-1}$ for a basal shear stress of 10kPa, whilst a shear stress of 50kPa yields a strain rate of $8000y^{-1}$.

The wide range of shear strain rate values obtained reflects the sensitivity of the flow law.

5.11.3 Determination of Till Velocity

Till velocity can be calculated by integrating the shear strain rate over the thickness of the deforming layer if a number of assumptions are made:

(i) the effective pressure gradient in the till is 10 $kPam^{-1}$,
(ii) the deforming bed is 5m thick (equivalent to the till thickness),
(iii) shear stress is constant with depth,
(iv) the till rheology is as determined in the ring shear experiments.

Mathematically, this is given by

$$v = \int \dot{\varepsilon}\, dz \qquad 5.8$$

which can be rewritten in terms of effective pressure as

$$v = \int \left(\frac{k\,\tau^n}{p'^m}\right)\left(\frac{dz}{dp'}\right) dp' \qquad 5.9$$

Substituting the above model values into the flow law and integrating with respect to effective pressure, gives till velocities at the base of the ice presented in table 5.4. A wide range of values are obtained, again reflecting the sensitive nature of the flow

law and the narrow band of effective pressures over which stable deformation can occur.

The velocity distribution with depth in the till can also be obtained by integrating between the relevant effective pressures within the deforming bed. Examples of the resulting velocity/depth profiles are given in figure 5.17 and the full data set in appendix D. Velocity/depth profiles for three different effective pressures at a constant basal shear stress (5.17a) and for three different basal shear stresses at constant effective pressure (5.17b) are illustrated, showing that the bulk of the velocity of the till occurs at the top of the deforming bed, decreasing rapidly with depth.

As with the strain rate/depth profiles, the velocity at the top of the deforming bed is greatest for the greatest basal shear stress and lowest effective pressure. At a constant effective pressure of 50kPa, till velocity increases with increasing basal shear stress from approximately $0.2my^{-1}$ for a basal shear stress of 10kPa, to around $2800my^{-1}$ for a shear stress of 20kPa. For a constant basal shear stress of 20kPa, velocity decreases with increasing effective pressure from about $2800my^{-1}$ for an effective pressure of 50kPa to around $0.0002my^{-1}$ for an effective pressure of 150kPa. These values again reflect the sensitive nature of the flow law.

5.12 Comparison with Modern Day Examples

Alley (1991) summarises the deforming bed model stating that high ice velocities (> 100 my^{-1}) with low basal shear stresses (10 kPa) require thawed beds with high porosity and high basal water pressures almost equal to overburden pressures. If these values of ice sheet velocity and basal shear stress are taken and substituted into the flow law determined above, and the effective pressure at the base of the till assumed to be 64.8kPa (for a strain rate of $0.01y^{-1}$), an effective pressure of 33kPa is obtained. This lies within the probable values of effective pressure at the base of the ice at Noord Bergum determined from the consolidation experiments suggesting that subglacial sediment deformation is possible in this area.

There are very few direct measurements of subglacial bed deformation and thus it is difficult to compare the flow law determined above with modern day examples. However data does exist from Blue Glacier, Washington, U.S.A. (Engelhardt *et al.*, 1978), from Breidamerkurjökull, Iceland (Boulton, 1979; Boulton and Jones, 1979;

Boulton and Hindmarsh, 1987), and from Ice Stream B, Antarctica (Alley *et al.*, 1987a; Alley, 1989 a&b; Engelhardt *et al.*, 1990).

The values of shear stress and effective pressure for Breidamerkurjökull and Ice Stream B are plotted on figure 5.18, alongside the values obtained from the ring shear experiments and the calculated values for the Saalian ice sheet at Noord Bergum. The resulting graph (figure 5.18) suggests that the flow law for the Dutch till fits well with the data set for Ice Stream B, but not for Breidamerkurjökull. This may be due to the dependence of the flow law on grain size and/or the differences in experimental procedure.

Measured velocities of ice flow for these ice sheets can be compared to those calculated from the flow law. Unfortunately there are large uncertainties in the effective pressure and basal shear stress values obtained from these real examples, and, coupled with the non-linearity of the flow law, these result in a wide range of strain rates. Modern day examples of ice sheets moving on a deforming bed are thus of limited use in constraining the flow law. Nevertheless the fact that they are moving in a stable manner does illustrate the requirement of a stabilising mechanism since it is known that bed deformation occurs at these locations and in the Breidamerkurjökull and Blue Glacier cases is the dominant mechanism by which the ice sheet flows (Boulton and Jones, 1979; Engelhardt *et al.*, 1978).

5.13 Conclusions

A non-linear flow law is determined for a typical sample of Dutch till and compared to the flow laws of Boulton and Hindmarsh (1987) and Kamb (1991). The flow law for the Dutch till is more sensitive to changes in subglacial conditions than that of Boulton and Hindmarsh (1987) but less sensitive than that of Kamb (1991). It is suggested that the sensitivity of the flow law is dependent on the amount of clay in the sediment.

The flow law determines the range of conditions over which stable sediment deformation can occur. The more sensitive the flow law, the smaller the range of effective pressures over which stable deformation can occur for a constant basal shear stress. The flow law for Dutch till suggests that stable sediment deformation can occur within a relatively narrow range of effective pressures.

Strain rate and velocity profiles in the till are determined for a range of basal effective pressures and shear stresses, illustrating the sensitivity of the flow law to changes in these parameters and confirming that stable sediment deformation can only occur in a narrow range of effective pressures.

It is concluded that if ice sheet motion is governed by pervasive deformation of subglacial sediments, there must be a mechanism which constrains the effective pressure within this narrow band. This will be further discussed in the following chapter.

The effective pressure and shear stress parameters will have to be constrained even more accurately before ice sheet dynamics can be fully understood or predicted.

a

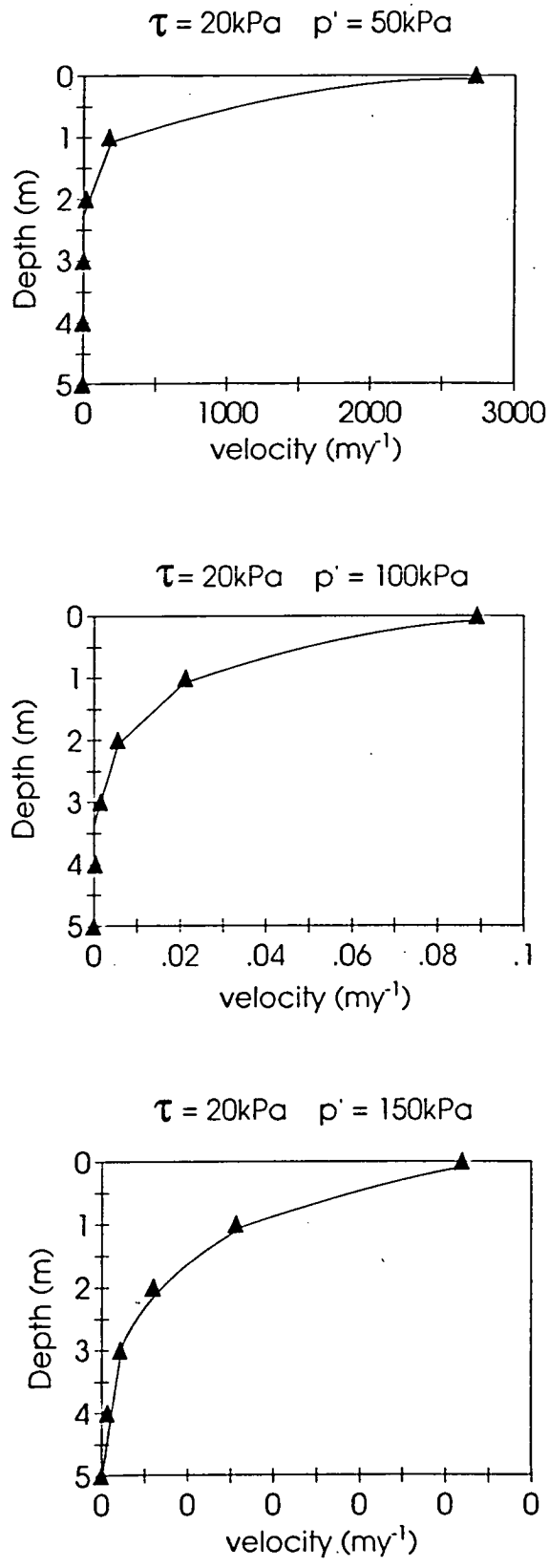

Figure 5.17 (a): The distribution of velocity with depth in a 5m thick bed of till for a constant basal shear stress of 20kPa at effective pressures at the top of the bed of 50, 100 and 150kPa.

b

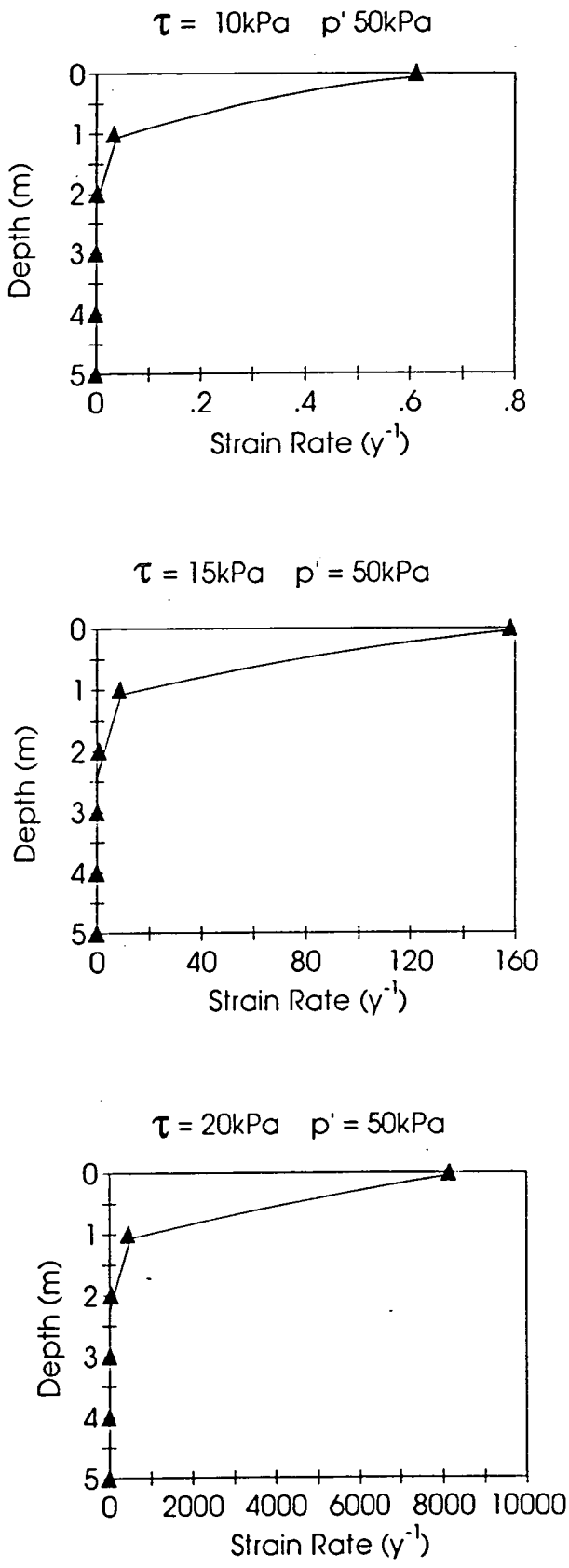

Figure 5.17 (b): The distribution of velocity with depth in a 5m thick bed of till for a constant effective pressure at the base of the ice of 50kPa at basal shear stresses of 10, 15 and 20kPa.

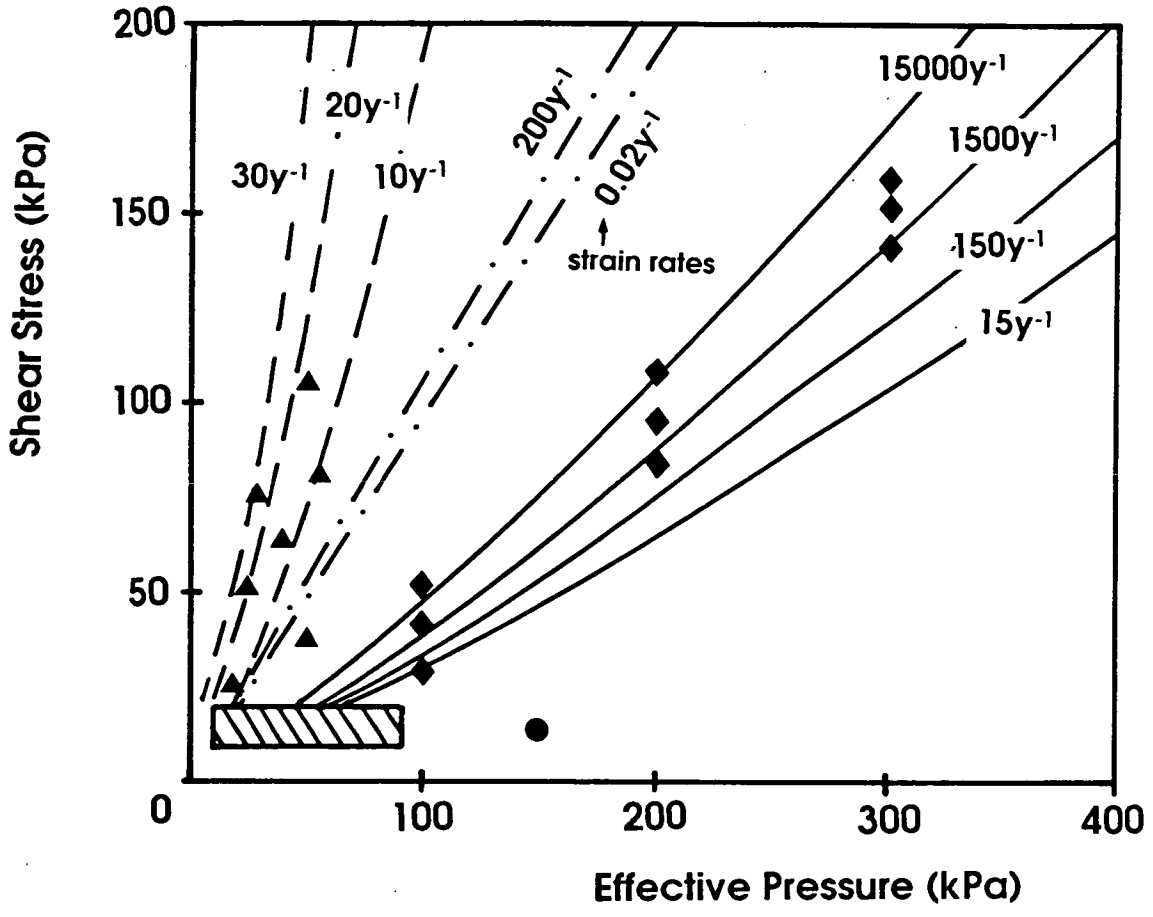

Boulton and Hindmarsh (1987) Flow Law

Boulton and Hindmarsh (1987) Data Points

Kamb (1991) Flow Law (without a constant)

Flow Law for Dutch Till

Data Points from Ring Shear Tests on Dutch Till

Basal Shear Stress/Effective Pressure Conditions for the Maximum Extent of the Saalian Ice Sheet at Noord Bergum

Range of Possible Basal Shear Stresses and Effective Pressures for Ice Stream B (Alley et al., 1987; Blankenship et al.,1987)

Figure 5.18: A comparison of the flow laws with data obtained from modern ice sheets and the ring shear experiments on a plot of shear stress against effective pressure.

CHAPTER 6

RECONSTRUCTION OF SUBGLACIAL CONDITIONS FROM ICE DYNAMICS

6.1 Introduction

The profile of the Saalian ice sheet in the Netherlands and the resulting basal shear stress are inferred from information obtained in the consolidation tests (chapter 4). The longitudinal ice sheet profile obtained is lower, and the basal shear stress therefore lower, than values typical of modern ice sheets flowing over hard beds. It is suggested that this is a result of the ice sheet flowing over unlithified sediments which deform, thus contributing to the forward motion of the ice. Ice sheet motion as a result of internal deformation of the ice body is negligible under such low shear stresses (see section 6.2 below). Sliding over unconsolidated sediments is also likely to be insignificant because such materials are typically rough compared to glacially polished bedrock (Engelhardt *et al.*, 1978; Boulton and Hindmarsh, 1987; Alley, 1989b; Alley, 1991). Thus subglacial sediment deformation will account for most of the ice velocity if basal effective pressures and shear stresses are low.

In the preceding chapter a flow law for till is determined and, from this law, a range of basal shear stresses and effective pressures over which stable sediment deformation can occur are established. Vertical profiles of strain rate and velocity in the till are obtained for sediment deforming under these conditions.

This chapter considers the inverse situation in which the ice sheet velocity is inferred by applying a standard mass balance distribution to the predicted ice sheet profile. The velocity of the deforming till is then determined by assuming that it is the dominant component of the ice sheet velocity. The theoretical effective pressure at the glacier sole and the thickness of the deforming layer are then calculated from these results.

The values of effective pressure and deforming layer thickness found are relatively constant along the ice sheet profile and it is suggested that there must be another mechanism which controls these parameters. One possible mechanism relates to control by subglacial tunnel formation. This is discussed in more detail below.

6.2 Ice Sheet Motion as a Result of Ice Deformation

There are three components which may contribute to the forward movement of an ice sheet: internal deformation of the ice (Nye, 1957), sliding at the basal boundary (Weertman, 1967; Liboutry, 1968), and deformation in any subglacial sediments (Engelhardt *et al.*, 1978; Boulton and Jones, 1979; Alley *et al.*, 1986; Boulton and Hindmarsh, 1987).

The velocity of ice is determined by the ice thickness and surface slope; according to Paterson (1981), the velocity at a depth z in an ice sheet as a result of internal deformation is given by

$$u_z = u_s - \frac{2A(\rho g \sin\alpha)^n z^{n+1}}{n+1} \qquad 6.1$$

where u_z is the horizontal velocity of ice at a depth z in the ice sheet

u_s is the horizontal velocity of ice at the glacier surface

ρ is the density of ice

g is the acceleration due to gravity

α the surface slope

A and n are ice flow law constants.

The velocity is a maximum at the surface and decreases with depth. Inserting the inferred values of shear stress and ice thickness from Noord Bergum into equation 6.1, and assuming the flow law parameters suggested by Paterson (1981) of $A = 5.2 \times 10^{-16}$ $(kPa)^{-3}s^{-1}$ and $n = 3$, results in the velocity profile in the ice shown in figure 6.1 for the ice sheet at Noord Bergum. The average velocity of the ice column at Noord Bergum can be obtained by integrating the above expression in equation 6.1 over the thickness of the ice sheet with respect to z to obtain the ice flux and then dividing by the ice thickness:

$$\bar{u} = \frac{2A(\rho g \sin\alpha)^n h^{n+1}}{(n+1)(n+2)} \qquad 6.2$$

where $\bar{u}$ is the average ice velocity

h is the ice thickness.

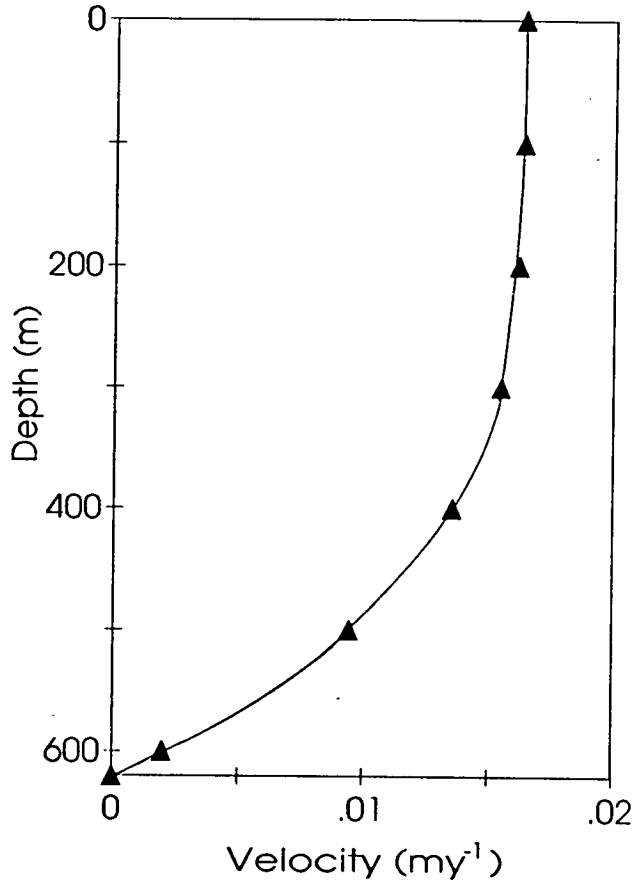

Figure 6.1: Velocity profile in an ice sheet due to internal deformation of the ice.

This results in internal flow velocities of the order of 10^{-2} my^{-1} for ice at Noord Bergum. It is therefore concluded that ice deformation does not play a significant role in ice sheet movement in this case. The dominant role must therefore be played by motion at the base of the ice sheet. It is thus possible to assume plug flow in the ice, where velocity is independent of depth.

6.3 Determination of Ice Sheet Velocity from Mass Balance Considerations

6.3.1 Dependence of Surface Profile on Mass Balance

The longitudinal ice sheet profile inferred in the northern Netherlands was assumed to be parabolic. This is expressed mathematically as (Paterson, 1981):

$$\left(\frac{h}{H}\right)^2 + \left(\frac{x}{L}\right) = 1 \qquad 6.3$$

where H is the thickness of ice at the ice divide
h the ice thickness at a point x along the profile.
L the distance from the ice divide to the terminus
x is the distance of the point x from the terminus

The resulting profile is shown in figure 6.2, where H is 1720m (the average ice sheet profile from chapter 4) and L is 1000km (the distance from the Saalian margin in the central Netherlands to the assumed ice divide over central Sweden).

The surface profile of an ice sheet is a function of the accumulation/ablation pattern. Superimposing a mass balance distribution on the predicted ice sheet profile allows the ice flux at any point along the flow line to be obtained. The resulting mass balance velocity can be calculated if plug flow in the ice is assumed.

6.3.2 Mass Balance Distribution

The net mass balance varies continuously along a flow line. It is positive in the accumulation area and negative in the ablation area. In a steady state, the mass balance at any point along the flow line must remain constant and the ice flux at this point must balance the net upstream accumulation.

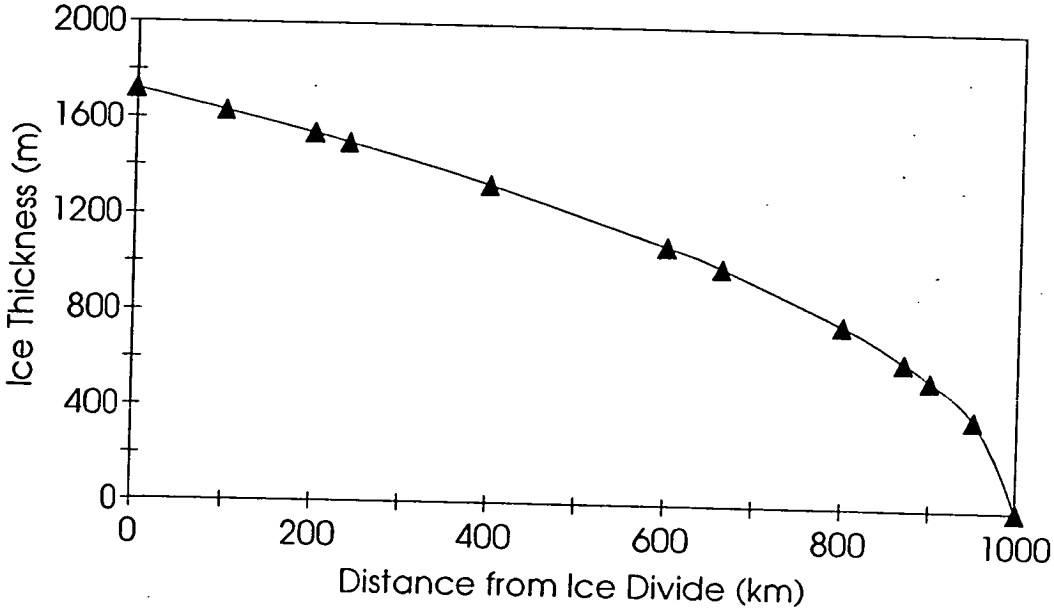

Figure 6.2: The reconstructed Saalian ice sheet profile in the northern Netherlands assuming basal melting occurs in a zone 600km from the terminus.

Table 6.1: Parameters for normalised accumulation/ablation patterns determined by Boulton *et al.* (1984).

Climate/ Parameter	1	4a	5b
Q_s	2	0.375	0.25
g_s	-0.5	0	-0.25
$a_1 = g_a$	19	8	1.5
a_2	-54	-46	1
a_3	40	80	12

The mass balance distribution depends on the climate. It is a function of latitude and the location of the ice sheet in relation to moisture sources. Boulton *et al.* (1984) construct ice sheet profiles for various accumulation/ablation patterns. In their model, surface accumulation (q) is a function of altitude. Altitude is equal to the ice thickness if the glacier bed is flat and at zero height and is thus defined as h. They plot mass balance against altitude for a large number of modern glaciers and normalise the profiles giving the results as a series of physically meaningful variables. The resulting patterns range from low gradients (effectively a cold, dry continental climate) to high gradients (a warm, wet, maritime climate). The normalised profiles Q(H) are shown in figure 6.3, and can be represented mathematically as:

$$\begin{aligned} Q &= g_a (H - H_e) && 0 \le H \le H_e \\ Q &= \sum_{r=1}^{3} a_r (H - H_e)^r && H_e \le H \le H_s \\ Q &= Q_s + g_s (H - H_s) && H_s \le H \end{aligned} \qquad 6.4$$

where H_e is the normalised equilibrium line altitude (ELA), g_a the ablation gradient, g_s the gradient of the linear portion of the accumulation curve and Q_s the value of Q at $H = H_s$ (where H_s is the normalised snow line altitude). The constants a_1, a_2 and a_3 are given by

$$\begin{aligned} a_1 &= g_a \\ a_2 &= (H_s - H_e)^{-2} \{3 Q_s - (g_s + 2g_a)(H_s - H_e)\} \\ a_3 &= -(H_s - H_e)^{-3} \{2 Q_s - (g_s + g_a)(H_s - H_e)\} \end{aligned} \qquad 6.5$$

For each accumulation/ablation pattern Q(H), g_a, g_s and Q_s are fixed. The difference H_s-H_e is estimated from a large number of glaciers and taken to be 0.25, equal to a 500m difference in altitude.

Three mass balance distributions are considered in this study. One typical of a highly maritime climate, one typical of a highly continental climate and a third of an intermediate climate. These profiles are presented in figure 6.3 and the relevant accumulation/ablation parameters listed in table 6.1. The mass balance conditions are superimposed on the ice sheet profile inferred for the northern Netherlands (figure 6.2) to obtain the mass balance distribution along the flow line. This is shown in figure 6.4.

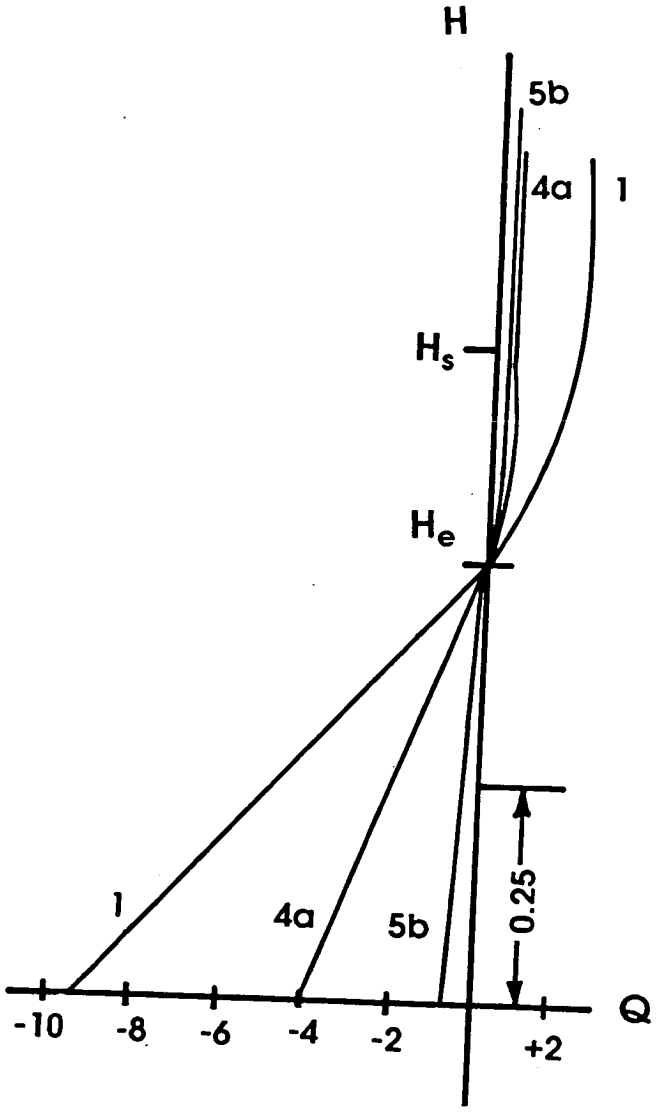

Figure 6.3: Normalised profiles of discharge against altitude for different climate patterns. Climate 1 is typical of a warm, wet maritime climate, climate 5b typical of a cold, dry polar climate and climate 4a typical of an intermediate climate.

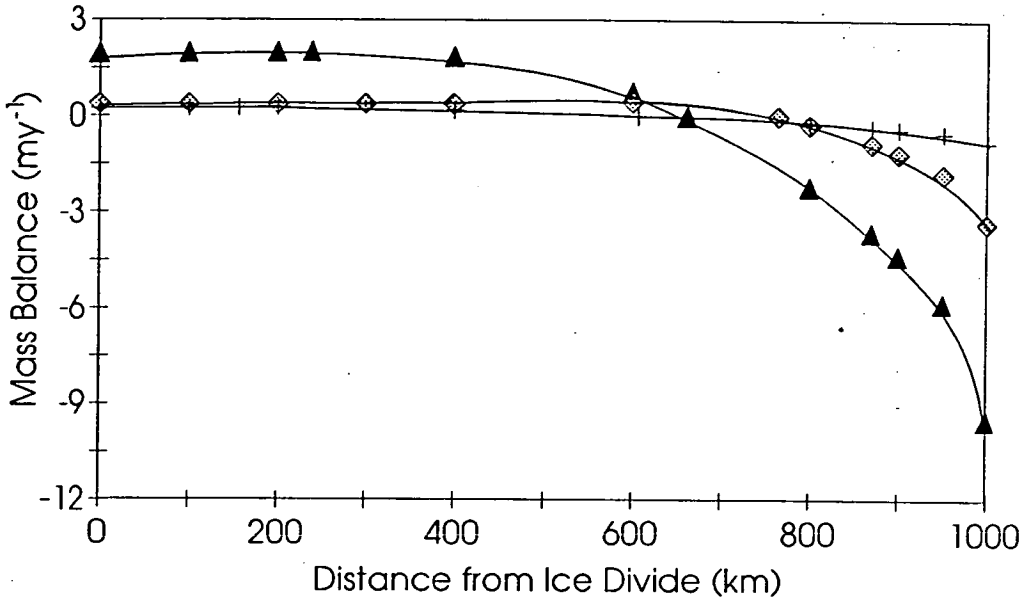

Key to Figures 6.4, 6.6 and 6.7

▲ **Climate profile 1**

◆ **Climate profile 4**

\+ **Climate profile 5**

Figure 6.4 Distribution of mass balance with distance along the flow line for each climate profile.

Table 6.2: Location and altitude of the equilibrium line and snow line for the Saalian ice sheet for the different climate patterns considered.

Climate/ Parameter	1	4a	5b
h_e	1000m	835m	1080m
x_e	662km	764km	606km
h_s	1500m	1335m	1580m
x_s	239km	398km	156km

Guiot et al. (1989) have reconstructed palaeoclimate curves for the last 140,000 years for La Grande Pile and Les Echets in eastern France using pollen stratigraphic records. This has been further refined by Seret et al. (1992) who incorporate sedimentological information into the reconstruction. They suggest that precipitation during the late Saalian was 60 - 75% less than the modern values of 1080mmy^{-1} for La Grande Pile and 800mmy^{-1} for Les Echets (Pons et al., 1992). Applying a similar factor to the modern day precipitation of the northern Netherlands suggests a glacial period precipitation of 200 - 400 mmy^{-1}. Such a precipitation is typical of areas such as southern Greenland and eastern Baffin Island today, suggesting that the mass balance distribution corresponding to the intermediate profile 4a in figure 6.3 is the most appropriate for modelling the Saalian ice sheet over the northern Netherlands.

6.3.3 Ice Flux Variation along the Flow Line

6.3.3.i Integration of Mass Balance Distribution

The net upstream accumulation b (the discharge of ice at a point x along a flow line) can be obtained by integrating the relevant mass balance distribution functions (equations 6.4) with respect to distance along the flow line;

$$b = \int_0^x Q \, dx \qquad 6.6$$

where X is a point on the flow line. This is illustrated in figure 6.5a

In the above equations Q is given as a function of H, whereas in the ice sheet profile equation h is given as a function of x. Hence to integrate Q with respect to x, it is necessary to change variables so that Q becomes a function of x. For a parabolic ice sheet the mass balance equations (6.4) become:

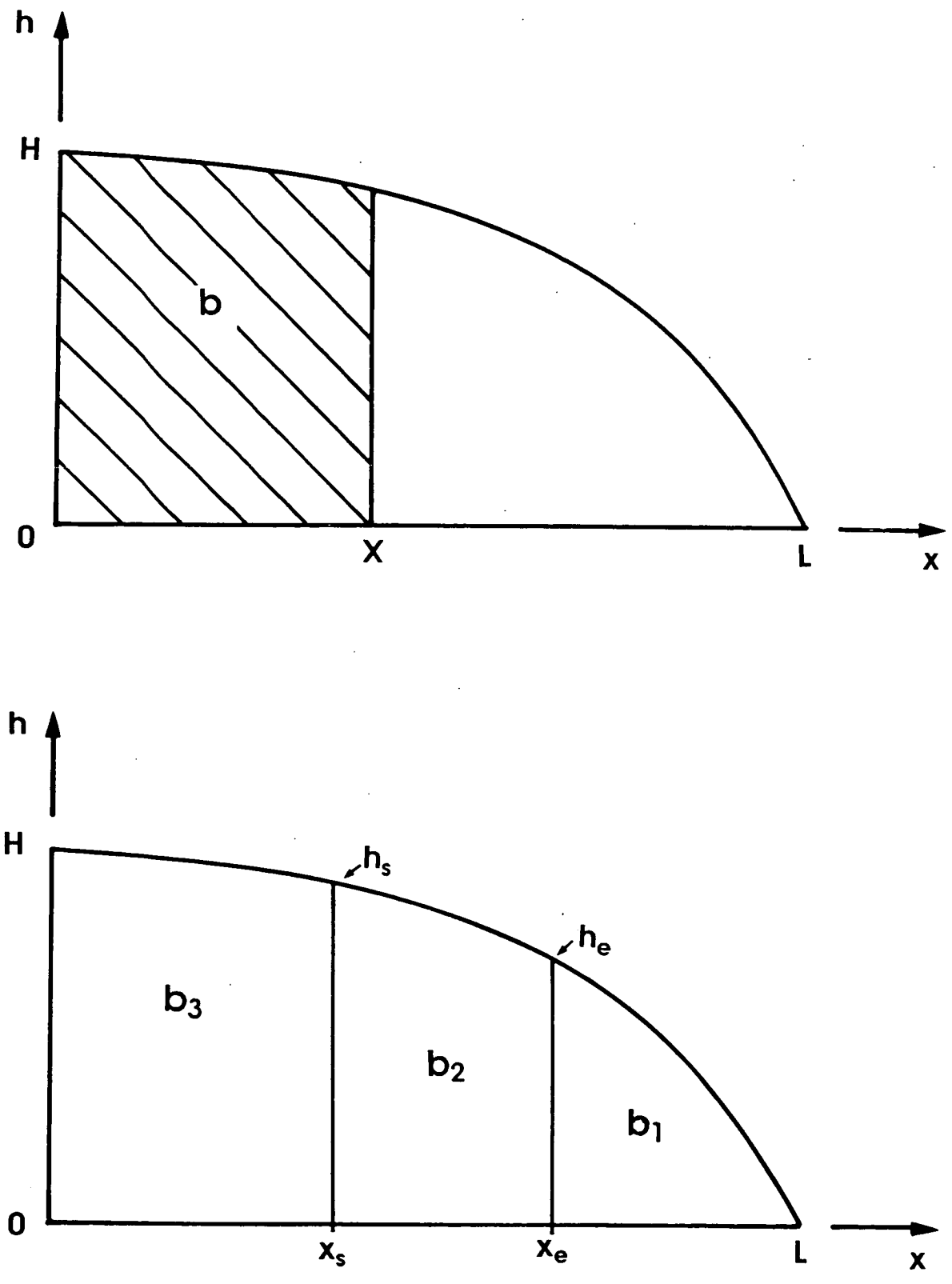

Figure 6.5: **(a)** General determination of the net upstream accumulation by integrating the mass balance function; **(b)** The three parts of an ice sheet considered in the determination of the net upstream accumulation.

$$Q = \left\{\left(\frac{H}{L^{0.5}}\right)(L-x)^{0.5} - H_e\right\} \qquad 0 \le H \le H_e$$

$$Q = \sum_{r=1}^{3} \left\{\left(\frac{H}{L^{0.5}}\right)(L-x)^{0.5} - H_e\right\}^r \qquad H_e \le H \le H_s \qquad 6.7$$

$$Q = Q_s + g_s \left\{\left(\frac{H}{L^{0.5}}\right)(L-x)^{0.5} - H_s\right\} \qquad H_s \le H$$

Integrating these (equations 6.7) with respect to distance gives the area under the mass balance curve (the net upstream accumulation). Thus for the three portions of the ice sheet illustrated in figure 6.5b, the net upstream accumulation is:

$$b_1 = -\frac{g_a L h_e^3}{3H^2} \qquad 6.8$$

for the area between the terminus and the ELA (the ablation area);

$$b_2 = \left\{\frac{2 L a_3}{3H^2}\left(h_s^5 - h_e^5\right)\right\} + \left\{\frac{L a_2 - 3 h_e L a_3}{2H^2}\left(h_s^4 - h_e^4\right)\right\}$$
$$+ \left\{\frac{6 h_e^2 L a_3 + 2 L a_1 - 4 h_e L a_2}{3H^2}\left(h_s^3 - h_e^3\right)\right\} \qquad 6.9$$
$$+ \left\{\frac{h_e^2 L a_2 - h_e L a_1 - h_e^3 L a_3}{H^2}\left(h_s^2 - h_e^2\right)\right\}$$

for the accumulation area between the ELA and the snow line;

$$b_3 = Q_s L\left(1 - \frac{h_s^2}{H^2}\right) + \left(\frac{g_s L h_s^3}{3H^2}\right) + \left(\frac{2 g_s H L}{3}\right) - g_s h_s L \qquad 6.10$$

for the accumulation area between the snow line and the ice divide.

The net upstream accumulation for the ice sheet profile inferred in the northern Netherlands, for the above three mass balance distributions, can thus be calculated

if the position of the ELA is known. Since $h_e - h_s$ is fixed, this also allows the position of the snow line to be determined.

6.3.3.ii Location of the Equilibrium Line

At the ELA, the mass balance on the ice sheet surface is zero. If the part of the mass balance curve integrated between the terminus and the ELA (b_1) is equated to the sum of the portions of the curve integrated between the ELA and the ice divide ($b_2 + b_3$), and superimposed on the ice sheet profile, using the relevant climate parameters, the position of the ELA can be determined for each climate profile. The position and altitude (ice sheet thickness) of the equilibrium line and snow line for each mass balance distribution is given in table 6.2.

Mass balance distribution 4a, the preferred solution for the Saalian ice sheet in the northern Netherlands, gives an ELA of 835m at 764km from the ice divide and a snow line altitude of 1335m at 398km from the divide. In the following discussion all three mass balance profiles are included for comparison.

6.3.3.iii Calculation of Net Upstream Accumulation

Once the position of the ELA is known, the net upstream accumulation can be calculated along the ice sheet profile by integrating the mass balance curve with respect to distance. The variation of net upstream accumulation with distance along the flow line is illustrated in figure 6.6.

6.3.4 Determination of Mass Balance Velocity

The mass balance velocity of the ice at any point is then obtained by dividing the net upstream accumulation by the thickness of ice at that point, allowing the construction of a mass balance velocity profile along the flow line (figure 6.7).

6.4 Determination of Velocity Distribution in the Till

If it is assumed, for the reasons given above (section 6.1), that the ice sheet velocity is due entirely to subglacial sediment deformation, then the ice velocity will equal the velocity of the till at the top of the deforming layer.

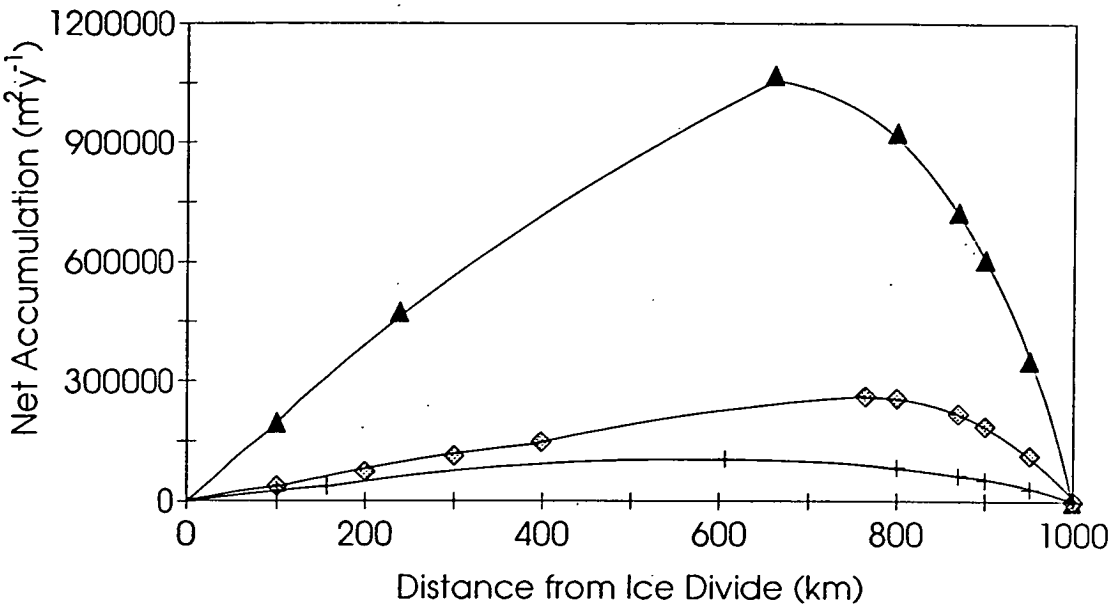

Figure 6.6: Distribution of net upstream accumulation with distance along the flow line.

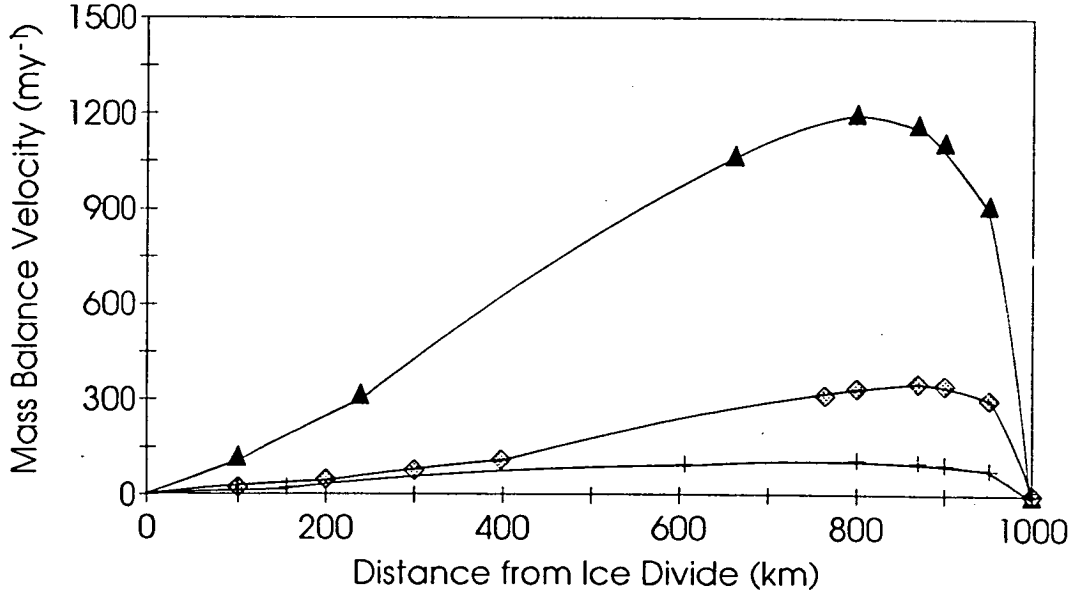

Figure 6.7: Distribution of mass balance velocity with distance along the flow line.

6.4.1 Determination of Effective Pressure at the Top of the Deforming Layer

The flow law for till underlying the Saalian Ice Sheet in the northern Netherlands was determined in the ring shear tests of chapter 5. This relates the shear strain rate in the till to the shear stress and effective pressure acting on it. A non-linear relationship was obtained;

$$\dot{\varepsilon} = 10^{13.1} \frac{\tau^{13.7}}{p'^{15.9}} \qquad 6.11$$

where $\dot{\varepsilon}$ is the strain rate

τ is the shear stress

p' is the effective pressure.

At small strain rates, the velocity of the till due to sediment deformation will be negligible and thus it is possible to set the bottom boundary of the deforming layer by assuming no effective deformation will occur below a strain rate of $0.01y^{-1}$. Effective pressures at the base of the deforming layer (p'_b) can therefore be calculated from the above flow law for a variety of shear stresses by substituting in the value of strain rate ($0.01y^{-1}$) and the value of basal shear stress obtained in chapter 5. The resulting effective pressures are listed in table 6.3.

Integrating the strain rate with respect to depth gives the velocity in the till.

$$v = \int \dot{\varepsilon}\, dz = \int k \frac{\tau^n}{p'^m} \frac{dz}{dp'} dp' \qquad 6.12$$

where n = 13.7 and m = 15.9 determined for the flow law for Dutch till (equation 6.11).

The velocity of till at the top of the deforming layer (v) is already known from mass balance calculations (section 6.3.4) and thus, assuming shear stress is constant with depth, an expression can be obtained for the effective pressure at the top of the deforming layer:

$$p'_t = \left\{ \frac{v + \frac{dz}{dp'} \frac{k\,\tau^n}{(-m+1)} \left(p'_b{}^{(-m+1)}\right)}{\frac{dz}{dp'} \frac{k\,\tau^n}{(-m+1)}} \right\}^{\frac{1}{-m+1}} \qquad 6.13$$

where p'_t is the effective pressure at the top of the deforming layer

k, n and m are the flow law parameters

dp'/dz is the effective pressure gradient.

The effective pressure at the top of the deforming layer is the effective pressure at the ice/bed interface.

Substituting in the values of mass balance velocity along the flow line obtained in section 6.3.4, gives the effective pressure profile along the ice/bed interface. This relationship is illustrated in figure 6.8 for various basal shear stresses and the different mass balance distributions.

Figure 6.8 shows that for a basal shear stress of 15kPa and mass balance distribution profile 4a (conditions inferred for Noord Bergum), the effective pressure at the base of the ice at the ice divide is 52.5kPa. This decreases towards the terminus to a value of 43.7kPa, 200km from the terminus, then increases slightly to a value of 44.2kPa near the terminus. Each basal shear stress and mass balance distribution considered give an effective pressure profile of a similar shape but with the effective pressure value increasing with basal shear stress.

6.4.2 Determination of Deforming Layer Thickness

As the effective pressure at both the top and bottom of the deforming layer is known, and the effective pressure gradient in the till is assumed to be a gravitational gradient of $10kPam^{-1}$, the thickness of the deforming layer can be calculated. The deforming layer thickness is thus determined for various basal shear stresses and mass balance distributions and shown in figure 6.9.

For a basal shear stress of $15kPam^{-1}$ and mass balance distribution 4a, the deforming layer is 3.7m thick. This increases to 4.7m, 200km from the terminus before decreasing slightly to 4.5m near the terminus. Each basal shear stress and mass balance profile follow a similar trend, illustrated in figure 6.9.

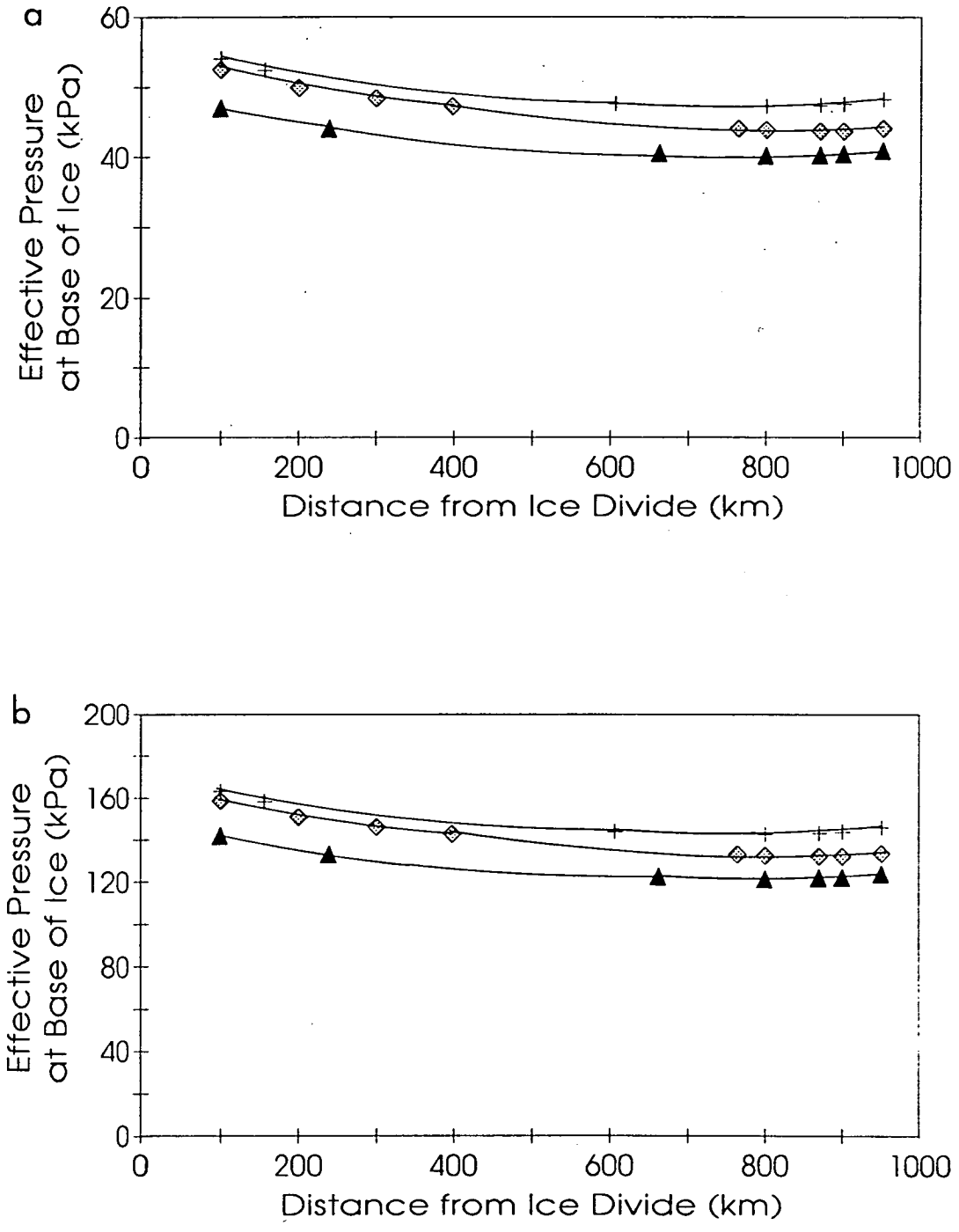

Figure 6.8: Effective pressure at the base of the ice along the flow line for each climate profile and basal shear stresses of (a) 15, (b) 50 kPa.

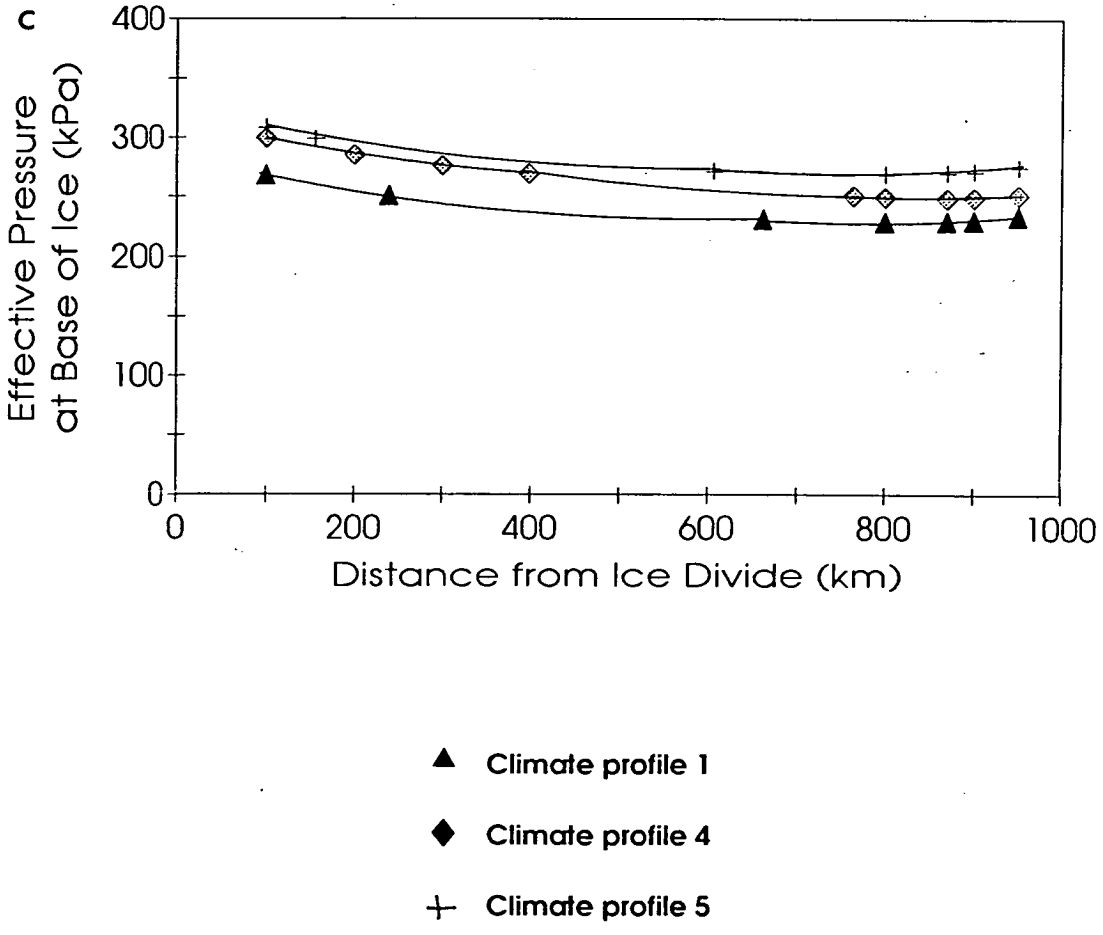

Figure 6.8: Effective pressure at the base of the ice along the flow line for each climate profile and a basal shear stresses of (c) 100kPa.

Table 6.3: Effective pressure at the base of the deforming layer.

τ_b (kPa)	p'_b (kPa)
15	89.42
50	251.83
100	457.09

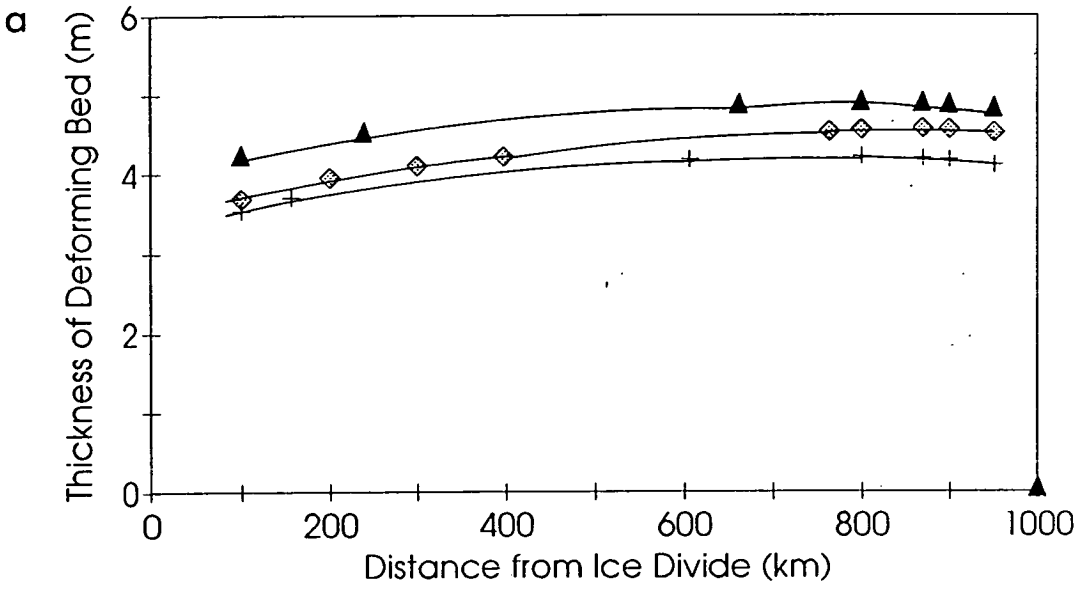

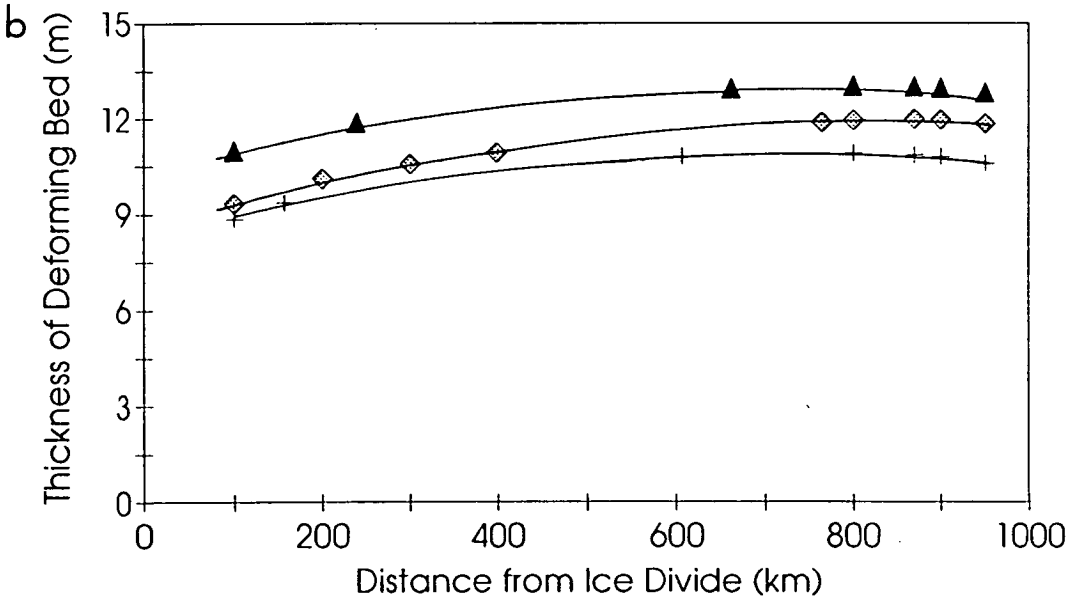

Figure 6.9: The thickness of the deforming layer for each climate profile and basal shear stresses of (a) 15, (b) 50 kPa.

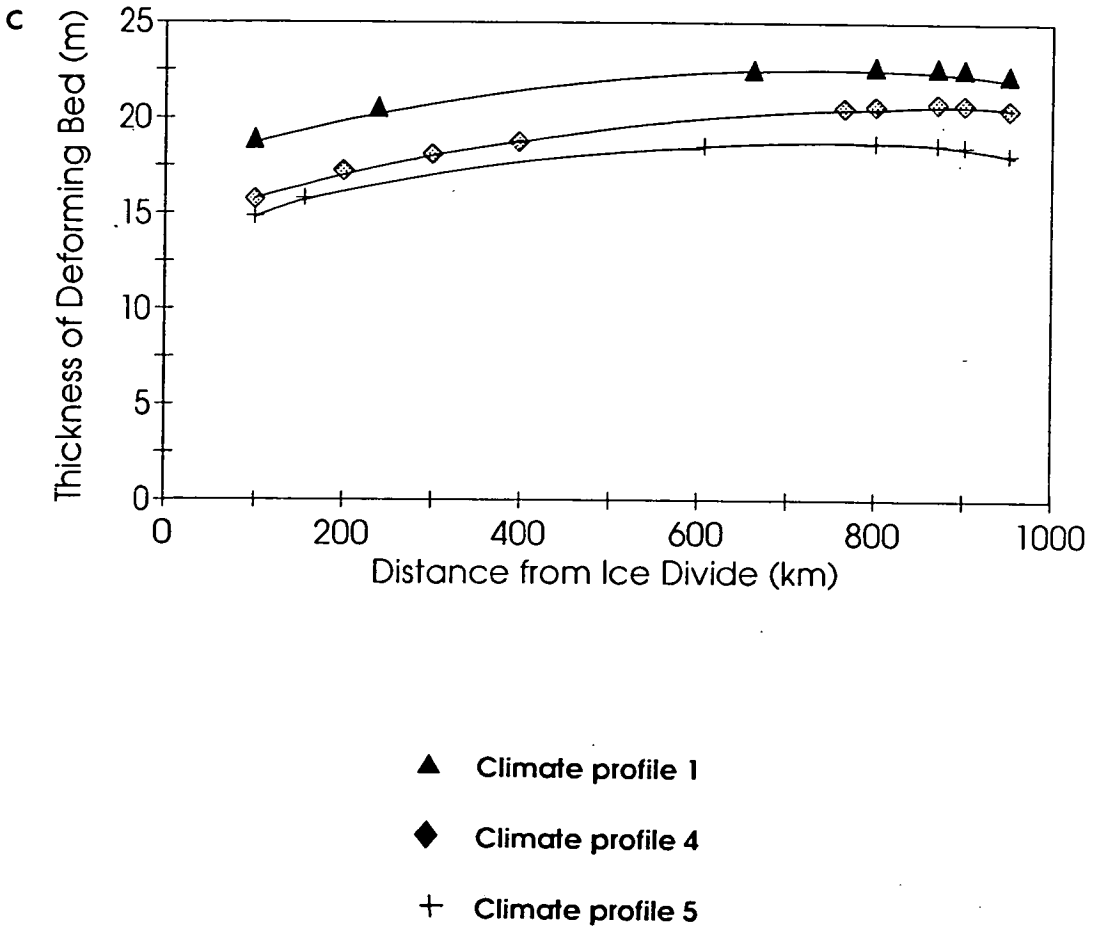

Figure 6.9: The thickness of the deforming layer for each climate profile and a basal shear stresses of (c) 100kPa.

6.4.3 Determination of Velocity Profile in Till

The velocity profile in the deforming layer can be determined by integrating the strain rate with respect to effective pressure. This results in velocity profiles of the form shown in figure 6.10. This particular example is for the preferred mass balance profile 4a at Noord Bergum for an ice thickness of 620m and a basal shear stress of 15kPa. In this case the velocity of the till is approximately $400my^{-1}$ at the surface of the deforming layer but decreases rapidly with depth becoming almost zero 2m below the surface.

6.5 Discussion of Results

In general the energy of glacier systems decreases from temperate maritime to polar continental climates (Sugden and John, 1976). This is reflected in the mass balance profiles shown in figure 6.4., in which temperate maritime climates are associated with greater accumulation and ablation rates than polar continental climates. This difference is more pronounced in the net upstream accumulation profile (figure 6.6), in which temperate conditions result in a much greater ice flux than polar conditions. This contrast is also illustrated in the mass balance velocity profiles of figure 6.7.

In all cases, the effective pressure at the glacier sole is greatest at the ice divide, decreasing towards the terminus, reaching a minimum value around 200km from the terminus, before increasing slightly again towards the terminus. For each shear stress considered, the effective pressure is greatest for the polar climate and least for the temperate climate, although the difference is not great. The effective pressure is greatest for the largest basal shear stress. Plotting effective pressure at the ice/bed interface against distance along the profile for each basal shear stress on a compilation diagram (figure 6.11) illustrates this point. Sediment deformation will therefore only occur when effective pressures are low. At higher effective pressures the basal shear stresses required to deform subglacial sediment are so great that the ice will begin to deform instead and the forward motion of the ice sheet is due to internal deformation of the ice body itself.

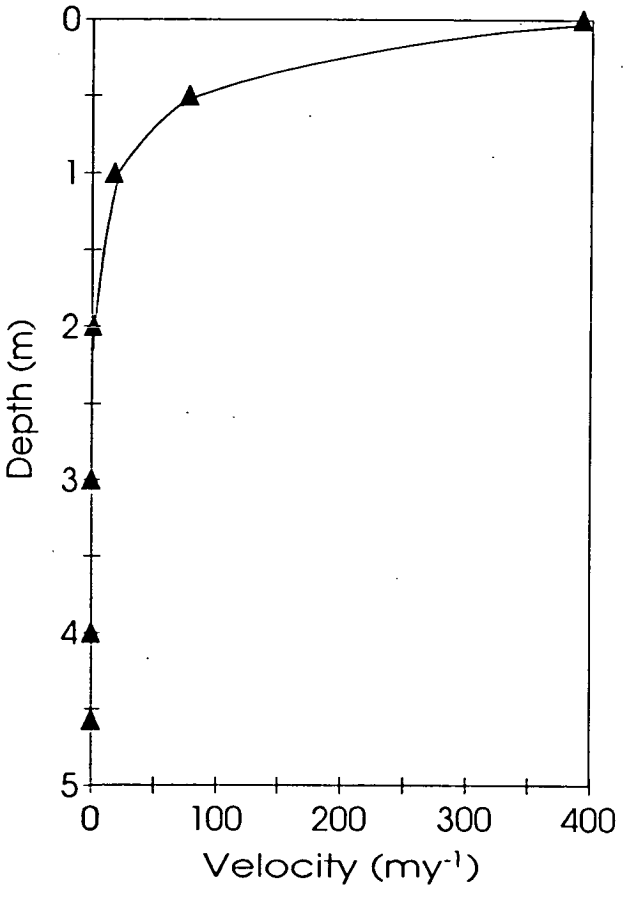

Figure 6.10: A typical profile of velocity with depth in a deforming layer. This particular example is for climate pattern 4a with an ice thickness of 620m and a basal shear stress of 15kPa as found at Noord Bergum.

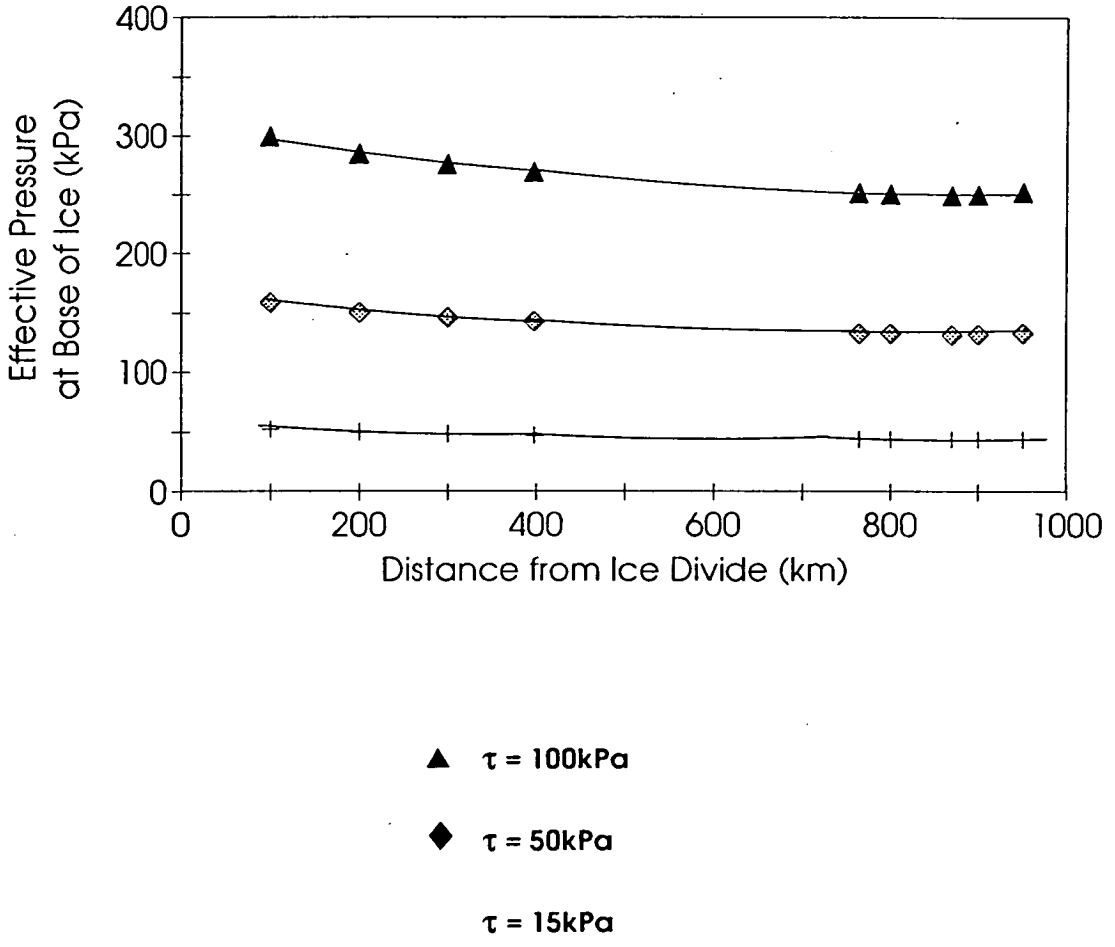

Figure 6.11: Compilation diagram showing the effective pressure distribution with distance along the flow line for climate profile 4a and basal shear stresses of 15, 50 and 100 kPa.

The thickness of the deforming bed (figure 6.9) increases from a minimum at the ice divide to a maximum around 200km from the terminus before decreasing slightly towards the terminus. There is, however, not a great difference along the profile. Neither is there a great difference between climate profiles. For a basal shear stress of 15kPa the deforming sediment bed is approximately 4m thick whilst for a shear stress of 50kPa it is 10m thick and for a shear stress of 100kPa it is about 20m thick. As shear stress increases, the difference in deforming bed thickness for the different climates increases. Temperate climate glaciers will tend to have a thicker deforming bed than polar climates although the difference is not great.

6.6 Implications of Results

If the ice sheet has a profile such as that determined in chapter 4, and it is underlain by till that behaves according to the flow law established in chapter 5, whose deformation is the dominant flow component in glacier movement, then the effective pressure at the base of the ice, determined from mass balance considerations, must be approximately constant along the flow line.

In other words, the stability of an ice sheet whose motion is controlled by a deforming sediment bed is dependent on the basal effective pressure being controlled within a narrow range of values.

6.7 Summary of Argument

If the ice sheet profile is as reconstructed in chapter 4, and the associated basal shear stress relatively low, then glacier flow by internal deformation of the ice will be negligible. Sliding of ice over the unlithified substrate is also likely to be negligible (e.g. Boulton and Hindmarsh, 1987) and thus the dominant mode of ice sheet flow can only be by deformation of the subglacial sediment bed.

The ice sheet is assumed to be in a steady state and not surging. Boulton and Hindmarsh suggest from a two dimensional analysis, that the time dependent response of subglacial deformation to changing external controls is of the order of 10^3-10^4 years for fine grained impermeable sediments, the response time being a function of permeability. If the ice advanced over the northern Netherlands at velocities typical of surging glaciers, then the subglacial groundwater system is unlikely to have achieved equilibrium as any excess pore water pressure induced in

the underlying fine grained sediments would have been unable to dissipate in such a short time. However the preconsolidation pressures preserved in the Peelo Clays are greater than would be expected for the transient ice cover of a surge. Hence it is assumed that the ice sheet had attained an equilibrium profile and was in a steady state.

A mass balance distribution, consistent with palaeoclimatic data, is adopted and superimposed on the predicted ice sheet profile, allowing the ice flux and thus the velocity of ice to be calculated. The ice velocity is equated to the velocity of the deforming till at the base of the ice, from which the effective pressure at the ice/till interface is determined.

For the low basal shear stress suggested by the reconstructed ice sheet, the effective pressure at the ice/bed interface is relatively constant at a low value along the flow line (see figure 6.11). Figure 6.8 shows that the flow law established for the Dutch till requires effective pressures to be in a narrow range for stable deformation to occur at low basal shear stresses. There must therefore be a mechanism whereby effective pressures can be maintained within this narrow range. One possible mechanism is the formation of subglacial tunnels and is investigated in the following discussion.

6.8 Tunnels as a Possible Control Mechanism

6.8.1 Tunnel Formation

If for some reason the subglacial sediments cannot drain all the water reaching the glacier bed, water will build up at the base of the ice and counteract the weight of the ice. This results in reduced effective pressures. If the water pressure equals or exceeds the ice pressure, the system will become unstable, as the theoretical shear strength of many sediments will be reduced to zero. Under these circumstances, channels are generally supposed to develop at the ice/bed interface. Boulton and Hindmarsh (1987) have suggested that the role played by channels would be to reduce water pressures so that instability is prevented. In the case discussed in section 8.4.1 above, where a relatively constant effective pressure is required so that sediment deformation can discharge the ice flux for a given profile, the discharge of water through tunnels would be that required to maintain this balance.

6.8.2 Stability of Tunnels

Tunnels are known to form at the ice/bed interface where they discharge large water fluxes (Röthlisberger, 1968). Röthlisberger (1972) suggested two opposing effects act to maintain channels in a steady state. Once formed, the water pressure in the channel falls as water drains from the system via the channel. The pressure of the overlying ice then exceeds the water pressure and the channel tends to close by creep deformation in the ice. Meanwhile, the energy dissipated by turbulent water flow, melts ice from the channel wall, enlarging the conduit. These two competing processes allow the system to adjust to variations in the amount of meltwater and thus may control the effective pressure at the ice/bed interface. This is illustrated in figure 6.12.

6.8.3 Water Pressure in a Horizontal Conduit Surrounded by Ice

6.8.3.i Variation of Water Pressure with Distance along a Tunnel

Röthlisberger (1972) studied theoretically the closure of a cylindrical hole by radial ice flow from all sides towards its centre. He obtained an expression describing how water pressure varies with horizontal distance along a conduit;

$$\frac{dp_w}{dx} = B\, k^{\frac{-6}{11}} (n\, A)^{\frac{-8n}{11}} Q^{\frac{-2}{11}} (p_i - p_w)^{\frac{8n}{11}} \qquad 6.14$$

where k is a roughness coefficient,

n and A are flow law parameters for ice,

Q is discharge and

B is a constant, where

$$B = 2^{\frac{12}{11}} \pi^{\frac{2}{11}} \left(\frac{c_m \rho_i}{0.684}\right)^{\frac{8}{11}} (\rho_w g)^{\frac{3}{11}} \qquad 6.15$$

where c_m is the energy of fusion of water,

ρ_i the density of ice,

ρ_w the density of water,

g the acceleration due to gravity.

Using standard values $B = 6.33 \times 10^7\ Nm^{-2}m^{(-3/11)}$.

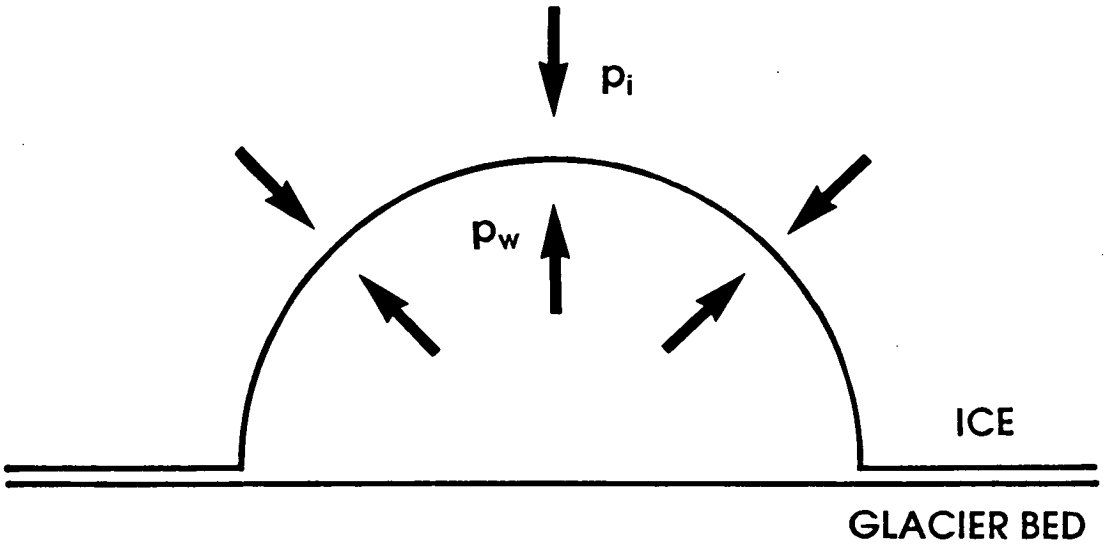

Figure 6.12: Cross section through a Röthlisberger channel showing the opposing pressures due to ice (p_i) and water (p_w).

This equation (6.14) shows that the water pressure gradient dp_w/dx increases with the pressure difference (p_i-p_w) and channel roughness, and with decreasing ice viscosity. The dependence on discharge is such that the greater the discharge, the smaller the water pressure gradient. However, although the dependence on discharge is very weak, it cannot be ignored due to the wide range of possible values (Röthlisberger, 1972).

This differential equation can be solved for simple cases to obtain the water pressure in the channel. Röthlisberger (1972) assumes that at the terminus water pressure is zero and obtains a solution for constant discharge in a horizontal conduit under a uniform thickness of ice. He noted that this may not be directly applicable to channels of different cross section at the base of an ice sheet but then suggested that it may not be too dissimilar when the additional frictional effects at the base of the channel are taken into account.

Röthlisberger's theory (Röthlisberger, 1972; Weertman, 1972) assumes that the channel is water filled and that ice-water interaction controls the pressure in the channel. However, when ice flows over unlithified sediment the water pressure in the tunnel depends on both the ice-water interaction and the sediment-water interaction. Nevertheless the Röthlisberger (1972) equation is used for simplicity as the basis for calculating how water pressure would vary in a channel at the ice/bed interface under the inferred Saalian Ice Sheet in the northern Netherlands. A number of assumptions have to be made before this can be undertaken.

6.8.3.ii Assumptions Required for the Determination of Water Pressure along a Tunnel

In the following discussion it is assumed that:

(i) Water pressure is zero at the terminus.

(ii) Water discharges horizontally. Discharge increases along the flow line according to;

$$Q = m\,(L - x) \qquad 6.16$$

where m is the melt rate, L is the length of the melt zone, and x is the distance from the terminus.

(iii) Melting occurs in a zone 600km from the terminus (the average of the two melt zones considered in chapter 4, giving rise to the average ice sheet profile considered in this chapter).

(iv) The ice flow law parameters are constant, n being 3, and A either 580 x 10^5 Pas^{-1} (Nye, 1953), 317 x 10^5 Pas^{-1} (Röthlisberger, 1972) or 194 x 10^5 Pas^{-1} (Nye, 1953).

(v) The roughness parameter k is 10 $m^{0.33}s^{-1}$ (Nye, 1953, Röthlisberger, 1972) and constant along the channel.

6.8.3.iii Determination of Water Pressure along a Channel

Equation 6.14 is rearranged and integrated to obtain the variation of water pressure in a channel with distance along the flow line;

$$\int (p_i - p_w)^{\frac{-24}{11}} dp_w = B\, k^{\frac{-6}{11}} (3A)^{\frac{-24}{11}} \int \{m(L-x)\}^{\frac{-2}{11}} dx \qquad 6.17$$

For the conditions $p_w = 0$ at $x = 0$ and $p_w = P_w$ at $x = X$, solving equation 6.17 for p_w gives

$$p_w = p_i - \left\{ \left(\frac{-13\, B\, k^{\frac{-6}{11}} (3A)^{\frac{-24}{11}}}{9\, m^{\frac{2}{9}}} \right) \left((L-x)^{\frac{9}{11}} - L^{\frac{9}{11}} \right) + p_i^{\frac{-13}{11}} \right\}^{\frac{-11}{13}} \qquad 6.18$$

This solution assumes that the ice pressure does not vary along the flow line. However this is unlikely to be the case. To estimate the effect of varying ice thickness, different values of ice pressure were substituted into the second pi term in the above equation (6.18). Figure 6.13 shows that this makes very little difference to the water pressures obtained except near the terminus (compare figures 6.13 a&b).

If it is assumed therefore that water pressure in the channel is independent of ice sheet thickness, substituting values of the relevant parameters into equation 6.18 results in the relationship illustrated in figure 6.13b. This shows that water pressure in the tunnel decreases towards the terminus and is very similar to the pressure due to the weight of overlying ice, suggesting that the channels must be stable as the

pressure difference acting to close them is very small. The water pressure also appears to be almost independent of discharge for the range of values considered in this analysis, suggesting that the tunnels could adjust to cope with variations in meltwater flux.

Tunnels in the ice may therefore form and act as a stabilising mechanism since these permit the large range of discharges considered here to result in a relatively small range in water pressures. These could constrain effective pressures within the narrow band required allowing stable sediment deformation to occur.

6.9 Conclusions

The Röthlisberger channel theory (Röthlisberger, 1972; Weertman, 1972) leads to the conclusion that the pressure acting to close the tunnels, the difference between the ice overburden pressure and the water pressure in the tunnel, can be roughly constant at a low value along the flow line. This confirms that channel flow can be a mechanism through which effective pressures are sensitively adjusted so that they fall within the relatively narrow range of values that permit till deformation to balance the ice flux and thus stabilise the system. However Röthlisberger's theory has not been coupled to water flow in the subglacial sediment and thus interactions between the sediment bed and water in the channel are not properly analysed. Nevertheless it is expected that the results obtained in the above analysis yield a rough quantitative pattern, which could be further constrained by the development of a theory of subglacial channels in a deforming substrate.

The very recent theoretical analysis by Alley (1992), at an order of magnitude scale, suggests that deforming till could creep towards a low pressure channel and thus be removed from the system. This would, however, only occur in a relatively narrow zone around the channel where the till would thin. Alley (1992) concludes that low pressure channels and soft glacial sediments could coexist providing the spacing of the channels is greater than twice the till catchment area, the magnitude of the catchment area depending on the rheology of the till.

It is shown that tunnels can form at the ice/bed interface and remain stable, therefore providing a mechanism which permits the effective pressure at the base of the ice to remain constant, independent of meltwater flux. This allows stable deformation of the subglacial sediment to occur at low basal shear stresses and accounts for the motion of the ice.

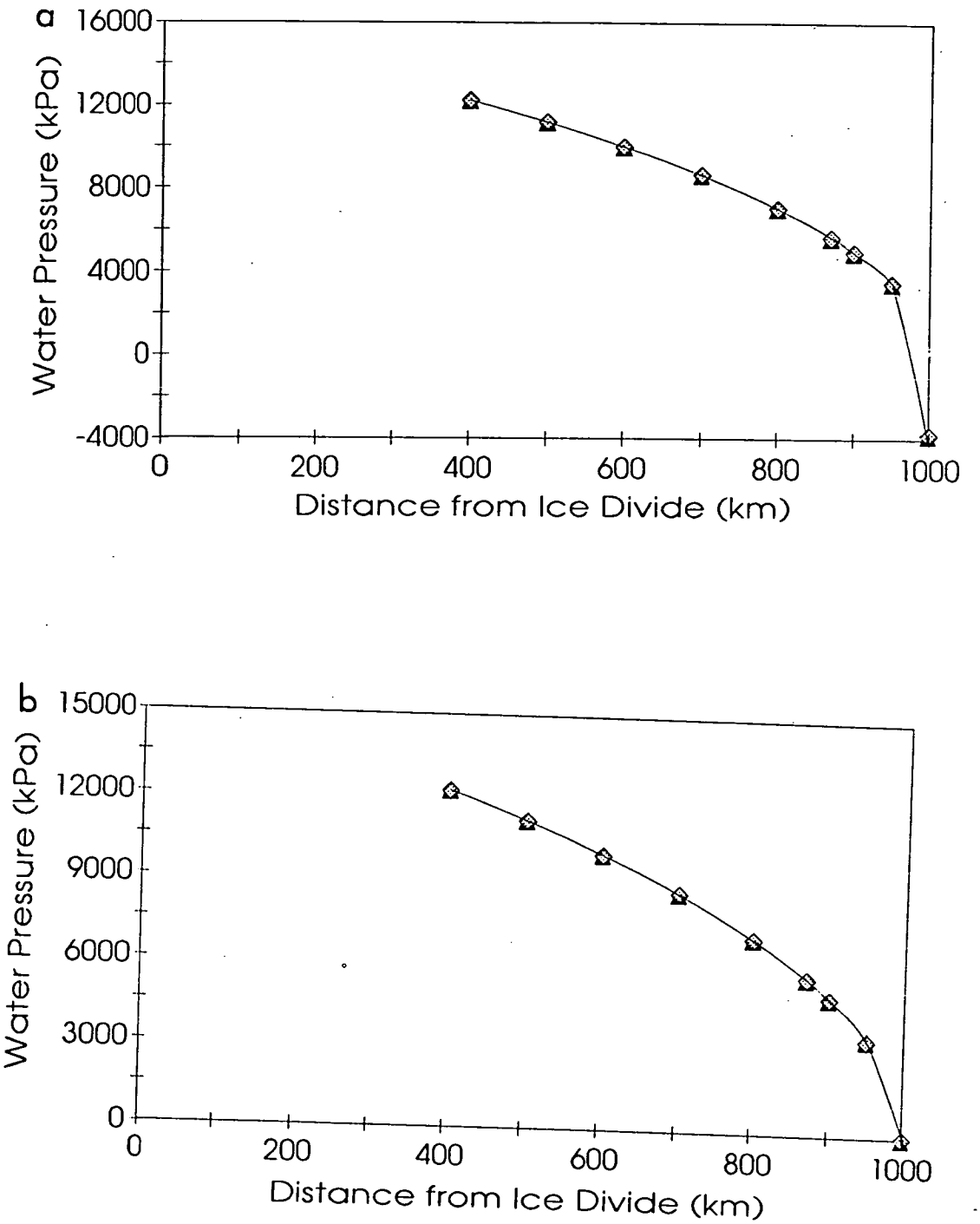

Figure 6.13: The variation of water pressure with distance along a Rothlisberger channel; **(a)** shows the effect of including a term accounting for the variation of ice thickness whereas **(b)** assumes that the ice is of uniform thickness.

◆ **melt rate = 1 my^{-1}** ▲ **melt rate = 0.001 my^{-1}**

CHAPTER 7

CONCLUSIONS

7.1 Conclusions

This thesis employs indirect methods of determining important ice sheet parameters, such as the basal melt rate and ice thickness, from the geotechnical properties of former subglacial sediments. The rheology of subglacial sediment is investigated. Results confirm that there is an intimate relationship between the properties of subglacial sediment, and the basal shear stress and effective pressure, controlling the flow of ice in an ice sheet.

The shear strength of a sediment depends on effective pressure. High water pressures can be sustained in subglacial sediments and reduce the effective pressure to such an extent that the shear strength of the sediment is less than the yield strength of ice. Sediment deformation can therefore occur at a low shear stress thus contributing to the forward motion of the ice and influencing ice sheet dynamics.

The character and geometry of subglacial sediments are fundamental determinants of the nature and rate of ground water drainage. A one dimensional drainage model is developed and the theoretical relationship between groundwater flow, sediment properties and ice sheet dynamics explored. This model assumes that the ice sheet is in a steady state and that sediment deformation does not occur. A theory is developed in which meltwater drains vertically through an upper sediment layer of low permeability into an aquifer. The vertical distribution of pressure is determined and a relationship between the vertical potential pressure gradient, vertical effective pressure gradient and vertical gravitational gradient in the sediment established. It is assumed that all meltwater drains vertically through the underlying sediment, hence the velocity of water flow can be equated to the melt rate of ice. The melt rate of the ice can therefore be determined using Darcy's law.

An advancing ice sheet loads the sediments over which it flows. Sediments consolidate in response to this additional load, providing water can drain from the sediment pores. If the ice sheet is melting at its base, the sediment must also discharge a melt water flux. It will therefore not consolidate to the same degree as it

would for the same load applied under non-glacial conditions. The sediments expand on retreat of the ice, however, they retain a record of the maximum pressure to which they have been subjected. This is assumed to have occurred at the maximum extent of an ice sheet. The past maximum pressure can be determined from the results of one dimensional consolidation tests, however, the presence of a meltwater flux means that the preconsolidation pressure preserved in the sediment is not a simple consequence of the overburden of ice and sediments.

This theory was tested for a site in the northern Netherlands which was over-ridden by the Saalian ice sheet. A vertical preconsolidation pressure profile is determined in Peelo Clays from a borehole drilled near Noord Bergum. This is assumed to represent the effective pressure conditions of the sediment at the glacial maximum. A palaeopotential pressure gradient in the clay is inferred from the theory and a melt rate of $1.4 mm y^{-1}$ calculated.

The effective pressure at the base of the ice is obtained indirectly from preconsolidation measurements in the Peelo Clay. A one dimensonal drainage system is assumed, allowing groundwater flow in the northern Netherlands at the glacial maximum to be modelled and the potential pressure at the base of the ice inferred. The ice overburden is determined from the values of effective pressure and potential pressure at the glacier sole, resulting in an ice sheet thickness of 495 - 745m at Noord Bergum.

Melt rate and ice sheet thickness are important predictions from numerical ice sheet models (e.g. Huybrechts,1992). It has previously been impossible to test such predictions. The values obtained in this thesis can therefore be used as a constraint on ice sheet modelling, allowing more realistic models to be developed.

The Saalian ice sheet is assumed to be perfectly plastic and to have a parabolic ice sheet profile. The resulting basal shear stress at Noord Bergum is found to be 9 - 20 kPa, very much less than the yield strength of ice. Hence the forward motion of the ice sheet could not have been due primarily to the internal deformation of ice.

This steady state solution ignores the possibility that subglacial sediments can deform. The shear strength of a sediment depends on effective pressure. In the subglacial environment, where basal melting occurs, the flux of water through the sediment reduces the effective pressure acting on it, thus lowering its shear strength. If its shear strength is reduced below the yield strength of ice, then the sediment will deform at lower basal shear stresses than the ice. Sediment deformation may therefore

contribute to the forward motion of the ice sheet. This is the basis of the deforming bed model first proposed by Boulton and Jones (1979).

Although the mechanical properties of subglacial sediments are a fundamental component of the deforming bed model, they are poorly constrained. Till rheology is defined by a flow law in which the shear strain rate in a sediment is related to the shear strength of the sediment and the effective pressure acting on the sediment. Boulton and Hindmarsh (1987) determine a weakly non-linear flow law for a sandy till from field experiments in Iceland. Most subsequent deforming bed models have been based on this flow law. However Kamb (1991) proposes an extremely non-linear flow law based on soil mechanics tests on clay rich soils. These flow laws are significantly different, prompting the present investigation of till rheology.

Ring shear tests are carried out on a typical till from the northern Netherlands and a non-linear flow law determined from the results. This suggested that the subglacial system was sensitive to variations in effective pressure and shear stress, much more so than the flow law determined by Boulton and Hindmarsh (1987) but not as extreme as that suggested by Kamb (1991).

Till deformation is modelled using the experimentally determined flow law. Strain rate and velocity profiles are found for a deforming layer of Saalian till. This showed that, for a constant shear stress, stable sediment deformation could only occur within a narrow range of effective pressures. Similar modelling was carried out for the flow laws of Boulton and Hindmarsh (1987) and Kamb (1991). In the former case, this showed that stable sediment deformation in the sandy Iceland till could occur over a wide range of effective pressures for a constant shear stress. Whilst in the latter case, stable deformation in a clay rich sediment requires a very narrow range indeed. Hence, if ice sheet motion is governed by a fine grained deforming sediment bed, then there must be a mechanism which constrains effective pressures within the narrow band of the flow law.

An inverse model is developed in which ice sheet velocity is inferred by superimposing a mass balance distribution onto the parabolic ice sheet profile reconstructed for the northern Netherlands. The ice flux is calculated and assumed to be maintained by till deformation alone. This allows the till velocity to be inferred. The effective pressure at the top of the deforming layer and the thickness of the deforming layer are determined and are relatively constant along the ice sheet profile. This reinforces the view that a control mechanism must exist to constrain the effective pressures within a narrow range of values.

A possible control mechanism is that of the formation of subglacial channels. Such channels could form at the ice/bed interface and allow melt water drainage. Röthlisberger type channels are modelled (Röthlisberger, 1972) and the variation of water pressure along a channel for various discharges calculated. This shows that tunnels can act as a stabilising mechanism, because they allow a large range of water fluxes to result in a relatively small range of water pressures. Effective pressure is thus constrained within a narrow range, allowing stable sediment deformation to occur.

7.2 Future work

This thesis has determined the various pressure components imposed by a basally melting ice sheet on the subglacial sediments of the northern Netherlands during the Saalian glaciation and established the corresponding ice sheet profile. The behaviour of subglacial sediments under such conditions has been considered and a relationship between rate of shearing, shear stress and effective pressure applied by the ice sheet has been established. To achieve these aims, a one dimensional drainage model has been adopted. However this model is very much a simplified representation in which various assumptions have been made.

Consolidation and shear deformation of sediments are discussed separately in the one dimensional model. However they are not entirely independent. The relationship between consolidation and shearing is described by critical state theory (Roscoe *et al.*, 1958). Critical state theory should therefore be considered in any further investigation of till rheology and thus contribute to a more realistic deforming bed model.

It is assumed in the one dimensional model that there was no permafrost in the proglacial zone at the glacial maximum. However, this is unlikely to have been the case. The presence of a frozen zone at the terminus of the ice sheet would alter the subglacial drainage pattern and thus the subglacial pressure regime, consequently affecting the calculation of ice sheet thickness and ice sheet profile. A permafrost component should therefore be introduced as part of any future research.

One of the principal assumptions made in the one dimensional model was that any permafrost present before the advance of the ice sheet had thawed, and its effects overprinted by subsequent shearing and consolidation of the sediment as a result of stresses imposed by the overriding ice. Consolidation as a result of freezing-induced desiccation was therefore assumed not to have occurred after the ice advanced. Further detailed study of the sediment fabric could confirm this.

In view of the results obtained from this study, it is clear that a more realistic model in which the ice sheet motion, sediment deformation and subglacial hydrology are considered together is required to predict more accurately the response of a soft based ice sheet to external forcing. Much more experimental data would be required to constrain such a model.

BIBLIOGRAPHY

Aber, J.S., 1979. The character of glaciotectonism. Geologie en Mijnbouw, **64**, 389 - 395.

Agassiz, L., 1840. Études sur les glaciers (two volumes). Neuchâtel, H. Niolet.

Agassiz, L., 1867. Studies on glaciers, preceded by the 'Discourse of Neuchâtel'. Translated and edited by Carozzi, A.V. Hafner Publishing Co. New York and London.

Alley, R.B., 1989a. Water pressure coupling of sliding and bed deformation: I. Water system. Journal of Glaciology, **35**, 108 - 118.

Alley, R.B., 1989b. Water pressure coupling of sliding and bed deformation: II. Velocity - depth profiles. Journal of Glaciology, **35**, 119 - 129.

Alley, R.B., 1991. Deforming - bed origin for southern Laurentide till sheets? Journal of Glaciology, **37**, 67 - 76.

Alley, R.B., 1992. How can low - pressure channels and deforming tills coexist subglacially? Journal of Glaciology, **38**, 200 - 207.

Alley, R.B., Blankenship, D.D., Bentley, C.R. and Rooney, S.T., 1986. Deformation of till beneath Ice Stream B, West Antarctica. Nature, **322**, 57 - 59.

Alley, R.B., Blankenship, D.D., Rooney, S.T. and Bentley, C.R., 1987a. Till beneath Ice Stream B, 3. Till deformation: evidence and implications. Journal of Geophysical Research, **92**, 8921 - 8929.

Alley, R.B., Blankenship, D.D., Rooney, S.T. and Bentley, C.R.,1987b. Till beneath Ice Stream B, 4. A coupled ice - till flow model. Journal of Geophysical Research, **92**, 8931 - 8940.

Alley, R.B., Blankenship, D.D., Rooney, S.T. and Bentley, C.R., 1989. Water pressure coupling of sliding and bed deformation: III. Application to Ice Stream B, Antarctica. Journal of Glaciology, **35**, 131 - 139.

Åmark, M., 1986. Glaciotectonics and deposition of stratified drift during formation of tills beneath an active glacier - examples from Skåne, southern Sweden. Boreas, **15**, 155 - 171.

Atkinson, J.H. and Bransby, P.L., 1978. The Mechanics of Soils. McGraw - Hill (U.K.) Ltd. 375pp.

Berg, M.W. van den, and Beets, D.J., 1987. Saalian glacial deposits and morphology in the Netherlands. In: Meer, J.J.M. van der (ed.), 'Tills and Glaciotectonics'. Balkema, Rotterdam, 235 - 251.

Bishop, A.W., Green, G.E., Garga, V.K., Andersen, A. and Brown, J.D., 1971. A new ring shear apparatus and its application to the measurement of residual strength. Géotechnique, **21**, 273 - 328.

Blankenship, D.D., Bentley, C.R., Rooney, S.T., and Alley, R.B., 1986. Seismic measurements reveal a saturated porous layer beneath an Antarctic ice stream. Nature, **322**, 54 -57.

Boulton, G.S., 1979. Processes of glacial erosion on different substrata. Journal of Glaciology, **23**, 15 - 38.

Boulton, G.S., 1986. A paradigm shift in glaciology? Nature, **332**, 18.

Boulton, G.S., 1987. Progress in glaciol geology during the last fifty years. Journal of Glaciology, Special Issue, 25 - 32.

Boulton. G.S., Dent, D.L. and Morris, E.M., 1974. Subglacial shearing and crushing, and the role of water pressures in tills from south east - Iceland. Geografiska Annaler, **56**, 135 - 145.

Boulton, G.S. and Paul, M.A., 1976. The influence of genetic processes on some geotechnical properties of glacial tills. Quarterly Journal of Engineering Geology, **9**, 159 - 194.

Boulton, G.S. and Jones, A.S., 1979. Stability of temperate ice caps and ice sheets resting on beds of deformable sediment. Journal of Glaciology, **24**, 29 - 43.

Boulton, G.S., Smith, G.D. and Morland, L.W., 1984. The reconstruction of former ice sheets and their mass balance characteristics using a non - linearly viscous flow model. Journal of Glaciology, **30**, 140 - 152.

Boulton, G.S. and Hindmarsh, R.C.A., 1987. Sediment deformation beneath glaciers: rheology and geological consequences. Journal of Geophysical Research, **92**, 9059 - 9082.

Breeuwsma, A., Balkema, W., and Zwijnen, R., 1984. Kleimineralogisch onderzoek van enkele kwartaire en tertiare afzettingen. Stichting voor Bodemkartering Rapport nr. 198.

BS 1377, 1975. British standard methods of test for soils for civil engineering purposes.

Casagrande, A., 1936. The determination of the preconsolidation load and its practical significance. Proceedings of the First International Conference on Soil Mechanics and Foundation Engineering, **3**, 60 - 64.

Casagrande, A., 1948. Classification and identification of soils. Transactions of the American Society of Civil Engineers, **113**, 901 - 930.

Clarke, G.K.C., 1987. Subglacial till: a physical framework for its properties and processes. Journal of Geophysical Research, **92**, 9023 - 9036.

Coulomb, C.A., 1776. Essai sur une application des règles des maximis et minimis à quelque problemes des statique relatifs à l'architecture. Mem. Acad. Roy. Pres. Divers Savants, Paris, **7**.

Darcy, H., 1856. Les fontaines publiques de la ville de Dijon. V. Dalmont, Paris. 647pp.

Das, B.J., 1985. Advanced Soil Mechanics. McGraw Hill Book Company, 511pp.

Deeley, R.M. and Parr, P.H., 1913. The viscosity of glacier ice. Philosophical Magazine, **26**, 85 - 111.

Deeley, R.M. and Parr, P.H., 1914. The Hintereis Glacier. Philosophical Magazine, **27**, 153 - 176.

Derbyshire, E., Edge. M.J. and Love, M., 1985. Soil variability in some glacial diamicts. In Forde, M.C. (ed.) 'Glacial Tills 85', Proceedings of the International Conference on Construction in Glacial Tills and Boulder Clays, Edinburgh, 169 - 175, Engineering Technics Press, Edinburgh.

Douma, J., Rooijen, H den, and Schokking, F., 1989. Anisotropy detected in shallow clays using shear - wave splitting in a VSP survey. Preprint 51st EAEG Meeting, Berlin.

Drewry, D., 1986. Glacial Geologic Processes. Edward Arnold Ltd. 276pp.

Ehlers, J., Meyer, K-D and Stephan, H-J., 1984. The pre - Weichselian glaciations of north - west Europe. Quaternary Science Reviews, **3**, 1 - 40.

Ehlers, J. and Linke, G., 1989. The origin of deep buried channels of Elsterian age in Northwest Germany. Journal of Quaternary Science, **4**, 255 - 265.

Engelhardt, H.F., Harrison, W.D. and Kamb, B., 1978. Basal sliding and conditions at the glacier bed as revealed by bore - hole photography. Journal of Glaciology, **20**, 469 - 508.

Engelhardt, H.F., Humphrey, N., Kamb, B. and Fahnestock, M., 1990. Physical conditions at the base of a fast moving ice stream. Science, **248**, 57 - 59.

Forbes, J.D., 1842. On a remarkable structure observed by the author in the ice of glaciers. Edinburgh New Philosophical Journal, **32**, 84 - 91.

Forbes, J.D., 1845. Travels through the Alps of Savoy (second edition). A. and C. Black, Edinburgh.

Fowler, A.C., 1986. A sliding law for glaciers of constant viscosity in the presence of subglacial cavitation. Proceedings of the Royal Society of London, **407**, 147 - 170.

Freeze, R.A. and Cherry, J.A., 1979. Groundwater. Engelwood Cliffs, NJ, Prentice Hall.

Glen, J.W., 1952. Experiments on the deformation of ice. Journal of Glaciology, **2**, 111 - 114.

Glen, J.W., 1955. The creep of polycrystalline ice. Proceedings of the Royal Society, **228**, 519 -538.

Goldthwait, R.P., 1960. Formation of ice cliffs. In 'Study of Ice Cliffs in Nunatarssuaq, Greenland', SIPRE Technical Report, **39**, 139 - 150.

Greeuw, G. and Schokking, F.,1990. Piezocone and other measurements in an overconsolidated glacial clay. 6th International IAEG Congress, Balkema, Rotterdam, 303 - 308.

Guiot, J., Pons, A., Beaulieu, J.L. de, and Reille, M., 1989. A 140,000 - year continental climate reconstruction from two European pollen records. Nature, **338**, 309 - 313.

Haldorsen, S., Jorgensen, P., Rappol, M. and Riezebos, P.A., 1989. Composition and source of the clay - sized fraction of Saalian till in the Netherlands. Boreas, **18**, 89 - 97.

Harrison, W., 1958. Marginal zones of vanished glaciers reconstructed from the preconsolidation pressure values of overridden silts. Journal of Geology, **66**, 72 - 95.

Hart, J.K., 1987. The genesis of the north east Norfolk drift. Unpublished Ph.D. thesis, University of East Anglia.

Head, K.H., 1982. Manual of Soil Laboratory Testing Volume 2: permeability, shear strength and compressibility tests. Pentech Press Ltd., Plymouth.

Hindmarsh, R.C.A., Boulton, G.S. and Hutter, K., 1989. Modes of operation of thermo - mechanically coupled ice sheets. Annals of Glaciology, **12**, 57 - 69.

Hobbs, B.E., Means, W.D. and Williams, P.F., 1976. An Outline of Structural Geology. John Wiley and Sons, Inc. New York.

Hodge, S.M., 1979. Direct measurements of basal water pressures: progress and problems. Journal of Glaciology, **23**, 309 - 319.

Holdsworth, G. and Bull, C., 1970. The flow law of cold ice; investigations on Meserve Glacier, Antarctica. International Association of Scientific Hydrology, **86**, 204 - 216.

Hopkins, W., 1845. On the motion of glaciers. Philosophical Magazine, **26**, 1 - 16.

Hopkins, W., 1849. On the motion of glaciers. Transactions of the Cambridge Philosophical Society, **8**, 50 - 74.

Huybrechts, P., 1992. The Antarctic ice sheet and environmental change: a three dimensional modelling study. Reports on Polar Research, **99**.

Hvorslev, M.J., 1937. Uber die Festigkeitseigenschaften gestorter bindiger Boden. Ingenoirvidenskabelige, **45**. Copenhagen.

Hvorslev, M.J., 1939. Torsion shear tests and their place in the determination of the shearing resistance of soils. Proceedings of the American Society of Testing Materials, **39**, 999 - 1022.

Jellinek, H.H.G., 1959. Adhesive properties of ice. Journal of Colloid Science, **14**, 268 - 280.

Jong, J.D. de and Maarleveld, G.C., 1983. The glacial history of The Netherlands. In: Ehlers, J. (ed.), 'Glacial Deposits in North - west Europe', Balkema, Rotterdam, 353 - 365.

Kamb, B., 1970. Sliding motion of glaciers: theory and observation. Reviews of Geophysics and Space Physics, **8**, 673 - 728.

Kamb, B., 1991. Rheological nonlinearity and flow instability in the deforming bed mechanism of ice stream motion. Journal of Geophysical Research, **96**, 16585 - 16595.

Kamb, B. and LaChapelle E.R., 1964. Direct observation of the mechanism of glacier sliding over bedrock. Journal of Glaciology, **5**, 159 - 172.

Kazi, A. and Knill, J.L., 1969. The sedimentation and geotechnical properties of the Cromer Till between Happisburgh and Cromer, Norfolk. Quarterly Journal of Engineering Geology, **2**, 63 - 80.

Kenney, T.C., 1967. The influence of mineral composition on the residual strength of natural soils. Proceedings of. Geotechnical Conference, Oslo, **1**, 123 - 129.

Kenney, T.C., 1977. Residual strengths of mineral mixtures. Proceedings of the 9th International Conference on Soil Mechanics, **1**, 155 - 160.

Khera, R.P. and Schulz, H., 1984. Past consolidation stress estimates in Cretaceous clay. ASCE Journal of Geotechnical Engineering, **110**, 189 - 202.

Kuster, H. and Meyer, K - D., 1979. Glaziäre Rinnen im mittleren und nordöstlichen Niedersachsen. Eiszeitalter und Gegenwart, **29**, 135 - 156.

La Gatta, D.P., 1970. Residual strength of clays and clay - shales by rotation shear tests. Harvard Soil Mechanics Series No. 86. Cambridge, Massachusetts.

Lingle, C.S. and Brown, T.J., 1987. A subglacial aquifer bed model and water pressure dependent basal sliding relationship for a west Antarctic ice stream. In: Veen, C.J. van der, and Oerlemans, J. (eds.), "Dynamics of the west Antarctic ice sheet". D. Reidel Publishing Company, 249 - 285.

Liboutry, L., 1958. Frottement sur le lit et mouvement par saccades d'un glacier. Comptes Rendus Hebdomadaires des Séances de l'Académie des Sciences, Paris, **247**, 228 - 230.

Liboutry, L., 1959. Une théorie du frottement du glacier sur son lit. Annales de Géophysique, **15**, 250 - 265.

Liboutry, L., 1968. General theory of subglacial cavitation and sliding of temperate glaciers. Journal of Glaciology, **7**, 21 - 58.

Lupini, J.F., 1980. The residual strength of soils. Unpublished Ph.D. thesis, University of London.

Lupini, J.F., Skinner, A.E. and Vaughan, P.R., 1981. The drained residual strength of cohesive soils. Géotechnique, **31**, 181 - 213.

MacAyeal, D.R., 1989. Large scale ice flow over a viscous basal sediment: theory and application to Ice Stream B, Antarctica. Journal of Geophysical Research, **94**, 4071 - 4087.

MacDonald, A.B. and Sauer, E.K., 1970. The engineering significance of Pleistocene stratigraphy in the Saskatoon area, Saskatchewan, Canada. Canadian Geotechnical Journal, **7**, 116 - 126.

Mathews, W.H., 1964. Water pressure under a glacier. Journal of Glaciology, **5**, 235 - 240.

Mathews, W.H., 1974. Surface profiles of the Laurentide ice sheet in its marginal areas. Journal of Glaciology, **13**, 37 - 43.

Mathews, W.H. and MacKay, J.R., 1960. Deformation of soils by glacier ice and the influence of pore pressures and permafrost. Transactions of the Royal Society of Canada, **54**, 27 - 36.

Meene, E.A. van de and Zagwijn, W.H., 1978. Die Rheinläufe im deutsch - niederländischen Grenzgebeid seit der Saale - Kaltzeit. Überblick neuer geologischer und pollenanalytischer Unterschungen. Fortschr. Geol. Rheinl. 4. Westfalen, **28**, 345 - 359.

Mohr, O., 1914. Abhandlungen aus den Gebiete der Technischer Mechanik. W. Ernst, Berlin, second edition.

Nye, J.F., 1951. The flow of ice sheets and glaciers as a problem in plasticity. Proceedings of the Royal Society, **207**, 554 - 572.

Nye, J.F., 1952a. The mechanics of glacier flow. Journal of Glaciology, **2**, 82 - 93.

Nye, J.F., 1952b. A method of calculating the thickness of the ice - sheets. Nature, **169**, 529 - 530.

Nye, J.F., 1953. The flow law of ice from measurements in glacier tunnels, laboratory experiments and the Jungfraufim borehole experiment. Proceedings of the Royal Society of London, **219**, 477 - 489.

Nye, J.F., 1957. The distribution of stress and velocity in glaciers and ice sheets. Proceedings of the Royal Society of London, **239**, 113 - 133.

Nye, J.F., 1959. The motion of ice sheets and glaciers. Journal of Glaciology, **3**, 493 - 507.

Nye, J.F., 1969. A calculation on the sliding of ice over a wavy surface using a Newtonian viscous approximation. Proceedings of the Royal Society, **311**, 445 - 467.

Nye, J.F., 1970. Glacier sliding without cavitation in a linear viscous approximation. Proceedings of the Royal Society of London, **315**, 381 - 403.

Nye, J.F., 1973. Water at the bed of a glacier. International Association of Scientific Hydrology, **95**, 189 - 194.

Nye, J.F., 1976. Water flow in glaciers: Jökulhaups, tunnels and veins. Journal of Glaciology, **17**, 181 - 207.

Orowan, E., 1949. Remarks at joint meeting of the British Glaciological Society, the British Rheologists Club and the Institute of Metals. Journal of Glaciology, **1**, 231 - 239.

Pannekoek, A.J. (ed.), 1956. Geological history of The Netherlands. Explanation to the general geological map of The Netherlands on the scale 1:200000. Staatsdrukkerij - En Uitgeverijbedrijf, 's-Gravenhage, 147pp.

Paterson, W.S.B., 1981. The Physics of Glaciers (second edition). Pergamon Press. 380pp.

Pons, A., Guiot, J., Beaulieu, J.L. de, and Reille, M., 1992. Recent contributions to the climatology of the last glacial - interglacial cycle based on French pollen sequences. Quaternary Science Reviews, **11**, 439 - 448.

Rijks Geologische Dienst, 1990. Nadere ordening van zoutstructuren ex fase I met de nadruk op (peri-)glaciale verschijnselen in de komende 100,000 jaar. Rapport 30,010. Haarlem.

Rappol, M., 1984. Till in southeast Drenthe and the origin of the Hondsrug Complex, the Netherlands. Eiszeitalter und Gegenwart, **34**, 7 - 27.

Rappol, M., 1987. Saalian till in the Netherlands: a review. In: Meer, J.J.M. van der, 'Tills and Glaciotectonics'. Balkema, Rotterdam, 3 - 21.

Rappol, M. and Stoltenberg, H.M.P., 1985. Compositional variability of Saalian till. Boreas, **14**, 33 - 50.

Rappol, M., Haldorsen, S., Jorgensen, P., Meer, J.J.M. van der, and Stoltenberg, H.M.P., 1989. Composition and origin of petrographically - stratified thick till in the northern Netherlands and a Saalian glaciation model for the North Sea basin. Meded. Werkgr. Tert. Kwart. Geol., **26** (2), 31 - 64.

Rendu, M. le C., 1841. Theorie des glaciers de la Savoie. Memoire de l'Academie des Sciences, Belles-Lettres et Arts de Savoie, **10**, 39 - 158.

Rooney, S.T., Blankenship, D.D., Alley, R.B., and Bentley, R.B., 1987. Till beneath Ice Stream B. 2. Structure and continuity. Journal of geophysical Research, **92**, 8913 - 8920.

Roscoe, K.H., Schofield, A.N. and Wroth, C.P., 1958. On the yielding of soils. Géotechnique, **14**, 77 - 102.

Röthlisberger, H., 1968. Erosive processes which are likely to accentuate or reduce the bottom relief of valley glaciers. Union de Geodesie et Geophysique Internationale d'Hydrologie Scientifique, Assemblee Generale de Berne, 25 Sept. - 7 Oct. 1967. IHSA, publication number 79, 87 - 97.

Röthlisberger, H., 1972. Water pressure in intra- and subglacial channels. Journal of Glaciology, **11**, 177 - 203.

Rubey, W.W. and Hubbert, M.K., 1959. Role of fluid pressure in mechanics of overthrust faulting; part II, overthrust belt in geosynclinal area of western Wyoming in light of fluid pressure hypothesis. Bulletin of the Geological Society of America, **70**, 167 - 206.

Ruiter, J. de, 1982. The static cone penetration test. State of the art report. Proceedings of the 2nd European Symposium on Penetration Testing, Amsterdam, 24 - 27.5.82, 389 - 405.

Sauer, E.K. and Christiansen, E.A., 1988. Preconsolidation pressures in an intertill glaciolacustrine clay near Blain Lake, Saskatchewan. Canadian Geotechnical Journal, **25**, 831 - 839.

Schmertmann, J.H., 1953. Estimating the true consolidation behaviour of clay from laboratory test results. Proceedings of the American Society of Civil Engineers, **79**, 1 - 26.

Schokking, F., 1984. Inventarisatie van slecht - doorlatende laagpakketten in de ondergrond van het Nederlandse vasteland. Rept. Rijks Geologische Dienst, OP 6009, Haarlem, 131pp.

Schokking, F., 1990a. A sub - glacial sediment deformation model from geotechnical and structural properties of an overconsolidated lacustro - glacial clay. Geologie en Mijnbouw, **69**, 291 - 304.

Schokking, F., 1990b. On estimating the thickness of the Saalian ice sheet from a vertical profile of preconsolidation loads of a lacustro - glacial clay. Geologie en Mijnbouw, **69**, 305 - 312.

Schuddebeurs, A.P. and Zandstra, J.G., 1983. Indicator pebble counts in the Netherlands. In: Ehlers, J. (ed.) "Glacial Deposits in North - west Europe". Balkema, Rotterdam, 357 - 360.

Schytt, V., 1969. Some comments on glacier surges in eastern Svalbard. Canadian Journal of Earth Sciences, **6**, 867 - 873,

Seret, G., Guiot, J., Wansard, G., Beaulieu, J.L. de, and Reille, M., 1992. Tentative palaeoclimate reconstruction linking pollen and sedimentology in La Grande Pile (Vosges, France). Quaternary Science Reviews, **11**, 425 - 430.

Shoemaker, E.M., 1986. Subglacial hydrology of an ice sheet resting on a deformable aquifer. Journal of Glaciology, **32**, 20 - 30.

Skempton, A.W., 1953. The colloidal activity of clays. Proceedings of the Third International Conference on Soil Mechanics and Foundation Engineering. Switzerland, **1**, 57 - 61.

Skempton, A.W., 1964. Long term stability of clay slopes. Géotechnique, **14**, 75 - 101.

Skempton, A.W., 1970. The consolidation of clays by gravitational compaction. Quarterly Journal of the Geological Society, **125**, 373 - 411.

Skempton, A.W., 1985. Residual strength of clays in landslides, folded strata and the laboratory. Géotechnique, **35**, 3 - 18.

Smith, G.N., 1982. Elements of Soil Mechanics for Civil and Mining Engineers (fifth edition). Granada, 493pp.

Staalduinen, C.J. van, Adrichem Boogaert, H.A. van, Bless, M.J.M., Doppert, J.W.Chr., Harsveldt, H.M., Montfrans, H.M. van, Oele, E., Wermuth, R.A. and Zagwijn, W.H., 1979. The geology of The Netherlands. Mededelingen Rijks Geologische Dienst, **31 - 2**, 9 - 49.

Stephan, H - J., 1983. XI. INQUA-Kongress Moskau, Bericht uber die Exkursion C-5 vom 11.-7.8.1982, Weissrussland. Eiszeitalter und Gegenwart, **33**, 117 - 180.

Sugden, D.E. and John B.S., 1976. Glaciers and Landscape. Edward Arnold, 376pp.

Terzaghi, K., 1925. Erdbaumechanik auf Bodenphysikalischer Grundlage. Deuticke, Vienna.

Terzaghi, K., 1936. Relation between soil mechanics and foundation engineering. Proceedings of the First International Conference on Soil Mechanics and Foundation Engineering, **3**, 13 - 18.

Terzaghi, K., 1943. Theoretical Soil Mechanics. Wiley, New York.

Todd, D.K., 1959. Ground Water Hydrology. John Wiley and Sons, Inc. 336pp.

Walder, J.S., 1982. Stability of sheet flow of water beneath temperate glaciers and implications for glacier surging. Journal of Glaciology, **28**, 273 - 293.

Ward, R.C., 1975. Principles of Hydrology (second edition). McGraw - Hill (U.K.) Ltd. 367pp.

Wee, M.W. ter, 1983a. The Saalian glaciation in the northern Netherlands. In Ehlers, J. (ed.), 'Glacial Deposits in North - west Europe'. Balkema, Rotterdam, 405 - 412.

Wee, M.W. ter, 1983b. The Elsterian glaciation in the Netherlands. In Ehlers, J. (ed.), 'Glacial Deposits in North - west Europe'. Balkema, Rotterdam, 413 - 415.

Weertman, J., 1957. On the sliding of glaciers. Journal of Glaciology, **3**, 33 - 38.

Weertman, J., 1962. Catastrophic glacier advances. Union Géodésique et Géophysique Internationale. Association Internationale d'Hydrologie Scientifique. Commision des Neiges et Glaces. Colloque d'Obergurgl, **58**, 31 - 39.

Weertman, J., 1964. The theory of glacier Sliding. Journal of Glaciology, **5**, 287 - 303.

Weertman, J., 1967. An examination of the Liboutry theory of glacier sliding. Journal of Glaciology, **6**, 489 - 494.

Weertman, J., 1972. General theory of water flow at the base of a glacier or ice sheet. Reviews of Geophysics and Space Physics, **10**, 287 - 333.

Weertman, J., 1979. The unsolved general glacier sliding problem. Journal of Glaciology, **23**, 97 - 115.

Weinberg, B., 1907. Uber die Koeffizienten der inneren Reibung des Gletschereises und seine Bedeutung fur die Theorien der Gletscherbewegung. Zeitschrift fur Gletscherkunde, **1**, 321 - 347.

Wildenborg, A.F.B., Bosch, J.H.A., Mulder, E.F.J. de, Hillen, R., Schokking, F. and Gijssel, K. van., 1990. A review: effects of (peri-) glacial processes on the stability of rocks. 6th International IAEG Congres, 2763 - 2770. Balkema, Rotterdam.

Wingfield, R., 1990. The origin of major incisions within the Pleistocene deposits of the North Sea. Marine Geology, **91**, 31 - 52.

Woodland, A.W., 1970. The buried tunnel - valleys of East Anglia. Proceedings of the Yorkshire Geological Society, **37**, 4 (22), 521 - 578.

Zagwijn, W.H., 1973. Pollenanalytical studies of Holsteinian and Saalian beds in the Northern Netherlands. Mededelingen Rijks Geologische Dienst, **24**, 139 - 156.

Zagwijn, W.H., 1974. The palaeogeographic evolution of The Netherlands during the Quaternary. Geologie en Mijnbouw, **53**, 369 - 385.

Zagwijn, W.H., 1975. Variations in climate as shown by pollen analysis, especially in the Lower Pleistocene of Europe. In: Wright, A.E. and Moseley, F. (eds.). "Ice Ages, Ancient and Modern". Geological Journal Special Issue No. 6, Seel House Press, Liverpool.

Zagwijn, W.H., 1985. An outline of the Quaternary stratigraphy of The Netherlands. Geologie en Mijnbouw., **64**, 17 - 24.

Zagwijn, W.H. and Doppert, J.W.C., 1978. Upper Cenozoic of the southern North Sea Basin: palaeoclimatic and palaeogeographic evolution. Geologie en Mijnbouw, **57**, 577 - 588.

Zandstra, J.G., 1976. Sedimentpetrographische Untersuchungen des Geschiebelehms von Emmerschans (Drenthe, Niederlande) mit Bemerkungen uber eine Typeneinteilung der Saale-Grundmorane. Eiszeitalter und Gegenwart, **27**, 30 - 52.

Zandstra, J.G., 1983. Fine gravel, heavy mineral and grain size analyses of Pleistocene, mainly glacigenic deposits in the Netherlands. In: Ehlers, J. (ed.) 'Glacial Deposits in North - west Europe'. Balkema, Rotterdam, 361 - 376.

Zandstra, J.G., 1987. Explanation to the map 'Fennoscandian crystalline erratics of Saalian age in the Netherlands. In: Meer, J.J.M. van der, 'Tills and Glaciotectonics'. Balkema, Rotterdam, 127 - 132.

Singer, J.K., Anderson, J.B., Ledbetter, M.T., McCave, I.N., Jones, K.P.N. and Wright, R., 1988. An assessment of analytical techniques for the size analysis of fine grained sediments. Journal of Sedimentary Petrology, **58**, 534 - 543.

Swift, D.J.P., Schubel, J.R. and Sheldon, R.W., 1972. Size analysis of fine grained suspended sediments: a review. Journal of Sedimentary Petrology, **42**, 122 - 134.

APPENDIX A

A.1 Geophysical Logs

A.1.1 Gamma Log

This measures the natural gamma radiation emitted by the sediment. It is generally used to differentiate between argillaceous and nonargillaceous rocks, the former being more radioactive. In Quaternary sediments, gamma emission is usually due to the decay of ^{40}K which occurs in feldspars and clay minerals. Thus the gamma log helps determine the grain size composition of the drilled strata, since clays are represented by relatively high values whilst sands are represented by relatively low values. Tills have intermediate values.

A.1.2 Electrical Resistivity Log

In this case an electric current is passed through the sediment. The ease of passage of electricity through rock is generally determined by pore volume and the nature of any pore fluid present. Coarse sands with fresh water in their pores are more resistant than clay, which is a conductor. This therefore provides information about grain size.

A.1.3 Spontaneous Potential Log

A potential difference is set up between the pore fluid and the fluid in the drilling mud, creating an electric current. An electrode measures the spontaneous potential with respect to a reference electrode at infinity. More negative values of spontaneous potential are obtained from more sandy/permeable formations whilst more positive values are found in clay rich/impermeable horizons. Thus permeable and impermeable units can be identified.

The combination of gamma, spontaneous potential and resistivity logs are used in this study to differentialte between clay and sand. The logs are illustrated in figure 3.11.

A.2 Definitions of Geotechnical Parameters

Bulk density (ρ_b)*. The mass of a material per unit volume. For undisturbed samples it is measured by weighing a sample tube of known volume (V), initially when empty (m_1), then when full of soil (m_2), such that the bulk density is given by;

$$\rho_b = \frac{m_2 - m_1}{V}$$

Dry density (ρ_d)*. The mass of dried material contained in unit volume of the undried material.

Unit weight (γ). The ratio of the total weight (i.e. mass, m, multiplied by the acceleration due to gravity, g) to the total volume (V) of the soil;

$$\gamma = \frac{m\,g}{V}$$

Moisture content (w). The ratio of the weight of water to the weight of solid grains, generally quoted as a percentage.

Liquid limit (LL). The moisture content at which a soil passes from the plastic state to the liquid state, as determined by the liquid limit test.

Plastic limit (PL). The moisture content at which a soil becomes too dry to be in a plastic condition, as determined by the plastic limit test.

Plasticity index (PI). The numerical difference between the liquid and plastic limits of a soil.

Liquidity Index (LI). A measure of the relative consistency of sediment. It gives the relationship between the natural moisture content and the liquid and plastic limits;

$$LI = \frac{w - PL}{LL - PL}$$

Activity. The plasticity index divided by the percentage dry weight of clay sized particles. It is a function of the mineralogy of the sediment, particularly the type of clay minerals present.

Particle size distribution. The percentage of the various grain sizes present in a soil as determined by sieving and sedimentation or by optical methods.

Clay fraction. The fraction of a soil composed of particles smaller than 2μm.

Undrained shear strength. The point at which failure occurs if a shear stress is applied to a sediment which is not allowed to drain.

Consolidation. The process whereby soil particles are packed more closely together over a period of time by application of a continued pressure.

Compaction. The process of packing soil particles more closely together by rolling or other mechanical means, thus increasing the dry density of the soil.

The above definitions are from BS 892 and the symbols from BS 1991, except where asterisked.

A.3 Results of Geotechnical Tests

Table 1: Results of the geotechnical tests carried out on the sediments from the Noord Bergum core by the R.G.D.

Sample No.	Depth (m)	Unit Weight (kNm^{-1})	Moisture Content (%)	Liquid Limit	Plastic Limit	Plastcity Index	Undrained Shear Strength (kNm^{-2})
NB1	5.5	17.0	24				
NB2	9.4	18.8	15				
NB4	14.5	19.5	17				
NB8	26.4	18.4	32	53	17	36	144
NB10	32.5	19.0	19				54
NB14	44.5	19.1	32	66	20	44	72
NB16	49.8	17.4	45				54
NB18	53.5	19.4	33	89	23	66	
NB19	56.5	17.7	37				
NB21	61.0	19.2	40				186
NB23	64.0	17.9	37	99	26	73	
NB24	65.5	17.7	35				54
NB25	68.5	18.0	38				
NB26	74.5	18.1	34				
NB28	77.5	18.0	53				264
NB29	80.5	18.9	32	91	23	68	276
NB31	86.5	19.7	26				
NB32	89.5	20.1	34				270
NB34	95.5	21.0	19	57	18	39	
NB35	98.5	20.8	18				
NB36	101.7	21.1	18				66
NB37	104.5	21.3	17	40	15	25	
NB38	107.5	21.1	20				324
NB41	116.5	20.2	17				
NB42	119.5	19.9	17				
TILL			20	40	20	20	150

A.4 Particle Size Analysis

This was undertaken to determine the proportion of clay size particles in the sediment. Two techniques were employed in this study. The R.G.D. used a sedimentation technique whilst a diffraction technique was used in Edinburgh.

A.4.1 Sedimentation Technique

The first method, carried out in the Netherlands, was a sedimentation technique. This method is based on the fact that, in a dilute suspension, particles settle at a rate depending on their size. Thus if the speed at which particles settle through a water column is observed their diameter can be determined from Stokes' Law;

$$v_s = \frac{d^2 (\rho_s - \rho_w) g}{18 \mu} \qquad \text{A.1}$$

where v_s is the settling velocity

d the particle diameter

ρ_s and ρ_w are the density of solids and water respectively

g is the acceleration due to gravity

μ the dynamic viscosity of the fluid.

Method: the sample to be tested is air dried and ground down using a pestle and mortar. It is then sieved on a series of standard sieves to determine the proportions of the coarser fractions ($> 35 \mu m$).

The finer fractions ($< 35 \mu m$) are determined by a sedimentation technique, in this case by pipette analysis.

20g of the fine sediment are suspended in water in a $1000cm^3$ measuring cylinder. A dispersant is included ($50cm^3$ sodium hexametaphosphate solution per $1000cm^3$ water) to prevent the fine particles from flocculating. The suspension is thoroughly mixed then allowed to stand, at which point a clock is started.

A pipette is inserted gradually into the fluid so that its tip is 20cm below the surface and $20cm^3$ of the suspension is withdrawn 58s from the beginning of the settling process. This is transferred into a beaker of known mass. Succesive $20cm^3$ aliquots

are extracted from specific depths in the column at specified time intervals which calculations have shown reveal particles of known diameter.

The beakers are placed in an oven at 100°C for 24 hours, cooled in a desiccator, and weighed.

Calculations / Results: the mass of each sample is determined and since each aliquot is 2% of the original sample the full size distribution can be calculated. The presence of dispersant must be considered, hence the difference in weight between succesive withdrawals is taken, as both contain the same amount of dispersant. A graph of grain size against percentage weight of sample is plotted and the fraction < 2μm determined.

A.4.2 Diffraction Technique

was chosen as only a small amount of sediment was available for analysis. It
This method, carried out in Edinburgh, uses the principle of Fraunhofer diffraction of laser light. The laser light is shone through a suspension of particles and is diffracted by an amount depending on the particle size. A concentric series of light rings is produced, their intensity depending on the number of particles of the relevant size present in the suspension. These are detected and the information sent to a computer which calculates the particle sizes present and their abundance.

Method: approximately 0.6g of the sediment was weighed out and placed in a 25cm^3 beaker with 10cm^3 of distilled water. This was left for 24 hours to allow the sample to disaggregate. If disaggregation was not complete after this period, the beaker was placed in an ultrasonic bath for 5 minutes then left for a further 24 hours. This was repeated until the sample had fully disaggregated. It was then put through a 500μm sieve and the filtrate transferred to a 100cm^3 sample bottle and filled up with distilled water. This was then analysed in the LS 100 coulter counter.

Calculations / Results: the results are given as a print out of particle diameter against percentage volume of sample. From this the volume % < 20μm can be calculated and statistical analysis carried out.

The results of the particle size analyses are presented in table 2, and figure A.1.

Table 2: Results of Particle Size Analysis

Sample No.	Depth (m)	Weight % < 2 μm	Volume % < 20μm	Mean Grain Size (mm)	Median Grain Size (mm)	Modal Grain Size (mm)
NB6	20.5	46				
NB7	23.5	64	78	15	10	12
NB8	26.4	49	59	28	15	12
NB9	29.5	50	76	17	10	12
NB10	32.5	23	44		30	173
NB11	35.5	79				
NB12	38.5	3				
NB14	44.5	80				
NB16	49.8	65	79	13	8	10
NB18	53.5	46				
NB19	56.5	83	91	7	4	4
NB21	61.0	82	94	7	4	4
NB22	62.5	78				
NB23	64.0	80	95	6	4	4
NB25	68.5	79	94	7	5	5
NB28	77.5	84				
NB29	80.5		96	7	6	5
NB32	89.5	41				
NB34	95.5		49	68	22	192
NB35	98.5		41	66	43	173
NB36	101.7	65	32	99	83	214
NB37	104.5		16	154	147	214
TILL			25	130	123	238

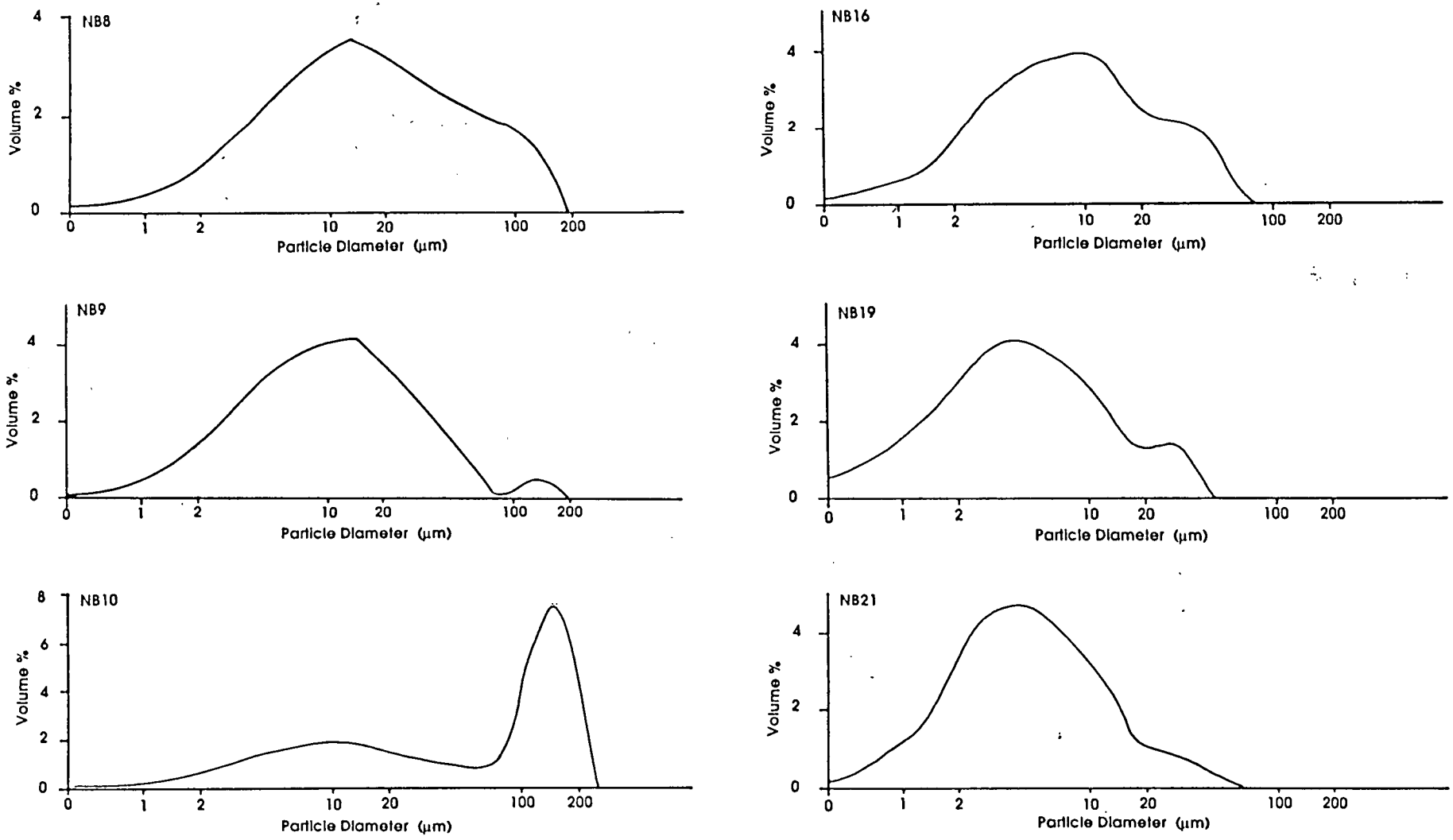

Figure A.1: Particle size distribution in sediment from the Noord Bergum borehole determined in the Coulter LS 100 analyser.

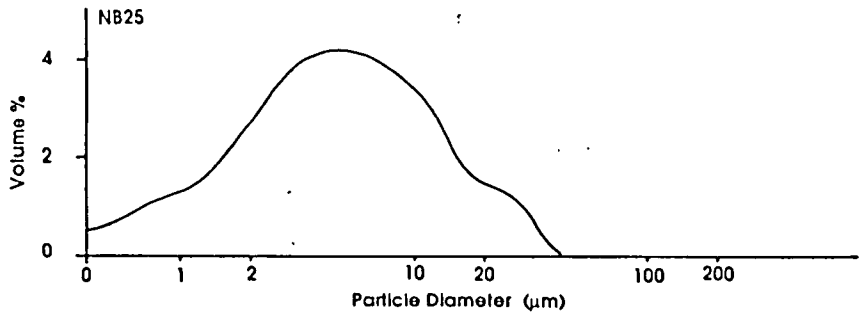

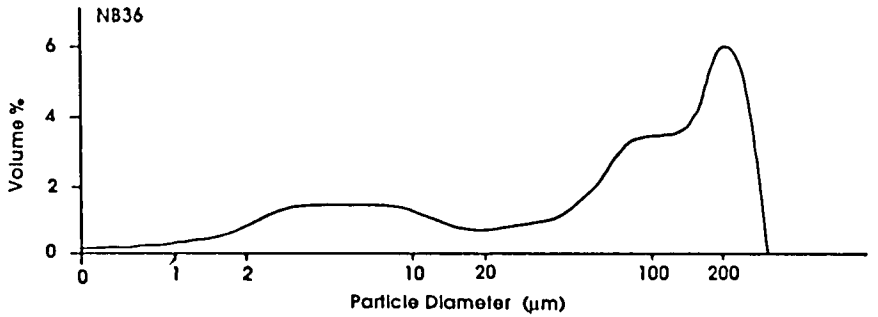

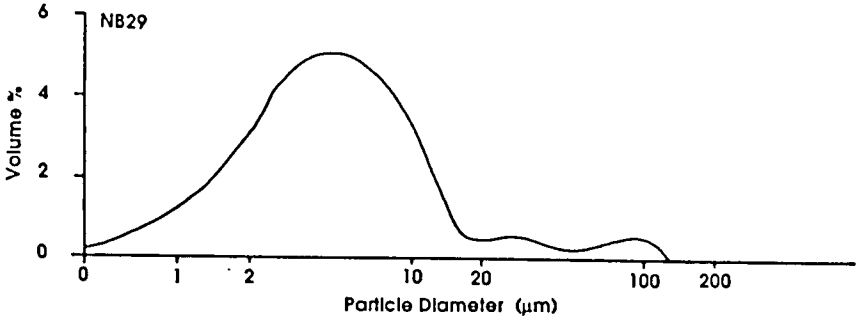

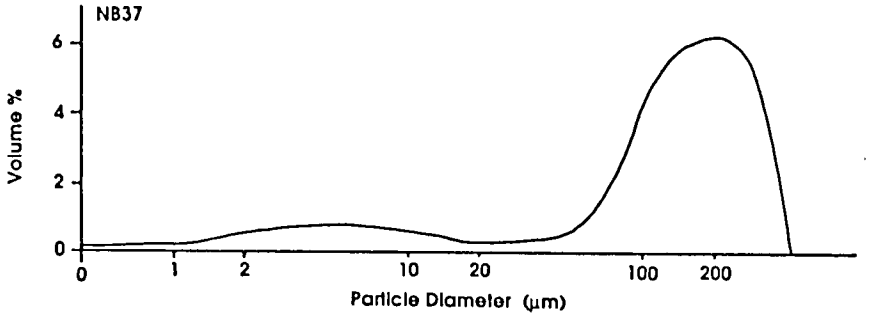

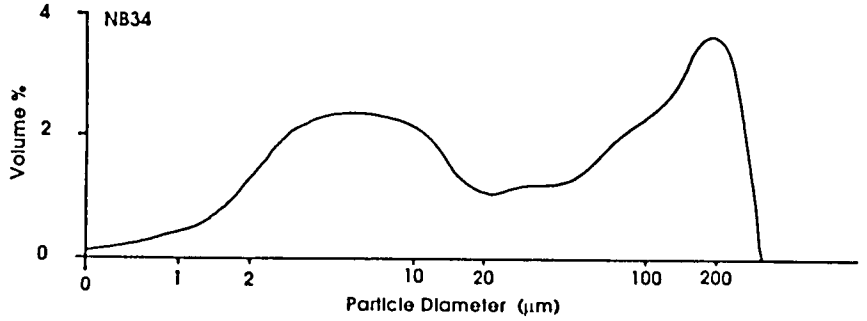

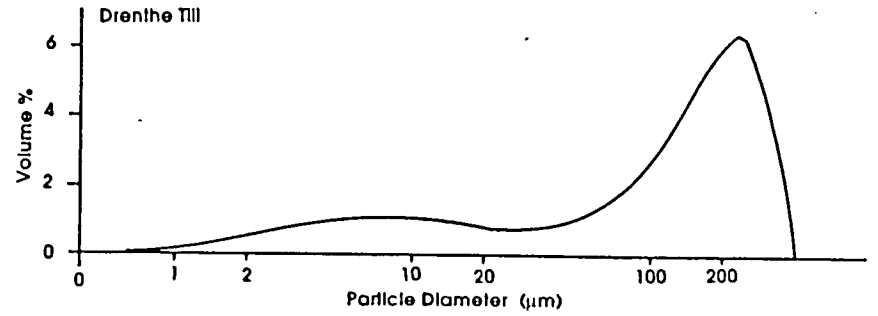

Figure A.1: (cont.) Particle size distribution in sediment from the Noord Bergum borehole determined in the Coulter LS 100 analyser.

A.5 X - Ray Diffraction Analysis

This is a routine technique used to identify minerals, especially clay minerals, in fine grained rocks. It exploits the fact that each mineral has a unique crystal structure and thus produces a unique diffraction pattern if bombarded with monochromatic x-rays. Braggs Law relates the incident wavelength of the radiation to the perpendicular spacing of the crystal planes and the angle of reflection from that plane. Braggs Law states that:

$$\lambda = 2d \sin\theta \qquad \text{A.2}$$

where λ is the incident wavelength

d is the perpendicular spacing of the crystal planes

θ is the angle of reflection from that plane.

The x-ray diffractometer uses monochromatic x-rays of known wavelength and measures the intensity of reflections at angles of 2θ obtained from the crystal planes in the sample. This gives a printout of intensity against 2θ on which peaks occur. Each mineral has a unique set of peaks which are stored on computer and can be compared to those occuring on the above plot, allowing the minerals present in a sediment to be identified. The experimental technique is outlined below.

Method: approximately 2g of the sediment was weighed out into a beaker and left to dry naturally. The sample was then ground down using a mortar and pestel and pressed into a small circular pellet in a sample holder. These pellets were then loaded into the APD 1700 x-ray diffraction machine and left to run. This gives information on the mineralogy of the whole sediment sample.

To determine the clay mineralogy, the pellets were returned to their beakers (as a powder) and $20cm^{-3}$ of distilled water added. The resulting suspension was mixed thoroughly and left to stand for two hours after which time the larger particles should have settled out. The remaining suspension was pipetted off and transferred to another beaker with a glass slide in the bottom. These were left until any remaining water had evaporated off. The glass slides were then placed in sample holders and loaded into the APD 1700 x-ray diffraction machine and left to run.

To obtain further information on the clay minerals present, nine of the samples were treated by placing the slides in a desiccator containing 0.25 l of ethylene glycol instead of the usual drying agent. They were left for 48 hours before being returned

to the APD 1700 x-ray diffraction machine. The ethylene glycol systematically intercalates itself into the lattice of "expanding" smectite group clays, changing the lattice spacing and thus the position of the diffraction peaks. This change can be identified on the diffraction trace.

Results: plots of 2θ against peak intensity are obtained from which it is possible to identify the minerals present in the sample. Examples of the x - ray diffraction traces are shown in the text.

A.6 Relationships Derived from the Geotechnical Tests

The liquidity index and activity were calculated for the Noord Bergum sediment samples and presented in table 3.

Table 3: Liquidity index and activity of the Noord Bergum sediment samples.

Sample No.	Sample Depth (m)	Liquidity Index	Activity
NB8	26.4	0.43	0.75
NB14	44.5	0.26	0.58
NB18	53.5	0.14	1.44
NB23	64.0	0.15	0.91
NB28	77.5	0.44	0.78
NB34	95.5	0.03	
NB35	98.5	0.12	
NB36	101.5	0.12	0.38

APPENDIX B

B1 The One Dimensional Consolidation Test

Object: to determine the consolidation characteristics of a low permeability sediment; specifically the preconsolidation pressure.

Principle: the test is carried out by applying a sequence of vertical loads to a laterally confined specimen and the vertical compression observed for a period of time (24 hours). Since no lateral deformation occurs the one dimensional consolidation characteristics are derived from the test. In practice, the water flow and displacements which occur during consolidation are normally three dimensional, however the analysis is complex and therefore not practical in this study.

Method: the apparatus required for the experiment is described fully in BS 1377 (1975). Since it is the past maximum pressure due to glacial loading that is of interest it is necessary to apply relatively high pressures to the sample and thus the experiment is carried out using Wykeham Farrance high loader oedometers (illustrated in figure B.1) with a 50mm diameter sample.

A sample, approximately 3cm in length, was cut from the end of the core section. The preweighed consolidation ring (50mm diameter, 20mm deep) is carefully pushed into the sample and the top and bottom surfaces pared off with a pallete knife until they are level with the ring. The sample thickness is measured and the ring and sample weighed. The moisture content of the clay is determined on the sample trimmings as described in section B.2.

Meanwhile the bottom porous stone is soaked in distilled water and placed centrally in the consolidation cell (shown in figure B.2). The ring and sample are positioned on top of the stone and secured in place by the ring retainer. The upper porous stone is placed on top of the sample and the whole cell positioned on the bed of the loading apparatus. After fixing the loading yoke in place, ensuring that the lever arm is adjusted such that it is inclined slightly above the horizontal and fixed in that position, a dial gauge is attached. This allows the relative change in height of the sample to be recorded. The dial gauge reading is noted.

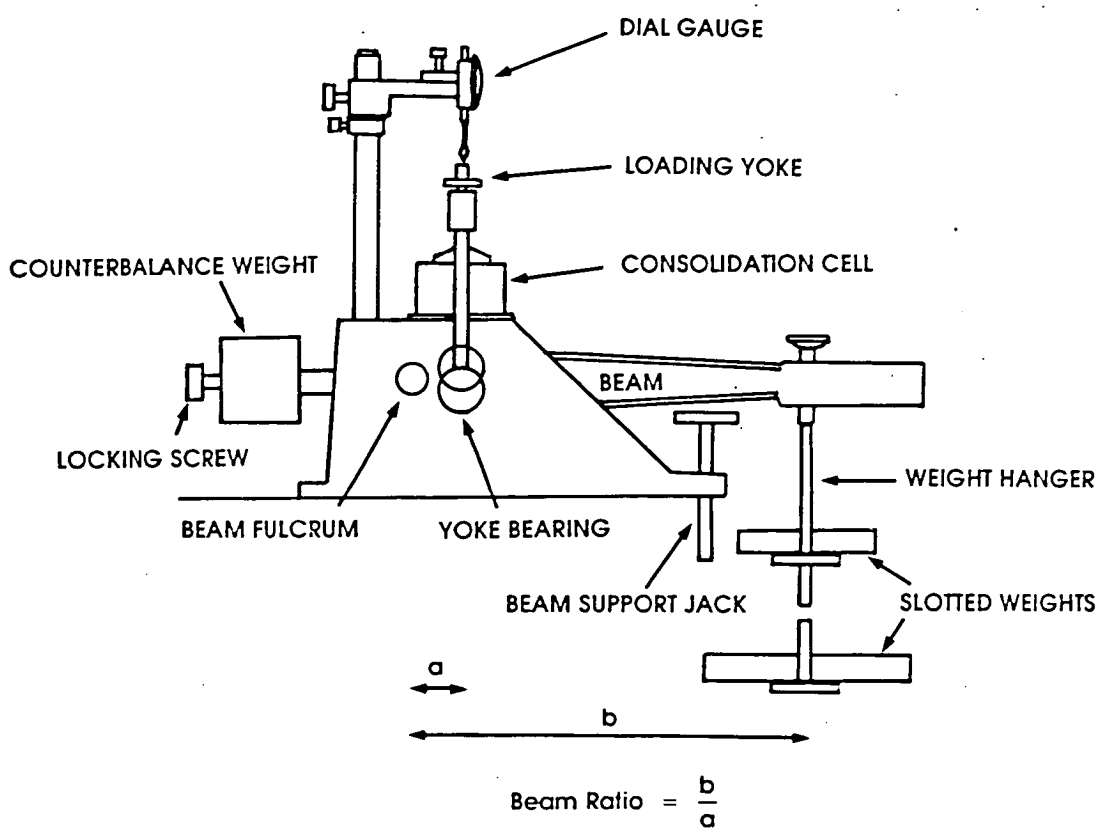

Figure B.1: General layout of the oedometer (modified from Head, 1982).

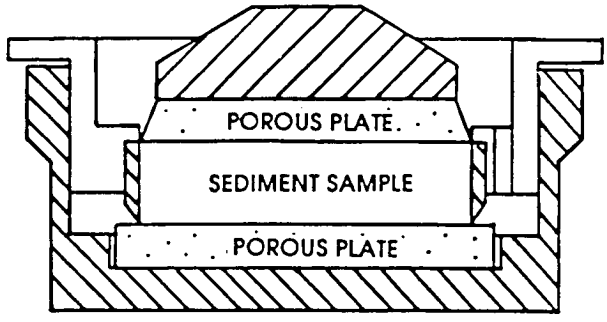

Figure B.2: The consolidation cell (BS 1377, 1975).

A loading sequence is devised taking into account the requirements of the preconsolidation pressure determination (described in section 4.3.2.iii). The weights giving a suitable initial pressure are added to the load hanger (the loading arm still held by the screw support), and the water bath surrounding the sample filled with distilled water at room temperature.

The beam support is then released, starting a clock at the same time. Dial gauge readings are taken at 0, 0.25, 0.5, 1, 2, 4, 8, 15, 30, 60 minutes and 2, 4, 8 and 24 hours later. After 24 hours, final readings of the dial gauge and clock are taken, the beam support screwed into place, and the next load increment applied. The beam support is again released, starting the clock, and readings of compression and time taken. This procedure is repeated as necessary until the maximum load increment has been applied whereupon the sample is unloaded. This is also done in stages, halving the load each time. It is not necessary to take readings throughout the 24 hour period; only initial and final measurements are required.

Once the sample has been unloaded, the loading apparatus is dismantled and the consolidation cell removed and drained. The sample in the ring is taken from the cell, weighed, and its thickness measured before transferring to a preweighed moisture content tin. It is dried in a thermostatically controlled oven at 105 - 110°C until it reaches constant mass, and the final moisture content calculated.

Calibration of the Apparatus: deformation of the apparatus must be allowed for when considering changes in sample height during the test and thus the load frame is calibrated. A metal disc, the same dimensions as the test specimen, with flat, smooth, parallel ends, is placed in the consolidation cell and the test set up as described above. After taking the dial gauge reading, the initial load is applied to the weights hanger and the dial gauge deflection noted. Load increments are then added in stages as in the consolidation test and the dial gauge readings for each stage recorded. This is repeated twice and a graph of compression against load plotted. A smooth curve drawn through the points is then taken as the calibration curve for the apparatus. The cumulative correction is subtracted from the cumulative settlement of the specimen at the end of each load increment to give the true settlement.

Results: from the results of the consolidation test, a graph of voids ratio against the log of the applied pressure, known as the e/logp curve, can be plotted. The preconsolidation pressure can be determined from the e/logp curve using the Casagrande (1936) construction. Further consolidation properties can be obtained

from the analysis of a plot of settlement against time for each load increment. A full explanation can be found in Head, 1982 and in BS 1377 (1975).

Calculations:

(i) Void Ratio Calculation

During consolidation volume change occurs in the voids only. The change in height δh of the sample from an initial height H_o corresponds to a change in void ratio δe from an initial value e_o. The actual change in height of the sample is the measured settlement less the correction for deformation of the apparatus.

The void ratio at the end of the test is calculated from the known mass of solids and liquids present in the sample at the end of the test obtained in the moisture content determination. Assuming the density of the solid particles to be 2700kgm^{-3}, a typical value for clay particles (Das, 1985), and water density to be 1000kgm^{-3}, the volumes of water and solids present can be calculated:

$$V_w = \frac{m_w}{\rho_w} \qquad \text{B.1}$$

$$V_s = \frac{m_s}{\rho_s} \qquad \text{B.2}$$

where m_s is the mass of solid particles
m_w is the mass of water
ρ_s is the density of solid particles
ρ_s is the density of water
V_w is the volume of solids
V_w is the volume of water.

The void ratio can then be calculated;

$$e = \frac{V_w}{V_s} \qquad \text{B.3}$$

where e is the void ratio.

The volume change δV for each load increment is calculated from the amount of settlement δh, corrected for rig stretch, occurring as a result of the applied load;

$$\delta V = \pi r^2 \delta h \qquad \text{B.4}$$

where r is the radius of the sample.

Since the volume change in the sample is assumed to be due entirely to the volume change in the voids (i.e. the volume of solids present is constant throughout the test), the void volume at the end of each loading stage can be determined and thus the voids ratio calculated.

This process is carried out in reverse from the information obtained at the end of the test to minimise errors arising from the fact that the initial sample may not have been fully saturated (although initially it is carried out from the beginning, and as the test proceeds, to monitor the shape of the curve). An example of an e/logp curve is given in figure B.3.

B.2 Moisture Content Determination (based on BS 1377:1975).

Object: to determine the moisture content of a sediment as a percentage of its dry mass.

Method: a dry, clean moisture content tin and lid are weighed (to the nearest 0.01g), and their mass noted (m_1). A sample of the material to be tested is placed in the tin, the lid secured, and the tin reweighed (m_2). The lid is then removed and, along with the tin and its contents, placed in a thermostatically controlled oven at 105 - 110 °C for 24 hours. After drying, the lid is replaced and the container and contents allowed to cool in a dessicator before being reweighed (m_3).

Calculations/Results: the moisture content is calculated as a percentage of the dry sediment mass from the equation;

$$w = 100 \left(\frac{m_2 - m_1}{m_3 - m_1} \right) \qquad \text{B.5}$$

where w is the moisture content, expressed as a percentage and quoted to two significant figures.

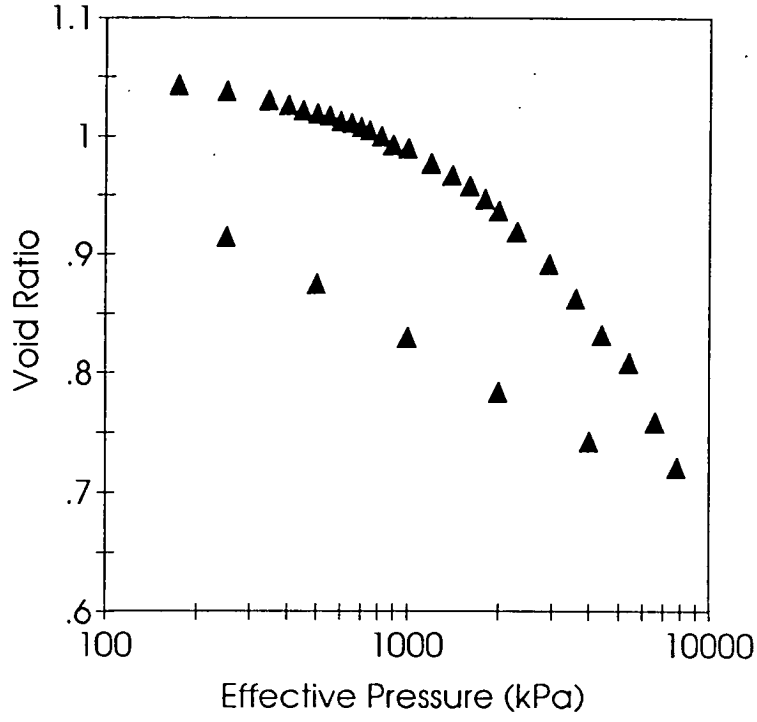

Figure B.3: A typical e/logp curve.

B.3 Consolidation Test Results for the Noord Bergum Borehole

B.3.1 Results of the Moisture Content Determinations

The moisture contents for the Noord Bergum samples were determined at the beginning and end of each consolidation test and are presented in table B.1.

Table B.1: Moisture content of the Noord Bergum samples at the end of the consolidation tests.

Sample No.	Sample Depth (m)	Moisture Content (%) at start of test	Moisture Content (%) at end of test
NB7	23.5	28.21	23.13
NB8	26.4	34.43	22.58
NB9	29.5	37.17	26.24
NB10	32.5	26.96	16.80
NB16	49.8	37.21	26.09
NB18	53.5	34.47	26.6
NB19	56.5	34.25	31.42
NB21	61.0	34.45	31.39
NB23	64.0	36.09	33.90
NB25	68.5	35.38	28.45
NB29	80.5	37.22	27.59
NB35	98.5	17.78	11.34
NB36	101.7	14.73	12.68

B.3.2 Results of the Void Ratio Calculations

The effective pressure and corresponding void ratio values for the consolidation tests carried out on the Noord Bergum samples are presented in table B.2.

Table B.2: Effective pressure and corresponding void ratio values for the consolidation tests.

NB7		NB8		NB9		NB10	
p' (kPa)	e	p' (kPa)	e	p' (kPa)	e	p' (kPa)	e
96.593	0.753	96.593	0.970	96.594	1.077	96.6	0.782
169.038	0.753	169.038	0.951	173.867	1.062	173.9	0.757
226.994	0.750	226.994	0.937	251.141	1.044	251.1	0.738
299.438	0.743	299.438	0.921	347.735	1.024	347.7	0.719
400.861	0.743	400.861	0.905	396.031	1.015	405.7	0.709
502.284	0.737	502.284	0.891	444.328	1.006	454.0	0.702
598.877	0.728	598.877	0.877	502.288	0.994	502.3	0.696
700.299	0.717	700.299	0.863	550.586	0.989	550.6	0.691
821.041	0.703	821.041	0.848	598.883	0.981	598.9	0.683
999.738	0.689	898.315	0.835	652.010	0.974	652.0	0.676
1197.753	0.675	999.738	0.826	700.307	0.970	700.3	0.671
1400.599	0.662	1197.753	0.804	748.604	0.964	748.6	0.667
1700.037	0.647	1400.599	0.783	821.041	0.953	821.0	0.659
1999.475	0.634	1700.037	0.756	898.324	0.932	898.3	0.652
2501.759	0.612	1999.475	0.731	999.748	0.928	999.7	0.644
2999.213	0.597	2501.759	0.696	1197.753	0.902	1226.7	0.624
3598.089	0.579	2999.213	0.667	1400.599	0.884	1497.2	0.606
4399.811	0.557	3598.089	0.638	1598.614	0.864	1748.3	0.593
5399.549	0.534	4399.811	0.607	1801.459	0.842	1999.5	0.581
6602.132	0.515	5399.549	0.575	1999.475	0.823	2506.6	0.560
7997.900	0.495	6602.132	0.545	2298.913	0.790	3197.2	0.538
3998.878	0.509	7785.396	0.521	2931.598	0.753	4003.4	0.517
1999.475	0.534	3998.878	0.527	3598.089	0.716	5201.5	0.489
999.738	0.564	1999.475	0.540	4399.811	0.680	6399.3	0.485
502.284	0.596	999.738	0.560	5399.549	0.653	7785.4	0.454
251.142	0.624	502.284	0.583	6602.132	0.607		
		251.142	0.610	7785.396	0.580		
				3998.950	0.590		
				1999.475	0.612		
				999.738	0.640		
				502.284	0.672		
				251.142	0.709		

Table B.2 cont

NB16		NB19		NB21		NB23	
p' (kPa)	e	p' (kPa)	e	p' (kPa)	e	p' (kPa)	e
96.593	1.037	96.594	0.977	96.593	0.988	96.594	1.044
169.038	1.005	173.867	0.973	169.038	0.985	173.867	1.043
226.994	0.982	251.141	0.965	226.994	0.983	251.141	1.038
299.438	0.956	347.735	0.954	299.438	0.978	347.735	1.030
400.861	0.929	400.861	0.950	400.861	0.971	400.861	1.026
502.284	0.911	449.162	0.945	502.284	0.966	449.162	1.022
598.877	0.890	502.288	0.941	598.877	0.960	502.288	1.019
700.299	0.870	550.586	0.938	700.299	0.954	550.586	1.017
821.041	0.851	598.883	0.935	821.041	0.947	598.883	1.013
898.315	0.838	652.010	0.932	999.738	0.937	652.010	1.011
999.738	0.828	700.307	0.929	1197.753	0.927	700.307	1.008
1197.753	0.804	748.604	0.926	1400.599	0.915	748.604	1.005
1400.599	0.781	821.041	0.921	1700.037	0.899	821.041	1.000
1700.037	0.755	898.324	0.914	1999.475	0.882	898.324	0.993
1999.475	0.733	999.748	0.910	2501.759	0.853	999.748	0.990
2501.759	0.703	1197.753	0.896	2999.213	0.832	1197.753	0.977
2999.213	0.677	1400.599	0.885	3598.089	0.804	1400.599	0.967
3598.089	0.651	1598.614	0.874	4399.811	0.767	1598.614	0.958
4399.811	0.624	1801.459	0.864	5399.549	0.727	1801.459	0.947
5399.549	0.595	1999.475	0.853	6602.132	0.698	1999.475	0.937
6602.132	0.567	2298.913	0.836	7997.900	0.659	2298.913	0.919
7997.900	0.539	2931.598	0.811	3998.878	0.682	2931.598	0.892
3998.878	0.560	3598.089	0.785	1999.475	0.720	3598.089	0.863
1999.475	0.592	4399.811	0.755	999.738	0.764	4399.811	0.832
999.738	0.629	5399.549	0.733	502.284	0.808	5399.549	0.809
502.284	0.678	6602.132	0.688	251.142	0.848	6602.132	0.759
251.142	0.704	7785.396	0.653			7785.396	0.721
		3998.950	0.679			3998.950	0.743
		1999.475	0.721			1999.475	0.784
		999.738	0.766			999.738	0.830
		502.284	0.808			502.284	0.875
		251.142	0.848			251.142	0.915

Table B.2 cont

NB25		NB29		NB35		NB36	
p' (kPa)	e	p' (kPa)	e	p' (kPa)	e	p' (kPa)	e
96.594	1.149	96.593	0.897	96.594	0.504	96.593	0.461
173.867	1.142	169.038	0.890	173.867	0.494	169.038	0.456
251.141	1.130	226.994	0.884	251.141	0.484	226.994	0.451
347.735	1.116	299.438	0.874	347.735	0.473	299.438	0.445
400.861	1.108	400.861	0.861	400.861	0.468	400.861	0.438
449.162	1.103	502.284	0.851	449.162	0.463	502.284	0.432
502.288	1.098	598.877	0.841	502.288	0.460	598.877	0.427
550.586	1.093	700.299	0.831	550.586	0.455	700.299	0.422
598.883	1.088	821.041	0.819	598.883	0.452	821.041	0.417
652.010	1.082	999.738	0.804	652.010	0.448	898.315	0.413
700.307	1.078	1197.753	0.789	700.307	0.445	999.738	0.411
748.604	1.073	1400.599	0.775	748.604	0.442	1197.753	0.404
821.041	1.066	1700.037	0.759	821.041	0.437	1400.599	0.398
898.324	1.060	1999.475	0.744	898.324	0.433	1700.037	0.390
999.748	1.053	2501.759	0.719	999.748	0.428	1999.475	0.383
1226.731	1.034	2999.213	0.702	1226.731	0.417	2501.759	0.373
1497.192	1.016	3598.089	0.680	1497.192	0.406	2999.213	0.365
1748.333	1.000	4399.811	0.653	1748.333	0.398	3598.089	0.356
1999.495	0.987	5399.549	0.623	1999.495	0.391	4399.811	0.346
2501.759	0.960	6602.132	0.599	2501.759	0.378	5399.549	0.335
3197.228	0.928	7997.900	0.568	3197.228	0.364	6602.132	0.324
3998.950	0.895	3998.878	0.590	3998.950	0.350	7997.900	0.313
5201.533	0.847	1999.475	0.623	5201.533	0.332	3998.878	0.315
6399.286	0.814	999.738	0.664	6399.286	0.321	1999.475	0.319
7997.900	0.768	502.284	0.705	7997.900	0.306	999.738	0.325
		251.142	0.745			502.284	0.332
						251.142	0.342

Table B.2 Cont.

NB18

p' (kPa)	e	p' (kPa)	e	p' (kPa)	e
109.916	1.019	2049.933	0.888	648.504	0.936
197.849	1.016			697.967	0.933
247.311	1.013	1099.16	0.896	747.429	0.931
302.269	1.008	549.58	0.915	796.891	0.928
351.731	1.005	318.756	0.933	851.849	0.925
450.655	0.995	197.849	0.949	901.311	0.923
500.118	0.991			1000.236	0.920
549.579	0.986	247.311	0.949	1247.547	0.908
599.042	0.982	302.269	0.948	1500.353	0.899
648.504	0.978	351.731	0.947	1747.664	0.891
697.967	0.974	401.193	0.945	2000.471	0.883
752.925	0.970	450.656	0.944	2599.513	0.863
802.387	0.964	500.118	0.942	3500.828	0.832
851.849	0.961	549.580	0.940	4599.985	0.799
1000.236	0.949	599.042	0.937	6199.262	0.758
1247.547	0.931	648.504	0.936	8001.885	0.718

B.3.3 Preconsolidation Results

The results of the preconsolidation pressure determinations are shown in table B.3.

Table B.3: Preconsolidation pressure values in the Noord Bergum sediments.

Sample No.	Sample Depth (m)	Preconsolidation Pressure (kPa)
NB7	23.5	850
NB8	26.4	750
NB9	29.5	1000
NB10	32.5	540
NB16	49.8	600
NB18	53.5	1500
NB19	56.5	1800
NB21	61.0	1800
NB23	64.0	2000
NB25	68.5	1700
NB29	80.5	1200
NB34	95.5	1300
NB35	98.5	700
NB36	101.7	900

B.4 The Cone Penetration Test

A cone penetration test was carried out by Delft Geotechnics for the University of Edinburgh and the R.G.D., close to the Noord Bergum borehole. A standard 10cm^2 cone with an apex angle of 60° was used for the test with a filter element, 3mm long, 6mm above the edge of the cone, to determine the pore pressure, and a 134mm long friction sleeve located above the conical tip to determine the side friction due to penetration. The excess pore pressure is found by stopping the test and allowing the pore pressure to dissipate to the equilibrium pressure. A 95m cone penetration test was carried out and the cone resistance, side friction and pore pressure measured simultaneously.

B.5 Dry Density and Porosity Measurements

The dry density of the sample was determined by the R.G.D. whilst the porosity was determined, where possible, at the preconsolidation pressure from void ratio calculations. The results are presented in table B.4 along with the calculated gravitational gradient.

Table B.4 Dry density and porosity of the sediment in the Noord Bergum borehole.

Sample No.	Sample Depth (m)	Dry Density (x 10^3 kgm^{-3})	Porosity	$(dp'/dz)_g$ ($kPam^{-1}$)
NB1	5.5	1.68	0.378	10
NB2	9.4	1.66	0.385	10
NB4	14.5	1.71	0.367	11
NB8	26.4	1.40	0.482	7
NB10	32.5	1.58	0.415	9
NB14	44.5	1.45	0.463	8
NB16	49.8	1.22	0.548	6
NB21	61.0	1.40	0.482	7
NB23	64.0	1.35	0.500	7
NB24	65.5	1.27	0.530	6
NB28	77.5	1.40	0.482	7
NB29	80.5	1.47	0.456	8
NB32	89.5	1.61	0.404	10
NB34	95.5	1.78	0.341	12
NB36	98.5	1.81	0.330	12
NB38	107.5	1.81	0.330	12
NB41	116.5	1.76	0.348	11
NB42	119.5	1.73	0.359	11

APPENDIX C

C.1 The Ring Shear Test

C.1.1 Apparatus

The ring shear apparatus used in this study is illustrated in figure C.1. It permits the determination of residual strength on a shear surface formed within the sediment sample away from the loading platens. The sample is annular in shape and contained within pairs of upper and lower rings. The radius of the inner ring is 50mm whilst the outer ring radius is 75mm. The sample, illustrated in figure C.2, is initially 20mm thick, allowing sediment containing coarse sand to be tested with an acceptable ratio of particle diameter to specimen thickness.

The sample is loaded vertically through annular platens by a dead load lever system. The lever ratio is 10.012:1 resulting in a vertical stress of 10kPa per kg applied. Drainage is obtained by means of sintered bronze plates screwed to the platens, while a perspex water bath prevents the sample from drying out during the test. The lower confining rings, loading platen and porous plate, are screwed onto the base plate which is carried on a rotating table and driven by a worm gear. The sample is placed between these rings. The upper rings are placed on top, and the top of the cell, with the upper porous plate attached, placed on top of the upper rings. The lower part of the sample is rotated, causing the upper half to react via a torque arm against a proving ring to which a dial gauge is attached. This allows the shear stress acting on the sample to be measured. The angular movement between the two halves of the specimen is measured by means of a vernier on a 360° protractor. The gap between the confining rings retaining the specimen can be adjusted to ensure that all stresses act across the sample and there is no metal to metal sliding contact. There is a slight but continuous loss of sediment through the gap throughout the test.

C.1.2 Results/Calculations

The direct results of a ring shear test are corresponding values of net normal load, total torque (measured as the "number of divisions" recorded on the proving ring) and angular displacement. Bishop *et al.*. (1971) considered several alternative assumptions for the determination of the stress-strain relationship and concluded that the most realistic choice was to assume that the sediment was plastic i.e. that the normal stress and the shear stress are uniformly distributed in the plane of relative

rotary motion (illustrated in figure B.2). This principle is used in the following calculations of residual shear stress.

The normal effective stress is obtained from

$$\sigma' = \frac{W}{\pi (r_2^2 - r_1^2)} \qquad \text{B.1}$$

where σ' is the normal effective stress,

W is the net normal load,

r_1 and r_2 are the inner and outer radii of the sample.

The shear stress is obtained from the torque. Mathematically this can be expressed as

$$M = \tau \int_{r_1}^{r_2} 2\pi r^2 \, dr \qquad \text{B.2}$$

where M is the torque,

t is the shear stress,

r is the radius.

The torque can also be obtained directly from the proving ring reaction;

$$M = F D a \qquad \text{B.3}$$

where F is the proving ring calibration factor (calculated to be 0.75 N (division)$^{-1}$),

D is the number of divisions recorded on the proving ring dial gauge,

a is the distance from the proving ring to the axis of the apparatus.

The residual shear strength (τ_r) can be calculated thus;

$$\tau_r = \frac{3 F D a}{2 \pi (r_2^3 - r_1^3)} \qquad \text{B.4}$$

The displacement used for the presentation of results is the "average" displacement and is computed at the mean radius of the sample so that;

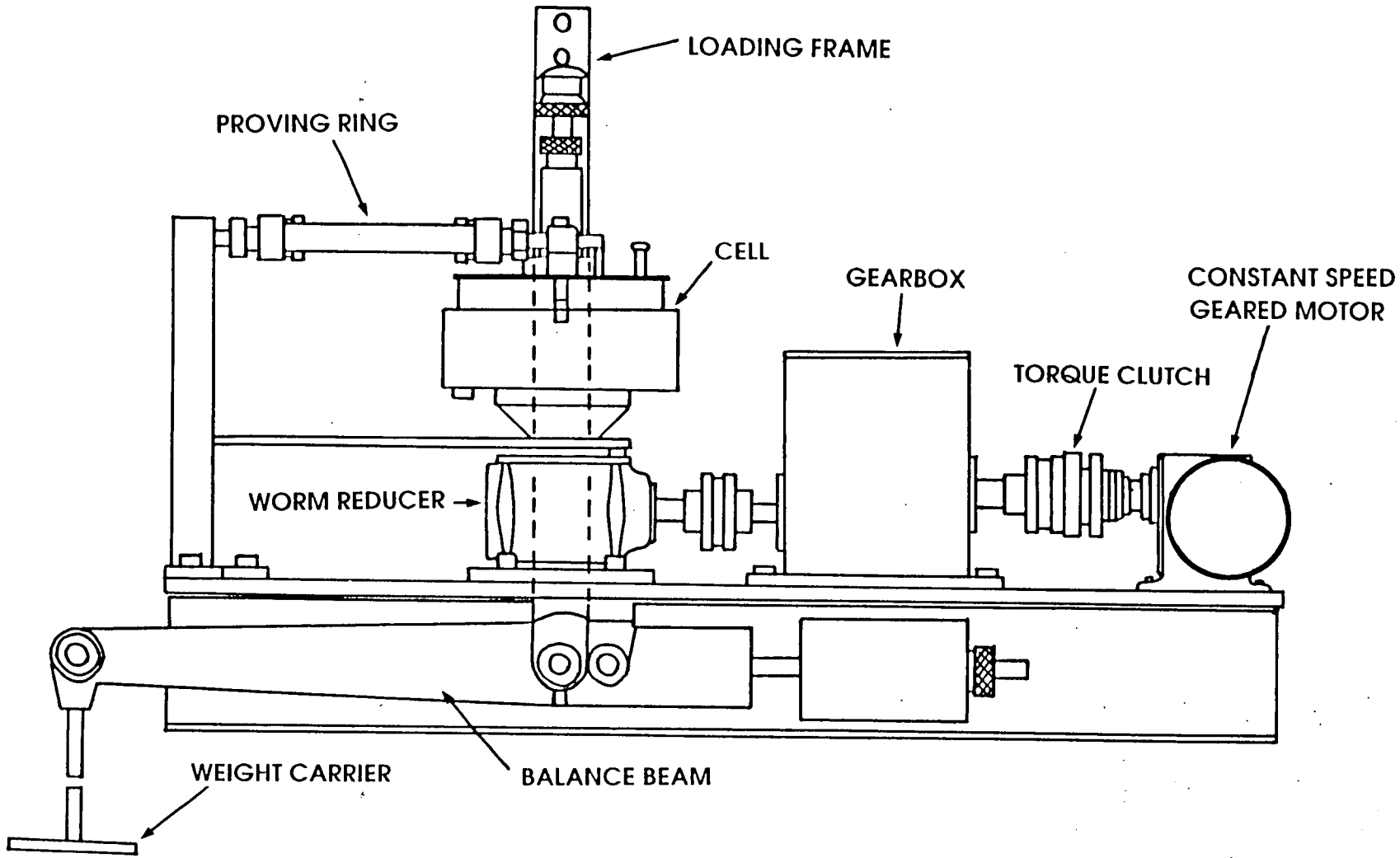

Figure C.1: General layout of the ring shear apparatus.

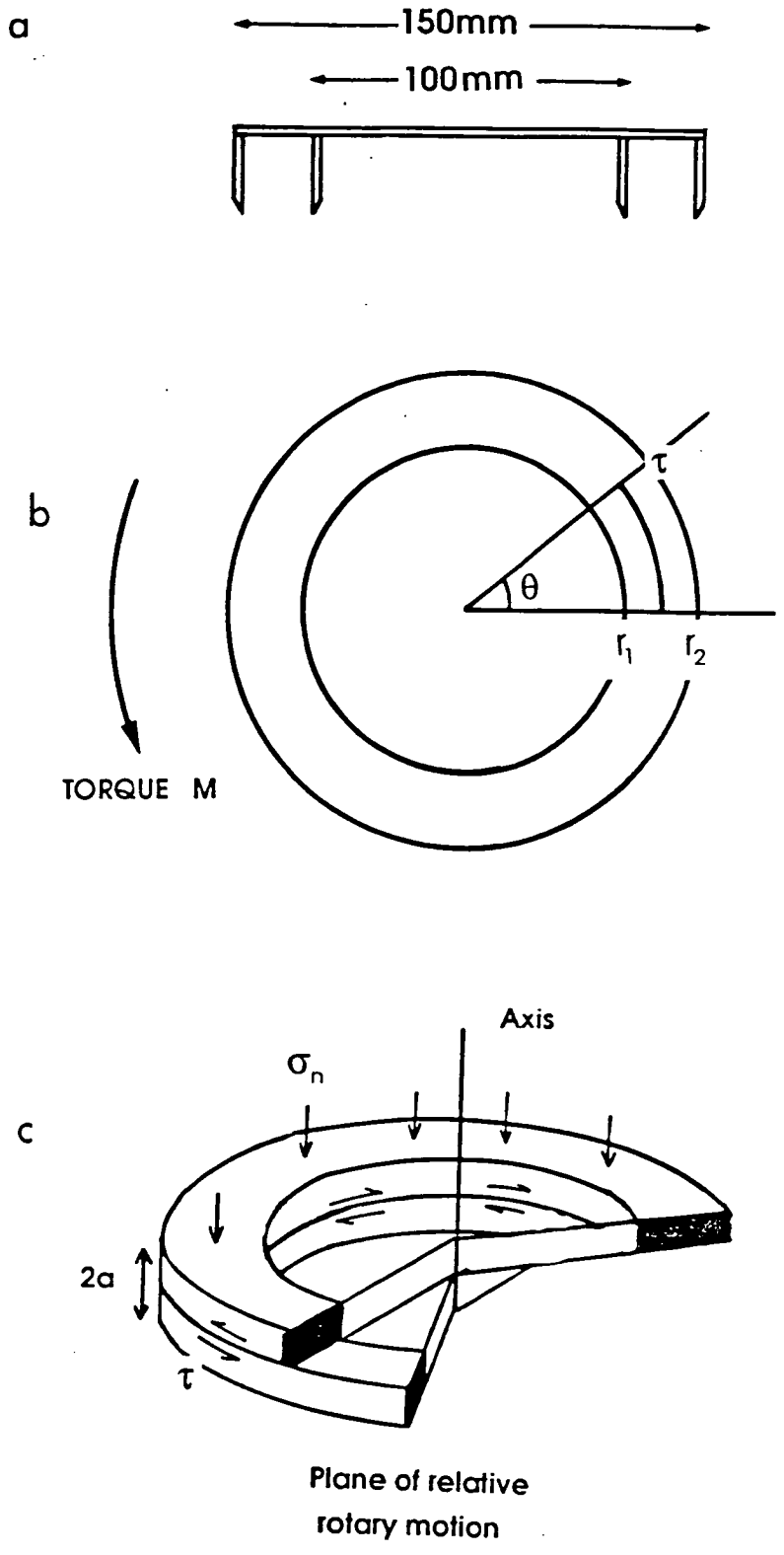

Figure C.2: (a) the sample cutter, (b) the sediment sample showing the relationship between the applied shear load and angular displacement and (c) the distribution of stresses in the ring shear sample on the plane of relative rotary motion.

$$d = \left(\frac{2\pi\theta}{360}\right)\left(\frac{r_1 + r_2}{2}\right) \qquad \text{B.5}$$

where d is the average displacement in units of length and θ is measured in degrees.

The residual strength is determined for each normal stress defining the residual shear envelope. From this, the residual angle of friction and cohesion can be calculated using the Mohr - Coulomb equation. This determination is described in the text.

C.2 Ring Shear Test Results

Key to the following tables of results:

Table	Test No.	Displacement Rate (ms^{-1})	Normal Stress (kPa)
1	3.1	5×10^{-8}	20
2	3.2	5×10^{-8}	40
3	3.3	5×10^{-8}	60
4	3.4	5×10^{-8}	80
5	3.5	5×10^{-8}	100
6	4.1	5×10^{-8}	100
7	4.2	5×10^{-8}	120
8	4.3	5×10^{-8}	140
9	4.4	5×10^{-8}	200
10	5.1	5×10^{-7}	100
11	5.3	5×10^{-7}	140
12	5.4	5×10^{-7}	150
13	5.6	5×10^{-7}	300
14	5.7	5×10^{-7}	400
15	5.8	5×10^{-7}	600
16	6.1	5×10^{-6}	100
17	6.2	5×10^{-6}	200
18	6.3	5×10^{-6}	300
19	6.4	5×10^{-6}	400
20	7.1	5×10^{-5}	100
21	7.3	5×10^{-5}	300
22	7.4	5×10^{-5}	400

C.2 Ring Shear Test Results

Table C.1: Ring Shear Test 3.1

Angular Disp. (°)	No. of Divisions	Angular Disp. (°)	No. of Divisions	Angular Disp. (°)	No. of Divisions	Angular Disp. (°)	No. of Divisions
0.1	0.75	0.4	81	1.3	85	2.5	84
0.1	2	0.5	82	1.4	85	2.5	84
0.1	6	0.7	82	1.6	85	2.6	81.5
0.1	8.5	0.7	81.5	1.7	81.0	2.8	81.5
0.1	13	0.7	81.5	2.2	85	3.1	78
0.1	22	1.0	84	2.2	85	3.2	79
0.1	34.5	1.0	87	2.2	79	3.3	79
0.1	44	1.1	89	2.2	85	5.9	73
0.2	62	1.2	87	2.3	86	5.9	73
0.2	71	1.2	87	2.3	87	6.0	74
0.2	75	1.2	86	2.3	86	6.0	74
0.2	78	1.2	85	2.3	85	6.0	74
0.3	79.5	1.3	85	2.4	85.5	6.1	74

Table C.2: Ring shear test 3.2

Angular Disp. (°)	No. of Divisions	Angular Disp. (°)	No. of Divisions	Angular Disp. (°)	No. of Divisions	Angular Disp. (°)	No. of Divisions
0	51	0.1	97	0.8	100.5	1.2	106
0	55	0.1	101	0.8	109.5	1.4	105
0	61	0.2	103.5	0.8	110.5	1.6	104.5
0	65	0.3	106	0.8	109	1.8	104.5
0.1	70	0.4	108	0.9	109	4.3	104.5
0.1	75	0.7	108	1.0	106.5	4.5	104.5
0.1	79	0.8	108	1.1	106.5		

Table C.3: Ring shear test 3.3

Angular Disp. (°)	No. of Divisions	Angular Disp. (°)	No. of Divisions	Angular Disp. (°)	No. of Divisions	Angular Disp. (°)	No. of Divisions
0	81	0.2	139	1.1	154	2.1	136
0	86.5	0.2	142	1.1	154	2.2	139.5
0	92	0.2	144	1.1	154	2.2	140
0	97.5	0.2	145.5	1.1	153.5	2.2	141
0	102.5	0.3	147.5	1.2	153.5	2.2	142.25
0.1	107.5	0.4	148	1.2	152.75	2.2	143
0.1	113	0.6	150	1.3	152.75	2.2	143
0.1	117	0.9	152	1.3	152.5	2.2	143
0.1	122.5	1	147	1.5	152.5	2.2	143
0.1	127	1	149.5	1.9	157	2.3	143.5
0.1	130	1	156	2	108	2.3	143.5
0.1	133	1.1	154	2	114	2.4	144
0.1	135	1.1	154	2.1	120	2.7	143.5
0.1	137	1.1	154	2.1	125	2.8	143.5
0.2	138	1.1	154	2.1	131	13.1	135.5

Table C.4: Ring shear test 3.4

Angular Disp. (°)	No. of Divisions	Angular Disp. (°)	No. of Divisions	Angular Disp. (°)	No. of Divisions	Angular Disp. (°)	No. of Divisions
0	117.5	0	153	0.1	171	0.4	182
0	123	0	156	0.1	177	0.6	183
0	129	0	160.5	0.2	178	0.8	183.5
0	135	0	164.5	0.2	178.5	3.6	183
0	141	0	168	0.2	179	3.7	183
0	146	0.1	169	0.3	181		

Table C.5: Ring shear test 3.5

Angular Disp. (°)	No. of Divisions	Angular Disp. (°)	No. of Divisions	Angular Disp. (°)	No. of Divisions	Angular Disp. (°)	No. of Divisions
0	166	0	198	0.1	219	1	233
0	171	0	202.5	0.1	224.5	3.6	238
0	177.5	0.1	205.5	0.2	227	3.7	239
0	183	0.1	209.5	0.3	227.5	3.8	240
0	187.5	0.1	213	0.4	229	3.9	242
0	193	0.1	217	0.5	230		

Table C.6: Ring shear test 4.1

Angular Disp. (°)	No. of Divisions	Angular Disp. (°)	No. of Divisions	Angular Disp. (°)	No. of Divisions	Angular Disp. (°)	No. of Divisions
0.1	58.5	0.2	118.5	0.6	208.5	1.8	244
0.1	61.5	0.2	126	0.6	211	1.8	245
0.1	65	0.2	134.5	0.6	215	1.8	244.75
0.1	68	0.2	141.5	0.6	215.5	1.8	244.25
0.1	71.5	0.3	149	0.7	218	1.8	243
0.1	75	0.3	155	0.8	222.75	1.9	240.75
0.1	77.5	0.3	165	0.9	234	1.9	241
0.1	80.5	0.3	168	1.3	236.75	1.9	235
0.1	83.5	0.3	171	1.6	235.75	1.9	236
0.1	86.5	0.3	175	1.6	232	2	237
0.2	90	0.3	179.5	1.6	231.25	2	237.5
0.2	92.5	0.4	183	1.6	230	2	237
0.2	95.5	0.4	186	1.7	233	2	236.5
0.2	98.5	0.5	190.25	1.7	238.5	2.1	236.5
0.2	101.5	0.5	194.75	1.7	244.5	2.1	236.75
0.2	104	0.5	201	1.7	250	2.1	237.5
0.2	107	0.5	203.5	1.8	239	2.1	239
0.2	109.5	0.5	205.75	1.8	241.5		

Table C.7: Ring shear test 4.2

Angular Disp. (°)	No. of Divisions	Angular Disp. (°)	No. of Divisions	Angular Disp. (°)	No. of Divisions	Angular Disp. (°)	No. of Divisions
0	203	0.5	482	1.1	498.5	3.8	457
0	209	0.6	492	1.2	494.5	3.8	462
0	215	0.6	483.5	1.3	492	3.8	467
0	222	0.6	487.5	1.4	492	3.8	471
0.1	226	0.7	490	1.6	491.5	3.9	475.5
0.1	232	0.7	494.5	1.8	491.25	3.9	480.5
0.1	238	0.7	499	2.0	485.5	3.9	485
0.1	243	0.8	498.5	2.6	486	3.9	486.75
0.1	248	0.8	502.5	2.6	480	3.9	487
0.1	253	0.8	506	2.6	484.5	4	483.5
0.1	257.5	0.8	507.5	2.6	483.5	4	479.5
0.1	263.5	0.8	506	2.6	435.75	4	478.5
0.1	268	0.9	505.5	2.6	487.5	4.1	478.25
0.1	282	0.9	504.75	2.6	488	4.1	477
0.1	296	0.9	503.5	2.6	486	4.1	476.4
0.1	299.5	0.9	503.25	2.7	485	4.2	472.75
0.1	304	0.9	502.5	2.7	484	4.3	464
0.1	319	1.0	501.75	2.7	482.75	4.4	461
0.1	349	1.0	501.25	2.7	481.5	4.6	454
0.1	378	1.0	500.75	2.9	482.5	4.8	449
0.1	402.5	1.0	501	3	475	5	449
0.1	426	1.0	501.25	3.1	466.5	5.5	445.75
0.2	444	1.1	501.25	3.3	460.5	6.2	428
0.2	457	1.1	501	3.6	449	7.4	451
0.4	473.25	1.1	499.5	3.8	466	7.5	450

Table C.8: Ring Shear Test 4.3

Angular Disp. (°)	No. of Divisions	Angular Disp. (°)	No. of Divisions	Angular Disp. (°)	No. of Divisions	Angular Disp. (°)	No. of Divisions
0.1	183	0.4	372.5	1.1	401	2.3	415.5
0.1	189	0.6	381	1.2	400.5	2.4	420.5
0.1	195	0.8	389	1.3	400.5	2.6	409.5
0.1	201.25	0.8	374	1.5	404	2.6	411
0.1	207.5	0.8	379	1.6	414	2.6	416
0.1	213	0.8	385.5	1.6	390	2.6	421
0.1	221	0.8	390	1.6	397.5	2.6	427
0.1	225	0.8	395	1.6	404	2.6	433
0.1	231	0.8	400.75	1.7	410	2.6	438
0.1	236.5	0.8	406	1.7	415	2.6	441
0.1	242.5	0.9	410.75	1.7	420	2.6	442.5
0.2	248	0.9	414	1.7	425.5	2.6	442.75
0.2	265	0.9	416.5	1.7	430.5	2.6	442
0.2	280.5	0.9	417.5	1.7	436	2.6	440
.2	294.5	0.9	418	1.7	439.5	2.6	439
0.2	307.5	0.9	416.25	1.7	442.5	2.7	437.5
0.2	316	0.9	412.5	1.7	439	2.7	431
0.2	317.5	0.9	409	1.8	432.5	2.8	430
0.3	324	1	406.75	1.8	418.5	3.0	428.5
0.3	332	1	404	1.9	417.5	3.2	428
0.3	346	1	403	2.0	416.5	3.4	432
0.3	355.5	1.1	401.25	2.2	416	3.6	433

Table C.9: Ring shear test 4.4

Angular Disp. (°)	No. of Divisions	Angular Disp. (°)	No. of Divisions	Angular Disp. (°)	No. of Divisions	Angular Disp. (°)	No. of Divisions
0	385	0.1	491	0.6	672.5	1.2	673
0	387	0.1	496.5	0.6	675.5	1.2	679
0	392	0.1	500	0.6	680	1.2	684
0	400	0.1	504	0.6	683	1.2	690.5
0	405.5	0.1	517	0.7	685.5	1.2	696
0	412	0.1	530	0.7	687.5	1.3	701.5
0	419	0.1	541	0.7	688.5	1.3	706
0	423	0.1	549.5	0.7	689	1.3	712
0	429	0.1	553	0.7	687	1.3	715.5
0	434	0.2	560	0.7	683	1.3	722
0	439	0.2	573	0.7	681	1.3	725
0	444	0.2	582.5	0.7	679	1.3	730
0	449	0.3	607.5	0.7	679	1.3	744.5
0	454.5	0.4	626	0.7	679	1.3	748
0	459	0.5	640.5	0.8	680	1.4	748.5
0.1	464	0.6	619	0.9	682	1.4	743.5
0.1	469	0.6	624	0.9	682.5	1.4	738
0.1	473	0.6	630	1.0	688.5	1.5	726
0.1	477.5	0.6	636	1.0	688.5	1.6	722
0.1	482.5	0.6	663.5	1.1	694	1.8	722
0.1	486	0.6	668	1.2	668	2.2	724

Table C.10: Ring shear test 5.1

Angular Disp. (°)	No. of Divisions	Angular Disp. (°)	No. of Divisions	Angular Disp. (°)	No. of Divisions	Angular Disp. (°)	No. of Divisions
0	8.5	2.1	261	5.6	322	8.2	338
0	18	2.2	260	5.8	323.5	8.4	338
0	29	2.3	262	5.9	321	8.5	337
0	37.5	2.4	266	6.0	315.5	8.7	335
0	47	2.5	271.5	6.1	318.5	8.8	337
0	55	2.6	274.5	6.3	324	8.9	338
0	61	2.7	280	6.4	328	9	338
0	67	2.8	280	6.5	329.5	9.1	339.5
0.1	74	2.9	280.5	6.6	329.5	9.2	340
0.1	90.5	3.1	283.5	6.8	327.5	9.4	341
0.1	102.5	3.2	290	6.9	327.5	9.6	341.5
0.1	128	3.4	291.5	7.0	327	9.6	340.5
0.2	142.5	3.5	297.5	7.1	331	10.6	342.5
0.3	151.5	3.6	302	7.3	335	10.6	340.5
0.4	159	3.7	302.5	7.4	336	10.8	340.5
0.4	171	3.8	304	7.4	309	10.9	340.5
0.5	173	3.8	305.5	7.4	320	11	338
0.7	176	4.0	310	7.4	331	11.1	338.5
0.8	186.5	4.1	311.5	7.4	342	11.3	336.5
0.8	196	4.3	312	7.4	350	11.5	335.5
0.9	202.5	4.3	293	7.5	356	11.6	337.5
0.9	208	4.4	319	7.5	360	11.7	335.5
1.1	216	4.5	320	7.5	360.5	11.8	333
1.3	224	4.6	322.5	7.5	359.5	11.9	332.5
1.4	232	4.8	320.5	7.5	357.5	13.6	337
1.4	238	4.9	318	7.6	355	14.8	340
1.6	239.5	5.0	324	7.7	343	15.7	333
1.7	246	5.1	324	7.8	340	19.3	341.5
1.8	250.5	5.2	320.5	7.9	339	21.1	345
1.9	256	5.4	319	8	338		

Table C.11: Ring shear test 5.3

Angular Disp. (°)	No. of Divisions	Angular Disp. (°)	No. of Divisions	Angular Disp. (°)	No. of Divisions	Angular Disp. (°)	No. of Divisions
0	153	2.1	530	6.7	556	10	552.5
0	165	2.2	536	6.8	553.5	10.2	553.5
0	177.5	2.3	537	6.8	533	10.2	534.5
0	190	2.4	536.5	6.9	547.5	10.2	545.5
0	201.5	2.5	539	6.9	558.5	10.2	559.5
0	212.5	2.7	540	6.9	568.5	10.2	575
0.1	223	2.8	532	6.9	571	10.2	580
0.1	233.5	3	527.5	7	572.5	10.2	583
0.1	243.5	3.1	530.5	7	572.5	10.2	578.5
0.1	254	3.2	538	7	572.5	10.2	565.5
0.1	263.5	3.3	547	7	570	10.3	563.5
0.1	274	3.4	548	7	567	10.3	563
0.1	281.5	3.5	552	7.1	567	10.3	560.5
0.1	299.5	3.7	555.5	7.1	569	10.3	556
0.1	325	3.8	555.5	7.2	571	10.4	551.5
0.1	336	3.9	557.5	7.3	571	10.4	548
0.1	351	4	561	7.4	575	10.4	547
0.2	363	4.2	558.5	7.6	564	10.5	543.5
0.3	388.5	4.3	559	7.8	562	10.6	534.5
0.3	403	4.4	559	7.9	565.5	10.7	535
0.4	420	4.5	559.5	8	567	10.9	535.5
0.4	437	4.6	559.5	8.2	563	11	530.5
0.5	445	4.8	557	8.3	560.5	11.1	527.5
0.6	452.5	5	550.5	8.4	564	11.2	523.5
0.7	463.5	5.2	551	8.5	567	11.3	525.5
0.9	477.5	5.3	551	8.6	573	11.4	526
1	489	5.3	551	8.8	575	11.6	509
1.1	491.5	5.4	551.5	8.9	571	11.8	515
1.2	507	5.6	548	9	571	11.9	518.5
1.3	512	5.9	549.5	9.2	570.5	12.1	525.5
1.4	514	6	547	9.3	565	12.2	528
1.6	519	6.2	551	9.4	564.5	12.3	525.5
1.7	524	6.3	552	9.5	558.5	13.5	532
1.8	528	6.4	563	9.6	554	13.9	525.5
2	531.5	6.5	569	9.8	552	14.1	528.5

Table C.12: Ring shear test 5.4

Angular Disp. (°)	No. of Divisions	Angular Disp. (°)	No. of Divisions	Angular Disp. (°)	No. of Divisions	Angular Disp. (°)	No. of Divisions
0	8	3.9	660	13.1	626	30.8	610.5
0	20	4	660.5	13.2	625.5	31	613
0	30.5	4.1	658	13.5	616	31.2	613
0	40.5	4.3	658.5	13.6	614	32.4	605
0	49	4.4	661	16.5	606	32.4	604.5
0	56.5	4.5	670.5	17.6	610	32.6	602
0	62.5	4.9	679.5	18.9	621	32.8	602.5
0	68.5	5	684	20.2	620.5	32.9	608.5
0	73.5	5.1	686.5	20.4	613	33	603
0	80	5.2	680	20.5	613	33.1	605.5
0	84	5.4	678.5	20.6	612	33.2	606
0	89	5.5	676	20.8	607	33.3	605.5
0	95	5.6	671	21	608.5	33.4	606.5
0	110.5	5.6	645.5	21.1	614	35.5	590
0.1	124.5	5.6	653	21.2	619	58.8	562
0.1	153	5.6	664	21.3	622.5	58.9	566
0.1	183	5.6	673	21.4	616	59	566
0.1	217.5	5.6	677	21.4	586	59.1	569
0.1	248	5.6	678	21.4	596.5	59.5	576.5
0.1	280.5	5.6	677.5	21.4	607.5	59.7	577
0.1	312.5	5.7	676.5	21.4	619.5	59.9	573
0.1	346.5	8.8	648.5	21.4	630	60	566.5
0.2	382	8.9	651	21.5	640	60.1	563
0.2	399.5	9.1	648	21.5	649	60.2	562
0.3	436	9.2	624.5	21.5	657	60.5	562
0.3	449	9.2	634.5	21.5	661	60.6	565.5
0.4	472	9.2	644.5	21.5	662	60.8	570.5
0.5	488.5	9.2	655	21.5	659	60.9	572
0.5	515	9.2	665	21.6	645	61	573.5

Table C.12: cont. Ring shear test 5.4

Angular Disp. (°)	No. of Divisions	Angular Disp. (°)	No. of Divisions	Angular Disp. (°)	No. of Divisions	Angular Disp. (°)	No. of Divisions
0.5	532	9.2	673.5	21.7	643	61.1	571
0.6	545	9.2	678	21.8	641	62.8	557.5
0.7	560.5	9.2	679	21.9	642	62.9	558.5
0.8	577	9.2	675.5	22	630	63	556.5
0.9	586	9.3	672	22.2	616	63.4	562
1	598	9.3	670	22.4	606	63.6	556.5
1.1	610	9.5	644	22.5	598	63.7	558
1.2	619.5	9.7	644.5	22.7	596.5	63.9	552
1.3	626	9.9	642	22.9	596.5	64	547
1.5	631.5	10	636.5	23	600	64.1	545
1.6	640.5	10.1	637	23.1	601	64.2	549
1.7	642	10.3	643	23.2	600.5	64.3	549
1.8	648	10.5	646.5	23.3	598.5	64.4	551
2	653.5	10.6	645	27.3	601	64.5	556
2.1	656	10.7	639.5	27.4	603	64.7	559.5
2.3	654	10.9	634.5	27.6	608.5	64.9	560
2.4	656	11	633.5	29.2	620	65	564
2.5	656.5	11.1	634.5	29.4	617	65.1	564
2.6	657	11.2	633	29.5	619	65.2	565
2.7	657	11.3	633.5	29.6	621	65.3	566
2.8	658	12	629	29.8	620.5	65.4	549.5
3	659.5	12.1	629	29.9	619	65.6	551
3.1	659.5	12.2	629.5	30	618.5	69	570.5
3.2	657.5	12.4	631.5	30.1	614	69.1	568
3.3	657.5	12.6	630.5	30.2	616	69.2	566
3.5	659	12.7	630	30.3	618	69.3	566
3.6	661	12.9	629	30.5	615.5	69.4	564
3.7	662	13	628	30.6	613	69.5	556.5

Table C.13: Ring shear test 5.6

Angular Disp. (°)	No. of Divisions	Angular Disp. (°)	No. of Divisions	Angular Disp. (°)	No. of Divisions	Angular Disp. (°)	No. of Divisions
0	14	0.8	1422	4.6	1447	48.8	1350
0	16.5	0.8	1466	4.7	1442	49	1357
0	23.5	0.9	1479	5.2	1435	49.1	1355.5
0	29	1	1483.5	5.6	1417.5	49.3	1357
0	35.5	1.1	1487	6	1407.5	50.5	1339.5
0	40.5	1.3	1485.5	6.5	1401	50.7	1340.5
0	46	1.4	1485.5	6.9	1386	50.8	1338.5
0	78	1.6	1486.5	7.3	1382.5	50.9	1338
0	122	1.7	1486	7.7	1368	51.1	1337
0	159	1.9	1482.5	9.8	1342	51.2	1338.5
0	197.5	2	1484.5	10.1	1334.5	52.8	1326
0	235	2.1	1484	11	1318	53.2	1325.5
0	272	2.3	1483.5	12.6	1300	54.6	1332
0	312	2.5	1481	15.1	1278.5	57.8	1313.5
0	358.5	2.6	1478	39.4	1327	67.8	1292.5
0	411	2.8	1478	39.5	1322.5	82.7	1290
0.1	434	2.9	1476.5	39.6	1324.5	82.8	1280
0.1	481	3	1470.5	39.7	1322	83	1273.5
0.1	522	3.1	1468.5	39.8	1324	83.1	1277.5
0.2	567	3.1	1401	39.9	1322.5	83.3	1262
0.2	612.5	3.1	1413	40	1321.5	83.4	1260
0.2	660	3.1	1427	41	1314.5	83.5	1263
0.2	706.5	3.1	1440.5	41.7	1318	83.6	1269
0.3	800	3.1	1454	47.5	1324.5	83.7	1280
0.3	847	3.1	1466.5	47.7	1288	88.8	1284
0.3	891	3.1	1478.5	47.7	1300	84.1	1277.5
0.3	935	3.1	1489	47.7	1313	84.2	1279.5
0.4	1058	3.1	1499	47.7	1325	84.3	1276
0.4	1099	3.2	1509	47.7	1338	84.4	1276
0.4	1142.5	3.2	1517	47.7	1349.5	84.6	1275.5
0.4	1180	3.2	1524.5	47.7	1363	84.7	1274
0.5	1226	3.2	1529	47.7	1374	84.8	1268.5
0.5	1252	3.2	1530	47.7	1382	84.9	1269.5
0.5	1287.5	3.2	1527	47.8	1398	85.1	1269.5
0.5	1322	3.3	1519.5	47.8	1409	86.4	1260.5
0.6	1345.5	3.5	1490	47.8	1410	86.6	1255.5
0.6	1366	3.6	1484.5	47.9	1406	86.7	1258
0.8	1400	3.8	1481	47.9	1384.5	86 .8	1259
0.8	1365	3.9	1471	48	1381	87	1257.5
0.8	1376	4.1	1459	48.2	1378.5	87.1	1257.5
0.8	1373.5	4.2	1459	48.4	1375	87.2	1260.5
0.8	1399	4.4	1457	48.5	1377	87.3	1261.5
0.8	1411	4.5	1452	48.7	1367	87.4	1260

Table C.14: Ring shear test 5.7

Angular Disp. (°)	No. of Divisions	Angular Disp. (°)	No. of Divisions	Angular Disp. (°)	No. of Divisions	Angular Disp. (°)	No. of Divisions
0	0	1.6	1893.5	10.1	1873.5	33.5	1710.5
0	23	1.7	1907	10.5	1872	33.7	1696.5
0	23	1.8	1919.5	10.9	1881	33.8	1697
0	23	1.9	1925	11.2	1882	33.9	1665.5
0	29	2	1921.5	11.8	1881.5	34.1	1658
0	38	2.1	1917	14.1	1835.5	34.2	1674.5
0.1	47	2.2	1914.5	14.7	1830.5	34.3	1691
0.1	55	2.3	1914.5	14.9	1824.5	34.5	1693.5
0.1	62	2.5	1913.5	15.2	1827.5	34.7	1702
0.1	70	2.7	1913	15.7	1826.5	60.6	1744
0.1	77	3.8	1909.5	16.7	1827	60.7	1744
0.1	82.5	3.9	1909.5	16.8	1825.5	60.8	1742
0.1	93	4.1	1910.5	17.1	1822.5	60.9	1742.5
0.1	101	4.4	1898	17.7	1817.5	61	1748
0.1	116.5	4.6	1892.5	18	1817	61.1	1755
0.1	135	4.8	1895	19.2	1815.5	61.2	1759
0.1	164.5	4.9	1896.5	23.7	1795	61.4	1762
0.1	196	5	1895.5	23.7	1732	61.5	1763.5
0.1	232	5.1	1891.5	23.7	1743.5	61.6	1768.5
0.1	266	5.3	1883.5	23.7	1757.5	61.7	1769
0.1	305.5	5.5	1874	23.7	1769.5	61.8	1768.5
0.1	350	5.6	1863	23.8	1783	62	1766.5
0.1	392.5	5.7	1873.5	23.8	1795	62.9	1764
0.1	435	5.8	1879.5	23.8	1807	63	1761.5
0.1	491.5	5.9	1812	23.8	1818	63.1	1763
0.1	529	5.9	1823	23.8	1830	63.3	1765
0.1	576.5	5.9	1835.5	23.8	1842	63.5	1765.5
0.2	623	5.9	1848	23.8	1870	63.6	1765.5
0.2	721.5	5.9	1860	23.8	1891.5	63.7	1764.5
0.2	759.5	5.9	1873	23.8	1894	63.9	1759.5
0.2	854	5.9	1887	23.8	1888	64	1757.5

Table C.14: cont. Ring shear test 5.7

Angular Disp. (°)	No. of Divisions	Angular Disp. (°)	No. of Divisions	Angular Disp. (°)	No. of Divisions	Angular Disp. (°)	No. of Divisions
0.2	989.5	5.9	1898	23.9	1869.5	64.1	1756.5
0.2	1126.5	5.9	1910	24.1	1822	64.2	1757.5
0.3	1256.5	5.9	1922	24.3	1816.5	64.3	1760
0.3	1376	5.9	1934.5	24.5	1813	64.5	1760
0.3	1413	5.9	1945	24.6	1817.5	64.6	1763
0.4	1448.5	5.9	1954	24.8	1815.5	67.6	1743
0.5	1484	5.9	1962	24.9	1814.5	67.7	1746.5
0.5	1516.5	5.9	1969.5	25	1816	67.8	1740
0.5	1549	5.9	1975	25.3	1821.5	67.9	1733
0.6	1581	6	1977	25.7	1804	68	1738.5
0.7	1608	6	1975	26	1782.5	68.1	1746
0.7	1635	6.1	1962	26.3	1785	68.2	1746.5
0.7	1664.5	6.3	1901	27.8	1799	68.4	1741
0.7	1633	6.5	1882.5	28.1	1758.5	68.6	1740.5
0.7	1645.5	6.7	1870.5	28.2	1761	68.7	1740
0.7	1657	6.8	1866	28.4	1763.5	68.8	1739
0.7	1669.5	6.9	1867	28.6	1772	68.9	1746
0.7	1679.5	7.1	1871.5	28.7	1785	69	1747
0.7	1689.5	7.2	1873	28.8	1789	70.8	1737.5
0.8	1698.5	7.3	1873.5	28.9	1775	70.9	1740.5
0.8	1739	7.5	1873	30.1	1773.5	71	1742
0.9	1770	7.5	1874.5	30.2	1780	71.1	1745
0.9	1792.5	7.7	1877.5	30.4	1782	71.3	1750
1	1794.5	8	1871.5	31.6	1769.5	71.5	1747
1.1	1800	8.1	1870	31.7	1764.5	71.6	1742.5
1.2	1814.5	8.3	1872	31.8	1751	71.7	1740.5
1.3	1832.5	8.5	1873	32	1732.5	71.8	1733
1.4	1849	9	1876.5	32.2	1731.5	71.9	1735.5
1.5	1862.5	9.3	1876.5	33.1	1733	72.1	1744
1.5	1879.5	9.8	1872.5	33.3	1728	72.2	1752.5

Table C.15: Ring shear test 5.8

Angular Disp. (°)	No. of Divisions	Angular Disp. (°)	No. of Divisions	Angular Disp. (°)	No. of Divisions	Angular Disp. (°)	No. of Divisions
0	10	0.7	2438	3.6	2565.5	6.5	2469
0	10	0.7	2453	3.6	2577	6.6	2497
0	10	0.7	2395	3.6	2588	6.7	2509.5
0	10.5	0.8	2434	3.6	2598	6.8	2517
0	14	0.8	2471	3.6	2608	6.9	2515.5
0	27	0.9	2504	3.6	2617.5	7	2497.5
0	46	1.1	2538	3.6	2627	7.2	2488
0	87	1.2	2546	3.6	2636	7.8	2485
0	117.5	1.3	2558	3.6	2645	7.9	2487.5
0	144	1.4	2566.5	3.6	2653	8	2482.5
0	174.5	1.5	2571.5	3.6	2660.5	8.2	2466
0	208	1.6	2578	3.6	2665.5	11.1	2430.5
0	241.5	1.7	2578.5	3.6	2668	11.3	2432
0	280.5	1.8	2575.5	3.6	2668	11.4	2435
0	321.5	2.1	2568	3.7	2661	11.5	2438
0.1	362.5	2.2	2559	3.7	2651	11.6	2441
0.1	754	2.3	2556	3.7	2640	11.7	2442
0.1	847	2.4	2556.5	3.8	2629	11.8	2439
0.1	973	2.6	2551.5	4	2590	12.3	2431.5
0.1	1034	2.7	2548	4.3	2508.5	12.7	2424
0.1	1176	2.9	2547	4.4	2519	14.4	2410
0.2	1310	3.1	2542	4.5	2527	14.7	2417
0.2	1902.5	3.2	2537.5	4.6	2532.5	15.2	2417
0.2	1946	3.3	2537	4.7	2533.5	15.5	2413
0.3	2142	3.4	2539.5	4.8	2538	15.8	2412
0.4	2130	3.5	2450.5	5	2545	42.4	2270
0.4	2216	3.5	2463	5.1	2546	42.5	2268
0.5	2295	3.5	2475.5	5.3	2508.5	42.6	2272
0.5	2361	3.5	2489	5.5	2511	42.7	2268.5
0.5	2372.5	3.5	2502.5	5.6	2512	42.9	2263
0.6	2358	3.5	2515.5	5.7	2527	43.1	2264
0.6	2367	3.5	2530	5.8	2526	43.2	2267
0.6	2378	3.6	2542.5	6.1	2516.5	43.3	2275
0.7	2412.5	3.6	2555	6.3	2484		

Table C.16: Ring shear test 6.1

Angular Disp. (°)	No. of Divisions	Angular Disp. (°)	No. of Divisions	Angular Disp. (°)	No. of Divisions	Angular Disp. (°)	No. of Divisions
0	24.5	5.2	433.5	32.1	444.5	55.7	461
0	91.5	5.5	437.5	33.4	463	55.9	448.5
0.1	158.5	5.7	436	34	466.5	56.2	460.5
0.1	211.5	5.9	440.5	34.7	462.5	56.7	454.5
0.2	259.5	6.2	434.5	36	454.5	57	439.5
0.3	311.5	6.4	445.5	37.4	454.5	58.6	447.5
0.5	338.5	6.8	439.5	38.7	425.5	59.7	444.5
0.7	361.5	7	435.5	40.2	440.5	60.9	450.5
0.9	371.5	7.3	438.5	41.1	463	62.1	444
1.1	384.5	7.6	438.5	42.6	451.5	63.6	439.5
1.3	401	9.2	413.5	43.8	426.5	64.9	442.5
1.6	399.5	10.2	420.5	45.1	455.5	66.2	434.5
1.9	407	11.6	421.5	46.5	443	67.4	446.5
2.1	418	12.9	435	47.8	461	68.8	440.5
2.4	419.5	14.2	426	49.1	459.5	70.1	435.5
2.6	428.5	14.8	426	50.3	455.5	74.1	441.5
2.9	429.5	16.8	429.5	51.7	462	78.3	438.5
3.1	435.5	23.8	423.5	52.9	458	90.3	432.5
3.4	436.5	24.5	444.5	54.2	447	91.2	440
3.6	454.5	24.7	452	54.3	432	92.6	441.5
3.9	461.5	25.7	437.5	54.3	449.5	93.8	439
4.2	435.5	27	432	54.6	461	95.1	438
4.4	440.5	28.3	432.5	54.9	461	96.5	432.5
4.7	440.5	29.7	429.5	55.1	455	97.8	435.5
5	445.5	30.8	439.5	55.4	467	99	448

Table C.17: Ring shear test 6.2

Angular Disp. (°)	No. of Divisions	Angular Disp. (°)	No. of Divisions	Angular Disp. (°)	No. of Divisions	Angular Disp. (°)	No. of Divisions
0	426.5	33.2	620	42.8	1068.5	92	924.5
0	553.5	33.2	743.5	43.1	1066	92.2	921.5
0	651.5	33.3	838.5	43.3	1066	92.4	924.5
0	738.5	33.5	855	43.6	1064	92.6	924
0.2	785.5	33.8	893.5	43.9	1060	92.9	921.5
0.4	809.5	34	918.5	44.1	1056	93.1	923.5
0.6	815.5	34.2	938.5	44.4	1055	95.3	920.5
0.9	830.5	34.4	957.5	44.7	1060.5	95.6	912.5
1.2	843.5	34.6	968.5	44.9	1058.5	95.8	906.5
1.3	856	34.9	986.5	45.2	1057	96	900.5
1.5	856	35.1	1005.5	45.8	1051	96.4	899
1.8	847	35.4	1013	46.6	1057	97.2	899.5
2.1	859.5	35.6	1028.5	47.8	1060.5	97.4	911.5
2.3	865	35.8	1036.5	49	1068	97.7	906
2.5	860.5	36	1046.5	50.4	1071.5	97.9	904.5
2.8	861.5	36.3	1048.5	51.7	1066.5	98.2	901
3.1	861.5	36.5	1057	52.9	1062.5	98.4	904
3.4	863.5	36.8	1055	59.6	1020.5	104	918.5
3.6	880.5	37.1	1057	60.8	1031	104.4	928.5
3.8	897.5	37.3	1058	64.7	1017.5	104.6	928
4	924.5	37.6	1055	68.5	1006	104.8	930.5
4.2	927.5	37.8	1060.5	72.3	988.5	105.1	929
4.4	929	38.1	1062	76.5	962.5	105.4	928.5
4.8	927.5	38.3	1062	76.6	936.5	105.7	935
5.1	919.5	38.6	1062	76.7	1015.5	106.2	922.5
5.3	904.5	38.9	1060	76.8	990.5	107.6	889.5
5.6	899.5	39.1	1064.5	77	966	108.6	916
6.9	915.5	39.5	1067	77.4	963	110.1	908.5
8.2	925.5	39.7	1068	77.6	961	111.4	929
9.7	927.5	39.9	1068	77.9	956	112.7	935.5
10.8	933.5	40.2	1067.5	78.1	951	113.9	928
12.1	935.5	40.5	1066.5	78.4	954	115.3	929.5
13.4	927.5	40.8	1067.5	78.7	945.5	116.5	925.5
14.7	939.5	41	1068.5	79.9	953.5	118.1	947.5
16.2	900.5	41.2	1071	81.3	951.5	119.6	896.5
17.4	898	41.5	1064.5	82.6	944.5	120.6	898.5
21.3	903	41.8	1065.5	83.9	937	121.8	896.5
25.3	849.5	42.1	1068	85.3	936	123.1	902.5
29.2	842.5	42.3	1068.5	87.9	929.5	124.4	909.5
33.2	823.5	42.5	1071	90.6	911.5		

Table C.18: Ring shear test 6.3

Angular Disp. (°)	No. of Divisions	Angular Disp. (°)	No. of Divisions	Angular Disp. (°)	No. of Divisions	Angular Disp. (°)	No. of Divisions
0	0	6.3	1445.5	98.2	1297.5	137.8	1309
0.1	68	6.8	1448.5	102.3	1301	139.3	1335
0.1	130	7.6	1430	105.7	1322	140.5	1341
0.1	184	8.9	1424	106	1295	141.9	1331
0.1	240	10.3	1417	106	1422	143.1	1348.5
0.1	307	11.6	1401	106.3	1400	144.4	1346
0.1	377.5	12.8	1399.5	106.7	1368	145.7	1338.5
0.2	436	14.1	1408	106.9	1347	147	1347
0.2	491	15.4	1418	107.2	1349	149.9	1352
0.2	552.5	16.7	1417	107.6	1348	150.5	1356
0.2	616	18	1424	107.8	1344	152.1	1357
0.3	687.5	19.2	1410	109.1	1336	153.5	1350
0.3	757.5	23.4	1386	110.4	1342.5	154.8	1361
0.4	832	27.1	1363	111.7	1352.5	179.7	1384.5
0.5	910	31.6	1352	113	1322.5	181.1	1287
0.6	985	36	1364	114.4	1321	182.3	1298
0.6	1054	53.3	1203	115.7	1296.5	183.6	1299
0.7	1117	55.1	1230	117	1287.5	184.8	1309.5
1	1252	58.9	1195	118.4	1308.5	186.1	1307
1.5	1295	62.9	1202.5	119.6	1315	187.5	1293.5
1.9	1343	66.8	1245	120.9	1328.5	188.8	1297
2.5	1387	70.7	1263	122.2	1322.5	190.1	1293.5
2.9	1426.5	74.9	1250	123.6	1315	191.7	1275
3.6	1451.5	78.6	1265.5	133.6	1312.5	192.7	1290.5
4.3	1443	82.5	1278	134	1323	194	1270
4.9	1428	91.6	1287.5	135.2	1320.5	195.5	1266.5
5.6	1437	94.3	1294	136.6	1312	196	1236.5

Table C.19: Ring shear test 6.4

Angular Disp. (°)	No. of Divisions	Angular Disp. (°)	No. of Divisions	Angular Disp. (°)	No. of Divisions	Angular Disp. (°)	No. of Divisions
0	0	5.4	1781.5	14.2	1873	38.4	1954
0.1	73	5.6	1776	16.8	1850.5	39.5	1974
0.1	135	5.8	1787	18.2	1853	41.3	1965
0.1	203	6.1	1802.5	19.6	1847.5	42.2	1953
0.1	272	6.1	1800	20.9	1856.5	43.5	1923
0.1	753	6.6	1808	22.2	1877	71.2	1945
0.1	1023	6.8	1825	23.6	1889	72.3	1933
1.3	1005.5	7.1	1836	24.7	1890.5	73.4	1936
1.8	1338	7.3	1848	28.6	1922	73.9	1898
2.3	1428	7.5	1854.5	32.3	1913.5	74.6	1962.5
2.8	1490.5	7.7	1869	32.6	1912.5	75.9	1985
3.1	1418	7.9	1886.5	33.1	1917.5	77.2	2011
3.2	1520	8.2	1911	33.6	1920.5	78.4	2035
3.4	1579	8.4	1922.5	33.7	1847.5	79.6	2033.5
3.5	1618	8.7	1906.5	33.7	1984	80.8	2034
3.6	1644	9	1905.5	33.8	2013	82.2	2043.5
3.7	1680	9.3	1911	34.3	1970	83.6	2042
4.1	1694	9.5	1908.5	34.7	1954	84.7	2037
4.3	1707.5	9.7	1914.5	34.8	1954	88.7	2055
4.5	1724	10.1	1884	35	1956	91.8	2073
4.7	1740.5	10.3	1915.5	35.3	1958	92.2	2011
5	1753	11.6	1877	35.6	1962.5	92.6	2028
5.2	1770	0.13	1874	36.8	1962	96.7	2018

Table C.20: Ring shear test 7.1

Angular Disp. (°)	No. of Divisions	Angular Disp. (°)	No. of Divisions	Angular Disp. (°)	No. of Divisions	Angular Disp. (°)	No. of Divisions
0	0	26.5	667.5	59.2	581	184.8	489.5
1.1	413	29	672	65.9	577	187.9	524
3.5	564	31.8	648	79.1	550.5	190.4	510
5.8	615	34.3	648	92.1	517	203.5	506
8.4	650.5	36	637	105.5	515	216.4	518
11.1	644	39.4	638	118.4	532	229.4	498
13.8	658	42.1	613	131.4	510.5	245.1	499
16.4	657.5	44.5	625	145	512	255.3	533
18.9	663	47.4	613	158	514.5	269	498
21.8	665.5	50.1	607.5	171.2	480.5	281.5	563
24	668	52.9	602	184.3	495.5	294.4	579

Table C.21: Ring shear test 7.3

Angular Disp. (°)	No. of Divisions	Angular Disp. (°)	No. of Divisions	Angular Disp. (°)	No. of Divisions	Angular Disp. (°)	No. of Divisions
0	51	16	1268	68.5	1260	127.2	1295
0.1	295	18.6	1265	73.8	1277.5	132.7	1289
0.1	710	21	1225	80.3	1250.5	139.2	1265
0.1	1140	23.7	1248	86.8	1280	145.7	1290
3.7	1030	26.1	1302.5	93.3	1280	152.3	1282.5
5.8	1115	28.8	1292.5	106.7	1265	158.7	1272.5
8.2	1215	48.8	1272	113.2	1270	165.7	1252.5
10.7	1258	54.1	1270	119.6	1286	172.3	1232.5
13.1	1255	60.8	1287.5				

Table C.22: Ring shear test 7.4

Angular Disp. (°)	No. of Divisions	Angular Disp. (°)	No. of Divisions	Angular Disp. (°)	No. of Divisions	Angular Disp. (°)	No. of Divisions
0	37	7.8	1585	29.9	1595	101.3	1714
0.1	395	10.6	1595	36.7	1637	114.1	1706
0.1	785	12.9	1630	42.7	1690	127.6	1742
0.1	1240	16	1575	49	1697.5	143.8	1720
2.2	985	19	1585	62.3	1657.5	153.3	1704
3.2	1320	21	1568	75.3	1717	166.7	1710
5.3	1501	23.3	1571	88.1	1715		

C.3 Residual Shear Strength for Till in the Ring Shear Tests

Table C.23: Effective pressure/shear strength results of ring shear test 4.

Displacement Rate (ms^{-1})	Effective Pressure (kPa)	Residual Shear Strength (kPa)
4.7×10^{-8}	100	28.1
4.7×10^{-8}	120	41.5
4.7×10^{-8}	140	51.2
4.7×10^{-8}	200	86.0

Table C.24: Effective pressure/shear strength results of ring shear test 5.

Displacement Rate (ms^{-1})	Effective Pressure (kPa)	Residual Shear Strength (kPa)
4.7×10^{-7}	100	40.3
4.7×10^{-7}	140	62.8
4.7×10^{-7}	150	66.9
4.7×10^{-7}	300	151.1
4.7×10^{-7}	400	207.3

Table C.25: Effective pressure/shear strength results of ring shear test 6.

Displacement Rate (ms^{-1})	Effective Pressure (kPa)	Residual Shear Strength (kPa)
4.7×10^{-6}	100	52.2
4.7×10^{-6}	200	109.0
4.7×10^{-6}	300	153.6
4.7×10^{-6}	400	222.5

Table C.26: Effective pressure/shear strength results of ring shear test 7.

Displacement Rate (ms^{-1})	Effective Pressure (kPa)	Residual Shear Strength (kPa)
4.7×10^{-5}	100	60.0
4.7×10^{-5}	300	151.7
4.7×10^{-5}	400	204.2

APPENDIX D

D.1 Ice Flow Model for the Northern Netherlands

Table D.1: Distribution of strain rate with depth in the deforming layer.

τ (kPa)	depth (m)	p' (kPa)	$\dot{\varepsilon}$ (y^{-1})	p' (kPa)	$\dot{\varepsilon}$ (y^{-1})	p' (kPa)	$\dot{\varepsilon}$ (y^{-1})	p' (kPa)	$\dot{\varepsilon}$ (y^{-1})
10	0	50	0.61	100	1E-05	150	1.59E-08	200	1.64E-10
10	1	60	0.03	110	2.2E-06	160	5.69E-09	210	7.54E-11
10	2	70	0.003	120	5.51E-07	170	2.17E-09	220	3.6E-11
10	3	80	0.0003	130	1.54E-07	180	8.74E-10	230	1.77E-11
10	4	90	5.34E-05	140	4.75E-08	190	3.7E-10	240	9.02E-12
10	5	100	1E-05	150	1.59E-08	200	1.64E-10	250	4.71E-12
15	0	50	158.20	100	0.003	150	4.1E-06	200	4.23E-08
15	1	60	8.71	110	0.0006	160	1.47E-06	210	1.95E-08
15	2	70	0.75	120	0.0001	170	5.61E-07	220	9.3E-09
15	3	80	0.09	130	3.99E-05	180	2.26E-07	230	4.59E-09
15	4	90	0.014	140	1.23E-05	190	9.56E-08	240	2.33E-09
15	5	100	0.003	150	4.1E-06	200	4.23E-08	250	1.22E-09
20	0	50	8144.39	100	0.13	150	0.0002	200	2.18E-06
20	1	60	448.62	110	0.03	160	7.57E-05	210	1E-06
20	2	70	38.67	120	0.007	170	2.89E-05	220	4.79E-07
20	3	80	4.63	130	0.002	180	1.16E-05	230	2.36E-07
20	4	90	0.71	140	0.0006	190	4.92E-06	240	1.2E-07
20	5	100	0.13	150	0.0002	200	2.18E-06	250	6.27E-08
50	0	50	2.3E+09	100	37692.9	150	59.76	200	0.62
50	1	60	1.27E+08	110	8281.63	160	21.42	210	0.28
50	2	70	10944622	120	2076.24	170	8.17	220	0.14
50	3	80	1309570	130	581.51	180	3.29	230	0.067
50	4	90	201281.4	140	178.99	190	1.39	240	0.034
50	5	100	37692.9	150	59.76	200	0.62	250	0.017
100	0	50	3.07E+13	100	5.02E+08	150	795279	200	8203.395
100	1	60	1.69E+12	110	1.1E+08	160	285011.8	210	3776.45
100	2	70	1.46E+11	120	27630499	170	108700.8	220	1802.395
100	3	80	1.74E+10	130	7738758	180	43806.42	230	888.9922
100	4	90	2.68E+09	140	2381962	190	18543.35	240	451.87
100	5	100	5.02E+08	150	795279	200	8203.40	250	236.1155